



Science Reviews

from the end of the world

Volume 2
Number 1
December 2020



Marino Santa María - "Signos primarios" (1994)



Science Reviews

from the end of the world

Science Reviews - from the end of the world is a quarterly publication that aims at providing authoritative reviews on hot research topics developed mainly by scientists that carry out their work far away from the main centers of science. Its research reviews are short, concise, critical and easy-reading articles describing the state of the art on a chosen hot topic, with focus on the research carried out by the authors of the article. These articles are commissioned by invitation and are accessible not only to hardcore specialists, but also to a wider readership of researchers interested in learning about the state-of-the-art in the reviewed subject. The reviews cover all fields of science and are written exclusively in English. They are refereed by peers of international prestige and the evaluation process follows standard international procedures.

Centro de Estudios sobre Ciencia, Desarrollo y Educación Superior
538 Pueyrredón Av. - 2° C – Second building
Buenos Aires, Argentina - C1032ABS
(54 11) 4963-7878/8811
sciencereviews@centroredes.org.ar
www.scirevfew.net

Vol. 2, No. 1
December 2020

AUTHORITIES

AAPC President

Susana Hernández

Centro REDES President

María Elina Estébanez

EDITORIAL COMMITTEE

Editor-in-Chief

Miguel A. Blesa

Co-Editors

Daniel Cardinali (Medicine)

Diego de Mendoza (Biochemistry
and Molecular Biology)

Fabio Doctorovich (Chemistry)

Esteban G. Jobbagy (Ecology)

Karen Hallberg (Physics)

Víctor Ramos (Geology)

Carolina Vera (Atmospheric Science)

Roberto J. J. Williams (Technology)

TECHNICAL TEAM

Editorial Assistant

Manuel Crespo

Proofreader

María Fernanda Blesa

Journal Designer

Gabriel Martín Gil

ISSN 2683-9288

Our cover: *Signos primarios* (1994), by Marino Santa María. From the "Artistas Plásticos con la ciencia" collection. Reproduced by permission from the Comisión Administradora Permanente de la Exposición de Arte Centro Atómico Constituyentes, Comisión Nacional de Energía Atómica.



Science Reviews

from the end of the world

Table of Contents

INTRODUCTION

- 4** Research in the Frontiers between Biology, Chemistry and Physics
Silvia E. Braslavsky y Miguel A. Blesa

IN THIS ISSUE

- 6** List of Authors
Vol. 2, No. 1

ARTICLES

- 7** Illuminating the Inner Retina of Vertebrates: Multiple Opsins and Non-Visual Photoreceptors
Mario E. Guido

- 18** Biophotonics. Fluorescence and Reflectance in Living Organisms
M. Gabriela Lagorio, Gabriela B. Cordon, Analia Iriel, Juan M. Romero, Julián Faivovich and Carlos Taboada

- 42** Recalibrating Immunity in Cancer and Autoimmune Inflammation by Galectin-1-Driven Regulatory Circuits
Camila A. Bach, Anabela M. Cutine, Lorena Laporte, Yamil D. Mahmoud, Montana N. Manselle Cocco, Mora Massaro, Joaquín P. Merlo, Ramiro M. Perrotta, Nicolas Sarbia, Florencia Veigas and Gabriel A. Rabinovich

- 64** Coordination Chemistry of Nitric Oxide and Biological Signaling
José A. Olabe

INSTRUCTIONS FOR AUTHORS

- 82** Guidelines, Publication Ethics and Privacy Statement
Format, references and responsibilities

NEXT ISSUE

- 85** Articles
Vol. 2, No. 2

INTRODUCTION

Research in the Frontiers between Biology, Chemistry and Physics

In this issue of *SREW* we offer four reviews describing each of them several years of research work in their respective group in Argentina.

The interaction of light with the biosphere (area of research called photobiology) is of increasing interest in the world and the Argentinian scientists (from the end of the world) have not been absent.

In fact, there is a very active Argentinian Group of Photobiology (called GRAFOB from the name in Spanish, <https://grupoargentinodefotobiologia.info/site/site/grupar/>), created in 2011, that has already held five successful meetings in various cities in the country and counts with about 200 members from ca 20 groups in many places in Argentina, some of them with a very long tradition of and internationally appreciated research. Two of the several groups working in Photobiology in Argentina present in this issue an overview of their research.

Mario Guido tells us how research in his laboratory at the National University in Córdoba has provided important contributions to the discovery and understanding of the non-visual photoreceptors in vertebrates. These photoreceptors, present in the inner retina of the animals, furnish them with a broad spectral sensitivity and serve them to regulate several vital functions (non-image forming tasks), even before vision (image formation) occurs.

M. Gabriela Lagorio with her group at the University of Buenos Aires has developed fluorescence detection methods and the necessary models to study and interpret the emission of light by living organisms, i.e., by complete fruits, flowers and plants in general as well as by reptiles. Using these methods, in a real multidisciplinary effort and carrying on sophisticated experiments, performed all in Argentina and Brazil, the first emission from frogs (from *Boana punctata*, a South-American species) could be analyzed, quantified, and its origin traced back to a novel fluorophore.

The group led by Gabriel Rabinovich has made breakthrough contributions about the role of galectins, a family of soluble lectins as regulators of immune responses. In this issue we offer their authoritative review on the role of Galectin-1-driven regulatory circuits for immunity in cancer and autoimmune inflammation. As stated by the authors, *understanding the cellular pathways that control Gal-1 expression and function in tumor and inflammatory microenvironments will set the bases for the design of rational therapies based on positive or negative modulation of this endogenous lectin in cancer and autoimmune diseases.*

José A. Olabe is well known for his seminal work on the role of coordination chemistry in the modulation of the properties of the bound ligands. In his article he reviews in deep the fascinating chemistry of nitric oxide, a key intermediate in the nitrogen redox cycles that operate in soils, water and human fluids to provide reversible interconversion pathways between nitrate and ammonia.

All in all, the four reviews comprising this issue of *Science reviews from the end of the world* provide a good insight on the research being carried out in Argentina in the frontiers between biology, chemistry and physics.



Silvia E. Braslavsky



Miguel A. Blesa

Bio**Miguel A. Blesa**

Ph D in Chemistry, La Plata University. Formerly: Chemistry Manager (Atomic Energy Commission); Federal Undersecretary of Science and Technology; Senior Researcher (CONICET); Full Professor (San Martín University); President (Argentine

Association for the Advancement of Science). Past President, Interciencia Association. Member of the National Academy of Science (Córdoba), National Academy of Exact, Natural and Physical Sciences (ANCEFN) and Academy of Sciences of Latin America. TWAS Prize in Chemistry (2004). Konex Merit Diploma in Chemistry (2003). President for Argentina in the Bilateral French Argentine Cooperation Program (ECOS-SUD). Main research interests: chemistry of metal oxide particles immersed in water; environmental chemistry.

Guest Editor of this Issue**Silvia E. Braslavsky**

Silvia E. Braslavsky is Ph.D. of the Univ. Buenos Aires (UBA, 1968). She was a Professor at the Universidad Nacional de Rio Cuarto (1972-75). From 1976 until her retirement in 2007 she led studies on the molecular properties of biological photoreceptors at the Max-Planck Institute for Radiation Chemistry (today for Chemical

Energy Conversion). She is a corresponding member of CONICET and Dr. *honoris causa* of the Univ. Ramon Llull (Barcelona) and of UBA, is Honorary (Univ. La Plata) and Distinguished (Univ. Ottawa and Univ. Cordoba) Professor. From 2000 to 2018 she chaired the IUPAC Subcommittee on Photochemistry. She was de scientific chair of the International Congress on Photobiology (Cordoba, 2014), received the Raices Prize (2011, MINCyT, Argentina) and the Finsen medal (2019, International Union on Photobiology).

IN THIS ISSUE

Illuminating the Inner retina of Vertebrates: Multiple Opsins and Non-Visual Photoreceptors

Received: 08/24/2020 – Approved for publication: 11/05/2020

Mario E. Guido

Biophotonics. Fluorescence and Reflectance in Living Organisms

Received: 08/24/2020 – Approved for publication: 11/05/2020

M. Gabriela Lagorio, Gabriela B. Cordon, Analia Iriel, Juan M. Romero, Julián Faivovich and Carlos Taboada

Recalibrating Immunity in Cancer and Autoimmune Inflammation by Galectin-1-Driven Regulatory

Received: 09/10/2020 – Approved for publication: 09/22/2020

Camila A. Bach, Anabela M. Cutine, Lorena Laporte, Yamil D. Mahmoud, Montana N. Manselle Cocco, Mora Massaro, Joaquín P. Merlo, Ramiro M. Perrotta, Nicolas Sarbia, Florencia Veigas and Gabriel A. Rabinovich

Coordination Chemistry of Nitric Oxide and Biological Signaling

Received: 10/03/2020 – Approved for publication: 11/09/2020

José A. Olabe

Illuminating the Inner Retina of Vertebrates: Multiple Opsins and Non-Visual Photoreceptors

Mario E. Guido

CIQUIBIC-CONICET, Departamento de Química Biológica "Ranwel Caputto", Facultad de Ciencias Químicas, Universidad Nacional de Córdoba, Córdoba, Argentina.
E-mail: mguido@fcq.unc.edu.ar

"Just as our ears provide us with the sense of balance and hearing, each of our eyes is essentially two organs in one"

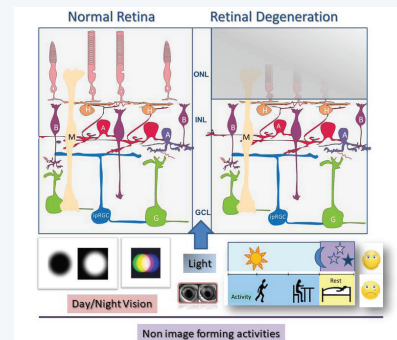
Ignacio Provencio, Scientific American 2011

Abstract

Throughout evolution, the need to detect light has generated highly specialized photoreceptor cells that in vertebrates are mainly located in the retina. The most studied photodetectors within these cells are the visual photoreceptors "cones and rods" responsible for day and night vision, respectively. These cells contain photosensitive molecules consisting of a protein part called "opsin" that binds a chromophore derived from vitamin A, retinaldehyde, capable of photoisomerizing from 11-cis retinal to all-trans retinal form, and triggering the light responses that lead to vision. However, other cells of the inner retina of vertebrates [retinal ganglion cells (RGCs), horizontal cells (HCs), and Muller's glial cells] are currently known to express non-visual photopigments such as melanopsin (Opn4), encephalopsin (Opn3) and neuropsin (Opn5), which would be involved in diverse functions not associated with imaging. Melanopsin is the most widely studied of them, it is expressed in intrinsically photosensitive RGCs (ipRGCs) and HCs of the chicken retina and participates in setting the biological clock, the pupillary light reflex, and presumably in other reflex and subconscious functions, in addition to the lateral interaction between visual photoreceptors and HCs. It is noteworthy that these non-visual photopigments (Opn3, Opn4 and Opn5) respond to blue and/or near violet region light. This particular photosensitivity may provide individuals with a broader spectrum of response to light stimulation within the visible beyond the scope of the visual photoreceptors, regulating an important number of functions not yet completely identified. We can conclude that "a constellation of cells and photoreceptor molecules are present in the inner retina of vertebrates, and from very early stages of development, even before any sign of vision may occur."

Keywords:

retina, non-visual phototransduction, opsins, blue light, non-image forming activities, ganglion cells, horizontal cells, photoreceptors



Introduction

Light is itself an essential source of energy and life on the planet. Many living organisms have developed specific molecules for the detection of light, known as "photopigments" mainly in the visible spectrum. They are located in specialized cells called "photoreceptor cells" placed in the retina of all vertebrates including man (Fig. 1), and in other photosensitive structures in non-mammalian vertebrates such as the pineal gland and nuclei of the deep brain.

The detection of light by such photopigments triggers both the functions associated with vision that involve image formation, and a significant number of reflex and subconscious activities, not associated with imaging. These functions include phototaxis, setting of biological clock by light, pupil constriction, sleep, light inhibition of the hormone “melatonin” in the pineal gland (night signal) and photophobia, among others. Likewise, prolonged deficits or persistent alterations in the lighting environmental conditions due to seasonal changes (short days with low light intensity and long nights), industrialized modern life with continuous artificial lighting day and night, night exposure to daylight tablets, notebooks, cell phones, LED screens and televisions, night work-shifts, or trans-meridian flights, cause marked alterations in physiology and behavior. These include sleep disturbances, the desynchronization of daily behavioral and hormonal rhythms, jet lag, seasonal depression, etc. The latter, called SAD (Seasonal Affective Disorder), are precisely treated with phototherapy by exposure to bright blue light at day to counteract the poor ambient light on short winter days.

Through the perception of light, most living beings can adequately visualize the surrounding environment, as well as perceive the marked changes in light intensity, spectral composition, duration and contrasts that occur throughout the day and night. In animals, such light perception constitutes the primary event that triggers more complex processes leading to the formation of images and non-visual functions. For this, photopigments capture photons and convert them within photoreceptor cells into chemical information and electrical signals. In higher animals, these signals propagate through nerve impulses from the retina to different brain regions. Photopigments called “opsins” are proteins that bind a vitamin A derivative, the retinaldehyde, as a chromophore, able to photoisomerize, making them sensitive to light. Opsins are located in the membranes of specialized cells: “the photoreceptors”. Visual photoreceptors are grouped together forming structures of varying complexity: the eyes (Fig. 1).

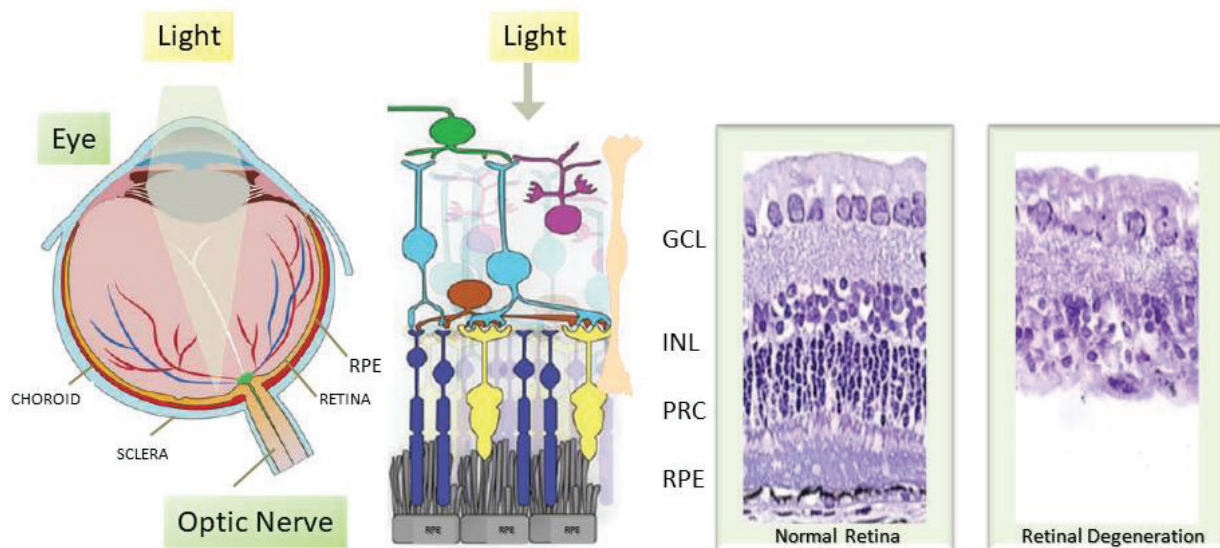


Figure 1. Illustration of the Eye and Retina of vertebrates. Left panels: The retina lies at the back of the eye, it is a multilayered structure that is in contact with the pigment epithelium (RPE) and is made up of Photoreceptor Cells (PRC): cones (yellow) and rods (blue) with external and inner segments and their nuclei forming the outer nuclear layer (ONL). This layer synapses with the outer plexiform layer (OPL) of the inner nuclear layer cells (INL) made up of interneurons: Horizontal Cells (brown), Amacrine (violet) and Bipolar (light blue) whose processes form the inner plexiform layer (IPL) that contacts the Ganglion Cells (GCs, green) of the ganglion cell layer (GCL) whose axons form the optic nerve (green) and project to the brain. Light first strikes these GCs, which in turn contact the feet of Muller Glial Cells (pink) whose body extends throughout the entire inner retina. Right panels: Histological staining of the retina from a healthy control and from a blind animal suffering retinal degeneration and lacking the photoreceptor cell layer (PRC), whereas the inner retina remains viable (INL and GCL).

From an evolutionary point of view, the vertebrate eye has a very important morphological and functional complexity, comprising the eye chamber, which has a set of systems that collects light and projects it onto the retina, located at the back of the eye (Fig. 1). The retina is a multilayered structure that is part of the central nervous system and consists of three neuronal layers (layers of neuron nuclei) and two layers of processes (plexiform layers). The retinal photoreceptor cells

(PRCs), so-called “visual photoreceptors”, are the rods and cones, which are responsible for daytime (color) and night (black and white) vision, respectively. The PRCs are in contact with the retinal pigment epithelium (RPE) that prevents the diffusion of light, and that are in charge of recycling the visual chromophore through the process called “visual cycle”. The interneurons (horizontal cells or HCs, bipolar and amacrine cells), through synapses, connect the PRCs with the retinal ganglion cells (RGCs) whose axons form the optic nerve that conducts nerve information to different areas of the brain involved in vision (visual circuit) and / or through an independent “non-visual” circuit, responsible for the control of subconscious and reflex functions (Fig. 2).

Visual & Non Visual Circuits

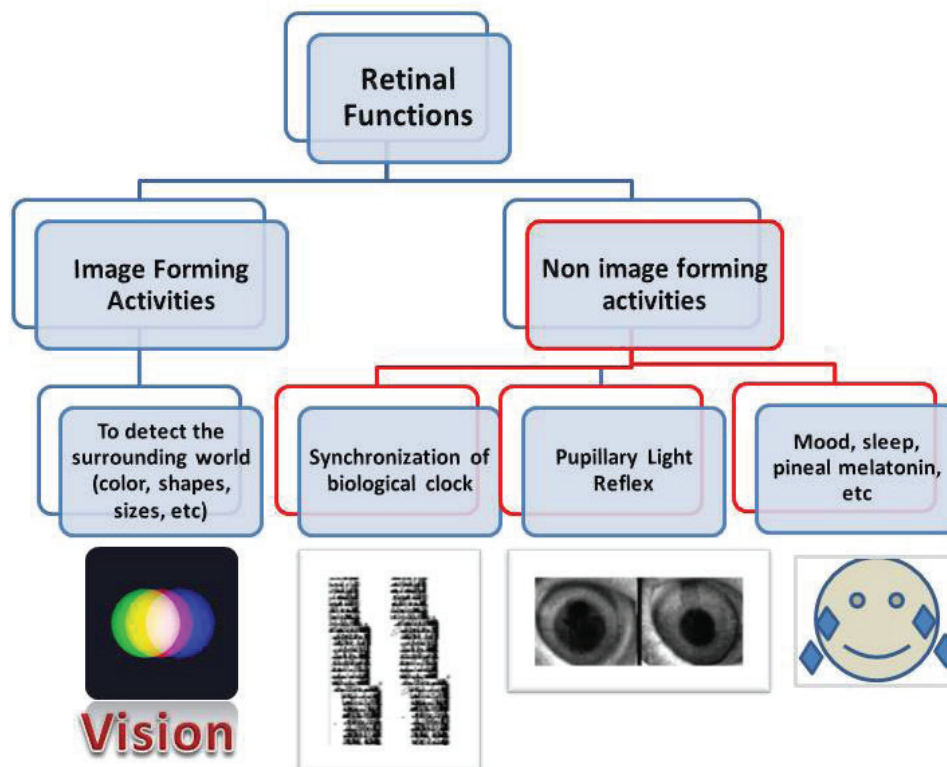


Figure 2. Visual and Non-visual Circuits. Retinal functions. Image forming and Non-image forming tasks. The Visual Circuit (blue) projects from the retina to the brain (visual cortex and other brain areas) and is responsible for coordinating the image-forming activities that lead to vision and allow us to visualize the surrounding environment. The non-visual circuit (red) projects from the retina to various brain areas regulating the physiology and behavior of vertebrates mainly related to subconscious and reflex functions. In non-mammalian vertebrates, light can be detected by the retina, the pineal gland, and deep brain photoreceptors. In GUCY1 * chickens that are blind from birth, light still regulates the daily timing of feeding rhythms (double plot actogram shown below) and the pupillary light reflex (image of a GUCY1 * chicken pupil before and after light stimulation). Light is detected through retinal ganglion cells (RGCs), intrinsically photosensitive (ipRGCs) that project to the brain areas forming a non-visual circuit (red), independent of image-forming activities. This circuit regulates synchronization of daily rhythms by light, pupillary light reflexes, photic inhibition of pineal melatonin, mood, sleep, and other non-visual functions. See text for further details.

At the beginning of the last century, an advanced student at Harvard, Clyde Keeler (1927) observed that his blind pet experienced constriction of the pupils when exposed to light. This intriguing observation induced the question whether it is possible to perceive light even in the absence of vision. These and closely related questions have motivated numerous researchers around the world throughout the last decades and have stimulated them to answer these questions.

Unknown functions for photosensitive cells of the inner retina

Only at the beginning of the 21st century, two fundamental studies shed light on the existence of a circuit different from that related to image-formation, which would be responsible for such photosensitivity. One of these investigations was carried out by Ignacio Provencio and colleagues (2000) who identified a photopigment called melanopsin (Mel or Opn4) (Fig. 3) expressed in mammals in a subpopulation of RGCs. The other by David Berson together with Samer Hattar and collaborators (2002) who described that a subpopulation of RGCs responded directly to light, calling them intrinsically photosensitive RGCs (ipRGC). The peculiarity of these cells is that they project to the anterior hypothalamus, specifically to a small nucleus called the suprachiasmatic nucleus (SCN) and to other “brain” regions. The SCN constitutes the master clock of mammals and is responsible for the temporal control of physiological and behavioral rhythms (Fig. 2). Furthermore, these ipRGCs express the melanopsin photopigment and are also present in non-mammalian vertebrates such as birds, fish and amphibians. Within these vertebrates, the chicken has been the working animal model in our laboratory and we currently know that these birds also contain photosensitive cells in their inner retinas, forming a neural network that feeds an independent non-visual circuit. Specifically, these ipRGCs would be responsible, through projections to specific areas of the brain, of daily synchronizing the biological clock to external lighting conditions, of controlling the pupillary reflex, and of regulating by light other processes not associated with imaging (review: Guido et al., 2010) (Fig. 2).

Against this background, a fundamental question arises about how these ipRGCs act and transmit information to the brain. To answer this question, we had to isolate the ipRGCs, keep them in culture and study their responses to light, at the biochemical and molecular levels, as well analyze the nature of the potential phototransduction cascade. Our group first described the photocascade that takes place in any vertebrate ipRGCs through studies with primary cultures of chicken RGCs at early embryonic stages, in which the only differentiated retinal cells are these RGCs. We applied molecular, biochemical and pharmacological tools (Contin et al., 2006; 2010). From these studies, we observed that these photosensitive cells act through a photocascade that involves retinaldehyde as the chromophore, a Gq protein as a transducin, and a phospholipase C, - an enzyme that hydrolyzes phosphoinositides - as an effector enzyme, ultimately causing mobilization of intracellular calcium, and the activation of TRP-like transient potential receptors (Contin et al., 2006; 2010; Diaz et al 2014; 2017) (Fig. 4). The mobilization of intracellular calcium induces the depolarization of the cell and the light-triggered process is highly similar in its biochemical nature to the phototransduction cascade that occurs in invertebrate photoreceptors (rhabdomeric photoreceptors). Furthermore, these ipRGCs would derive from an ancestral photoreceptor common with invertebrate photoreceptors, which has endured throughout evolution coexisting with the rods and cones within the retina, in order to complement the activity of these visual photoreceptors (day and night vision). Likewise, ipRGCs appear very early in the development of vertebrates, before any specific signal of formal vision is detected. The question that then arises is: What would be the function of these early photoreceptor cells? In fact, it is sensing light and darkness at day and night. We currently know that these intrinsically photosensitive cells are responsible for photodetection mainly associated with light control of various non-visual functions.

VISUAL AND NON VISUAL PHOTOPIGMENTS

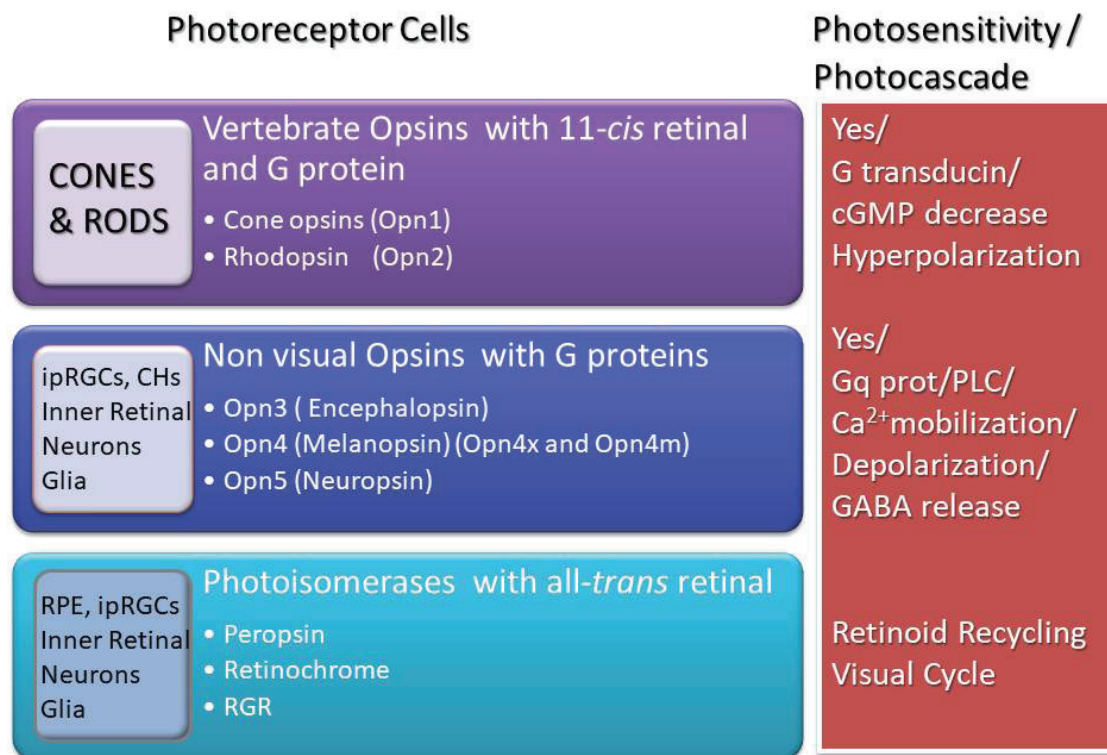


Figure 3. Visual and Non-visual Photopigments and Photoisomerases. Visual Opsins are the visual photopigments that include short, medium and long wavelength opsins (Opn1) and rhodopsin (Opn2) present in the outer segments of cones and rods (visual photoreceptor cells) and are involved in day and night vision, respectively. The chromophore 11-*cis* retinal (vitamin A derivative) is bound to a lysine residue in the protein part of the photopigment. Upon light stimulation, 11-*cis* retinal is photoisomerized to all-*trans* retinal. Opsins are coupled to a G protein that acts as the light transducer.

Non-Visual Opsins: include opsins that use retinal as a chromophore and bind to a G protein. These opsins include: Opn3 (encephapsin), Opn4 (melanopsin), and Opn5 (neuropsin). The peculiarity of these opsins is that they respond to blue (Opn3 and Opn4) and UV (Opn5) light and are involved in the regulation of various light-driven non-visual functions. Melanopsin: Throughout evolution, vertebrates have conserved 2 Opn4 genes (Opn4m and Opn4x). Opn4x has been lost in mammals along with other opsins, likely during the mammalian entrance into the nocturnal phase. Non-mammalian vertebrates (birds, fish, etc.) possess both Opn4 genes (Opn4m and Opn4x), which encode for the corresponding proteins and isoforms differentially expressed in ipRGCs and HCs of the inner retina. The phototransduction cascade triggered by Opn4 activation, involves the Gq protein, phospholipase C (PLC) activation, Ca²⁺ mobilization, and membrane depolarization with GABA release in the inner retina. Opn3 and Opn5 are expressed in neurons of the inner retina and in Müller glial cells through cascades and functions not yet fully elucidated. The third group involves **Photoisomerases** that bind all-*trans* retinal: **Peropsin, Retinochrome and RGR**. They are expressed in the retina of vertebrates, mainly in the retinal pigment epithelium (RPE), inner retinal cells and Muller glial cells, and involved in the recycling of the chromophore required to constitute an active photopigment.

Various photoreceptors/photopigments coexist in the vertebrate eye

It is really remarkable that, although there is a variety of eye types with greater or lesser complexity in nature, only a very limited number of photoreceptor cell types are observed: the photoreceptors of invertebrates called “rhabdomerics” and the ciliated photoreceptors of vertebrates (PRCs cones and rods, Fig. 1), and photoreceptors of the pineal gland in non-mammalian vertebrates. Rhabdomeric photoreceptors present a membrane arrangement organized in microvilli where the photopigments are concentrated, whereas the ciliated photoreceptors present the cilium folded back on itself, forming saccules in the external segment that contains the opsins. In both types of photoreceptors, opsins are covalently bound to the vitamin A-derived chromophore, the retinal. However, and beyond the fact that the different types of opsins have a certain homology, they use different nervous transduction systems with opposite electrochemical signals. Rhabdomeric photoreceptors are depolarized by light (becoming more positive inside), whereas ciliated photoreceptors

are hyperpolarized by light (becoming less positive inside). In invertebrates, rhabdomeric photoreceptors, associated with pigment cells, form the eyes, whereas in vertebrates they would have transformed into RGCs (ipRGCs) and other cells of the inner retina such as amacrine and horizontal cells (HCs). These retinal neurons are evolutionarily sister cells with RGCs by sharing specification factors and also retaining intrinsic photosensitivity as described above (Fig. 3). On the other hand, ciliated photoreceptors evolved into photoreceptors of the pineal organ of the brain and in the retina into rods and cones. The cones are sensitive to intense light and have opsins that respond to different wavelengths (short, medium and long; day vision, color), whereas the rods are sensitive to low-intensity light (night vision).

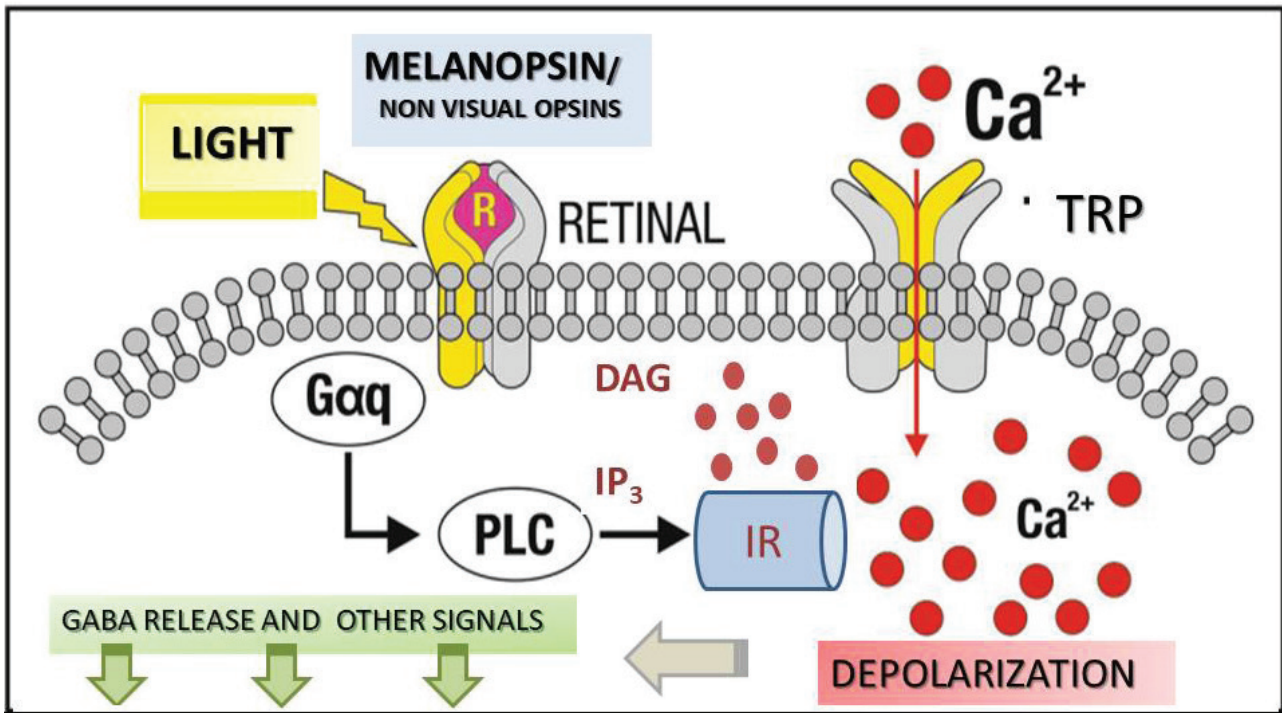


Figure 4. Phototransduction cascade of non-visual photoreceptors of vertebrates. This photocascade operates in intrinsically photosensitive ganglion cells (ipRGCs) and horizontal cells (HCs) expressing melanopsin proteins (Opn4m and Opn4x). Once a photon strikes the melanopsin or another non-visual photopigment, the retinal chromophore isomerizes from 11-*cis* retinal to all-*trans* retinal. This photoisomerization activates a Gq protein that acts as a light signal transducer activating an effector protein, the enzyme phospholipase C (PLC). In turn, PLC hydrolyzes the phosphoinositides (PIP₂), minor lipids of the membranes, producing intracellular lipid mediators (inositol-triphosphates IP₃ and diacylglycerol DAG) with the consequent Ca²⁺ mobilization inside the cell through inner reservoirs (IR) or transient potential channels located in the membrane (TRP) (Contin et al., 2006; 2010, Diaz et al., 2014). The increase of Ca²⁺ inside the cell produces the depolarization of the membrane, making it more positive inside with the consequent release of the GABA neurotransmitter in HCs (Morera et al., 2016) or other neurochemical signals.

In the vertebrate retina, photoreceptors also differ in the functions they regulate since PRCs are responsible for the processes required directly for vision, and associated with imaging, whereas ipRGCs regulate reflex and subconscious functions (Fig. 2). Based on the presence of the melanopsin photopigment, on the biochemical characteristics of the photocascade triggered in response to light, and on a group of transcription and specification factors, phylogenetically conserved and expressed by these cells (Pax6, Ath5, Brn3 and BarH genes), it could be concluded that these inner retina cells of vertebrates (ipRGCs, HCs and amacrine) share a common evolutionary ancestor with the photoreceptors of invertebrates. Furthermore, our group also recently demonstrated that in the chicken embryonic retina, HCs that express a particular isoform of the melanopsin photopigment (mel x) exhibit photosensitivity to blue light causing cell depolarization with calcium mobilization and GABA release (Morera et al., 2016). It is noteworthy that these HCs are in direct contact with the visual photoreceptor cells “cones and rods” through the outer process / plexiform layer, and could have the dual role of regulating lateral interaction in response to blue light or cooperate with the ipRGCs circuit to control light-triggered non-visual functions.

A variety of new photopigments illuminate the inner retina of vertebrates

The first evidence supporting the concept that the melanopsin photopigment is responsible for the aforementioned photosensitivity came from a series of pioneering studies showing that immortalized non-retinal cells became photosensitive after induction of melanopsin expression (heterologous expression), whereas on the other hand, genetically engineered mice not expressing melanopsin and lacking functional cones and rods, completely fail to detect all types of light stimulation (reviewed in Guido et al., 2010, and Diaz et al., 2015).

The photopigment melanopsin was initially described by Ignacio Provencio in the frog (*Xenopus*) and later it was found that it is also expressed in the brain, iris and retinal cells of most vertebrates (Provencio et al., 2000). There are at least 2 genes that encoded for melanopsin: Mel-x (Opn4x) and Mel-m (Opn4m), with homologies to the *Xenopus* (Opn4x) or mammalian (Opn4m) genes, respectively (Bellingham et al., 2006) (Fig. 3). It is noteworthy that Mel-m is only expressed in mammals, whereas in birds, amphibians and fish both Mel-m and Mel-x are expressed. The loss of Mel-x by mammals could be due to the entry of mammals into the night niche, which produced a significant reduction in photosensitivity, so that as compared to marsupials, mammals suffered the loss of the genes of Mel-x and of some visual opsins. Although some of the visual opsins were later recovered by gene duplication it was not the case of Mel-x. On the other hand, in birds and other non-mammalian vertebrates, more complex photodetection systems were preserved during evolution including the pineal organ and deep brain photoreceptors, responsible for measuring day length and involved in processes such as seasonal migration and reproduction (Valdez et al., 2009; 2013; reviewed in Guido et al., 2010).

In birds, the presence of messenger RNAs and proteins has been reported for both Mel-x and Mel-m photopigments. The different melanopsin proteins and their isoforms display sensitivity to blue light close to 480 nm, are expressed in the retina and are confined in a first stage of development to the RGCs, their axonal fibers and along the optic nerve that connects the retina with the brain (Verra et al., 2011). All these findings were observed at stages at which retino-tectum projections are formed. At later and postnatal embryonic stages, a marked spatial separation is observed between both proteins, whereas Mel-m remains confined to a subpopulation of RGCs, Mel-x is also expressed very strongly in other cells of the inner retina, reaching maximum expression in the outer plexiform layer that contacts rods and cones and comprises HCs. Such HCs reach their differentiation and final destination within the retina, coinciding with the robust expression of Mel-x and its colocalization with the transcription factor Prox1, specific marker of HCs. Indeed, the opsin Mel-x is expressed in sister cells of the ipRGCs, the HCs, which have also retained the intrinsic photosensitivity as we recently demonstrated (Morera et al., 2016).

Non-visual opsins and photoisomerases present in the inner retina of vertebrates

In addition to the melanopsin that is expressed in ipRGCs and HCs, other photopigments have been described in the inner retina of vertebrates; they are the opsins Opn3 (called encephalopsin) and Opn5 (called neuropsin), and the photoisomerase RGR (Retinal G protein coupled Receptor), whose expression we have found in rat and chicken retina (Nieto et al., 2011; Diaz et al., 2017; Rios et al., 2019) (Fig. 3). The Opn3 and Opn5 photopigments belong to the family of G protein-coupled opsins that bind retinaldehyde as a chromophore, and respond to blue and UV light, respectively. The generic name of both opsins is due to the fact that they were first found expressed in the brain, but today it is known that they are expressed in the vertebrate retina, and in extra-retinal tissues, such as the skin, with potential functions not yet fully characterized. In chicken, both opsins are expressed in nerve cells of the embryonic inner retina and in Müller glial cells (Rios et al., 2019). Furthermore, primary cultures enriched in Müller's glial cells that express these photopigments respond to blue light of high intensity and prolonged duration (> 20 seconds), mobilizing intracellular calcium, through a cascade not completely characterized even from the biochemical point of view (Rios et al., 2019) (Fig. 3). These novel findings suggest the possibility that these retinal glial cells are detecting long-term light (prolonged stimuli) and generating responses that modulate the interaction between cells or between glia and neurons.

Likewise, other studies carried out in our laboratory showed that RGR photoisomerase is expressed in early stages of embryonic development in neurons and glia, and especially in melanopsin (+) ipRGCs (Diaz et al., 2017). This photoisomerase would be essential to regulate by light the endogenous content of retinoids (retinals, retinols and retinyl esters) required by the inner retina to provide the photopigments with enough active chromophore needed for the photic responses.

From the retina to the brain. Retinal photoreceptor cells and visual circuits. Experimental models for the study of non-visual photoperception.

The vertebrate eye always acts as a sensor for ambient lighting conditions even in the absence of vision. In any case, and even in the face of these conditions, the retina is the gateway for light information that regulates different non-visual

functions that synchronize the physiology and behavior of organisms with the external environment (day-night / light cycles- darkness) (review in Guido et al., 2010) (Fig. 1 and 2). Indeed, the presence of a different group of photoreceptors housed in the inner retina of vertebrates and containing non-visual photopigments of maximum absorbance in the blue region, has given vertebrates the evolutionary advantage of higher photosensitivity in a spectral region wider than that covered by rods and cones, and has enabled them to regulate other functions, not only those associated with imaging.

In humans, even suffering certain types of blindness with progressive retinal degeneration, reflection of their pupils to light stimulation or acute inhibition by light of the nocturnal pineal melatonin production can be observed. This strongly indicates that a light detection system that functions to regulate such non-visual functions by light still remains in the retina of these individuals. These observations, transferred to animal models of mammals with retinal degeneration, mainly in mice, with the consequent loss of their PRCs, show the existence of a different population of non-canonical retinal photoreceptors - the ipRGCs - responsible for regulating functions not associated with imaging. To perform studies on non-mammalian vertebrates, we used wild-type Rhode Island chickens as healthy controls together with GUCY1* chickens suffering a retinopathy similar to Leber's congenital amaurosis (LCA) in humans. These chickens suffer blindness from birth and have their PRCs (cones and rods) non-functional and subject to progressive degeneration (Valdez et al., 2009; 2013). However, these animals maintain functional the rest of their retina, constituting an experimental model of important utility to evaluate the persistence of photoperception under pathological conditions, the functioning of RGCs and other cells of the inner retina (neuronal or glial types), the participation of them in non-visual photoreception mechanisms, and the type of photocascade and mechanisms that take place in response to light. GUCY1* chickens carry a mutation in the guanylate cyclase enzyme involved in phototransduction that inactivates this enzyme, with the consequent lack of production of cyclic GMP, the second messenger essential in the activation of cationic channels that generate the dark current in the absence of light in visual photoreceptors (cones and rods).

After developing a colony of this LCA model in Córdoba, in a first stage we proceeded to characterize these animals with histological and electroretinographic studies. These animals were clinically blind, with their PRCs cones and rods completely non-functional. During the first weeks of life, the retinas of GUCY1* chickens appear morphologically normal. However, after ca. 3 months of life, the PRC layer shows signs of degeneration, whereas the rest of the inner retina (inner nuclear layer and RGCs) remains intact (Fig. 1, histological staining in right panel). On the other hand, these animals do not show any electrical activity in response to light of diverse intensities and wavelengths, at any age (Valdez et al., 2009). In a second stage we proceeded to study possible responses to light, evaluating behavioral and physiological parameters that were light regulated. To this end, and since the chickens have daytime habits, we investigated the light synchronization of the daily feeding rhythms and the pupillary constriction reflex. Every time the animals are fed, a signal is recorded through a feeding system with an infrared detector, which generates 24-hour recordings collected for weeks and months so-called "actograms". These "feeding rhythms" recordings were utilized with both GUCY1* chickens and their healthy controls after exposure to different lighting conditions (see bottom panel Fig. 2). The blind animals adjusted their daily feeding rhythms with precision to the different imposed lighting phases and to light-darkness (LD) patterns with 4 hours advance or delay, in the same way as the control animals. These daily rhythms persisted in the blind even with occlusion of their extra-retinal photoreceptors located in the pineal gland and deep brain, and / or after the surgical removal of the pineal gland (pinealectomy) (Valdez et al., 2009, 2013). Even in blindness, these animals perceive light that accurately synchronizes their rhythms of feeding activity to the imposed cycles or enter "free run" (endogenous rhythm) in constant conditions of darkness (DD) or light (LL) with periods close to 24 h. However, these responses are lost with enucleation (removal of eye cells), indicating that cells of the inner retina (ipRGCs) are responsible for this light regulation.

By measuring pupil constriction in GUCY1*, in response to different light intensities and wavelengths within the visible spectrum, another light-controlled function can be addressed, and by performing a sensitivity spectrum, we were able to investigate what type of photopigment is controlling such a function. From a dose-response curve, we determined the sensitivity spectrum (responses to light of certain wavelengths) for the consensual pupillary reflex (one eye exposed to lights and recorded in the other). Indeed, the GUCY1* chickens maintain the consensual pupillary light reflexes as well as the control animals, so that the contraction of the pupil persists in response to light stimulation, even in the absence of classic PRCs (Valdez et al., 2009; 2011) (see bottom panel Fig. 2). The responses obtained indicated that pupillary light reflexes are mediated by an opsin based on vitamin A2, with maximum absorbance at 484 nm, coinciding with the the photopigment melanopsin absorption spectrum (Valdez et al., 2009). Our studies also showed that this photopigment is expressed in the RCCs of healthy and blind chickens (Valdez et al., 2009, Verra et al., 2011). The pupillary reflex is mediated by a subpopulation of RGCs projecting to the pretectal region (OPN) and the Edinger-Westphal nucleus (EW) that bilaterally innervate the ciliary ganglion (CG), producing constriction of the pupil of both eyes (illuminated and contralateral) and indicating the integrity and functionality of the whole circuit (Fig. 2). From these series of studies, it is concluded that GUCY1* chickens, despite clinical blindness, perceive light through the inner retina and their ipRGCs. This perception allows them to regulate different non-visual activities: the setting of the daily rhythms, and the pupillary light reflex. Furthermore, subsequent studies showed that the maximum pupillary constriction is observed during the day and with exposure to blue light (Valdez et al., 2015).

Conclusions

From this set of studies carried out with cell cultures and “*in vivo*” experiments, we can conclude that:

- a constellation of cells and photoactive molecules are present in the inner retina of vertebrates and very early in embryonic development, even before there are concrete signs of the functioning of the vision processes. This happens in different populations of retinal cells that have the ability to respond to light, mainly in the blue spectral region, and complementing the visual function associated with imaging. These populations are: i- Isolated chicken RGRs, characterized and maintained in culture, at very early stages of development. These cells are intrinsically sensitive to light through a transduction cascade with depolarization of the membrane and mobilization of calcium (Contin et al., 2006; 2010; Diaz et al., 2014). These cells express Mel-x and Mel-m as well as the RGR photoisomerase that allows them to recycle the chromophore in light (Contin et al., 2006; 2010; Verra et al., 2011; Diaz et al., 2014; 2017) (Fig. 3).



Aerial view photography of Córdoba International Airport area (Córdoba, Argentina) that somehow resembles the multilayer organization of the vertebrate retina and its illuminated visual/non-visual circuits.

ii- The HCs expressing Mel-x that respond to blue light through a photocascade that involves calcium mobilization and release of the GABA neurotransmitter (Fig. 4). These HCs probably act in processes of lateral interaction in contact with cones and rods, and/or cooperating with the ipRGCs in non-visual functions (Morera et al., 2016).

iii- Muller’s glial cells and other cells, which express Opn3 and Opn5, respond to longer-time light stimuli, mainly blue light, mobilizing intracellular calcium through a mechanism not yet elucidated (Rios et al., 2019), and collaborating potentially in processes related to neuron-glia or glia-glia interaction under prolonged light stimuli (Figs. 3).

- Through “*in vivo*” studies with the GUCY1* chickens, we observed that: i) although these animals suffer blindness from birth, they perceive light through their inner retina and their ipRGCs, regulating the pupillary reflex and daily feeding activity (Valdez et al., 2009; 2011; 2013) (Fig. 2). Such photoperception persists even under conditions of occlusion or

loss of extraocular photoreceptors. However, this photosensitivity is lost with enucleation. These findings highlight a non-visual circuit similar to that described in mammals involving cells of the inner retina, specifically the RGCs and their projections to different brain areas. In fact, their projections to the hypothalamic SCN regulate the photic synchronization of behavior, whereas projections to the pretectal region produce the constriction of the pupil of both eyes (illuminated and contralateral). Nevertheless, new evidence obtained in mammals indicates that ipRGCs could also contribute in some way to vision since some RGCs that express melanopsin also project to visual areas, which opens an intriguing panorama of even greater complexity, potential impact and great challenge for their future study.

Acknowledgments

This work has been supported by the National Agency for Scientific and Technical Promotion (FONCyT) (PICT 2004 Nr 967, PICT 2006 Nr 898, PICT 2010 Nr 647, PICT 2013 Nr 021, PICT 2016 Nr 0187), National Council for Scientific and Technical Research of Argentina (CONICET), Ministry of Science and Technology of Córdoba (MinCyT-Cba), Secretariat of Science and Technology-National University of Córdoba (SeCyT-UNC); Antorchas Foundation, Florencio Fiorini Foundation, CAEN-ISN and John Simon Guggenheim Memorial Foundation (2009). Author is grateful to *Ciencia Hoy* for the kind authorization to use Figure 1 from Guido ME (2016) *Ciencia Hoy* 151, 43-46. ISSN 1666-5171.

References

- [1] Bellingham, J.; Chaurasia, S.S.; Melyan, Z.; et al. Evolution of melanopsin photoreceptors: discovery and characterization of a new melanopsin in nonmammalian vertebrates. *PLoS Biology* 2006, 4, e254.
- [2] Berson, D.M.; Dunn, F.A.; Takao, M. Phototransduction by retinal ganglion cells that set the circadian clock. *Science*, 2002, 295, 5557, 1070-1073.
- [3] Contin, M.A.; Verra, D.M.; Salvador, G.; Ilincheta, M.; Giusto, N.M.; Guido, M.E. Light-activation of the Phosphoinositide Cycle in Intrinsically Photosensitive Chicken Retinal Ganglion Cells. *Invest. Ophthalmol Vis. Sci.* 2010, 51, 11, 5491-5558.
- [4] Contin, M.A.; Verra, D.M.; Guido, M.E. An invertebrate-like phototransduction cascade mediates light detection in the chicken retinal ganglion cells. *The FASEB J.* 2006, 20, 14, 2648-50.
- [5] Diaz, N. M.; Morera, L. P.; Verra, D. M.; Contin, M. A.; Guido, M.E. Early appearance of non-visual and circadian markers in the developing inner retinal cells of chicken. *BioMed Res. Int.* 2014, 1-9, dx.doi.org/10.1155/2014/646847.
- [6] Díaz, N. M.; Morera, L. P.; Guido, M.E. Melanopsin and the Non-visual Photochemistry in the Inner Retina of Vertebrates. *Photochem. Photobiol.* 2015, 92, 1, 29-44. doi: 10.1111/php.12545.
- [7] Díaz, N. M.; Morera, L. P.; Tempesti, T.; Guido, M.E. The Visual Cycle in the Inner Retina of Chicken and the involvement of Retinal G-Protein-coupled Receptor (RGR). *Mol. Neurobiol.* 2016, 1-11, doi:10.1007/s12035-016-9830-5.
- [8] Guido, M.E.; Garbarino, E.; Contin, M.A.; Valdez, D.; Nieto, P.; Verra, D.; Acosta, V.; de Zabalia, N.; Rosenstein, R.E. Inner retinal circadian ccks and non-visual photoreceptors: novel players in the circadian system. *Prog. Neurobiol.* 2010, 92, 4, 484-504.
- [9] Hattar, S.; Liao, H.W.; Takao, M.; Berson, D.M.; Yau, K.W. Melanopsin-containing retinal ganglion cells: architecture, projections, and intrinsic photosensitivity. *Science*. 2002, 295, 5557, 1065-70.
- [10] Keeler, C. E. Iris movements in blind mice. *Am. J. Physiol.* 1927, 81, 107-112.
- [11] Morera, L. P.; Díaz, N. M.; Guido, M.E. Horizontal cells expressing melanopsin x are novel photoreceptors in the avian inner retina. *Proc. Natl. Acad. Sci. USA.* 2016, 113, 46, 13215-13220.
- [12] Nieto, P.S.; Valdez, D.J.; Acosta-Rodriguez, V.A.; Guido M. E. Expression of novel opsins and intrinsic light responses in the mammalian retinal ganglion cell line RGC-5. Presence of Opn5 in the rat retina. *PLoS One*, 2011, 6, 10, e26417. ISSN 1932-6203.
- [13] Provencio, I. Hidden Organ in Our Eyes Found to Control Circadian Rhythms and Emotions. *Scientific American* 2011, 304, 5, 54-59.

- [14] Provencio, I.; Rodriguez, I.R.; Jiang, G.; Hayes, W.P.; Moreira, E.F.; Rollag, M.D. A novel human opsin in the inner retina. *J Neurosci*, 2000, 20, 2, 600-605.
- [15] Rios, M.N.; Marchese, N.A.; Guido, M.E. Expression of non-visual opsins Opn3 and Opn5 in the developing inner retinal cells of birds. Light-responses in Muller glial cells. *Front. Cellular Neurosci*. 2019, doi: 10.3389/fncel.2019.00376
- [16] Tessier-Lavigne M. Phototransduction and information processing in the Retina. *In Principles of Neural Science*, 3rd edn (Edited by E. R. Kandel, J. H. Schwartz and T. M. Jessell), 1991, 401–418. Appleton & Lange, Norwalk.
- [17] Valdez, D. J.; Nieto, P. S.; Garbarino-Pico, E.; Avalle, L. B.; Díaz-Fajreldines, H.; Schurrer, C.; Cheng, K.; Guido, M. E. A Non-Mammalian Vertebrate Model of Blindness Reveals Functional Photoreceptors in the Inner Retina. *The FASEB J*, 2009, 23, 4, 1186-1195.
- [18] Valdez, D.; Nieto, P.; Diaz, N.; Garbarino-Pico, E.; Guido, M. E. Differential Regulation of Feeding Rhythms through a Multiple-Photoreceptor System in an Avian Model of Blindness. *The FASEB Journal*, 2013, 27, 7, 2702-12.
- [19] Valdez, D.J.; Nieto, P.S.; Della Costa, N.S.; Schurrer, C.; Guido M. E. Circadian control of the pupillary light responses in an avian model of blindness, the GUCY1* chickens. *Invest Ophthalmol Vis Sci*. 2015, 56, 2, 730-737.
- [20] Verra, D. M.; Contin, M. A.; Hicks, D.; Guido, M. E. Early onset and differential temporospatial expression of melanopsin isoforms in the developing chicken retina. *Invest. Ophthalmol. Vis. Sci*. 2011, 52, 5111-5120.

Bio



Mario E. Guido

Mario E. Guido is a full professor at the Department of Biological Chemistry “Ranwel Caputto” (DQBRC), School of Chemistry, National University of Córdoba (UNC), Argentina and Principal Research Investigator of CONICET in the Centro de Investigaciones en Química

Biológica de Córdoba (CIQUIBIC)-CONICET. He did a PhD in neurochemistry at the UNC (1986-91) and a postdoctoral training in chronobiology at Dalhousie University, Halifax, Canada (1993-97). He runs a laboratory dedicated to investigate the molecular basis of circadian rhythms in lipid metabolism in the nervous system and nonvisual phototransduction mechanisms in the retina. He is vice director of CIQUIBIC, member of the Latin America Academy of Sciences, and JS Guggenheim Memorial Foundation fellow (2009).

Biophotonics. Fluorescence and Reflectance in Living Organisms

M. Gabriela Lagorio,^{1,2,*} Gabriela B. Cordon,^{3,4,*} Analia Iriel,^{5,*} Juan M. Romero,^{1,2,*} Julián Faivovich,^{6,7,*} and Carlos Taboada^{8,*}

¹ CONICET, Universidad de Buenos Aires, INQUIMAE, Facultad de Ciencias Exactas y Naturales, Buenos Aires, Argentina.

² Universidad de Buenos Aires, Facultad de Ciencias Exactas y Naturales, Dpto. de Química Inorgánica, Analítica y Química Física, Ciudad Universitaria. Plaza Gregorio Klimovsky, Pabellón II, 1er piso, C1428EHA, Buenos Aires, Argentina.

³ Universidad de Buenos Aires, Facultad de Agronomía, Área de Educación Agropecuaria, Buenos Aires, Argentina.

⁴ CONICET, Universidad de Buenos Aires, Instituto de Investigaciones Fisiológicas y Ecológicas Vinculadas a la Agricultura (IFEVA), Buenos Aires, Argentina.

⁵ CONICET, Universidad de Buenos Aires, Instituto de Investigaciones en Producción Animal (INPA), Facultad de Ciencias Veterinarias, Buenos Aires, Argentina.

⁶ División Herpetología, Museo Argentino de Ciencias Naturales "Bernardino Rivadavia", Consejo Nacional de Investigaciones Científicas y Técnicas (CONICET), Ciudad de Buenos Aires C1405DJR, Argentina.

⁷ Departamento de Biodiversidad y Biología Experimental, Facultad de Ciencias Exactas y Naturales, Universidad de Buenos Aires, Ciudad de Buenos Aires C1428EHA, Argentina.

⁸ Department of Biology, Duke University, Durham, NC, 27708, USA

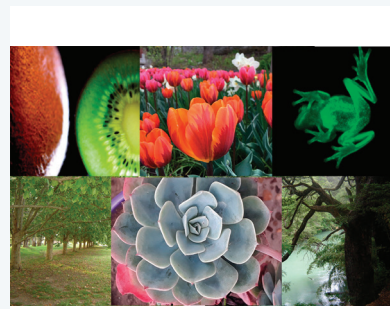
* These authors contributed equally to this work.

** Corresponding author. E-mail: mgl@qi.fcen.uba.ar

Dedicated to the memory of Professor Enrique San Román

Abstract

The light that emerges from a biological entity is relevant from many aspects. In the first place, it allows the construction of the organism's image and consequently it is responsible for visual perception and communication. Secondly, it can become an important tool in obtaining both physiological and chemical information from the observed entity, in a non-destructive way. When an organism is illuminated, the non-absorbed energy emerges as transmitted or reflected light. Additionally, fluorescence, phosphorescence or bioluminescence may be emitted. In our research group, we have studied and modelled the light released as reflectance and fluorescence for different biological systems like flowers, fruits, plant leaves, canopies, bird's plumage and amphibians. In this review, we present the advances we have made in this area. They range from the development of theoretical approaches to the implementation of optical methodologies for practical applications. The analysis of light interaction with biological material, which is the domain of biophotonics, has recently acquired great importance in view of the increasing use of optical techniques to the study of living tissues. However, the interpretation of the photophysical and spectroscopic properties of these systems is usually complicated by several factors: elevated chromophore's concentration, optical inhomogeneity, multi-scattering of photons and presence of multi-layered structures in most cases. Because of these, the accurate modelling of the interaction with light helps to avoid artifacts and to better interpret the processes that take place. Physical models used in the analysis of chlorophyll fluorescence in leaves and canopies with application in remote sensing, optical methodologies for food control and quantification of fluorescence *in vivo* for evaluation of its biological relevance are examples of the use of the emission of light and will be presented in this review.



Keywords:

chlorophyll fluorescence, fluorescence quantum yield, scattering media, light re-absorption, fluorescence modelling, plant biophotonics, optical biosignals

Introduction

The study of light and its interaction with matter has been relevant since ancient times and has now acquired an unusual prominence within the field of biophotonics [1].

The term biophotonics comes from the Greek “bios= life” and “phos= light” and the word photonics involves all methodologies and technologies that generate, manipulate and detect photons (UV, visible or IR). So, biophotonics can be briefly defined as the study of optical processes in biological systems. It is concerned with the development of spectroscopic and imaging techniques to non-destructively obtain information from intact cells, organelles, tissues or organisms. In practice, it is a real challenge because biological tissues are usually rich in chromophores, optically non-homogeneous, multi-layered and multi-dispersive in photons. These features of biological entities complicate the interpretation of the light processes that take place in them and physical models to achieve a thorough comprehension of what is really happening in the system are necessary. Modelling also allows for the correction of distortions and artifacts and therefore introduces greater reliability in the information obtained from the analysis of the light released by the material [2].

Biophotonics is applicable to any type of biological tissue and is particularly useful in biomedical and clinical research activities [3]. Similarly, the field of plant biophotonics has been growing rapidly in recent years [4]. In fact, the optical technology resulting from these studies can improve agricultural production and crop quality. It serves to predict the optimal amount of fertilizers to be used, avoiding overdoses and thus preventing undue environmental damage. It also allows the determination of the harvest time and even the surveillance of vegetables and fruits during the post-harvest period. It is also applicable in environmental sciences since natural or anthropogenic alterations in the surroundings affect organisms and usually induce changes in their absorption, reflectance or emission of light. This is particularly true for plants and algae where there is a great interconnection among light absorption, reflectance, fluorescence and photosynthesis [5].

The study of the light emanating from a biological entity is not only interesting for the aspects described above but also for its primary function as a signal in visual connection and communication. A light stimulus from a “sender” is considered an optical communication signal if it is capable of influencing the behaviour of a “receiver”. From a physical point of view, to evaluate the relevance of released photons as visual signals, the characteristics of the emitted light (intensity and wavelength) and the sensitivity spectral curves of the optical photoreceptors of the receiver should be analysed in conjunction [6].

This review addresses the analysis of light emanating from biological entities, with emphasis on reflected light and light emitted as fluorescence. Various physical models are presented to correct distortions and to improve the understanding of what is actually observed in the different systems. Advances in the interpretation of signals in the field of biology, recent contributions in the area of chlorophyll fluorescence to assess plant health and the development of non-destructive optical methods for food quality assessment are shown.

1. Reflectance in biological systems

1.1. Connecting reflectance with chromophore concentration

When a beam of light strikes a tissue, some of the light is absorbed, some is transmitted, and some is reflected. In turn, some of the absorbed light can be emitted as luminescence.

In a general case, reflected light consists of two components: specular and diffuse reflection. While the specular component is reflected at one definite angle, diffuse reflection is scattered in all directions. In fact, the diffuse component is due to the penetration of a fraction of the incoming light into the sample and a subsequent return of the non-absorbed radiation to the surface after multiple scattering at the boundaries present inside the material [7]. In biological entities the diffuse component and consequently light scattering are usually remarkably large.

One of the most used theories to quantify the interaction of light with materials containing small particles which absorb and scatter radiant energy is the Kubelka–Munk (K-M) approach. This theory applies to diffuse reflection and it assumes that the sample is made up of randomly distributed uniformly absorbing fragments. It is a two-flow theory (only two flows: a flow in the direction of incident light and a flow in the direction of reflected light are assumed to move in opposite directions perpendicular to the irradiated surface) [7].

For an infinitely thick layer with zero transmittance, K-M theory predicts that the remission function ($F(R)$), which can be calculated by measuring the reflectance (R_∞) of the thick opaque layer, is proportional to the chromophore concentration in the sample (eq. 1)

$$F(R) = \frac{(1-R_\infty)^2}{2R_\infty} = \frac{k}{s} = \frac{\sum_i w_i k_i}{\sum_i w_i s_i} \quad (1)$$

In the above equation, k and s are the absorption and scattering coefficients, respectively, with $k = 2\varepsilon C$ and $s = 2\sigma$, where ε is the molar Napierian absorption coefficient, and C the chromophore concentration expressed in mol per unit volume and σ is the fraction of light scattered per unit path length in the sample.

When a mixture of chromophores is present, global absorption and dispersion coefficients may be considered additive functions of the respective coefficients (k_i and s_i) for the components, weighed according to their mass fractions (w_i) (see the fourth member in eq. 1).

Provided that diffuse reflectance, R , and diffuse transmittance, T , for a single transmitting layer of the studied material is known, separate values for k and s coefficients may be calculated from eqs. 2 to 6 [8].

$$k = \frac{a-1}{a+1} \log b \quad (2)$$

$$s = \frac{2a}{a^2-1} \log b \quad (3)$$

$$a = \frac{1+R^2-T^2+\Delta}{2R} \quad (4)$$

$$b = \frac{1+T^2-R^2+\Delta}{2T} \quad (5)$$

$$\Delta^2 = (1+R+T)(1+R-T)(1+T-R)(1-R-T) \quad (6)$$

Both $F(R)$ and k are very valuable parameters when information about the content of a certain component in a light-scattering material is required. Several examples in biological samples can be found in literature. For instance, a linear relation was found for $F(R)$ values at 533 nm in *Rhododendron indicum* petals as a function of anthocyanin chemically determined concentration (Figure 1) [9]. Good linear correlations were also obtained for plant leaves between the water content in mmol/cm² and $F(R)$ at 1456 nm as for total chlorophyll in mmol/cm² and $F(R)$ at 700 nm. The correlation with chlorophyll content was improved when using k at 700 nm instead of the remission function [10]. This last result is to be expected since $F(R)$ is directly proportional to the chromophore concentration but only at constant s . In contrast, the proportionality between k and C is kept independently of the value of the s coefficient.

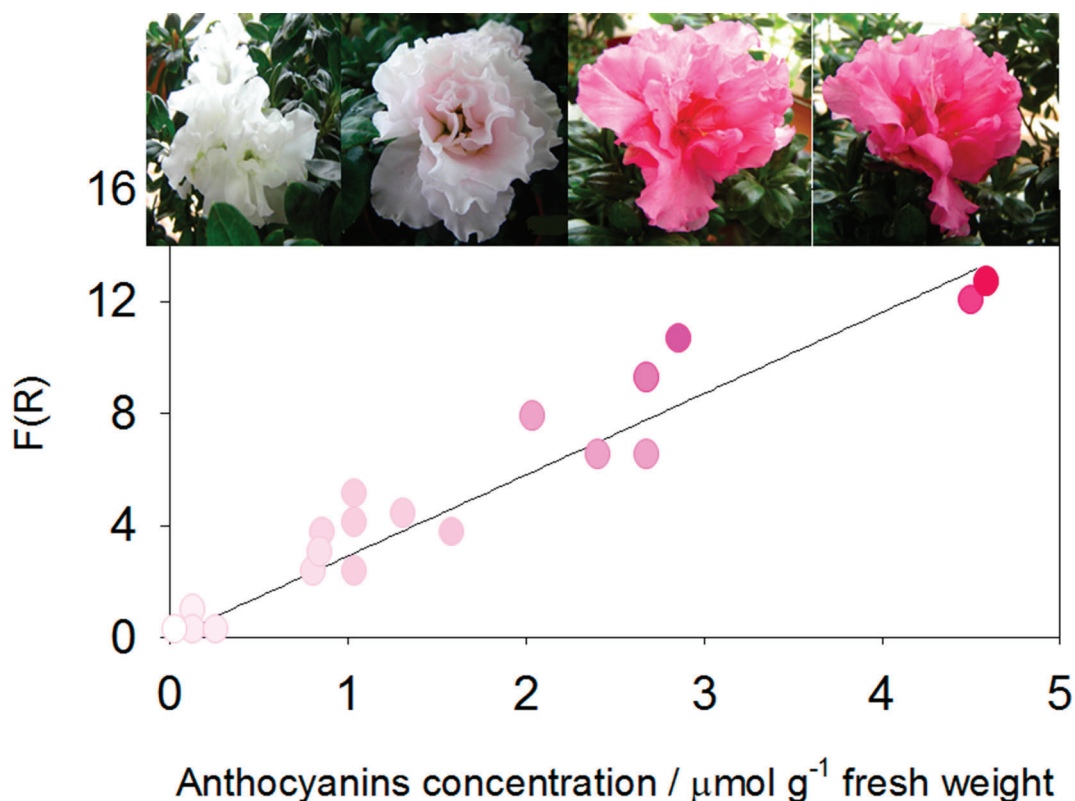


Figure 1. Remission function values at 533 nm from *Rhododendron indicum* petals as a function of anthocyanin concentration, ($R^2 = 0.9730$). Reproduced from [9] with permission from the European Society for Photobiology, the European Photochemistry Association, and The Royal Society of Chemistry.

1.2. Reflectance and colour coordinates. Related but quite different concepts

Since a relationship between the reflected light and the chromophore concentration can be found, as illustrated above, and since the reflected light is in turn related to the colour coordinates, it is appealing to examine whether it is also feasible to correlate the chromophore concentration with the sample colour.

At this point, it is important to emphasize that the reflectance spectrum of a sample is a property of the material whereas the color is not. Indeed, colour is a sensation created by the brain of an observer. This perception depends not only on the reflectance spectrum of the “sender” but also on the spectral distribution of the light source and the sensitivity curve of the observer’s visual photoreceptors.

To transform reflectance spectra to colour coordinates for a particular observer under specific lighting conditions, different color spaces may be used [11]. Cordon and Lagorio used color coordinates to sense various photosynthetic pigments in plant leaves, with spatial resolution, from digital images [12]. First, they obtained correlations between **RGB** colour coordinates of plant leaves and the pigment concentration determined by a standard wet method. Then, these authors obtained images of green and senescent leaves with a commercial scanner (TIFF format with a resolution of 300 dpi and a depth of 24 bits). Using the program ERDAS IMAGINE 8.4, they converted the images from TIFF to IMG format and then separated into their **R**, **G** and **B** bands. Finally, using the correlations between each color coordinate and the pigment concentration, maps of pigment contents were obtained in gray scale. To improve visual interpretation, the grayscale images were transformed to pseudocolour coding. Figure 2 illustrates the concentration maps obtained from images of *Liquidambar styraciflua* leaves.

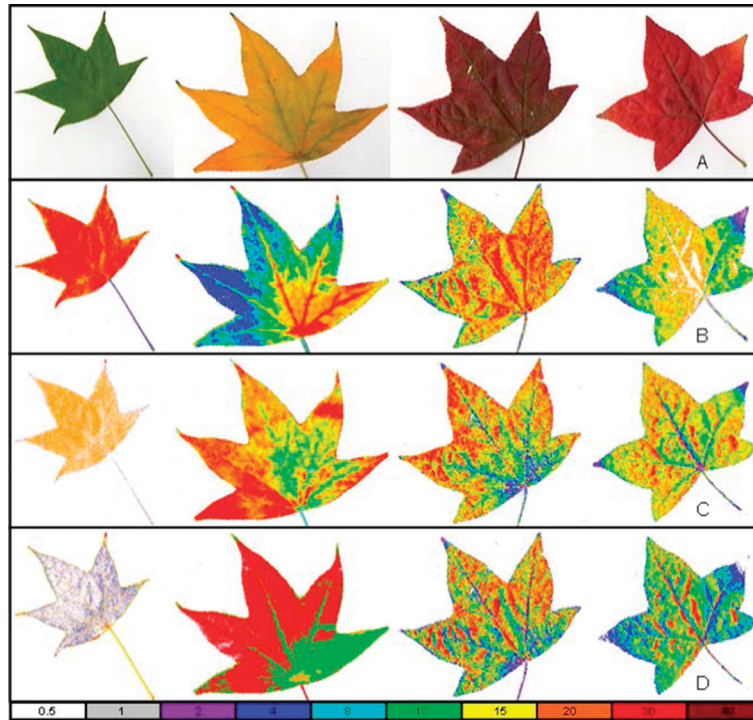


Figure 2. A. Images of *Liquidambar styraciflua* captured with a commercial scanner. B, C and D. Concentration maps of total chlorophyll, carotenoids and anthocyanins, respectively. Numbers express concentration in nmol/cm².

1.3. Reflectance as a bio-signal. Quantum catches and vision contrasts

Some examples to illustrate the usefulness of reflectance and imaging as tools for determining analyte contents were exemplified in the previous sections. In nature, however, reflected light provides photons detected in visual perception. Thus, reflected light plays a primary role in optical biosignaling and in visual communication.

In this context, an important parameter is the quantum catch or stimulus strength, Q_i , which represents the relative amount of light absorbed by a given photoreceptor per unit time (eqs. 7-9) [6].

$$Q_i = k_i \cdot P_i \tag{7}$$

$$\text{With } P_i = \int_{300}^{700} R(\lambda) \cdot S_i(\lambda) \cdot I(\lambda) \cdot d\lambda \tag{8}$$

$$k_i = 1 / (\int_{300}^{700} S_i(\lambda) \cdot I(\lambda) \cdot d\lambda) \tag{9}$$

Where i stands for the type of the photoreceptor (L: long wavelength, M: medium wavelength, S: short wavelength or VS: very short wavelength), λ is the wavelength, $S_i(\lambda)$ is the photoreceptor spectral sensitivity, $R(\lambda)$ is the reflectance spectrum of the observed object, $I(\lambda)$ is the illuminant spectrum and $d\lambda$ is the differential of wavelength.

Even more important to distinguish an object from its background is the chromatic contrast (C_i) which may be calculated dividing P_i by the total number of photons absorbed by receptor i from the background (P_{ib}) (eqs. 10 and 11).

$$C_i = P_i / P_{ib} \tag{10}$$

$$P_{ib} = \int_{300}^{700} R_b(\lambda) \cdot S_i(\lambda) \cdot I(\lambda) \cdot d\lambda \tag{11}$$

Figure 3 shows typical values for quantum catches and contrasts calculated for the visual perception of bees, birds and humans when looking at *Rhododendron indicum* petals with different colour and illuminated with a standard D65 light simulating daylight.

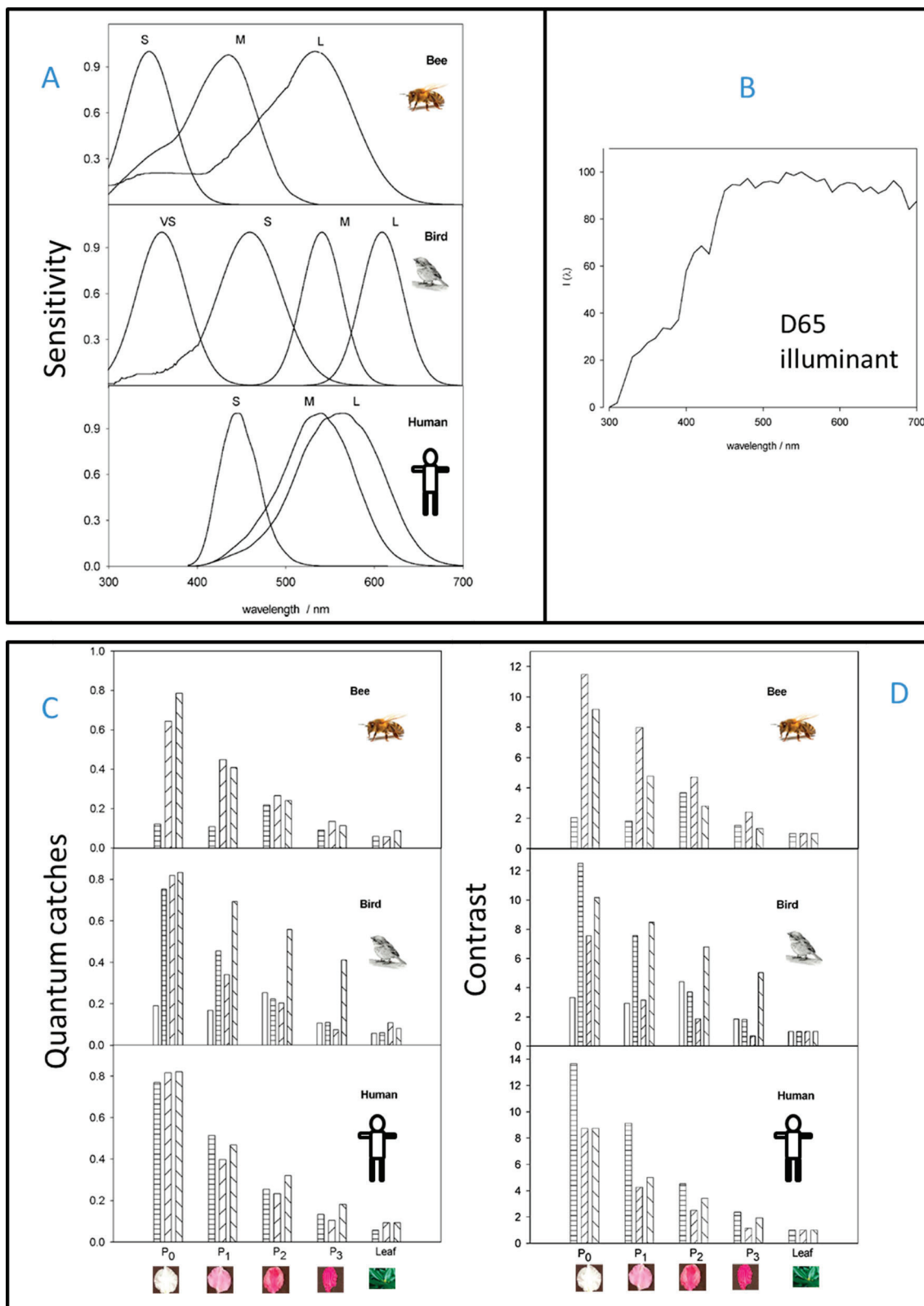






Figure 3. A) Photoreceptor sensitivities for the honeybee *Apis mellifera*, for the bird *Leiothrix lutea* and for humans. The letters VS, S, M and L mean very short, short, medium and long wavelengths, respectively. B) Spectral distribution of D65 illuminant. C) Quantum catches and D) Contrasts to background for the honeybee *Apis mellifera*, for the bird *Leiothrix lutea* and for humans. The different bars stand for:  very short,  short,  medium and  long wavelengths. Adapted from Ref. [6] with permission from the European Society for Photobiology, the European Photochemistry Association, and The Royal Society of Chemistry.

Humans see the white petal as achromatic because their three photoreceptors are excited in a similar degree during the observation in daylight (see Figure 3C). In contrast, a bird or bee looking at the same flower does not capture the same number of photons in each of their receptors so that the “white” petals will look chromatic to their eyes. Figure 3A shows that the darker a tissue is, the lower the value of the quantum catches, which is an obvious consequence of the lower number of photons reaching the eye from the light reflected by the petal. It is also evident that bees do not have photoreceptors in the red and then, they can poorly capture light with long visible wavelengths.

It is assumed that the contrast between the flowers and the background helps pollinators to find flowers. The greatest contrast to the background in Figure 3D is given for the white flowers for all the observers. In the case of dark pink flowers, the contrast to the background is low for humans and bees. For birds, on the contrary, the contrast of the red receptor is relatively high. This is consistent with the fact that red and pink flowers are attractive to birds and are mostly pollinated by them [6 and references therein]. Therefore, as a general rule, in order to evaluate visual signals, it is essential to handle the concepts of quantum catches and contrasts, and if feasible, to complement this information with behavioural experiments.

From this, the enormous relevance of having experimental information on the sensitivity curves of the optical photoreceptors of different species becomes evident. Although for humans and a few other species these aspects have been studied in depth, this is not the case for most animals. This is certainly an interesting field to develop in the field of photobiology.

2. Fluorescence in biological systems

2.1 How to quantify fluorescence in scattering media. Determination of fluorescence quantum yield

To analyse the relevance of fluorescence as a signal in nature, it is essential to quantify fluorescence. In the case where the number of fluorescence photons is negligible compared to that of reflected photons, the fluorescence has little chance of having biological relevance. On the contrary, if the number of emitted photons is comparable with the number of reflected photons, then a contribution of the fluorescence to the image of the organism will surely take place. These evaluations should be conveniently complemented with behavioural experiments to fully discuss the possible role of fluorescence in communication.

Knowledge of the fluorescence quantum yield (number of photons emitted per absorbed photon) is an initial step for the quantification of fluorescence. The intact organisms generally have considerable scattering and high chromophore concentration and consequently the quantification of fluorescence cannot be carried out by traditional methods in solution. Several methodologies are reported in literature for the determination of fluorescence quantum yields in scattering media. Some of them use an integrating sphere [13-17], whereas others use a standard spectrofluorometer without sphere [17]. In our studies on intact biological samples [6, 18-20] we proceeded according to reference [17] for the determination of the fluorescence quantum yield.

In brief (see also Figure 4):

1. The sample is placed in front-face geometry within a standard steady-state spectro-fluorometer and the total number of emitted photons J_f , at excitation wavelength λ_θ , is obtained as the area under the emission spectra.
2. The sample is then replaced by a blank (100% reflecting material as BaSO₄) and an optical filter (for instance a glass Schott, NG4, 0.5 mm) is inserted at the emission slit to avoid detector damage. The light reaching the detector is registered by varying the emission wavelength from ($\lambda_0 - 15$ nm) to ($\lambda_0 + 15$ nm) and the number of photons scattered by the blank (J_θ) are calculated from the area under the recorded peak divided by the transmittance spectrum of the filter.
3. Step 2 is repeated replacing the blank by the sample and the integrated reflected light from the sample, J , is obtained.

To take into account differences in light scattering between sample and blank, two additional measurements are performed:

4. Keeping the filter at the emission window, the sample is excited at a wavelength where the sample does not absorb and emission spectra is recorded from ($\lambda - 15$ nm) to ($\lambda + 15$ nm). Under these conditions, the area under the recorded peak divided by the transmittance spectrum of the filter yields the integrated scattered light intensity from the sample (I).

5. Proceeding as in step 4 with the blank, the integrated scattered light intensity from the blank (J_0) is obtained.

Then, the fluorescence quantum yield is calculated as:

$$\Phi_f = \frac{\text{number of emitted photons}}{\text{number of absorbed photons}} = \frac{J_f}{J_0 \left(\frac{I}{I_0} - 1 \right)} \quad (12)$$

In the case that the absorption of the sample at wavelength λ is low but not strictly null (reflectance, $R \neq 1$), the correction factor in eq. 12 should be replaced by $I/(I_0 R)$ (For more details see ref. [20]). Following this methodology, we quantified and reported sexual dichromatism in fluorescence in avians for the first time [19]. In fact, sexual dichromatism in birds, which is very frequent, is the presence of sexual differences in plumage coloration. Sometimes, these differences cannot be detected by humans but are discernible to avian eyes. Furthermore, when plumage emits, there may be differences also in fluorescence between sexes. For the blue-winged parrotlet *Forpus xanthopterygius*, the male rump emits blue fluorescence that is absent in the female. Additionally, the male chest emits a green fluorescence which is much more intense than that emitted by females.

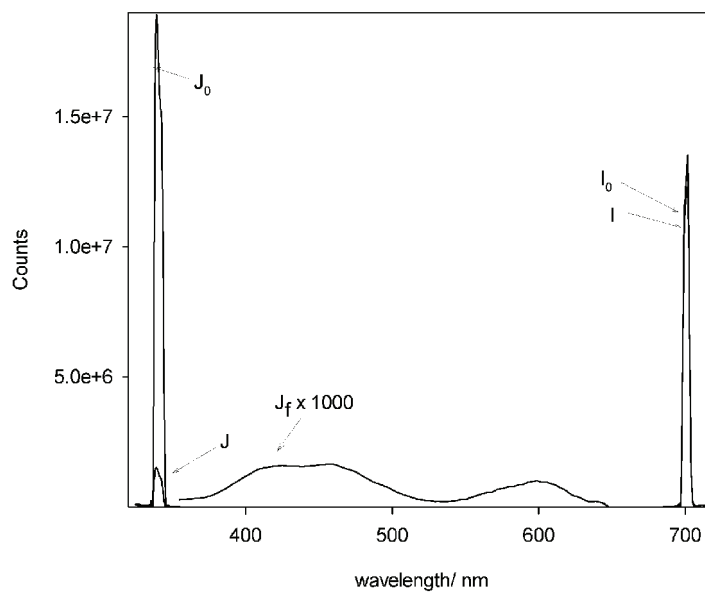


Figure 4. Raw data necessary for the determination of the fluorescence quantum yield of light scattering samples. J_0 : integrated scattered light from the blank, J : integrated scattered light from the sample, J_f : emission spectrum from the sample, I : scattered light from the sample, I_0 : scattered light from the blank. Reproduced from [6] with permission from the European Society for Photobiology, the European Photochemistry Association, and The Royal Society of Chemistry.

Determinations of fluorescence quantum yields in scattering media are reviewed in [16]

2.2. Fluorescence vs. Reflectance in nature. How to quantitatively estimate the relative importance of fluorescence

From a biological perspective, an important question is whether fluorescence in organisms plays a role or is simply a non-functional consequence of the chemical nature of the molecules involved. The search for the answer to this question can be addressed from diverse aspects and by both behavioural and photophysical experiments.

Focusing on optics, a first idea of the contribution of fluorescence can be obtained by comparing the number of fluorescent photons with the number of reflected ones. For analysing the relevance of fluorescence in flowers [6, 18], as a first step, we have compared the fluorescence intensity per incident photon, calculated as $\phi_f \cdot f_a(\lambda)$ (where $f_a(\lambda)$ is the fraction of photons absorbed by the sample at wavelength λ) with the fraction of reflected photons. For the opaque samples, as no light was transmitted through the material, $f_a(\lambda)$ was directly obtained as $[1-R(\lambda)]$. Nevertheless, a more rigorous analysis that properly includes the environmental lighting conditions is even more convenient for a better comprehension of the system and is described below.

When a fluorescent organism is illuminated by a polychromatic light, with a spectral distribution $I(\lambda)$, the total number of fluorescence photons may be calculated by eq. 13.

$$F_t = \int_{\lambda_{ex1}}^{\lambda_{ex2}} \phi_f(\lambda) \cdot I(\lambda) \cdot f_a(\lambda) \quad (13),$$

where integration is performed over the interval of excitation wavelengths λ_{ex1} - λ_{ex2} .

For a translucent sample, $f_a(\lambda)$ is calculated as $[1 - R(\lambda) - T(\lambda)]$ which reduces to $[1 - R(\lambda)]$, when transmittance (T) is zero.

The spectral photon flux distribution of fluorescence $F_t(\lambda)$ may be calculated as the product between F_t and the normalized spectral distribution of fluorescence $g(\lambda)$ (with $\int g(\lambda) = 1$):

$$F_t(\lambda) = F_t \cdot g(\lambda) \quad (14)$$

Similarly, the photon flux distribution of reflected photons is estimated by equation (15).

$$R_t(\lambda) = R(\lambda) \cdot I(\lambda) \quad (15)$$

Finally, for a given spectral range λ_1 - λ_2 , the contribution of fluorescence (F_{cont}) to the total number of photons released by the entity, may be estimated as the fraction of fluorescence photons relative to the total number of photons (reflected plus fluorescent) according to eq. 16.

$$F_{cont} = \frac{\int_{\lambda_1}^{\lambda_2} F_t(\lambda) d\lambda}{\int_{\lambda_1}^{\lambda_2} (F_t(\lambda) + R_t(\lambda)) d\lambda} \quad (16)$$

This approach was applied to estimate the relevance of fluorescence for the first naturally fluorescent frog reported in scientific literature [20]. In that case, fluorescence contribution turned out to be almost 30% under twilight conditions (Figure 5), a result very interesting as it suggests a possible role of fluorescence in visual communication among individuals [21].

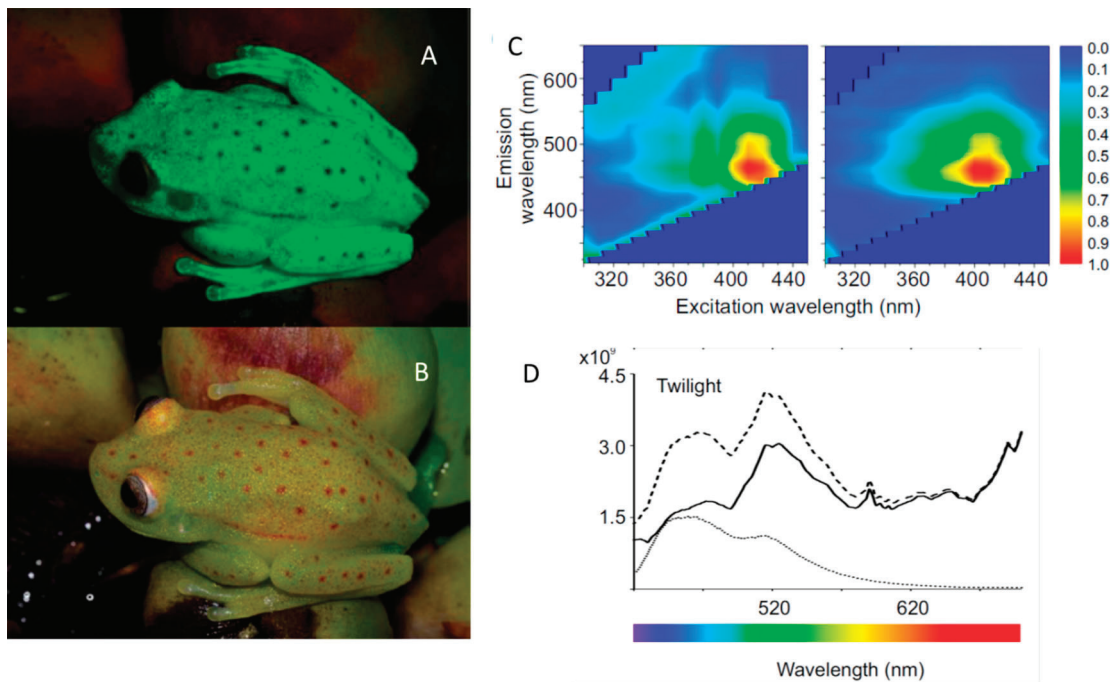


Figure 5. Fluorescence in the frog *Boana punctata*. Adult male (A) under UV-blue light and (B) white light. Excitation-emission matrices of the dorsal surfaces of female (Left) and male (Right) specimens (C). Contribution of fluorescence to total emerging light. (B) Spectral photon flux (photons/[cm².s.nm]) emerging from the dorsal surfaces of one of the

specimens under twilight illumination. Reflected light (solid line) fluorescence light (dotted line), and the sum of both components (dashed line). Adapted from [20] (Taboada, C.; Brunetti, A. E.; Pedron, F. N.; Carnevale Neto, F.; Estrin, D. A.; Bari, S. E.; Chemes, L. B.; Peporine Lopes, N.; Lagorio, M. G.; Faivovich, J. Naturally occurring fluorescence in frogs. *PNAS*, 2017, 114, 3672–3677) with permission from the National Academy of Sciences, USA.

2.3. Fluorescence in multilayered systems. How to retrieve the observed total fluorescence from the spectroscopic information of each layer

It is common to find multilayered structures in biological organisms. Very often, each part fluoresces in a specific way and contributes to the total fluorescence emitted by the intact organism. In these cases, it may be interesting to know where the global fluorescence mainly originates. Modelling can help to provide an answer and determine the contribution of each individual layer.

Let's consider a system of n layers each characterized by their respective reflectance R_i , transmittance T_i and fluorescence intensity I_{fi} (see Figure 6). As the excitation light (I_0) enters the system, it suffers attenuation due to the filter effect of each layer. It can be roughly considered that a photon flux I_0 reaches layer 1, a flux $I_0 \cdot T_1(\lambda_0)$ (where λ_0 is the excitation wavelength) reaches layer 2, $I_0 \cdot T_1(\lambda_0) \cdot T_2(\lambda_0)$ reaches layer 3 and so on. In each layer, the generated flux of fluorescent photons is the product of the fluorescence quantum yield (ϕ_{fi}), the photon flux reaching the layer ($I(\lambda_0)$) and the fraction of light absorbed by the sample (f_{ai}) (equation 17)

$$I_{fi} = \phi_{fi} \cdot I(\lambda_0) \cdot f_{ai}(\lambda_0) = \phi_{fi} \cdot I(\lambda_0) \cdot (1 - R_i(\lambda_0) - T_i(\lambda_0)) \quad (17)$$

The fluorescence originated in each layer travels outwards and it is attenuated by the transmittance of the upper layers. The global fluorescence may be estimated as the sum of all the contributions (equation 18).

$$I_{ft} = I_{f1}(\lambda) + I_{f2}(\lambda) \cdot T_1(\lambda) + I_{f3}(\lambda) \cdot T_1(\lambda)T_2(\lambda) + \dots + I_{fn}(\lambda) \cdot T_1(\lambda)T_2(\lambda) \dots T_{n-1}(\lambda) \quad (18)$$

From eqs. 17 and 18, eq. 19 arises:

$$I_{ft} = \phi_{f1} \cdot I_0(\lambda_0) \cdot (1 - R_1(\lambda_0) - T_1(\lambda_0)) + \phi_{f2} \cdot I_0(\lambda_0) \cdot (1 - R_2(\lambda_0) - T_2(\lambda_0)) \cdot T_1(\lambda_0)T_1(\lambda) + \phi_{f3} \cdot I_0(\lambda_0) \cdot (1 - R_3(\lambda_0) - T_3(\lambda_0)) \cdot T_1(\lambda_0) \cdot T_2(\lambda_0)T_1(\lambda)T_2(\lambda) + \dots + \phi_{fn} \cdot I_0(\lambda_0) \cdot (1 - R_n(\lambda_0) - T_n(\lambda_0)) \cdot T_1(\lambda_0) \cdot T_2(\lambda_0) \dots T_{n-1}(\lambda_0) \cdot T_1(\lambda) \cdot T_2(\lambda) \dots T_{n-1}(\lambda) \quad (19)$$

In eq. 19, it is important to highlight the difference between the excitation wavelength (λ_0) and the emission wavelength (λ).

It should be also noted that eq. 19 may be re-written in terms of the experimentally determined fluorescence intensities of each layer (I_{fi}^{iso}) when they are isolated and irradiated directly by a photon flux I_0 (eq. 20)

$$I_{ft} = I_{f1}^{iso} + I_{f2}^{iso} \cdot T_1(\lambda_0)T_1(\lambda) + I_{f3}^{iso} \cdot T_1(\lambda_0) \cdot T_2(\lambda_0)T_1(\lambda)T_2(\lambda) + \dots + I_{fn}^{iso} \cdot T_1(\lambda_0) \cdot T_2(\lambda_0) \dots T_{n-1}(\lambda_0) \cdot T_1(\lambda) \cdot T_2(\lambda) \dots T_{n-1}(\lambda) \quad (20)$$

It should be noticed that if I_p , R and T are experimentally determined for each layer, it is possible to validate the model by comparing the experimental global fluorescence spectrum with the calculated spectrum resulting from the sum of contributions given by eq. 20. Moreover, the relative participation of each layer may be estimated. This type of physical modeling is extremely simplified since it does not take into account multiple reflections. Even so, it was successful when applied to the comprehensive study of the global spectrum of the frog *Boana punctata* [20] and that of the kiwi fruit [22]. In the supplementary material of ref. [22] the validity of neglecting multiple reflections for the excitation beam and for the fluorescence emission (in the case of kiwifruit) is thoughtfully discussed.

This model was also applied for the analysis of fluorescence in eggplants fruits [23]. In this case, the observed spectrum for the whole intact fruit was reproduced by eq. 20 with an additional term which stood for the peel fluorescence generated internally, reflected by the pulp and filtered by the peel. In other words, when an internal layer (IL) has high reflectance, as it happens for the eggplant pulp, the internal fluorescence of the upper layer (UL) can be reflected in the lower layer (LL) and comes out after suffering a filtering effect when it passes through the upper layer. The additional term for the system of two layers may be written then as $I_{UL} \cdot R_{LL} \cdot T_{UL}$ (details can be found in ref. [23]).

Using this kind of modelling it was concluded that skin and lymph were the layers mostly contributing to the observed fluorescence in the *Boana punctata* frog. In the case of kiwi fluorescence, it could be shown that the relative contribution of the pulp fluorescence to the total emission for the intact fruit depended on the peel transmittance, which was, in turn, a function of the excitation wavelength. For an excitation in the blue, the contributions were 81% and 19% for the peel and the pulp respectively, whereas for excitation in the orange the contributions changed to 75 and 25%, respectively.

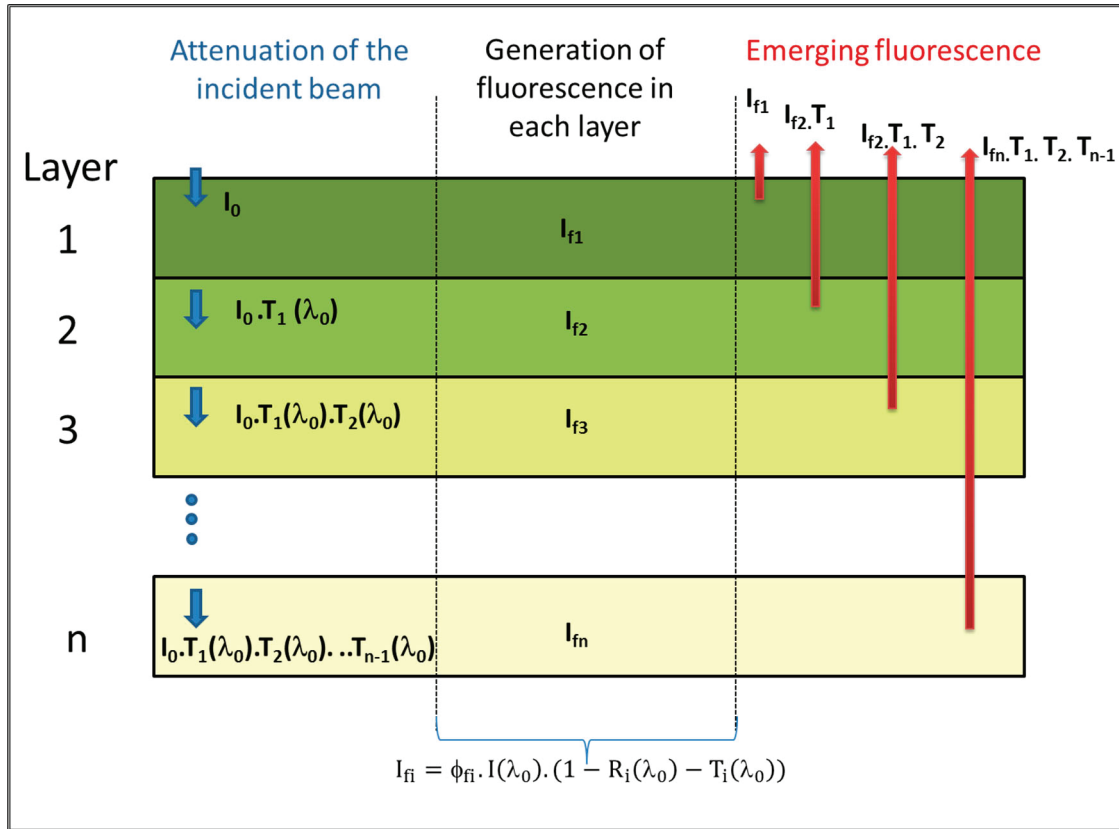


Figure 6. Multilayered system. Pictorial description of: the processes of attenuation of the excitation beam (I_0) through the different layers (left sector), generation of fluorescence in each layer (middle sector) and attenuation of the fluorescence on its way out of the system (right sector).

Future research analyzing how frogs’ emission impacts on their chromatic and achromatic contrast with their environment, as seen by predators and by predated species, will be planned. Knowledge on the sensitivity curves of the observer’s photoreceptors is essential for that study.

2.4 Plant biophotonics. Chlorophyll fluorescence: a quite singular type of fluorescence in nature

Plants emit fluorescence in the blue and in the red part of the electromagnetic spectrum. Blue fluorescence (around 450 nm) is due to emission from phenolic substances (caffeic, ferulic, chlorogenic, coumaric and rosmarinic acids) [24], whereas red emission is originated from chlorophyll-a in photosystem II (PSII) and photosystem I (PSI) [25].

Chlorophyll fluorescence is strongly related to photosynthesis and it is used as a tool to assess plant health. The photosynthetic process in plants causes variability in chlorophyll emission. This variable emission is usually analysed by means of a pulse amplitude modulated (PAM) fluorometer [26]. In fact, when dark-adapted leaves are illuminated by a low photon flow, a constant initial fluorescence F_0 is recorded (Figure 7). If a saturation light pulse is then applied, the primary electron acceptors in the photosynthetic chain are reduced and are unable to acquire another electron before they have effectively passed the received electron on to the next acceptor. As a consequence, the fluorescence emission increases to a maximum F_m and subsequently decays. In a typical experiment, an actinic light is then switched on and the fluorescence reaches a peak and then falls to a steady state (F_s), in a process called fluorescence quenching. This quenching has two contributions: the photochemical quenching, due to the activation of enzymes in carbon metabolism by

light, and the non-photochemical quenching on account of the enhancement of heat dissipation. Subsequent applications of saturating light pulses lead to increases in fluorescence (F_m') (Figure 7).

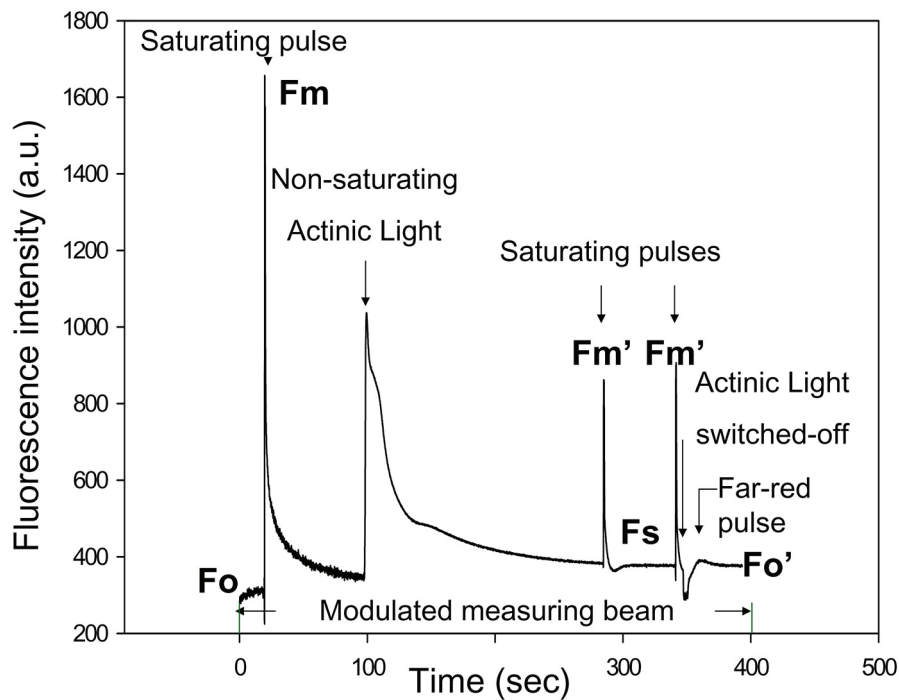


Figure 7. Variable chlorophyll fluorescence recorded with a pulse modulated fluorometer for a typical plant leaf of *Spathiphyllum wallisi*. Reproduced with permission from Ref. [27] Copyright 2014 Wiley.

Several photosynthetic parameters can be derived from an experiment on variable chlorophyll fluorescence. The main parameters are listed below:

-the maximum quantum yield of photosynthesis for dark-adapted leaves F_v/F_m (eq. 21).

$$\frac{F_v}{F_m} = \frac{F_m - F_0}{F_m} \quad (21)$$

-the coefficient for the photochemical quenching, q_p (equation (22)).

$$q_p = \frac{F_m' - F_s}{F_m' - F_0} \quad (22)$$

-the coefficient for the non-photochemical quenching, q_{NP} (eq. 23) and its alternative expression NPQ (eq. 24), representing the magnitude of heat dissipation under a given actinic light.

$$q_{NP} = \frac{F_m - F_m'}{F_m - F_0} \quad (23)$$

$$NPQ = \frac{F_m - F_m'}{F_m'} \quad (24)$$

-the efficiency of PSII, Φ_{PSII} (eq. 25), representing the photosynthetic activity under a defined actinic light.

$$\Phi_{PSII} = \frac{F_m' - F_s}{F_m'} \quad (25)$$

- the quantum yield of NPQ, Φ_{NPQ} (eq. 26).

$$\Phi_{NPQ} = NPQ \times \frac{F_s}{F_m} \tag{26}$$

- the quantum yield of photophysical decay (representing the deactivation of the excited reaction center at PSII by internal conversion, intersystem crossing and fluorescence, under a particular actinic light), Φ_C (eq. 27),

$$\Phi_C = \frac{F_s}{F_m} \tag{27}$$

The derivation of these relationships and their physical meaning may be found in references [28-32].

It is important to notice that the sum of the last three parameters (each of which is a function of the actinic light intensity) gives unity, so that an increase in one of them leads to a decrease in one or both other two [33]. These parameters enable us to visualize the partition of energy within the plant among photosynthesis, heat dissipation and photophysical decay (which includes fluorescent emission). Clearly, this is of huge value in photosynthesis studies and in evaluating the harnessing of solar energy to produce organic matter.

Under low illumination such as not to induce Kautsky kinetics, a spectral distribution for the initial fluorescence of plant leaves may be recorded. At room temperature, this fluorescence is characterized by two peaks: one in the red, F_{red} (around 680 nm, due to PSII) and one in the far-red, $F_{far-red}$ (around 730 nm, due to both photosystems) [27, 34].

The fluorescence ratio $F_{red}/F_{far-red}$ has been widely related to plant stress and photosystems stoichiometry [23, 33, 35]. However, the spectral distribution of fluorescence at leaf level is distorted compared to the spectral distribution at chloroplast level. This is caused by light re-absorption and greatly affects the red band (Figure 8) [36, 37]. As the connection between the fluorescence ratio and plant physiology is strictly valid when artifacts are absent, it is extremely relevant to correct spectra for light re-absorption processes.

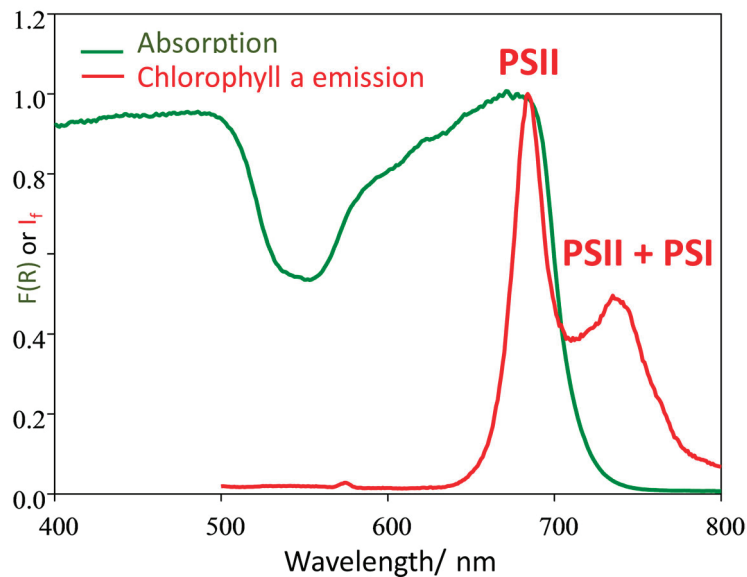


Figure 8. Typical absorption and emission spectra of plant leaves. The red emission band, which is due to PSII emission, significantly overlaps the absorption spectrum and undergoes severe re-absorption processes. The far-red emission band caused by emission from both photosystems is less affected by light re-absorption.

Chlorophyll fluorescence can be measured at different scales: at chloroplast level, at leaf level and at canopy level. In turn, the fluorescence of the canopy can be recorded at ground, airborne or space borne scale. Each level of observation has its own particularities, both in terms of how the experimental measurements are carried out and in developing models capable of correcting distortions by light re-absorption processes.

2.4.1. Light re-absorption processes

2.4.1.1. From the leaf to the chloroplast

In literature, there are three proposed models to correct light re-absorption processes in plant leaves [36, 38-39]. They were compared and discussed in detail in a paper from Cordon and Lagorio [37]. According to the analysis described in this latter paper, one of the correction methods [39] would be subject to conceptual controversies, whereas the other two [36, 38] are supported by good validations and lead to similar results.

The main objective of the light re-absorption correction is to obtain the spectral distribution at the chloroplast level (corrected spectrum, $I_f^c(\lambda)$) from the experimental spectrum at leaf level (equation 28). This is generally achieved by multiplying the experimental leaf-level fluorescence spectrum $I_f^e(\lambda)$ by a correction factor f (see equation 28) that will have different expressions depending on the model used for its deduction.

$$I_f^c(\lambda) = I_f^e(\lambda) \cdot f \quad (28)$$

In the correction methodology proposed by Agati et al. [38], the correction factor f is a function of the reflectance (R) and transmittance (T) of a single leaf at the emission and excitation wavelengths (λ and λ_0 respectively) (eq. 29).

$$f = \frac{\ln \frac{1}{(R_{\lambda_0} + T_{\lambda_0})} + \ln \frac{1}{(R_{\lambda} + T_{\lambda})}}{\ln \frac{1}{(R_{\lambda_0} + T_{\lambda_0})}} \frac{1 - R_{\lambda_0} - T_{\lambda_0}}{1 - (R_{\lambda_0} + T_{\lambda_0})(R_{\lambda} + T_{\lambda})} \quad (29)$$

This approach considered an infinitesimal layer of leaf where fluorescence was generated and was then exponentially attenuated due to light re-absorption. Lateral light losses were neglected and light scattering was taken into account by considering an effective pathlength. This model was validated by comparing the corrected emission spectra for *Aurea* mutant and for the wild type of tomato leaves, which had different chlorophyll concentration and chloroplast ultrastructure. Matching of both spectra proved the effectiveness of the model.

The second methodology was applied to leaves by Ramos and Lagorio [36] in 2004, but it had already been developed and applied for inert materials in 1998 by Lagorio et al. [40]. It is a two-flux model based on the Kubelka- Munk theory [2]. It assumes that leaves act as ideal diffusers and that the emission produced in each element may be decomposed in two flows with opposite directions and the same magnitude. In this case, the correction factor f is given by eq. 30.

$$f = \left[\frac{1}{1 + \sqrt{\frac{F(R_{\lambda})}{F(R_{\lambda})+2}}} \frac{1}{1 + \sqrt{\frac{F(R_{\lambda})[F(R_{\lambda})+2]}{F(R_{\lambda_0})[F(R_{\lambda_0})+2]}}} \right]^{-1} \quad (30)$$

For the derivation of the correction factor according to Lagorio et al. [40], it was assumed that no light was transmitted through the system, so this approach is strictly applicable to opaque samples. Thus, when working with plants, a non-transmitting pile of leaves should be used in fluorescence measurements for the correct application of the approach (Figure 9).

The model was validated by comparing the corrected spectral distribution of fluorescence of a group of stacked leaves with the spectral distribution of fluorescence emerging from a thin layer of chloroplasts.

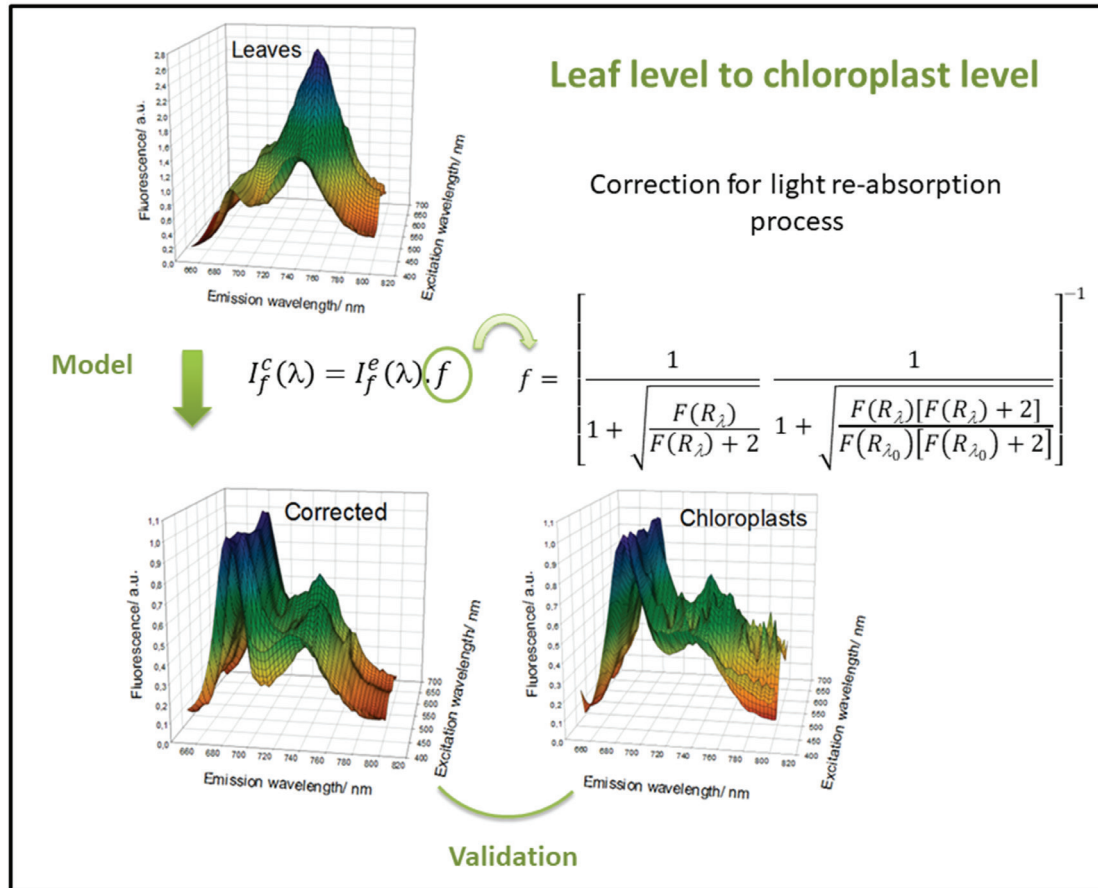


Figure 9. Normalized fluorescence spectra of *Ficus benjamina* leaves before and after correction for light re-absorption processes. The corrected spectra were compared with those obtained from a thin layer of chloroplasts (free from re-absorption). The corrected spectra agree with chloroplasts spectra thus validating the model. Adapted from [36] with permission from the European Society for Photobiology, the European Photochemistry Association, and The Royal Society of Chemistry.

In principle, a two-flux model is expected to be better than a single flux model. However, in practice, both Agati et al. and Lagorio et al. models give close results. The choice of which one to use will depend in part on the possibility of having only a single leaf or a group of leaves for the measurements.

Leaf fluorescence measurements are carried out by means of a standard spectrofluorometer in front face geometry. In case the method described by Agati et al. is applied for corrections, the experimental fluorescence spectrum should be obtained for a single leaf. On the other side, if the method described by Lagorio et al. is used, it should be recorded for a group of stacked leaves that do not transmit light.

2.4.1.2. From the canopy to the leaf

Remote sensing of chlorophyll fluorescence tracks the emission from a canopy and is becoming an interesting tool for the assessment of plant health from a distance [41]. This technique is currently highly appreciated because it allows the study of anthropogenic or natural effects on large areas of plantations, the adequate monitoring of forests health and crop production and also the estimation of carbon flows between vegetation and the atmosphere which is closely related to global climate change [42].

There are passive and active methods for the remote sensing of chlorophyll fluorescence. Passive methods measure fluorescence excited directly by sunlight as irradiation source [43], whereas active methods use illumination with artificial light, usually high-energy LASERS or LEDS [44].

Chlorophyll fluorescence emitted by a canopy is only 1 or 2% of the light absorbed and is very small compared to the fraction of light reflected. The measuring instrument (spectro-radiometer) used in the field, collects the total radiance composed by both the light reflected by vegetation and a contribution of its fluorescence at each wavelength. In passive methods, the two signals need to be decoupled using the Fraunhofer line discrimination principle (for detailed information see [45]). A very recent work proposed a new and promising active methodology to measure the chlorophyll fluorescence emission spectral distribution of canopies *in situ*, upon inducing the fluorescence with light emitting diodes at night [44].

Within a canopy, light re-absorption processes are also present and the spectrum recorded for a canopy is distorted from that of a single leaf. It is therefore worthwhile exploring models to correct this distortion. Recently, Romero et al. developed an approach to obtain the spectral distribution of fluorescence at leaf level from the experimental fluorescence spectrum at canopy level [46].

The model assumes that the system is the set composed of canopy plus soil. The vegetation homogeneously covers all the land and there is no fraction of bare soil. No light is transmitted through the system and the canopy is formed by units (leaves) that emit fluorescence. Mono exponential attenuation of light within the canopy is assumed for both the excitation light and for the generated fluorescence (which is reduced by the process of re-absorption). Light scattering is taken into consideration by determining an effective pathlength. The excitation beam is considered monochromatic; therefore, this model is applicable to data remotely obtained with active methods. It is not suitable for data produced by passive measuring methods that employ polychromatic light.

According to this approach, to perform the correction, the experimental spectrum should be multiplied by the correction factor which is given by eq. 31:

$$f = \left[1 + \frac{\ln \xi(\lambda)}{\ln \xi(\lambda_0)} \right] \left[\frac{1 - \xi(\lambda_0)}{1 - \xi(\lambda_0) \xi(\lambda)} \right] \quad (31)$$

With

$$\xi(\lambda) = R_\lambda + Tc_\lambda(1 - Rb_\lambda) \quad (32)$$

R_λ is the total reflectance of the system, Tc_λ is the canopy transmittance and Rb_λ is the soil reflectance at wavelength λ in all the cases.

This approach was successfully validated by comparing the corrected spectral distribution of fluorescence from the canopy with that experimentally obtained for a leaf (Figure 10).

Thus, by the successive application of the models described above “canopy to leaf” and “leaf to chloroplast” (sections 2.4.1.2. and 2.4.1.1), it is possible to retrieve the spectral distribution of fluorescence at chloroplast level from that measured at canopy level. This is **the fundamental** feature of this modelling, which permits to derive information at microscopic level from data recorded at a scale about one million times larger.

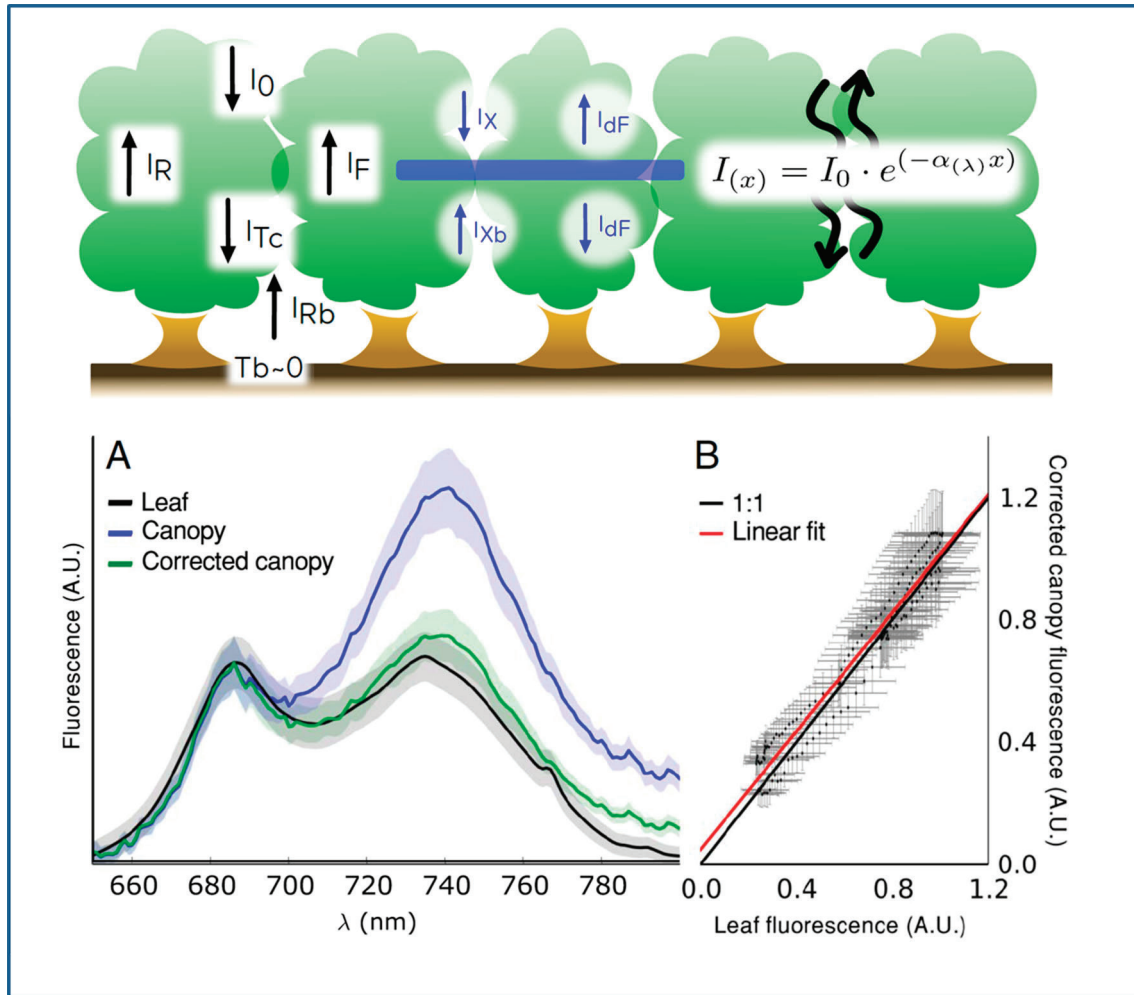


Figure 10. Fluorescence spectra and model validation: from canopy to leaf level. (A) Normalized fluorescence spectra for leaf (black), canopy (blue) and corrected canopy (green). Shadows show the standard error. (B) Correlation between the canopy fluorescence corrected by light re-absorption and leaf fluorescence. Linear fit: $y = (0.97 \pm 0.02) \cdot x + (0.05 \pm 0.01)$, $R^2 = 0.94$. Adapted with permission from [46], Copyright 2018 Elsevier.

3. Reflectance and Fluorescence. Practical applications

The analysis of the light reflected or emitted as fluorescence by organisms is an excellent tool for the development of non-destructive methods for quality and health assessment. These methods are attractive for monitoring the status of countless products. Some cases of application in foodstuff, in crops production and in environmental issues developed in our research group, are illustrated below.

Biospectroscopy and imaging were used to evaluate the quality of yerba mate (YM), a commercial product composed of dried leaves of *Ilex paraguariensis* mixed with fragments of dried sticks. This herb is extensively used in South America to prepare drinkable infusions (Figure 11) rich in polyphenols and antioxidants [47]. The results were complemented with bio-spectrometric studies based on MALDI techniques [48]. The stick/leaf mass ratio is a standard parameter in the quality control of yerba mate, which is limited by food code regulations. The nutraceutical content is higher in leaves than in stems and therefore the frequent adulteration of yerba mate with the addition of powdered stick leads to a reduction in the quality of the product. In effect, from MALDI analysis, it was shown that rutin and metasaponins 2 and 4, which have healing properties, are found in leaves and missing in sticks (both for the intact product and for the infusions) [47]. The excitation-emission matrixes of YM excited in the UV (300-400 nm) showed emission from YM in the blue and in the red part of electromagnetic spectrum. The fluorescence ratio Blue (469 nm)/Red (680 nm) displayed a linear relation with the percentage of sticks in the sample. Additional linear correlations were found between other optical parameters as sample reflectance at 669 nm or color coordinates (RGB) and the sample composition in percentage of sticks [47]. These results offer the chance to use non-destructive methods to determine the yerba-mate composition. Moreover, as fluorescence and reflectance differ for the stick and the leaf, it is possible to detect adulteration with stick, when it has been added in ground form.



Figure 11. Yerba Mate is extensively used in South America to prepare drinkable infusions (Mate) rich in polyphenols and antioxidants.

A similar initiative was carried out for oregano (*Origanum vulgare*), which is an herb with properties used in medicine, cosmetics, flavors and scents and which is marketed as a mixture of dried leaves and inflorescences with a maximum of 3% of stems. This percentage is particularly important for its essential oil content, which is rich in phenolic monoterpenes and carvacrol [49]. The essential oil is contained in trichomes and the density of these glands follows the order: inflorescences > leaves > stems (Figure 12). The various organs of the oregano plant showed fluorescence emission in the blue, green, red and far red part of the electromagnetic spectrum. For leaves, the ratio of fluorescence intensities green to far-red and blue to far-red maintained a linear relationship with water content. In addition, at constant humidity the blue/far-red peak ratio was a fingerprint for each organ of the plant. It was further observed that, for the commercial product, both the fluorescent emission at 310 nm (induced by excitation at 275 nm) and the absorption band at 811 cm^{-1} obtained by attenuated total reflectance Fourier transform infrared spectroscopy could be correlated with the essential oil content (details can be found in [49]).

The non-destructive determination of moisture in intact packaged oregano by measuring the diffuse reflectance in the near IR (through the packaging) has also been reported. This methodology is applicable as long as the wrapping film does not show absorption at 1440 or 1920 nm [50].

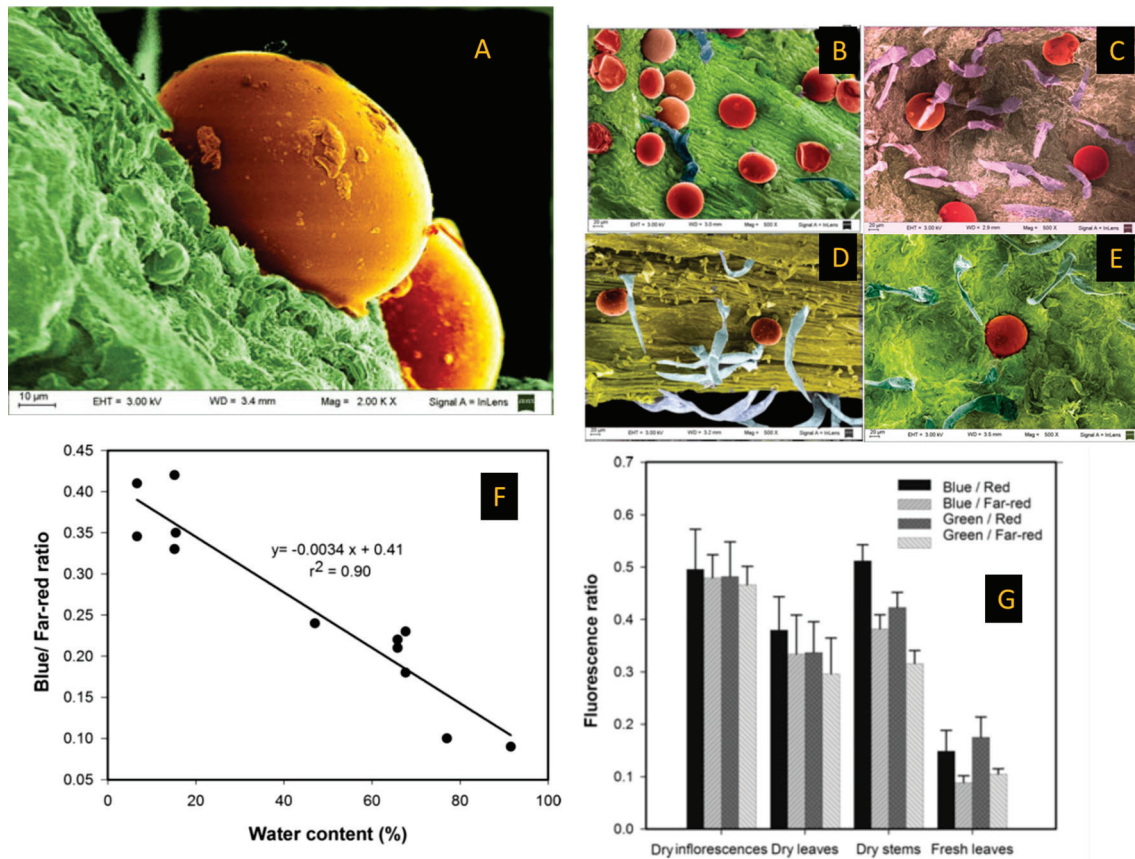


Figure 12. Oregano. A) SEM image in false colours for oregano glandular trichomas containing the essential oil (2000 x), B), C), D) and E) SEM images in false colours (500 x) for dry floral bracts, dry flower, dry stem and dry leaf respectively, F) Linear correlation between the fluorescence ratio Blue/Far-red and the water content in oregano leaves, G) Fluorescence ratios for oregano organs. Adapted with permission from [49] Copyright 2013 Wiley.

The analysis of variable chlorophyll fluorescence, described in section 3.4, was successfully applied in literature for the post-harvest screening of fruit and vegetables [5]. Recently, this technique was used to monitor the status of kiwifruit [22] and eggplant [23] under different storage conditions.

Our research group also used reflectance and chlorophyll fluorescence for environmental applications such as the study of the effect of diverse pollutants on plants: arsenic [51-53], combined presence of arsenic, vanadium, boron and fluoride [54], atrazine and methyl viologen [27] and nanoparticles [55], among others.

In addition, works related to agronomic sciences were carried out. Reflectance and chlorophyll fluorescence were used to detect phosphorous deficiency in crops [56]. Reflectance and radiance measurements were also recorded at canopy level in grass species during their senescence. The sun induced-chlorophyll fluorescence was extracted from the radiance spectra of canopies using the Fraunhofer Line Discrimination-method and was correlated with reflectance indexes used in literature as proxy for estimation of the Radiation Use Efficiency (RUE) [57].

Conclusions

The study of the interaction between light and biological entities is fundamental both to understand basic functions of the entities as well as for the development of new non-destructive technologies of analysis. As shown in this review, physical modelling greatly assists in the interpretation of the phenomena that take place upon illumination. For improved practical applications in the near future, the knowledge arising in this area should be integrated with other fields of science such as machine learning, remote sensing, artificial intelligence and computational vision. It is hoped that the new intelligent photonic technologies will be implemented in drones, robots and photonic sensor imaging.

Considering the transdisciplinary nature of this kind of projects, future success will surely rely on the degree of interaction among different sciences such as Physics, Chemistry, Biology, Bioengineering, Electronics and Computer Science.

Acknowledgments

The authors are grateful to the University of Buenos Aires (UBACyT 20020130100166BA, 20020170100037BA and 20020170200118BA) and to the Agencia Nacional de Promoción Científica y Tecnológica (PICT 2012-566 2357, PICT 2015-0396 and PICT 2015-820) for the financial support. JR developed his work with a fellowship from CONICET. MGL, AI, GBC and JF are Researchers of CONICET (Argentina). CT was supported by a Human Frontier Science Program (LT 000660/2018-L) postdoctoral fellowship. We also thank M. E. Ramos, J. Mendes Novo, B. Ospina Calvo, T.L. Parapugna, G. Petroselli, R. Erra, S. Gismondi, A. Nievas, V. Diz, R. Torres, C. Marchi, J. Paruelo, A. Barreira, P. Tubaro, G. Dundas, A. Fernández Cirelli for their collaboration in works related to the topic of this review. This review is dedicated to the memory of Professor Enrique San Román who introduced us in the study of high light- scattering materials.

References

- ^[1] Jurgens, M.; Mayerhöfer, T.; Popp, J. Introduction to Biophotonics. In *Handbook of Biophotonics*. Vol.1: Basics and Techniques, First Edition. Popp, J.; Tuchin, V. V.; Chiou, A.; and Heinemann, S. H., Ed.; Wiley-VCH Verlag GmbH & Co, 2011, Vol.1; ch. 1, p.1.
- ^[2] Rodríguez, H. B.; Miranda, M.; Lagorio, M. G.; San Román, E. Photophysics at Unusually High Dye Concentrations. *Acc. Chem. Res.*, 2019, 52, 1, 110-118.
- ^[3] Biophotonics for Medical Applications. In *Woodhead Publishing Series in Biomaterials Book*; Meglinski, I., Ed.; Elsevier Ltd., 2015.
- ^[4] Martinelli, F., Scalenghe, R., Davino, S., Panno, S., Scuderi, G., Ruisi, P., Villa, P., Stroppiana, D., Boschetti, M., Goulart, L. R., Davis, C. E., Dandekar, A. M. Advanced methods of plant disease detection. A review. *Agron. Sustain. Dev.*, 2015, 35, 1, 1-25.
- ^[5] DeEll, J. R.; Toivonen, P. M. A. Use of chlorophyll fluorescence in postharvest quality assessments of fruits and vegetables. In *Practical applications of Chlorophyll fluorescence in plant biology*. DeEll, J. R.; Toivonen, P. M. A., Ed. Kluwer Academic Publishers, London, 2003, ch. 7, p. 203.
- ^[6] Iriel, A.; Lagorio, M. G. Implications of reflectance and fluorescence of *Rhododendron indicum* flowers in biosignaling. *Photochem. Photobiol. Sci.*, 2010, 9, 342-348.
- ^[7] Wendlandt, W. W.; Hecht, H. G., *Reflectance Spectroscopy*, Wiley, New York, 1966.
- ^[8] Cordon, G. B.; Lagorio, M. G. Optical properties of the adaxial and abaxial faces of leaves. Chlorophyll fluorescence, absorption and scattering coefficients. *Photochem. Photobiol. Sci.*, 2007, 6, 873-882.
- ^[9] Iriel, A. and Lagorio M. G. Biospectroscopy of *Rhododendron indicum* flowers. Non-destructive assessment of anthocyanins in petals using a reflectance-based method. *Photochem. Photobiol. Sci.*, 2009, 8, 337-344.
- ^[10] Cordon, G. B.; Gismondi, S.; Nievas, A. V.; Lagorio, M. G.: Non-destructive assessment of water and pigments in leaves from the remission function using the Kubelka-Munk theory. *Proceedings of the International Color Association*, 2010, 397-400. ISSN 0280-2198.
- ^[11] <http://www.brucelindbloom.com/>
- ^[12] Cordon, G. B.; Lagorio, M. G. Sensing chlorophyll, carotenoids and anthocyanin concentration in leaves with spatial resolution from digital image. In *Color in Food: Technological and Psychophysical Aspects*. CRC Press, New York, USA. ISBN 978-1-43987-693-0, 2012, Ch.13, 121-132.
- ^[13] Leyre, S.; Coutino-Gonzalez, E; Joos, J. J.; Ryckaert, J.; Meuret, Y.; Poelman, D.; Smet, P. F.; Durinck, G.; Hofkens, J.; Deconinck, G.; Hanselaer, P. Absolute determination of photoluminescence quantum efficiency using an integrating sphere setup. *Rev. Sci. Instrum.*, 2014, 85, 123115.



- ¹⁴⁴ Valenta, J. Determination of absolute quantum yields of luminescing nanomaterials over a broad spectral range: from the integrating sphere theory to the correct methodology. *Nanosci. Meth.*, 2014, 3, 11-27.
- ¹⁴⁵ Würth, C.; Resch-Genger, U. Determination of Photoluminescence Quantum Yields of Scattering Media with an Integrating Sphere: Direct and Indirect Illumination. *Appl. Spectrosc.*, 2015, 69, 6, 749-759.
- ¹⁴⁶ Lagorio, M. G. Tutorial: Determination of Fluorescence Quantum Yields in Scattering Media. *Methods Appl. Fluoresc.*, 2020, 8, 4, 043001.
- ¹⁴⁷ Wrighton, M. S.; Ginley, D. S.; Morse, D. L. A Technique for the Determination of Absolute Emission Quantum Yields of Powdered Samples. *J. Phys. Chem.*, 1974, 78, 2229-2233.
- ¹⁴⁸ Iriel, A.; Lagorio, M. G. Is the flower fluorescence relevant in biocommunication? *Naturwissenschaften*, 2010, 97, 10, 915-924.
- ¹⁴⁹ Barreira, A. S.; Lagorio, M. G.; Lijtmaer, D. A.; Lougheed, C.; Tubaro, P. L. Fluorescent and ultraviolet sexual dichromatism in the blue-winged parrotlet. *J. Zoology*, 2012, 288, 135-142.
- ¹⁵⁰ Taboada, C.; Brunetti, A. E.; Pedron, F. N.; Carnevale Neto, F.; Estrin, D. A.; Bari, S. E.; Chemes, L. B.; Pepporine Lopes, N.; Lagorio, M. G.; Faivovich, J. Naturally occurring fluorescence in frogs. *PNAS*, 2017, 114, 3672-3677.
- ¹⁵¹ Lagorio, M. G.; Cordon, G. B.; Iriel, A. Reviewing the relevance of fluorescence in biological Systems. *Photochem. Photobiol. Sci.*, 2015, 14, 1538-1559.
- ¹⁵² Mendes Novo, J.; Iriel, A.; Lagorio, M. G. Modelling chlorophyll fluorescence of kiwi fruit (*Actinidia deliciosa*). *Photochem. Photobiol. Sci.*, 2012, 11, 724-730.
- ¹⁵³ Ospina Calvo, B.; Parapugna, T. L.; Lagorio, M. G. Variability in chlorophyll fluorescence spectra of eggplant fruit grown under different light environments: a case study. *Photochem. Photobiol. Sci.*, 2017, 16, 711-710.
- ¹⁵⁴ Lang, M.; Stober, F.; Lichtenthaler, H. K. Fluorescence emission spectra of plant leaves and plant constituents. *Radiat. Environ. Biophys.*, 1991, 20, 333-347.
- ¹⁵⁵ Pfündel, E. Estimating the contribution of photosystem I to total leaf chlorophyll fluorescence. *Photosynth. Res.*, 1998, 56, 2, 185-195.
- ¹⁵⁶ Lichtenthaler, H. K.; Buschmann, C.; Knapp, M. How to correctly determine the different chlorophyll fluorescence parameters and the chlorophyll fluorescence decrease ratio RFd of leaves with the PAM fluorometer. *Photosynthetica*, 2005, 43, 379-393.
- ¹⁵⁷ Iriel, A.; Mendes Novo, J.; Cordon, G. B.; Lagorio, M. G., 2014. Atrazine and methyl viologen effects on chlorophyll-a fluorescence revisited. Implications in photosystems emission and ecotoxicity. *Photochem. Photobiol.*, 2014, 90, 107-112.
- ¹⁵⁸ Korniyeyev D.; Hendrickson L. Research note: Energy partitioning in photosystem II complexes subjected to photoinhibitory treatment. *Funct Plant Biol.*, 2007, 34, 3, 214-220.
- ¹⁵⁹ Genty B.; Briantais J-M.; Baker N. R. The relationship between the quantum yield of photosynthetic electron transport and quenching of chlorophyll fluorescence. *Biochim. Biophys. Acta (BBA) - General Subj.*, 1989, 990, 1, 87-92.
- ¹⁶⁰ Hendrickson L.; Furbank R.T.; Chow W. S. A simple alternative approach to assessing the fate of absorbed light energy using chlorophyll fluorescence. *Photosynth. Res.*, 2004, 82, 1, 73-81.
- ¹⁶¹ Guadagno, C. R.; Virzo De Santo, A.; D'Ambrosio, N. A revised energy partitioning approach to assess the yields of non-photochemical quenching components. *Biochim Biophys Acta - Bioenerg.*, 2010, 1797, 5, 525-530.
- ¹⁶² Hendrickson, L.; Förster, B.; Pogson, B. J.; Wah, S. C. A simple chlorophyll fluorescence parameter that correlates with the rate coefficient of photoinactivation of photosystem II. *Photosynth. Res.*, 2005, 84, 43-49.
- ¹⁶³ Ospina Calvo, B.; Lagorio, M. G. Quantitative Effects of Pigmentation on the Re-absorption of Chlorophyll a Fluorescence and Energy Partitioning in leaves. *Photochem Photobiol.*, 2019, 95, 6, 1360-1368.
- ¹⁶⁴ Franck, F.; Juneau, P.; Popovic, R. Resolution of the photosystem I and photosystem II contributions to chlorophyll fluorescence of intact leaves at room temperature. *Biochim. Biophys. Acta*, 2002, 1556, 2, 239-246.

- ^{135]} Agati, G. Response of the in vivo chlorophyll fluorescence spectrum to environmental factors and laser excitation wavelength. *Pure Appl. Opt.* 1998, 7, 4, 797-807.
- ^{136]} Ramos, M. E.; Lagorio, M. G. True fluorescence spectra of leaves. *Photochem. Photobiol. Sci.*, 2004, 3, 1063-1066
- ^{137]} Cordon, G. B.; Lagorio, M. G. Re-absorption of chlorophyll fluorescence in leaves revisited. A comparison of correction models. *Photochem. Photobiol. Sci.*, 2006, 5, 735-740.
- ^{138]} Agati, G.; Fusi, F.; Mazzinghi, P.; Lipucci di Paola, M. A simple approach to the evaluation of the re-absorption of chlorophyll fluorescence spectra in intact leaves. *J. Photochem. Photobiol., B*, 1993, 17, 163-171.
- ^{139]} Gitelson, A. A.; Buschmann, C.; Lichtenthaler, H. K. Leaf Chlorophyll Fluorescence corrected for re-absorption by means of absorption and reflectance measurements. *J. Plant Physiol.*, 1998, 152, 283-296.
- ^{140]} Lagorio, M. G.; Dicelio, L. E.; Litter, M. I.; San Román, E. Modeling of Fluorescence Quantum Yields of Supported dyes. Aluminum carboxyphthalocyanine on cellulose. *J. Chem. Soc., Faraday Trans.*, 1998, 94, 3, 419-425.
- ^{141]} Guanter, L.; Zhang, Y.; Jung, M.; Joiner, J.; Voigt, M.; Berry, J. A.; Frankenberg, C.; Huete, A. R.; Zarco-Tejada, P. J.; Lee, J. -E.; Moran, M. S.; Ponce-Campos, G.; Beer, C.; Camps-Valls, G.; Buchmann, N.; Gianelle, D.; Klumpp, K.; Cescatti, A.; Baker, J. M.; Griffis, T. J. Global and time-resolved monitoring of crop photosynthesis with chlorophyll fluorescence. *Proc. Natl. Acad. Sci. U. S. A.*, 2014, 111, 14, E1327-E1333.
- ^{142]} Grace, J.; Nichol, C.; Disney, M.; Lewis, P.; Quaife, T.; Bowyer, P., Can we measure terrestrial photosynthesis from space directly, using spectral reflectance and fluorescence? *Glob. Ch. Biol.*, 2007, 13, 7, 1484-1497.
- ^{143]} Meroni, M.; Rossini, M.; Guanter, L.; Alonso, L.; Rascher, U.; Colombo, R.; Moreno, J. Remote sensing of solar-induced chlorophyll fluorescence: Review of methods and applications. *Remote Sens. Environ.*, 2009, 113, 10, 2037-2051.
- ^{144]} Atherton, J.; Liu, W.; Porcar-Castell, A. Nocturnal Light Emitting Diode Induced Fluorescence (LEDIF): A new technique to measure the chlorophyll a fluorescence emission spectral distribution of plant canopies in situ. *Remote Sens. Environ.*, 2019, 231, 111137.
- ^{145]} Alonso, L.; Gómez-Chova, L.; Vila-Francis, J.; Amorós-López, J.; Guanter, L.; Calpe, J.; Moreno, J. Improved Fraunhofer Line Discrimination Method for Vegetation Fluorescence Quantification. *IEEE Geosci. Remote S.*, 2008, 5, 4, 620-624.
- ^{146]} Romero, J. M.; Cordon, G. B.; Lagorio, M. G. Modeling re-absorption of fluorescence from the leaf to the canopy level. *Remote Sens. Environ.*, 2018, 204, 138-146.
- ^{147]} Parapugna, T. L.; Petroselli, G.; Erra-Basells, R.; Lagorio, M. G. Biospectroscopy, biospectrometry and imaging of *Ilex paraguariensis*. Basis for non-destructive quality evaluation using artificial vision. *Photochem. Photobiol. Sci.*, 2016, 15, 879-888.
- ^{148]} Petroselli, G.; Parapugna, T. L.; Lagorio, M. G.; Erra-Basells, R. MALDI- and LDI-MS saponin fingerprint of leaves and sticks components of commercial yerba mate (*Ilex paraguariensis*). *J. Mass Spectrom.*, 2019, 54, 2, 195-203.
- ^{149]} Mendes Novo, J.; Iriel, A.; Marchi, M. C.; Lagorio, M. G.. Spectroscopy, Microscopy and Fluorescence Imaging of *Origanum vulgare* L. Basis for Non-destructive Quality Assessment. *Photochem. Photobiol.* 2013, 89, 1383-1390.
- ^{150]} Mendes Novo, J.; Iriel, A.; Lagorio, M. G. Rapid spectroscopic method to assess moisture content in free and packaged oregano (*Origanum vulgare* L.) *JARMAP*, 2016, 3, 211-214.
- ^{151]} Iriel, A.; Dundas, G.; Fernández Cirelli, A.; Lagorio, M. G. Effect of arsenic on reflectance spectra and chlorophyll fluorescence of aquatic plants. *Chemosphere*, 2015, 119, 697-703.
- ^{152]} Iriel, A.; Lagorio, M. G.; Fernández Cirelli, A. Biosorption of arsenic from groundwater using *Vallisneria spiralis* plants. Kinetics, equilibrium and photophysical considerations. *Chemosphere*, 2015, 138, 383-389.
- ^{153]} Cordon, G. B.; Iriel, A.; Fernández Cirelli, A.; Lagorio, M. G. Arsenic effects on some photophysical parameters of *Cichorium intybus* under different radiation and water irrigation regimes. *Chemosphere* 2018, 204, 398-404.
- ^{154]} Iriel, A.; Cordon, G. B.; Fernández Cirelli, A.; Lagorio, M. G. Non-destructive methodologies applied to track the

occurrence of natural micropollutants in watering: *Glycine max* as a biomonitor. *Ecotoxicol. Environ. Saf.*, 2019, 182, 109368.

- ¹⁵⁵ Torres, R.; Diz, V.; Lagorio, M. G. Effects of gold nanoparticles on the photophysical and photosynthetic parameters of leaves and chloroplasts. *Photochem. Photobiol. Sci.*, 2018, 17, 505-516.
- ¹⁵⁶ Yaryura, P., Cordon, G., Leon, M., Kerber, N., Pucheu, N., Rubio, G., García, A., Lagorio, M. G., Effect of phosphorus deficiency on reflectance and chlorophyll fluorescence of cotyledons of oilseed rape (*Brassica napus* L.). *J. Agron. Crop Sci.*, 2009, 195, 186-196.
- ¹⁵⁷ Cordon, G. B.; Lagorio, M. G.; Paruelo, J. Chlorophyll fluorescence, photochemical reflective index and normalized difference vegetative index during plant senescence. *J. Plant Physiol.*, 2016, 199, 100-110.

Bios



María Gabriela Lagorio

María Gabriela Lagorio was born in Buenos Aires, Argentina. She obtained her B.S. (Chemical Sciences) in 1982 at UBA. She worked in the private industry from 1983 to 1987. Subsequently, she started her research activities, obtaining her PhD in Chemical Sciences (UBA) in 1991. She is presently Professor at UBA and scientist researcher of CONICET. She is the head of the Research Group in Photochemistry and Photobiology in the Department of Inorganic, Analytical and Physical Chemistry/ INQUIMAE (FCEN, UBA). Her research field is focused on the modeling and analysis of the interaction of light with biological entities.



Gabriela B. Cordon

Gabriela B. Cordon is Associate Scientist researcher of the National Research Council of Argentina (CONICET) and Assistant Professor at Faculty of Agronomy of Universidad de Buenos Aires. She is member of the Regional analysis and remote sensing laboratory (LART) and of the Agricultural plant physiology and ecology research institute (IFEVA). Her research focuses on the use of chlorophyll fluorescence and reflectance spectroscopy as non-destructive tools for agricultural and environmental monitoring at the leaf, plant and canopy level.



Analia Iriel

Analia Iriel was born in Santa Fe, Argentina in 1975. She received her chemistry degree in 1999 from the University of the Litoral. In 2006 she obtained her PhD at

the University of Buenos Aires under the supervision of Enrique San Román. She is currently Associate Professor at the Science and Technology School of San Martin University. She is an Associate Scientist researcher of CONICET. Her research interests include micropollutants in environmental matrixes, phytoremediation technologies to remove arsenic from groundwater and non-destructive methodologies to assess environmental risk associated to the presence of pesticides from agricultural activities.



Juan Manuel Romero

Juan Manuel Romero was born in Buenos Aires, Argentina. He has a degree in Biology (FCEN, UBA). Currently, he is completing his doctoral thesis under the direction of M. G. Lagorio and G. Cordon, in modeling the interaction of light with photosynthetic material, with the aim of using fluorescence as an indicator of physiological state. He is a CONICET fellow and a teacher in the Department of Inorganic, Analytical and Physical Chemistry.



Julián Faivovich

Julián Faivovich finished his undergraduate studies in biology in the Facultad de Ciencias Exactas y Naturales, Universidad de Buenos Aires, Buenos Aires, Argentina in 1999, and his doctoral studies in 2005, in Columbia University and the American Museum of Natural History, New York, U.S.A. After two years as a postdoc student in the Universidade Estadual Paulista, Rio Claro, São Paulo, Brazil, he returned to Argentina in 2008 as a researcher in CONICET, in charge of the herpetology division of the Museo Argentino de Ciencias Naturales "Bernardino Rivadavia." His research has always been focused in systematics and biology of amphibians.



Carlos Taboada

Carlos Taboada received his PhD in Biology in 2017 from the University of Buenos Aires. He is

currently a Human Frontier Science Program Fellow at Duke University, USA. His research focuses on organismal biology and combines various theoretical and experimental approaches in photophysics, biochemistry, spectroscopy and mass spectrometry to understand the basis of animal coloration and visual ecology.

Recalibrating Immunity in Cancer and Autoimmune Inflammation by Galectin-1-Driven Regulatory Circuits

Camila A. Bach*, Anabela M. Cutine*, Lorena Laporte*, Yamil D. Mahmoud*, Montana N. Manselle Cocco*, Mora Massaro*, Joaquín P. Merlo*, Ramiro M. Perrotta*, Nicolas Sarbia*, Florencia Veigas* and Gabriel A. Rabinovich**

Laboratorios de Inmunopatología, Glicómica Funcional e Inmuno Oncología Translacional, Instituto de Biología y Medicina Experimental (IBYME), Consejo Nacional de Investigaciones Científicas y Técnicas (CONICET), Buenos Aires, Argentina.

* These authors contributed equally to this work.

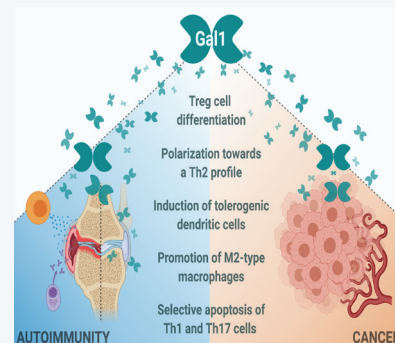
** Corresponding author. E-mail: gabyrabi@gmail.com

Abstract

Endogenous lectins play key roles in cell homeostasis by decoding the information encrypted in glycans present on the cell surface or extracellular matrix. Galectins, a family of soluble lectins, have emerged as central regulators of innate and adaptive immune responses. In this article, we review seminal work demonstrating the immunoregulatory roles of Galectin-1 (Gal-1), a proto-type member of the galectin family, and highlight central mechanisms that control its functions in cancer and autoimmune inflammation. Understanding the cellular pathways that control Gal-1 expression and function in tumor and inflammatory microenvironments will set the bases for the design of rational therapies based on positive or negative modulation of this endogenous lectin in cancer and autoimmune diseases.

Keywords:

galectins, immunomodulation, cancer, metastasis, inflammation, autoimmunity



Introduction: The cellular glycome

Every cell, from bacteria to neurons or lymphocytes, displays saccharide structures (glycans) covalently linked to proteins and lipids on the cellular surface. Glycans play crucial roles in several biological processes, such as cellular migration, differentiation, communication, immunity, and vascularization [1–4]. Our immune system harnesses the vast amount of information stored in glycan structures to control its activation, differentiation, and homeostasis [5]. Glycans are hierarchically assembled in proteins and lipids through the coordinated action of glycosyltransferases and glycosidases. In mammals, protein glycosylation occurs in parallel to protein synthesis in the endoplasmic reticulum, and then continues in the Golgi apparatus. To decipher the information encoded by glycoconjugates, dedicated glycan-binding proteins are required, which trigger distinct signaling pathways to modulate cell fate and function.

In the era of multi-omics, “glycomics” arises as a major challenge being tackled by scientists from different backgrounds and disciplines. Studying the structure, functions, and synthesis of lectins and glycans is the main goal of Glycobiology. Due to the high combinatorial possibilities of glycans present in cells and tissues, these structures emerge as a major source of biological information and diversity. This feature makes glycoconjugates attractive therapeutic targets and biomarkers in several pathologic conditions. First, their location on the cell surface makes them the first

contact point during cellular communication, thus operating as central regulators of a diversity of metabolic processes and host-pathogen interactions [6]. Second, specific glycan structures that are absent or are present in very low amounts in steady-state conditions can increase in proportion or alter their composition under stress or pathologic situations. Finally, lectin-glycan interactions may trigger, aggravate, or ameliorate pathological conditions by recalibrating immune cell homeostasis and rewiring signaling pathways in several cell types.

Glycosylation pathways and glycan-binding proteins

There are two major glycosylation pathways, namely *N*- and *O*-glycosylation (Figure 1). The prevalence of each individual pathway relies on several factors, including cell type and its physiologic activation, differentiation, and nutritional state. Furthermore, epigenetic regulation of glycosyltransferases and glycosidases, subcellular compartmentalization of individual components of the glycosylation machinery and nucleotidic sugar availability are also critical factors that affect the abundance of different glycans [7]. The presence of *N*- and *O*-glycans on a given cell type also depends on dynamic parameters of individual microenvironments including the oxygen levels, nutrient availability and prevalence of particular growth factors and cytokines. In this regard, a complex interplay occurs between the glycosylation profile of a given cell type and the development of particular disease states, highlighting the importance of studying the cellular glycome under physiologic and pathologic conditions [1]. In fact, particular glycosylation profiles have been associated with pathologic processes including chronic inflammation [8–10] and cancer [11,12].

The myriad of possible glycan combinations that can arise as a consequence of the coordinated action of glycosyltransferases and glycosidases has been shown to provide a valuable source of information that governs cell processes, including proliferation, survival, activation, differentiation, and migration [1]. *N*-glycosylation involves the addition of glycans on an asparagine residue within a consensus region -N-X-S/T, where X cannot be proline. This process involves sequential modification of an initial mannose-rich glycan by glycosidases and glycosyltransferases. Of particular interest for this review are *N*-acetylglucosaminyltransferases (MGAT1, 2, 4, and 5) that play critical roles as they generate the *N*-acetylglucosaminyl branches that serve as permissive sites for further extension of *N*-acetyl-lactosamine (Gal β 1-4GlcNAc; LacNAc) structures, which are the main target for galectins [13,14]. Furthermore, α 2,6-sialyltransferase 1 (ST6Gal-1), an enzyme that incorporates sialic acid to complex *N*-glycans in an α 2,6-linked position, inhibits binding of specific galectins (particularly Gal-1) to *N*-glycan structures. On the other hand, *O*-glycosylation occurs later, inside the Golgi apparatus, on serine or threonine residues, with T-synthase (C1GALT1) being critical for the formation of core-1-*O*-glycans and α 2,3-sialyltransferase (ST3Gal-1) further adding sialic acid to the galactose residue within the same structure [4].

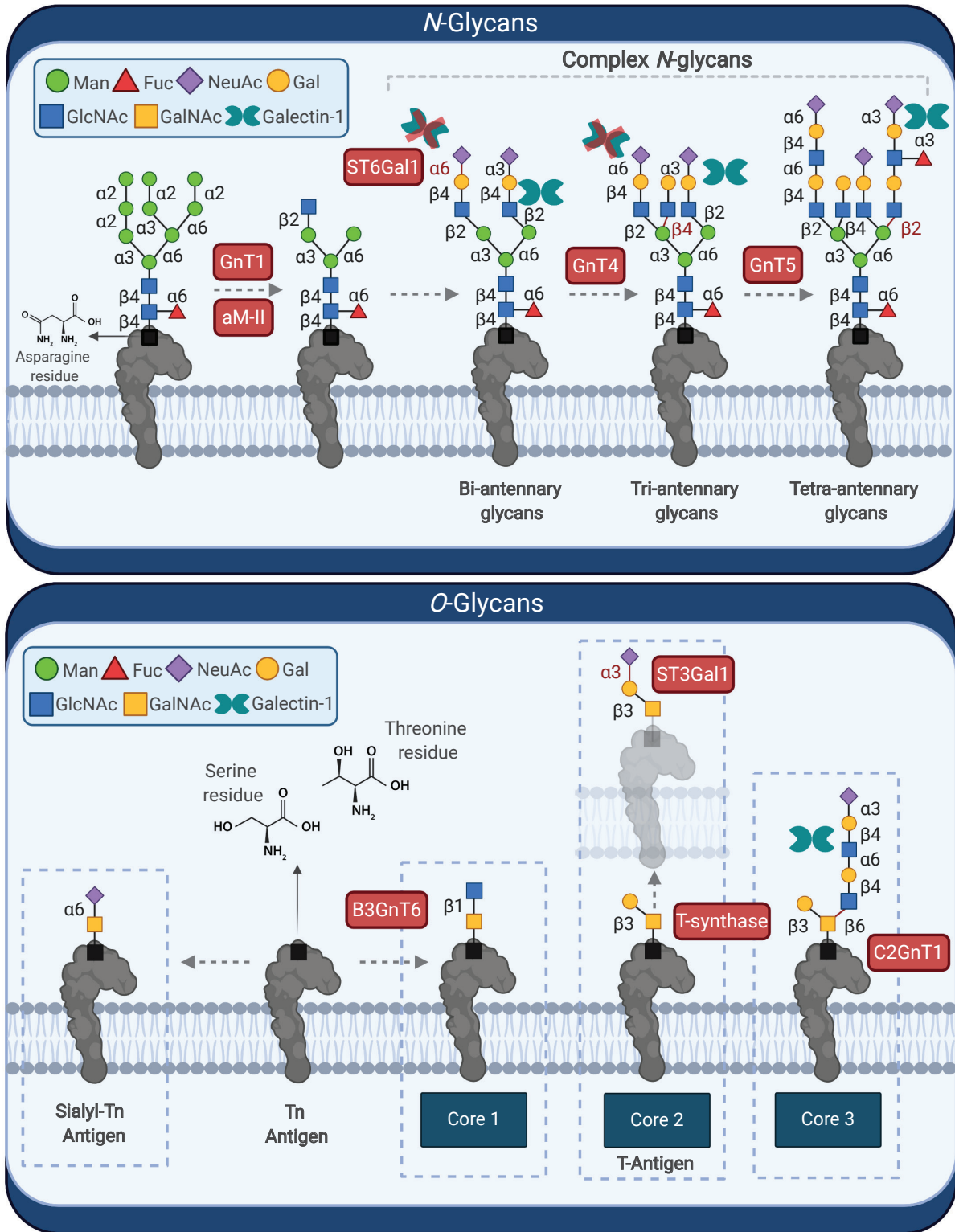


Figure 1. Glycosylation pathways involved in the synthesis of galectin ligands. The figure shows a summary of the main protein glycosylation pathways: *N*- and *O*-glycosylation and Gal-1 binding sites. Created with BioRender.com.

The responsibility of decoding the biologic information encrypted by glycans relies on endogenous glycan-binding proteins or lectins. Lectins are capable of recognizing complex glycosidic structures attached to proteins and lipids on the cell surface, triggering different cellular responses. The magnitude and quality of these responses ultimately rely on the multivalent nature of lectin-glycan interactions [15,16]. Several studies have shown, using computational modeling and biophysical approaches, that lectin-glycan interactions can lead to the formation of complex multivalent structures,

often termed “lattices”, on the surface of different cell types [16]. These structures may be assembled into supramolecular domains on the cell surface leading to glycoprotein segregation and control of signaling threshold, activation and endocytosis of cell surface receptors [17]. In several cases, these lectin-glycan complexes may substitute canonical ligands and activate surface receptors, triggering vital biologic responses such as activation, differentiation and survival [18]. Within the immune system, three major families of lectins play crucial stimulatory or inhibitory roles: a) C-type lectin receptors (CLRs); b) Sialic acid-binding immunoglobulin-type lectins (Siglecs) and c) galectins [9,10,12].

CLRs comprise a heterogeneous family of calcium ion-dependent lectins subdivided into two distinct categories based on the presence of an amino acid motif involved in glycan recognition and calcium coordination. Most of these lectins possess one or more carbohydrate recognition domains (CRDs) and are present on the surface of many immune cell types, such as macrophages and dendritic cells (DCs). CLRs containing the amino acid motif EPN (Glu-Pro-Asn) have an affinity for glycans containing mannose or fucose. This subgroup includes DC-Specific Intercellular adhesion molecule-3-Grabbing Non-integrin (DC-SIGN), the mannose receptor (MR), and Langerin. The other is composed of CLRs containing the QPD motif (Gln-Pro-Asp), which interacts specifically with *N*-acetyl-galactosamine present in the terminal position of glycans. MGL receptor (Macrophage Galactose-type Lectin), present in macrophages and DCs, is an example of this subgroup of CLRs [19]. It is worth mentioning that some CLRs do not have the Ca²⁺ requirement to interact with glycans, such as the Dectin-1 receptor that specifically recognizes β -glucans in yeasts [20]. The interaction between many specific CLRs and glycans leads to ligand internalization by endocytosis, followed by intracellular signaling pathways that lead to the expression of innate immunity-related genes [21]. Thus, CLRs are key lectins that participate in the innate immune response to bacterial and fungal infections, among other functions.

Siglecs are a family of lectins that have specificity for glycans containing sialic acid. Some of them have a restricted expression pattern, such as Siglec-2 (CD22) that is preferentially found on B cells, while others are expressed in several hematopoietic lineage cells, like B lymphocytes, macrophages, and eosinophils. To date, 16 Siglecs have been identified in humans, showing a variable number of immunoglobulin-like domains ranging from 2 in Siglec-3 (CD33) to 17 in Siglec-1 (Sialoadhesin, CD169) and slight differences in sialoside preferences. Several members of this family are relevant in many infectious diseases (e.g. HIV-1 and Group B Streptococcus infections), autoimmune diseases (e.g. rheumatoid arthritis), cancer (e.g. leukemia, lymphoma) and neurological diseases (e.g. Alzheimer disease) [6]. Recognition of sialic acid by siglecs usually promotes phosphorylation of the cytoplasmic ITIM motifs and further recruitment of phosphatases from the SHP family, which in turn inhibit diverse cell events including activation, signaling and proliferation [22].

While CLRs and siglecs act primarily as transmembrane proteins present on the surface of immune cells, galectins are soluble proteins secreted into the extracellular medium via a non-canonical secretory pathway (without involvement of the ER-Golgi system). Once in the extracellular space, galectins interact with a wide variety of glycosylated receptors through protein-glycan and protein-protein interactions, in a broad spectrum of cell types [10,12]. Intracellularly, galectins can modulate signaling pathways, control lymphocyte survival, and even interact with the RNA splicing machinery [10,23–26]. Fifteen members of the galectin family are known in mammals, although galectin-like domains have been identified in insects, fungi and plants [25, 27]. Galectins have at least one CRD of approximately 130 structurally-preserved amino acids and can be subdivided into three subgroups based on their structural features: a) “Proto-type” galectins (Gal-1, -2, -5, -7, -10, -11, -13, -14, and -15) have a single CRD and can be found as monomers or dimers; b) “Tandem repeat-type” galectins (Gal-4, -6, -8, -9, and -12) contain two tandem CRDs within the same polypeptide chain, joined by a separating region (linker) of up to 70 amino acids; and c) “Chimera-type” galectins have a single CRD together with a non-lectin N-terminal region necessary for its oligomerization, with Gal-3 being the only member of this subgroup. (Figure 2) [10, 25, 28].

Initially, galectins were defined by their ability to recognize the disaccharide LacNAc present in *N*- and *O*-glycans on cell surface glycoproteins [29]. However, galectins’ CRDs can differ in some amino acids, which are not in the conserved sequence, leading to their ability to recognize different structures. Furthermore, modifications to the LacNAc or poly-LacNAc structure can differentially affect galectin-glycan interactions. While some galectins tolerate the addition of a terminal sialic acid or internal fucose in the lactosamine sequence, others are not able to bind LacNAc modified with these residues [30, 31]. In this regard, we have recently found that Gal-12, a lectin preferentially expressed by adipocytes, binds to 3'-fucosylated structures with high affinity, making it the first member of the galectin family showing specificity for this glycan structure [32]. Besides, galectins differ in their ability to recognize LacNAc in a terminal position or internal repetitions within the glycan structure (Figure 2). This relative selectivity could explain, at least in part, the functional differences observed among individual family members [29, 33–35]. Several factors can influence the biological activity of galectins including their oligomerization status, exposure of *N*- and *O*-glycans on target cells and the prevailing oxidative or reducing conditions of different tissue microenvironments [10]. While some galectins have a ubiquitous expression pattern, others exhibit a specific tissue distribution. Within the immune system, galectins are expressed by virtually all cells either constitutively or in an inducible manner [10, 15, 25, 28]. Furthermore, galectins can recognize glycans present on the surface of microorganisms, suggesting an early evolutionary origin for these molecules as soluble proteins capable of recognizing pathogen-associated glycosylated patterns [15, 36, 37].

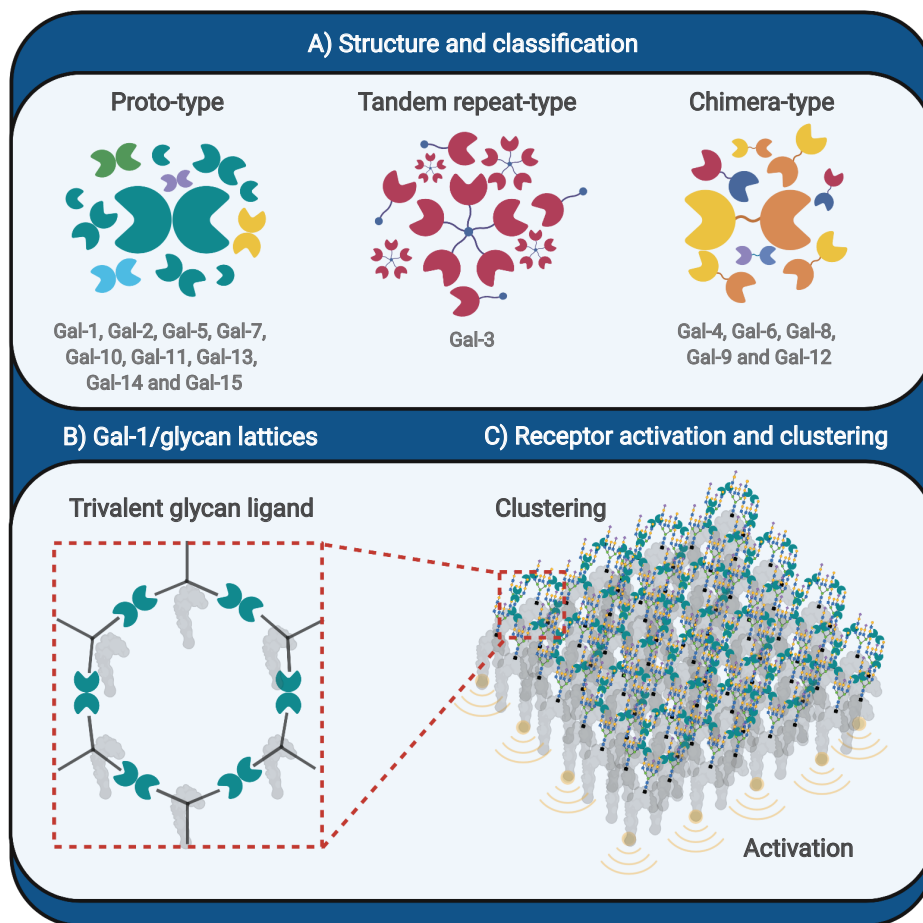


Figure 2. Classification of galectins: structure, function, and specificity. **A-** Schematic representation of the structure of the galectin family; **B-** Schematic representation of Gal-1 lattices upon trivalent glycan binding. **C-** Lattice formation gives rise to receptor clustering, activation triggering and altered internalization. Created with BioRender.com.

In the following sections, we will focus on seminal discoveries leading to the identification of central roles of Gal-1, crucial to immune tolerance and homeostasis in different physiopathologic conditions. We will discuss the therapeutic implications derived from the function of Gal-1 in chronic inflammation, vascularization, autoimmunity, pregnancy, and cancer, and we will highlight some of the contributions of our group to understanding these conditions from a glycobiological perspective.

Gal-1: A novel mechanism of tumor-immune escape and therapeutic target in cancer

During the last decade, the revolution of cancer immunotherapies changed our perspective on how our immune system interacts with tumors. However, the idea of the immune system playing a pivotal role in tumor biology dates back to more than a century ago when William Coley used extracts of heat-inactivated *S. pyogenes* and *S. marcescens* (termed as the Coley toxin) to treat cancer patients seeking to enhance their immune response [38, 39]. In 1909, Paul Ehrlich came up with the idea that our immune system is continuously eliminating transformed cells that could potentially cause tumors [38, 40]. Back to our days, it is well established that a fully competent immune system, composed of a variety of cell types including natural killer (NK) cells, CD8⁺ cytotoxic T lymphocytes, CD4⁺ helper T lymphocytes, macrophages, DCs and others, can identify and destroy transformed cells in pre-neoplastic and neoplastic lesions. Nevertheless, either due to a generalized state of immunosuppression or to specific inhibitory mechanisms displayed within the local tumor microenvironment, cancer cells have the ability to evade innate and adaptive immune responses. In fact, many cancer cells co-opt immunoregulatory programs that are commonly activated during the physiologic resolution of inflammation to restore immune cell homeostasis. For example, the expression of Programmed Cell Death Ligand-1 (PD-L1) on

the surface of tumor cells dampens the activation and proliferation of T cells, fostering a dysfunctional state called T cell exhaustion, which compromises cytotoxic anti-tumor immunity favoring tumor growth [38]. Among the several mechanisms implicated in immune evasion, the upregulation of inhibitory molecules termed as “immune checkpoints”, such as the PD-1/PD-L1 axis and the cytotoxic T-lymphocyte antigen receptor (CTLA-4), stand out among the others due to their clinical and therapeutic relevance in a broad range of cancers [41–44].

Understanding the mechanisms underlying tumor-immune escape led to the development of a broad range of immunotherapeutic modalities seeking to reverse the immune inhibitory mechanisms triggered by tumors and boosting the immune system to control tumor growth and metastasis. In particular, monoclonal antibodies targeting the immune checkpoint pathways CTLA-4 and PD-1/PD-L1 have generated unprecedented clinical success and therapeutic opportunities to treat a wide variety of tumors including melanoma, lung adenocarcinoma, renal cancer, gastrointestinal tumors, head and neck squamous cell carcinoma (HNSCC), triple negative breast cancer, non-melanoma squamous cell carcinomas, Hodgkin’s lymphoma, and others. Moreover, other therapeutic approaches are based on agonist antibodies to co-stimulatory molecules, tumor cell vaccines (like DC vaccines), or chimeric antigen receptors (CARs) [38]. Outstanding clinical benefits, including tumor size reduction and increased disease-free survival, have been observed in a large number of cancer patients receiving immunotherapy [41–45]. However, some patients are resistant to these treatments, either through intrinsic or acquired mechanisms, and experience a relapse characterized by tumor recurrence at the primary site or distant tissue outgrowth in a process known as metastasis [45, 46]. These compensatory mechanisms include the expression of alternative inhibitory molecules such as lymphocyte activation gene-3 (LAG-3) and T cell immunoglobulin mucin-3 (TIM-3), among others, whose autonomic functions can control various aspects of the anti-tumor immune response, promoting alternative escape pathways [47].

Our laboratory has focused on elucidating the immunoregulatory circuits triggered by Gal-1-glycan interactions in tumor and inflammatory microenvironments. Initially, we found that human and mouse melanoma cells secrete Gal-1, which substantially contributes to the immune privilege of these tumors by regulating distinct immune effector mechanisms. Gal-1 silencing in the B16 melanoma mouse model resulted in heightened tumor rejection, increasing expansion of T helper (Th1) and cytotoxic CD8⁺ T cells [48] (Figure 3). Investigation of the molecular mechanisms underlying Gal-1-driven immunoregulation revealed the ability of this lectin to induce selective apoptosis of cytotoxic CD8⁺ T cells, Th1, and Th17 lymphocytes, skipping Th2 and naïve T cells [48, 49]. This differential susceptibility to cell death was associated with dissimilar sialylation patterns among distinct effector T cells. Whereas activated CD8⁺ T cells as well as Th1, and Th17 display all of the essential glycans that are critical for Gal-1 binding (high frequency of non-sialylated glycans and elongated LacNAc residues on core-2- *O*-glycan structures), Th2 lymphocytes as well as naïve T cells exhibit high frequency of α 2,6 sialylation which prevents Gal-1 binding to terminal LacNAc residues [10, 49] (Figure 3). Interestingly, this tumor-immune privilege mechanism was also evident in classical Hodgkin’s lymphoma. In these tumors, Reed Sternberg cells up-regulate Gal-1 expression through the activation of an enhancer of the AP-1 transcription factor driven by the Epstein Bar virus (EBV), thereby supporting the Th2-dominant immunosuppressive microenvironment typical of this hematologic malignancy [50]. Accordingly, Gal-1 has been identified as a biomarker of refractory/resistant disease in classical Hodgkin lymphoma patients [51]. Furthermore, Gal-1 silencing in the triple negative breast cancer mouse model 4T1 resulted in reduced tumor size and metastases, accompanied by lower frequency of regulatory T cells (Treg) in the tumor microenvironment, lymph nodes and metastatic lungs [52] (Figure 3). Thus, both tumor and associated stroma may express and secrete Gal-1, promoting the generation of an immunosuppressive milieu and the activation of tolerogenic circuits that thwart the development of effective anti-tumor T cell responses.

In addition to modulation of adaptive T-cell responses, Gal-1 also controls innate immune pathways by modulating macrophage and DC function. In this regard, we found that Gal-1 triggers an M2 macrophage profile by regulating L-arginine metabolism and interfering with major histocompatibility complex (MHC)-II-dependent antigen presentation as well as Fc γ receptor I-dependent phagocytosis [53, 54]. Furthermore, silencing of tumor-derived-Gal-1 by short-hairpin RNA (shRNA) in the high-grade glioma mouse model GL261 decreased myeloid cell accumulation within the tumor microenvironment and prolonged survival in tumor-bearing mice [55]. In addition, Gal-1 induced differentiation of tolerogenic DCs by regulating phosphorylation of the signal transducer and activator of transcription 3 (STAT3) transcription factor, and favoring the expression of anti-inflammatory cytokines including IL-27 and IL-10, which dampen anti-tumor responses [56]. In addition, Gal-1 secreted by mouse and human neuroblastoma cells triggers immunosuppressive programs by compromising T cell and DC functions [57] (Figure 3).

The expression of Gal-1 in several cancer types, including prostate, breast, lung and pancreatic cancer, increases with tumor progression, thus underlining a central role of this lectin as a possible prognostic biomarker of neoplastic progression and an attractive therapeutic target in a variety of cancer types [58–60]. In this context, we found that Gal-1 exerts both paracrine and autocrine functions that control proliferation, anti-tumor immunity, and angiogenesis in pancreatic adenocarcinoma, thus reinforcing the multifunctional role of Gal-1 during tumor progression [60]. Supporting

these observations, high levels of Gal-1 were associated with lower infiltration of cytotoxic CD8⁺ T cells and poor clinical outcomes in T cell lymphomas [61]. Furthermore, Nambiar and colleagues recently reported a role for Gal-1 in resistance to immunotherapy in HNSCC. Particularly, Gal-1 blockade increased T cell infiltration, leading to superior responses to anti-PD-1 therapies in this tumor type [62]. Likewise, we found that Gal-1 secretion by tumor-driven $\gamma\delta$ T cells contributes to tumor progression by linking commensal microbiota, systemic inflammation, and unremitted immunosuppression [63].

In addition to the broad immune inhibitory mechanisms, Gal-1 also contributes to tumor growth and progression by favoring the generation of tumor-associated blood vessels. We found that Gal-1 promotes vascularization through direct association with the complex *N*-glycans present on the vascular endothelial growth factor (VEGF) type 2 receptor (VEGFR2). This pro-angiogenic program is triggered under hypoxic conditions, which up-regulate Gal-1 expression in tumor cells [64] and induce changes in VEGFR2 glycosylation characterized by high frequency of complex branched *N*-glycans and low levels of α 2,6 sialylation [65]. We found that Gal-1 blockade successfully counteracted resistance to anti-VEGF treatment by co-opting the VEGFR2 signaling pathway in different tumor models including mouse Lewis lung carcinoma and EL-4 thymic lymphoma [65]. Moreover, antibody-mediated Gal-1 neutralization promoted vessel normalization and influx of CD8⁺ T lymphocytes in different tumor types [65] (Figure 3). Interestingly, in melanoma patients treated with anti-VEGF (bevacizumab) and anti-CTLA-4 (ipilimumab), circulating Gal-1 levels are associated with a poor clinical outcome, while circulating anti-Gal-1 autoantibodies correlates with clinical response [66]. Thus, Gal-1 serves as a novel glyco-checkpoint that controls immune and vascular signaling programs and an attractive therapeutic target in various cancer types including melanoma, Hodgkin lymphoma, chronic lymphocytic leukemia (CLL), Kaposi's sarcoma, lung, breast, kidney, pancreatic, and prostate carcinomas, glioblastoma and neuroblastoma [58]. Thus, Gal-1 blockade, either alone or in combination, represents a promising immune therapeutic strategy to treat advanced stage and refractory tumors.

Gal-1: A key regulator of the metastatic cascade

Metastasis is a multistage program through which cancer cells detach from the tissue of origin, migrate through blood or lymphatic circulation and colonize a secondary organ [67, 68]. Besides serving as local regulators of immune responses, galectin-glycan interactions have emerged as key players of the metastatic cascade, influencing tumor cell migration, survival in the circulation, dissemination, and colonization of metastatic organs. Accordingly, Gal-1 can regulate cell-cell and cell-matrix interactions, a process associated with invasiveness and metastasis in several human tumor types [69]. Gal-1 also increases adhesion of cells to the extracellular matrix (ECM) by interacting with laminin and fibronectin via glycosylation-dependent mechanisms [70, 71, 72], and it promotes homotypic and heterotypic aggregation of cancer cells [73, 74]. In oral squamous cell carcinoma (OSCC), Gal-1 expression in cancer-associated stroma correlated with poor prognosis [75] and promoted tumor invasion by up-regulating metalloproteinase (MMP)-2 and -9 and increasing the number and length of filopodia on tumor cells [76]. Additionally, Gal-1 expression is up-regulated by stromal cells in invasive breast carcinoma patients when compared with *in situ* carcinomas [77]. Furthermore, Gal-1 induces up-regulation of mesenchymal markers and down-regulation of E-cadherin in hepatocellular carcinoma cell lines, promoting transition from epithelial morphology toward a fibroblastic mesenchymal phenotype [78]. In addition, studies in gastric cancer cells found that high Gal-1 expression levels in cancer-associated fibroblasts (CAFs) up-regulate the expression of β 1-integrin, inducing cancer cell migration and invasion [79], and promoted epithelial-to-mesenchymal transition (EMT) via the non-canonical activation of the Hedgehog pathway [80]. Moreover, in human pancreatic cancer cells, Gal-1 induced up-regulation of genes associated with migration and invasion and facilitated EMT through nuclear factor kappa B (NF- κ B) transcriptional regulation, thus influencing liver metastases [60, 81]. The pro-metastatic activity of Gal-1 was also observed in metastatic castration-resistant prostate cancer cell lines, where silencing of this lectin led to inhibition of migration and invasion via suppression of Akt and androgen receptor (AR) signaling [82]. Moreover, Gal-1 has also been identified as a key effector of tropomyosin receptor kinase-mediated invasiveness and migration in human neuroblastoma cell lines [83], highlighting diverse mechanisms underlying the pro-metastatic role of this lectin in tumor microenvironments.

In addition to the extracellular roles of Gal-1, this lectin has an important intracellular role in cancer by sustaining proliferative signals through specific interactions with oncogenic RAS, a well-known cancer driver gene mutated in several tumors. Constitutive activation of HRAS, KRAS, and NRAS proteins promotes continuous proliferation in different cancer types [84]. In this setting, Gal-1 facilitates RAS membrane anchorage and activation, thereby sustaining tumor cell proliferation [85, 86]. On the other hand, the interaction between Gal-1 and RAS in lung cancer leads to chemoresistance and tumor progression through the up-regulation of p38, cyclooxygenase-2 and extracellular regulated kinase (ERK) pathways [87]. Thus, Gal-1 association with oncogenic proteins, transcription factors, cell adhesion molecules and distinct signaling pathways can have an effect on the invasion, dissemination and colonization of cancer cells, emphasizing the relevance of Gal-1 blockade to control tumor progression and metastasis.

Gal-1: A potential therapeutic agent for autoimmune and chronic inflammatory diseases

Autoimmune diseases include a wide range of chronic inflammatory disorders generated by the interruption of immune tolerance and homeostatic mechanisms. Both genetic and environmental factors play key roles in the development of autoimmune and chronic inflammatory diseases. A deeper understanding of the cellular and molecular mechanisms underlying these immune-mediated disorders could lead to the development of new and more effective immunomodulatory therapies. Through interaction with glycosylated receptors on immune cells, Gal-1 exerts broad immunoregulatory functions promoting resolution of autoimmune inflammation [88]. The mechanisms underlying Gal-1 function involve selective deletion of Th1 and Th17 cells, inhibition of pro-inflammatory cytokines, promotion of tolerogenic DCs, expansion of Tregs and induction of M2 macrophage polarization [49,88, 89].

The precise description of different mechanisms underlying the immunoregulatory effects of different members of the galectin family in autoimmune inflammation has been reviewed recently [90]. In this section, we will focus on the role of Gal-1 in regulating immune tolerance and suppressing inflammation in different models of autoimmune disease. The immunosuppressive properties of Gal-1 have been evaluated in several diseases and experimental models of chronic inflammation and autoimmunity, including experimental autoimmune encephalomyelitis (EAE) [49], collagen-induced arthritis (CIA) [91, 92], Sjögren's syndrome [93], 2,4,6-trinitrobenzene sulfonic acid (TNBS)-induced colitis [94], celiac disease [88], experimental autoimmune uveitis (EAU), experimental induced uveitis (EIU) [95, 96], experimental autoimmune diabetes [97, 98], experimental autoimmune orchitis (EAO) [99] and allergic airway inflammation [100].

Multiple Sclerosis

Multiple Sclerosis (MS) is a chronic progressive brain and spinal cord degenerative disease characterized by the demyelination and inflammation of the central nervous system (CNS) [101, 102]. Gal-1 demonstrated immunomodulatory activity on experimental autoimmune encephalomyelitis (EAE), an animal model that recapitulates many of the clinical, histopathological, and immunological manifestations of MS [103, 104]. The resulting pathology can range from acute muscular paralysis episodes to chronic recurrent neurological processes leading to a general motor disability [105]. Th1 and Th17 lymphocyte subpopulations play key pathogenic roles in the autoimmune process underlying MS and EAE [106, 107]. It has been postulated that Th17 cells have a critical role in the initial stage of this disease, whereas IFN- γ -secreting Th1 cells are more important in later stages of autoimmune neuroinflammation [108]. In fact, myelin-specific infiltrating Th17 and Th1 cells determine where CNS inflammation occurs [109]. Brain tissue of MS patients displays an increased proportion of Th17 lymphocytes and elevated levels of IL-17A in comparison with healthy controls [106]. We studied the role of Gal-1 in EAE by immunization of mice lacking this protein (*Lgals1^{-/-}*) with myelin-oligodendrocyte glycoprotein (MOG)₃₅₋₅₅ peptide. Lack of endogenous Gal-1 resulted in greater disease severity as compared to wild-type (WT) mice [49]. Mice devoid of Gal-1 showed a more pronounced area of demyelination in spinal cord sections, increased frequency of antigen-specific Th1 and Th17 cells in the spleen, as well as a more vigorous antigen-specific proliferative T-cell response [49]. Accordingly, EAE mice treated daily with recombinant Gal-1 (rGal-1) from day 3 to 9 after immunization showed a decrease in clinical severity score [49]. We found that Gal-1 exerts its function by limiting the frequency of antigen-specific IL-17- and IFN- γ -producing CD4⁺ T cells as a result of selective apoptosis due to differential glycosylation of these immune cell populations [49] (Figure 3). In addition to the ability of Gal-1 to control T cell physiology, we found that this lectin instructs DCs to differentiate toward a tolerogenic profile. Gal-1-conditioned DCs acquired a regulatory signature characterized by IL-27 production and ability to induce IL-10-producing type-1 regulatory T (Tr1) cells [56]. Supporting these findings, *Lgals1^{-/-}* mice injected with MOG₃₅₋₅₅ showed a decrease in tolerogenic DCs and Tregs in comparison to WT mice [110]. Interestingly, a significant increase in Gal-1 expression has been reported during the peak and resolution phases of EAE [56], similar to the expression pattern documented for other inhibitory signals such as PD-L1 and its receptor PD-1 [111]. In addition, within the CNS, Gal-1 was mainly expressed by astrocytes during the resolution phase of EAE. Astrocyte-derived Gal-1 acts directly on microglia cells via interaction with core 2 O-glycans on CD45 phosphatase, changing the functional pattern of these cells from a pro-inflammatory M1 toward an anti-inflammatory M2 phenotype, which prevented inflammation-induced neurodegeneration [112] (Figure 3). Thus, Gal-1 triggers tolerogenic circuits within the CNS and peripheral lymphoid organs that control the severity of autoimmune neuroinflammation.

Rheumatoid Arthritis

Rheumatoid arthritis (RA) involves a chronic inflammation of synovial joints leading to cartilage destruction and bone erosion. Induction of autoantibodies, activation of resident fibroblasts, and expansion of activated autoreactive lymphocytes, macrophages, and plasma cells are typical hallmarks of this disease [113]. These innate and adaptive

immune cells proliferate abnormally, invading both cartilage and bone and inducing increased levels of pro-inflammatory cytokines and MMPs that promote the activation of osteoclasts [114]. We assessed the preventive and therapeutic effects of Gal-1 in a murine model of CIA by means of gene and protein therapy strategies (Figure 3). Mice were immunized with type-II collagen to elicit cellular and humoral arthritogenic responses [115, 116]. Daily injections of recombinant Gal-1 or transfer of genetically-modified fibroblasts secreting high levels of this lectin, reduced the frequency of circulating anti-collagen immunoglobulins, particularly IgG2a in mice with CIA. The mechanism underlying this effect involved a shift toward a Th2-like profile, with decreased IFN- γ and increased IL-5 production [91]. Further studies contributed to elucidate the role of Gal-1 in RA by showing that *Lgals1*^{-/-} mice had increased susceptibility to CIA, showing more vigorous T cell proliferation and augmented expression of IL-17 and IL-22 [92]. In RA patients, the concentration of Gal-1 in synovial fluid decreased significantly compared to healthy controls, even though plasmatic levels were comparable [117]. Likewise, we found a decreased expression of this lectin in synovial tissue of juvenile idiopathic arthritis patients [118]. Moreover, in a local cohort of RA patients, we found considerably higher levels of serum Gal-1 correlating with systemic inflammation compared to healthy individuals [89], suggesting differences in local versus systemic regulation of this lectin during the course of the disease. Thus, Gal-1 controls arthritogenic inflammation by restoring T cell homeostasis and modulating cytokine production.

Sjögren's syndrome

Sjögren's syndrome is characterized by lymphocytic infiltration of exocrine glands and the presence of different autoantibodies. In contrast to CIA and EAE models, where mice were immunized with arthritogenic and encephalitogenic peptides, mice lacking Gal-1 or complex branched *N*-glycans developed spontaneous age-dependent sialadenitis resembling Sjögren's syndrome manifestations [93]. Lack of Gal-1 disrupted tolerogenic circuits and enhanced T cell activation and recruitment to the salivary glands. We demonstrated that aged *Lgals1*^{-/-} mice had lower expression of PD-L1 in salivary gland cells and increased recruitment of IFN- γ -producing PD-1⁺ CD8⁺ T cells to this organ. Moreover, Gal-1-deficient mice showed higher frequency of DCs with immunogenic capacity [93]. We verified these findings in nonobese diabetic (NOD) mice, a well-established mouse model for Sjögren's-like syndrome. Administration of rGal-1 to NOD mice rescued the autoimmune phenotype showing a significant reduction of CD45⁺ cells within the salivary glands. Accordingly, labial biopsies from primary Sjögren's syndrome patients showed reduced Gal-1 expression concomitant with a higher number of infiltrating CD8⁺ T cells [93]. These findings demonstrate that endogenous Gal-1 plays a key role in preventing age-dependent development of spontaneous autoimmunity (Figure 3).

Inflammatory bowel disease

Inflammatory bowel diseases (IBD) constitute a group of multifactorial chronic disorders that affect the digestive tract, such as Crohn's disease (CD) and ulcerative colitis (UC). These disorders are characterized by a dysregulation of mucosal immune homeostasis, due to defects in tolerance induction against commensal microbiota or excessive activation of effector immune responses [119]. The 2,4,6-trinitrobenzenesulfonic acid (TNBS)-induced colitis mouse model recapitulates several features of IBD. In this model, the TNBS hapten is delivered into the mouse colonic lumen, eliciting an inflammatory immune response in the gut. The broad tolerogenic responses of Gal-1 prompted speculation on its potential regulatory role in the control of colitogenic immune responses in the inflamed gut. Administration of rGal-1 in this model resulted in an increased number of apoptotic T cells in the colonic lamina propria and a decreased frequency of Th1 cytokines in comparison with untreated mice [120]. Moreover, this lectin also maintained intestinal tissue homeostasis through the control of epithelial cell viability and regulation of epithelial-derived immunoregulatory cytokines [121] (Figure 3). Future studies should explore the exact role of this lectin and its glycosylated ligands on intestinal immune cell populations.

Celiac disease

Celiac disease is a T cell mediated disorder where chronic intestinal inflammation occurs as a result of immune responses to wheat gluten peptides. This dysregulated immune response has multifactorial etiology and up to now, the only effective treatment known is strict adherence to gluten-free diet [122]. We demonstrated an increased expression of Gal-1 in duodenal biopsies of celiac disease patients after a lifelong gluten-free diet, compared to patients who did not take this diet [88]. These findings suggested that this lectin might contribute to the resolution of chronic inflammation in response to gluten withdrawal. Moreover, Gal-1 could be considered as a potential biomarker for the follow-up of celiac disease patients [88]. Future studies should be aimed at analyzing the role of endogenous Gal-1 or exogenous rGal-1 administration in mouse models of celiac disease.

Uveitis

Autoimmune uveitis is characterized by an inflammatory response that occurs in the uvea and can adversely affect vision leading to blindness [123]. Experimental autoimmune uveitis (EAU) is a mouse model of this intraocular inflammatory disease characterized by the inflammation and destruction of the neural retina. The disease is induced by immunization with retinal antigens such as interphotoreceptor retinoid binding protein (IRBP) and adjuvants like pertussis toxin (PTX). In this model, we demonstrated that the administration of rGal-1 decreased disease severity, mainly by reducing immune cell infiltration and shifting the Th1 response towards a Th2 or Treg cell profile [95]. Meanwhile, in the endotoxin-induced uveitis (EIU) model, the disease is induced by inoculation with lipopolysaccharide (LPS) in the rat's paw. Administration of rGal-1 to LPS-treated rats attenuated the histopathological manifestations of EIU, suppressing the expression of pro-inflammatory cytokines such as IL-6, IL-1 β , and monocyte chemoattractant protein-1 (MCP-1), thus inhibiting polymorphonuclear cells infiltration [96]. Furthermore, in clinical settings, anti-Gal-1 autoantibodies correlated with the severity of ocular pathology in autoimmune and infectious uveitis [124]. Further studies should be aimed at analyzing the protective role of endogenous Gal-1 in preserving immune privilege in the eye and preventing ocular inflammation.

Diabetes

In type I diabetes, insulin-producing pancreatic β -cells are destroyed by autoreactive T cells [97]. Gal-1 demonstrated an anti-inflammatory role in spontaneous diabetes in NOD mice. This effect was accompanied by downregulation of T cell pro-inflammatory response and augmented frequency of Th2 responses, thus preventing hyperglycemia at early and subclinical stages [97]. Supporting these findings, patients with type 1 diabetes had lower serum levels of Gal-1 compared to healthy controls, mainly due to a reduced secretion of this lectin by monocytes [98] (Figure 3). Whether Gal-1-driven programs could link immune, endocrine, and metabolic pathways in diabetic individuals still remains to be elucidated.

Orchitis

Testicular inflammation and anti-sperm antibodies are the main features of autoimmune orchitis [125]. Given the high expression of Gal-1 in Sertoli testicular cells [126], we investigated the possible role of this lectin in autoimmune testicular inflammation. In a model of experimental autoimmune orchitis (EAO), we found that Gal-1 expression did not correlate with the extent of the inflammatory response. Paradoxically, in this model, *Lgals1*^{-/-} mice showed a reduction in the incidence and severity of the disease. However, when rGal-1 was administered exogenously, inflammation was dampened, and clinical symptoms were attenuated similarly to other autoimmune inflammation models [99]. These results highlight the dual role of endogenous versus exogenous Gal-1 in this particular experimental model. Further studies should be aimed at dissecting innate and adaptive components differentially regulated by exogenous and endogenous Gal-1 in autoimmune testicular inflammation.

Allergic Airway Inflammation

Allergic airway inflammation is characterized by elevated recruitment of eosinophils to the lung and increased activation of antigen-specific Th2 responses. Murine models resembling allergic asthma involve acute or chronic exposure to ovalbumin (OVA). We evaluated the relevance of the Gal-1-glycan axis in this model. An immunohistochemical analysis revealed recruitment of Gal-1-expressing inflammatory eosinophils to the inflamed lungs [100]. Interestingly, Gal-1 expression was up-regulated in the epithelial cells, smooth muscle cells and endothelial cells of the lungs and within the extracellular space as a result of allergen exposure. Recombinant Gal-1 inhibited eosinophil migration through specific recognition of LacNAc residues on the surface of these cells. Moreover, *in vivo* studies showed augmented eosinophil and T cell recruitment to the airways in allergen-exposed *Lgals1*^{-/-} compared to WT mice. Thus, allergen-challenged *Lgals1*^{-/-} mice exhibited airway hyperresponsiveness that could be attributed to a lack of eosinophilia regulation by Gal-1 at inflammation sites [100]. Overall, this study showed an important role for Gal-1 in the resolution of airway inflammation through the control of eosinophils' migratory and functional capacity, opening therapeutic avenues for eosinophil-dependent inflammatory responses (Figure 3).

Immune-related failing pregnancies

The elevated amounts of Gal-1 during gestation in different species and its high sensitivity to hormonal regulation [127, 128], prompted us to investigate the role of this lectin during pregnancy. Consistent with a marked decrease in Gal-1 expression during failing pregnancies, *Lgals1*^{-/-} female mice showed higher rates of fetal loss compared to WT mice in

allogeneic mating. Treatment with rGal-1 prevented fetal loss and restored tolerance through mechanisms involving expansion of IL-10-secreting Treg cells *in vivo* [129]. Supporting these findings, increased frequency of circulating anti-Gal-1 autoantibodies were detected in sera from women with spontaneous recurrent abortions compared to fertile women [130]. Interestingly, Gal-1 also controls sperm fertilizing activity [131], suggesting diverse roles for this lectin during mammalian reproduction and gestation.

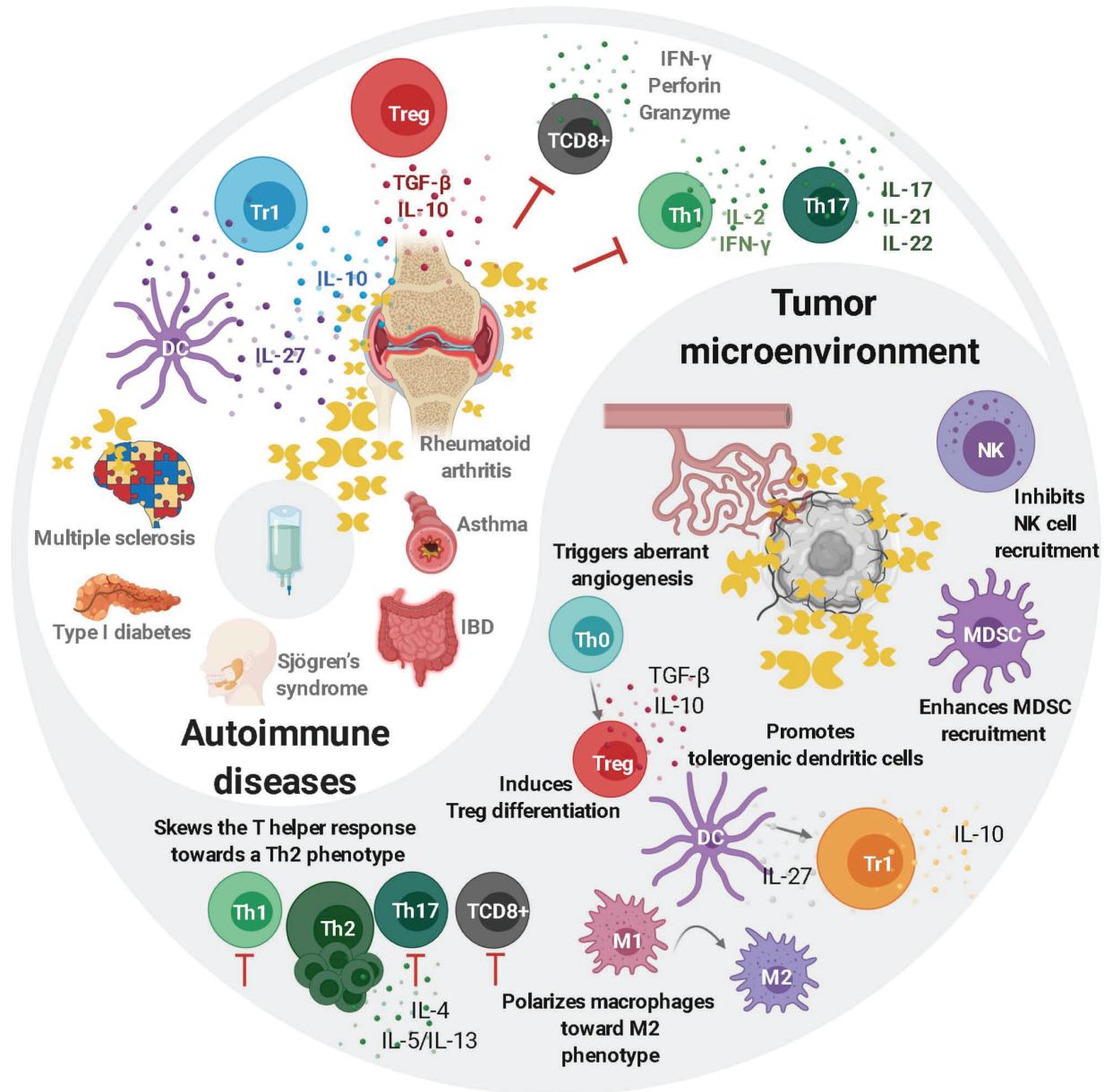


Figure 3. *Contrasting roles of Gal-1 in autoimmunity and cancer.* On the right, several immunosuppressive effects that Gal-1 exerts within the tumor microenvironment are illustrated, including induction of CD8⁺ T cell apoptosis, expansion of immunosuppressive Tregs, differentiation of tolerogenic DCs, induction of macrophage polarization from a pro-inflammatory M1 toward an anti-inflammatory M2 profile, and promotion of aberrant angiogenesis. Gal-1 blockade triggers an effective T cell-mediated anti-tumor response and control of tumor growth. On the left, the beneficial functions underlying the administration of rGal-1 in autoimmune diseases are outlined, including selective death of Th1 and Th17 lymphocytes, inhibition of pro-inflammatory cytokines, differentiation of tolerogenic DCs leading to expansion of Tr1 cells, and promotion of Treg cell expansion. Thus, administration of exogenous rGal-1 would favor the resolution of inflammatory and autoimmune processes. Created with BioRender.com.

Concluding remarks and future perspectives

In this review, we discussed the multifunctional roles of Gal-1, an endogenous immunomodulatory β -galactoside binding protein, in cancer and autoimmune inflammation. Through recognition of terminal LacNAc residues present in complex branched *N*-glycans and core-2 *O*-glycan structures, this lectin recalibrates innate and adaptive responses by modulating the survival, activation, trafficking, and differentiation of immune cells. Expression of Gal-1 during peak and resolution phases of inflammatory responses contributes to restoring immune homeostasis by blunting exacerbated immune responses through induction of glycosylation-dependent tolerogenic circuits. Accordingly, dysregulation of Gal-1 expression and/or its glycosylated ligands contribute to the establishment and perpetuation of pathologic conditions.

On the one hand, interruption of Gal-1-glycan interactions leads to exacerbation of inflammatory and autoimmune responses. It has been demonstrated in a wide range of experimental models of autoimmune diseases that the absence of Gal-1 aggravates the clinical severity of the disease [49, 56, 92, 93, 112]. In this regard, we recently found that aged *Lgals1*^{-/-} mice spontaneously develop a Sjögren's-like syndrome [93], providing clear-cut evidence of the central role of endogenous Gal-1 in the control of immune homeostatic programs. This effect was further validated by the broad immunomodulatory activity of exogenous rGal-1 in a broad range of autoimmune experimental models [90]. Interestingly, augmented T cell-dependent inflammatory responses have also been observed in mice lacking the *Mgat5* glycosyltransferase, responsible for generating galectin ligands [17]. These findings place the Gal-1-glycan axis at the center of the scene of immune tolerance and homeostasis, highlighting a potential therapeutic target for T cell-dependent autoimmune inflammation. Since current therapies in autoimmune diseases are not curative and show substantial side effects [132], Gal-1-based immunomodulatory agonists emerge as potential immunomodulators to recalibrate immunity and restore immunological homeostasis.

On the other hand, in the context of neoplastic diseases, Gal-1 favors tumor growth and metastasis by fostering immunosuppression and angiogenesis. Since our initial discovery showing that melanoma cells evade T cell-mediated antitumor responses by secreting Gal-1 [48], this paradigm has been extended to a broad range of tumors including lung adenocarcinoma, Hodgkin lymphoma, pancreatic adenocarcinoma, glioblastoma, neuroblastoma, breast adenocarcinoma, CLL and others [58]. Additionally, this lectin stimulates the generation of aberrant vascular networks at sites of tumor growth and facilitates tumor-stroma interactions, favoring dissemination, colonization, and metastatic disease [65, 133]. Remarkably, this endogenous lectin confers resistance to different treatments including anti-angiogenic therapy, immunotherapy, chemotherapy, radiotherapy, and targeted therapies [134]. Collectively, these results underscore the potential therapeutic value of Gal-1 blockade, using neutralizing monoclonal antibodies, synthetic or natural glycans or antagonistic peptides [135], either alone or in combination with other therapeutic modalities for treating a wide range of tumors. Future basic and clinical research is awaited to validate galectin-based therapeutic strategies and translate these findings from bench to bedside and back again.

Acknowledgements

Work in our laboratory is supported by grants from Agencia Nacional de Promoción Científica y Tecnológica (2017-0494), Fundación Sales, Fundación Bunge & Born and Richard Lounsbery Foundation to G.A.R. We thank all members of the Immunopathology, Functional Glycomics and Translational Immuno Oncology laboratories of IBYME for continuous support. C.A.B., A.M.C., Y.D.M., M.N.M.C., M.M., J.P.M., R.M.P., N.S., L.L. and F.V. thank CONICET for their PhD fellowships.

References

- ^[1] Ohtsubo, K. & Marth, J. D. Glycosylation in Cellular Mechanisms of Health and Disease. *Cell* **126**, 855–867 (2006).
- ^[2] Bard, F. & Chia, J. Cracking the Glycome Encoder: Signaling, Trafficking, and Glycosylation. *Trends Cell Biol.* **26**, 379–388 (2016).
- ^[3] Moremen, K. W., Tiemeyer, M. & Nairn, A. V. Vertebrate protein glycosylation: Diversity, synthesis and function. *Nat. Rev. Mol. Cell Biol.* **13**, 448–462 (2012).
- ^[4] Cerliani, J. P., Blidner, A. G., Toscano, M. A., Croci, D. O. & Rabinovich, G. A. Translating the ‘Sugar Code’ into Immune and Vascular Signaling Programs’. *Trends Biochem. Sci.* **42**, 255–273 (2017).
- ^[5] Marth, J. D. & Grewal, P. K. Mammalian glycosylation in immunity. *Nat. Rev. Immunol.* **8**, 874–887 (2008).

- ¹⁶¹ Duan, S. & Paulson, J. C. Siglecs as Immune Cell Checkpoints in Disease. *Annu. Rev. Immunol.* **38**, 365–395 (2020).
- ¹⁷¹ Chugh, S., Gnanapragassam, V. S., Jain, M., Rachagani, S., Ponnusamy, M. P. & Batra, S. K. Pathobiological implications of mucin glycans in cancer: Sweet poison and novel targets. *Biochim. Biophys. Acta* **1856**, 211–225 (2015).
- ¹⁸¹ Albrecht, S., Unwin, L., Muniyappa, M. & Rudd, P. M. Glycosylation as a marker for inflammatory arthritis. *Cancer Biomarkers* **14**, 17–28 (2014).
- ¹⁹¹ Johnson, J. L., Jones, M. B., Ryan, S. O. & Cobb, B. A. The regulatory power of glycans and their binding partners in immunity. *Trends Immunol.* **34**, 290–298 (2013).
- ¹⁰⁰ Rabinovich, G. A. & Toscano, M. A. Turning ‘sweet’ on immunity: galectin-glycan interactions in immune tolerance and inflammation. *Nat Rev Immunol* **9**, 338–352 (2009).
- ¹¹¹ Rodrigues, J. G., Balmaña, M., Macedo, J. A., Poças, J., Fernandes, Â., de-Freitas-Junior, J. C. M., Pinho, S. S., Gomes, J., Magalhães, A., Gomes, C., Mereiter, S. & Reis, C. A. Glycosylation in cancer: Selected roles in tumour progression, immune modulation and metastasis. *Cell. Immunol.* **333**, 46–57 (2018).
- ¹²¹ Rabinovich, G. A. & Croci, D. O. Regulatory Circuits Mediated by Lectin-Glycan Interactions in Autoimmunity and Cancer. *Immunity* **36**, 322–335 (2012).
- ¹³¹ Park, C., Jin, U. H., Lee, Y. C., Cho, T. J. & Kim, C. H. Characterization of UDP-N-acetylglucosamine:α-6-D-mannoside β-1,6-N- acetylglucosaminyltransferase V from a human hepatoma cell line Hep3B. *Arch. Biochem. Biophys.* **367**, 281–288 (1999).
- ¹⁴¹ Nagae, M., Kizuka, Y., Mihara, E., Kitago, Y., Hanashima, S., Ito, Y., Takagi, J., Taniguchi, N. & Yamaguchi, Y. Structure and mechanism of cancer-associated N-acetylglucosaminyltransferase-V. *Nat. Commun.* **9**, (2018).
- ¹⁵¹ van Kooyk, Y. & Rabinovich, G. A. Protein-glycan interactions in the control of innate and adaptive immune responses. *Nat. Immunol.* **9**, 593–601 (2008).
- ¹⁶¹ Dam, T. K. & Brewer, F. C. Maintenance of cell surface glycan density by lectin-glycan interactions: A homeostatic and innate immune regulatory mechanism. *Glycobiology* **20**, 1061–1064 (2010).
- ¹⁷¹ Dennis, J. W., Nabi, I. R. & Demetriou, M. Metabolism, Cell Surface Organization, and Disease. *Cell* **139**, 1229–1241 (2009).
- ¹⁸¹ Nabi, I. R., Shankar, J. & Dennis, J. W. The galectin lattice at a glance. *J. Cell Sci.* **128**, 2213–2219 (2015).
- ¹⁹¹ Drickamer, K. Engineering galactose-binding activity into a C-type mannose-binding protein. *Nature* **360**, 183–186 (1992).
- ²⁰¹ Brown, G. D. & Gordon, S. A new receptor for β-glucans. *Nature* **413**, 36–37 (2001).
- ²¹¹ Osorio, F. & Reis e Sousa, C. Myeloid C-type Lectin Receptors in Pathogen Recognition and Host Defense. *Immunity* **34**, 651–664 (2011).
- ²²¹ Crocker, P. R., Paulson, J. C. & Varki, A. Siglecs and their roles in the immune system. *Nat. Rev. Immunol.* **7**, 255–266 (2007).
- ²³¹ Liu, F.-T., Patterson, R. J. & Wang, J. L. Intracellular functions of galectins. *Biochim. Biophys. Acta* **1572**, 263–273 (2002).
- ²⁴¹ Rabinovich, G. A., Toscano, M. A., Jackson, S. S. & Vasta, G. R. Functions of cell surface galectin-glycoprotein lattices. *Curr. Opin. Struct. Biol.* **17**, 513–520 (2007).
- ²⁵¹ Yang, R. Y., Rabinovich, G. A. & Liu, F. T. Galectins: Structure, function and therapeutic potential. *Expert Rev. Mol. Med.* **10**, 1–24 (2008).
- ²⁶¹ Brinchmann, M. F., Patel, D. M. & Iversen, M. H. The role of galectins as modulators of metabolism and inflammation. *Mediators Inflamm.* **2018**, (2018).

- ¹²⁷ Vasta, G. R., Feng, C., González-Montalbán, N., Mancini, J., Yang, L., Abernathy, K., Frost, G. & Palm, C. Functions of galectins as 'self/non-self'-recognition and effector factors. *Pathog. Dis.* **75**, 1–12 (2017).
- ¹²⁸ Rabinovich, G. A., Toscano, M. A., Jackson, S. S. & Vasta, G. R. Functions of cell surface galectin-glycoprotein lattices. *Curr. Opin. Struct. Biol.* **17**, 513–520 (2007).
- ¹²⁹ Hirabayashi, J., Hashidate, T., Arata, Y., Nishi, N., Nakamura, T., Hirashima, M., Urashima, T., Oka, T., Futai, M., Muller, W. E. G., Yagi, F. & Kasai, K. I. Oligosaccharide specificity of galectins: A search by frontal affinity chromatography. *Biochim. Biophys. Acta - Gen. Subj.* **1572**, 232–254 (2002).
- ¹³⁰ Thiemann, S. & Baum, L. G. Galectins and Immune Responses-Just How Do They Do Those Things They Do? *Annu. Rev. Immunol.* **34**, 243–264 (2016).
- ¹³¹ Kamili, N. A., Arthur, C. M., Gerner-Smidt, C., Tafesse, E., Blenda, A., Dias-Baruffi, M. & Stowell, S. R. Key regulators of galectin-glycan interactions. *Proteomics* **16**, 3111–3125 (2016).
- ¹³² Maller, S. M., Cagnoni, A. J., Bannoud, N., Sigaut, L., Pérez Sáez, J. M., Pietrasanta, L. I., Yang, R. Y., Liu, F. T., Croci, D. O., Di Lella, S., Sundblad, V., Rabinovich, G. A. & Mariño, K. V. An adipose tissue galectin controls endothelial cell function via preferential recognition of 3-fucosylated glycans. *FASEB J.* **34**, 735–753 (2019).
- ¹³³ Patnaik, S. K., Potvin, B., Carlsson, S., Sturm, D., Leffler, H. & Stanley, P. Complex N-glycans are the major ligands for galectin-1, -3, and -8 on Chinese hamster ovary cells. *Glycobiology* **16**, 305–317 (2006).
- ¹³⁴ Stowell, S. R., Arthur, C. M., Mehta, P., Slanina, K. A., Blixt, O., Leffler, H., Smith, D. F. & Cummings, R. D. Galectin-1, -2, and -3 exhibit differential recognition of sialylated glycans and blood group antigens. *J. Biol. Chem.* **283**, 10109–10123 (2008).
- ¹³⁵ Ideo, H., Matsuzaka, T., Nonaka, T., Seko, A. & Yamashita, K. Galectin-8-N-Domain Recognition Mechanism for Sialylated and Sulfated Glycans. *J. Biol. Chem.* **286**, 11346–11355 (2011).
- ¹³⁶ Rabinovich, G. A. & Gruppi, A. Galectins as immunoregulators during infectious processes: From microbial invasion to the resolution of the disease. *Parasite Immunol.* **27**, 103–114 (2005).
- ¹³⁷ Vasta, G. R. Roles of galectins in infection. *Nat. Rev. Microbiol.* **7**, 424–438 (2009).
- ¹³⁸ Waldman, A. D., Fritz, J. M. & Lenardo, M. J. A guide to cancer immunotherapy: from T cell basic science to clinical practice. *Nat. Rev. Immunol.* 1–18 (2020) doi:10.1038/s41577-020-0306-5.
- ¹³⁹ Decker, W. K. & Safdar, A. Bioimmunoadjuvants for the treatment of neoplastic and infectious disease: Coley's legacy revisited. *Cytokine Growth Factor Rev.* **20**, 271–281 (2009).
- ¹⁴⁰ Decker, W. K., da Silva, R. F., Sanabria, M. H., Angelo, L. S., Guimarães, F., Burt, B. M., Kheradmand, F. & Paust, S. Cancer immunotherapy: Historical perspective of a clinical revolution and emerging preclinical animal models. *Front. Immunol.* **8**, (2017).
- ¹⁴¹ Topalian, S. L., Hodi, F. S., Brahmer, J. R., Gettinger, S. N., Smith, D. C., McDermott, D. F., Powderly, J. D., Carvajal, R. D., Sosman, J. A., Atkins, M. B., Leming, P. D., Spigel, D. R., Antonia, S. J., Horn, L., Drake, C. G., Pardoll, D. M., Chen, L., Sharfman, W. H., Anders, R. A., Taube, J. M., McMiller, T. L., Xu, H., Korman, A. J., Jure-Kunkel, M., Agrawal, S., McDonald, D., Kollia, G. D., Gupta, A., Wigginton, J. M. & Sznol, M. Safety, activity, and immune correlates of anti-PD-1 antibody in cancer. *N. Engl. J. Med.* **366**, 2443–2454 (2012).
- ¹⁴² Postow, M. A., Chesney, J., Pavlick, A. C., Robert, C., Grossmann, K., McDermott, D., Linette, G. P., Meyer, N., Giguere, J. K., Agarwala, S. S., Shaheen, M., Ernstoff, M. S., Minor, D., Salama, A. K., Taylor, M., Ott, P. A., Rollin, L. M., Horak, C., Gagnier, P., Wolchok, J. D. & Hodi, F. S. Nivolumab and ipilimumab versus ipilimumab in untreated melanoma. *N. Engl. J. Med.* **372**, 2006–2017 (2015).
- ¹⁴³ Schmid, P., Cortes, J., Pusztai, L., McArthur, H., Kümmel, S., Bergh, J., Denkert, C., Park, Y. H., Hui, R., Harbeck, N., Takahashi, M., Foukakis, T., Fasching, P. A., Cardoso, F., Untch, M., Jia, L., Karantza, V., Zhao, J., Aktan, G., Dent, R. & O'Shaughnessy, J. for the KEYNOTE-522 Investigators. Pembrolizumab for early triple-negative breast cancer. *N. Engl. J. Med.* **382**, 810–821 (2020).
- ¹⁴⁴ Gandhi, L., Rodríguez-Abreu, D., Gadgeel, S., Esteban, E., Felip, E., De Angelis, F., Domine, M., Clingan, P.,

- Hochmair, M. J., Powell, S. F., Cheng, S. Y., Bischoff, H. G., Peled, N., Grossi, F., Jennens, R. R., Reck, M., Hui, R., Garon, E. B., Boyer, M., Rubio-Viqueira, B., Novello, S., Kurata, T., Gray, J. E., Vida, J., Wei, Z., Yang, J., Raftopoulos, H., Pietanza, M. C. & Garassino, M. C. for the KEYNOTE-189 Investigators. Pembrolizumab plus chemotherapy in metastatic non-small-cell lung cancer. *N. Engl. J. Med.* **378**, 2078–2092 (2018).
- ¹⁴⁵¹ Fares, C. M., Van Allen, E. M., Drake, C. G., Allison, J. P. & Hu-Lieskovan, S. Mechanisms of Resistance to Immune Checkpoint Blockade: Why Does Checkpoint Inhibitor Immunotherapy Not Work for All Patients? *Am. Soc. Clin. Oncol. Educ. B.* 147–164 (2019) doi:10.1200/edbk_240837.
- ¹⁴⁶¹ Jenkins, R. W., Barbie, D. A. & Flaherty, K. T. Mechanisms of resistance to immune checkpoint inhibitors. *Br. J. Cancer* **118**, 9–16 (2018).
- ¹⁴⁷¹ Anderson, A. C., Joller, N. & Kuchroo, V. K. Lag-3, Tim-3, and TIGIT: Co-inhibitory Receptors with Specialized Functions in Immune Regulation. *Immunity* **44**, 989–1004 (2016).
- ¹⁴⁸¹ Rubinstein, N., Alvarez, M., Zwirner, N. W., Toscano, M. A., Ilarregui, J. M., Bravo, A., Mordoh, J., Fainboim, L., Podhajcer, O. L. & Rabinovich, G. A. Targeted inhibition of galectin-1 gene expression in tumor cells results in heightened T cell-mediated rejection; A potential mechanism of tumor-immune privilege. *Cancer Cell* **5**, 241–251 (2004).
- ¹⁴⁹¹ Toscano, M. A., Bianco, G. A., Ilarregui, J. M., Croci, D. O., Correale, J., Hernandez, J. D., Zwirner, N. W., Poirier, F., Riley, E. M., Baum, L. G. & Rabinovich, G. A. Differential glycosylation of TH1, TH2 and TH-17 effector cells selectively regulates susceptibility to cell death. *Nat. Immunol.* **8**, 825–834 (2007).
- ¹⁵⁰¹ Juszczynski, P., Ouyang, J., Monti, S., Rodig, S. J., Takeyama, K., Abramson, J., Chen, W., Kutok, J. L., Rabinovich, G. A. & Shipp, M. A. The AP1-dependent secretion of galectin-1 by Reed-Sternberg cells fosters immune privilege in classical Hodgkin lymphoma. *Proc. Natl. Acad. Sci. U. S. A.* **104**, 13134–13139 (2007).
- ¹⁵¹¹ Kamper, P., Ludvigsen, M., Bendix, K., Hamilton-Dutoit, S., Rabinovich, G. A., Møller, M. B., Nyengaard, J. R., Honoré, B. & d'Amore, F. Proteomic analysis identifies galectin-1 as a predictive biomarker for relapsed/refractory disease in classical Hodgkin lymphoma. *Blood* **117**, 6638–6649 (2011).
- ¹⁵²¹ Dalotto-Moreno, T., Croci, D. O., Cerliani, J. P., Martinez-Allo, V. C., Dergan-Dylon, S., Méndez-Huergo, S. P., Stupirski, J. C., Mazal, D., Osinaga, E., Toscano, M. A., Sundblad, V., Rabinovich, G. A. & Salatino, M. Targeting galectin-1 overcomes breast cancer-associated immunosuppression and prevents metastatic disease. *Cancer Res.* **73**, 1107–1117 (2013).
- ¹⁵³¹ Correa, S. G., Sotomayor, C. E., Aoki, M. P., Maldonado, C. A. & Rabinovich, G. A. Opposite effects of galectin-1 on alternative metabolic pathways of L-arginine in resident, inflammatory, and activated macrophages. *Glycobiology* **13**, 119–128 (2003).
- ¹⁵⁴¹ Barrionuevo, P., Beigier-Bompadre, M., Ilarregui, J. M., Toscano, M. A., Bianco, G. A., Isturiz, M. A. & Rabinovich, G. A. A Novel Function for Galectin-1 at the Crossroad of Innate and Adaptive Immunity: Galectin-1 Regulates Monocyte/Macrophage Physiology through a Nonapoptotic ERK-Dependent Pathway. *J. Immunol.* **178**, 436–445 (2007).
- ¹⁵⁵¹ Verschuere, T., Toelen, J., Maes, W., Poirier, F., Boon, L., Tousseyn, T., Mathivet, T., Gerhardt, H., Mathieu, V., Kiss, R., Lefranc, F., Van Gool, S. W. & De Vleeschouwer, S. Glioma-derived galectin-1 regulates innate and adaptive antitumor immunity. *Int. J. Cancer* **134**, 873–884 (2014).
- ¹⁵⁶¹ Ilarregui, J. M., Croci, D. O., Bianco, G. A., Toscano, M. A., Salatino, M., Vermeulen, M. E., Geffner, J. R. & Rabinovich, G. A. Tolerogenic signals delivered by dendritic cells to T cells through a galectin-1-driven immunoregulatory circuit involving interleukin 27 and interleukin 10. *Nat. Immunol.* **10**, 981–991 (2009).
- ¹⁵⁷¹ Soldati, R., Berger, E., Zenclussen, A. C., Jorch, G., Lode, H. N., Salatino, M., Rabinovich, G. A. & Fest, S. Neuroblastoma triggers an immunoevasive program involving galectin-1-dependent modulation of T cell and dendritic cell compartments. *Int. J. Cancer* **131**, 1131–1141 (2012).
- ¹⁵⁸¹ Rabinovich, G. A. & Conejo-García, J. R. Shaping the Immune Landscape in Cancer by Galectin-Driven Regulatory Pathways. *J. Mol. Biol.* **428**, 3266–3281 (2016).
- ¹⁵⁹¹ Laderach, D. J., Gentilini, L. D., Giribaldi, L., Delgado, V. C., Nugnes, L., Croci, D. O., Al Nakouzi, N., Sacca, P.,

- Casas, G., Mazza, O., Shipp, M. A., Vazquez, E., Chauchereau, A., Kutok, J. L., Rodig, S. J., Elola, M. T., Compagno, D. & Rabinovich, G. A. A unique galectin signature in human prostate cancer progression suggests galectin-1 as a key target for treatment of advanced disease. *Cancer Res.* **73**, 86–96 (2013).
- ¹⁶⁰ Orozco, C. A., Martinez-Bosch, N., Guerrero, P. E., Vinaixa, J., Dalotto-Moreno, T., Iglesias, M., Moreno, M., Djurec, M., Poirier, F., Gabius, H. J., Fernandez-Zapico, M. E., Hwang, R. F., Guerra, C., Rabinovich, G. A. & Navarro, P. Targeting galectin-1 inhibits pancreatic cancer progression by modulating tumor–stroma crosstalk. *Proc. Natl. Acad. Sci. U. S. A.* **115**, E3769–E3778 (2018).
- ¹⁶¹ Holst, J. M., Ludvigsen, M., Hamilton-Dutoit, S. J., Bendix, K., Plesner, T. L., Nørgaard, P., Møller, M. B., Steiniche, T., Rabinovich, G. A., D’Amore, F. & Pedersen, M. B. High intratumoural galectin-1 expression predicts adverse outcome in ALK– ALCL and CD30+ PTCL-NOS. *Hematol. Oncol.* **38**, 59–66 (2020).
- ¹⁶² Nambiar, D. K., Aguilera, T., Cao, H., Kwok, S., Kong, C., Bloomstein, J., Wang, Z., Rangan, V. S., Jiang, D., von Eyben, R., Liang, R., Agarwal, S., Colevas, A. D., Korman, A., Allen, C. T., Uppaluri, R., Koong, A. C., Giaccia, A., & Le, Q. T. Galectin-1-driven T cell exclusion in the tumor endothelium promotes immunotherapy resistance. *J. Clin. Invest.* **129**, 5553–5567 (2019).
- ¹⁶³ Rutkowski, M. R., Stephen, T. L., Svoronos, N., Allegrezza, M. J., Tesone, A. J., Perales-Puchalt, A., Brencicova, E., Escovar-Fadul, X., Nguyen, J. M., Cadungog, M. G., Zhang, R., Salatino, M., Tchou, J., Rabinovich, G. A. & Conejo-Garcia, J. R. Microbially driven TLR5-dependent signaling governs distal malignant progression through tumor-promoting inflammation. *Cancer Cell* **27**, 27–40 (2015).
- ¹⁶⁴ Croci, D. O., Salatino, M., Rubinstein, N., Cerliani, J. P., Cavallin, L. E., Leung, H. J., Ouyang, J., Ilarregui, J. M., Toscano, M. A., Domaica, C. I., Croci, M. C., Shipp, M. A., Mesri, E. A., Albini, A. & Rabinovich, G. A. Disrupting galectin-1 interactions with N-glycans suppresses hypoxia-driven angiogenesis and tumorigenesis in Kaposi’s sarcoma. *J. Exp. Med.* **209**, 1985–2000 (2012).
- ¹⁶⁵ Croci, D. O., Cerliani, J. P., Dalotto-Moreno, T., Méndez-Huergo, S. P., Mascanfroni, I. D., Dergan-Dylon, S., Toscano, M. A., Caramelo, J. J., García-Vallejo, J. J., Ouyang, J., Mesri, E. A., Junttila, M. R., Bais, C., Shipp, M. A., Salatino, M. & Rabinovich, G. A. Glycosylation-dependent lectin-receptor interactions preserve angiogenesis in anti-VEGF refractory tumors. *Cell* **156**, 744–758 (2014).
- ¹⁶⁶ Wu, X., Li, J., Connolly, E. M., Liao, X., Ouyang, J., Giobbie-Hurder, A., Lawrence, D., Mcdermott, D., Murphy, G., Zhou, J., Piesche, M., Dranoff, G., Rodig, S., Shipp, M. & Hodi, F. S. Combined Anti-VEGF and Anti-CTLA-4 therapy elicits humoral immunity to galectin-1 which is associated with favorable clinical outcomes. *Cancer Immunol. Res.* **5**, 446–454 (2017).
- ¹⁶⁷ Fidler, I. J. The pathogenesis of cancer metastasis: the ‘seed and soil’ hypothesis revisited. *Nat. Rev. Cancer* **3**, 453–458 (2003).
- ¹⁶⁸ Giancotti, F. G. XMechanisms governing metastatic dormancy and reactivation. *Cell* **155**, 750 (2013).
- ¹⁶⁹ Liu, F.-T. & Rabinovich, G. A. Galectins as modulators of tumour progression. *Nat. Rev. Cancer* **5**, 29–41 (2005).
- ¹⁷⁰ Ellerhorst, J. Differential expression of endogenous galectin-1 and galectin-3 in human prostate cancer cell lines and effects of overexpressing galectin-1 on cell phenotype. *Int. J. Oncol.* **14**, 217–224 (1999).
- ¹⁷¹ Moiseeva, E. P., Spring, E. L., Baron, J. H. & De Bono, D. P. Galectin 1 modulates attachment, spreading and migration of cultured vascular smooth muscle cells via interactions with cellular receptors and components of extracellular matrix. *J. Vasc. Res.* **36**, 47–58 (1999).
- ¹⁷² Van den Brûle, F., Califice, S., Garnier, F., Fernandez, P. L., Berchuck, A. & Castronovo, V. Galectin-1 accumulation in the ovary carcinoma peritumoral stroma is induced by ovary carcinoma cells and affects both cancer cell proliferation and adhesion to laminin-1 and fibronectin. *Lab. Invest.* **83**, 377–386 (2003).
- ¹⁷³ Lotan, R., Belloni, P. N., Tressler, R. J., Lotan, D., Xu, X. C. & Nicolson, G. L. Expression of galectins on microvessel endothelial cells and their involvement in tumour cell adhesion. *Glycoconj. J.* **11**, 462–468 (1994).
- ¹⁷⁴ Tinari, N., Kuwabara, I., Huflejt, M. E., Shen, P. F., Iacobelli, S. & Liu, F. T. Glycoprotein 90K/mac-2bp interacts with galectin-1 and mediates galectin-1-induced cell aggregation. *Int. J. Cancer* **91**, 167–172 (2001).

- ¹⁷⁵ Chiang, W. F., Liu, S. Y., Fang, L. Y., Lin, C. N., Wu, M. H., Chen, Y. C., Chen, Y. L. & Jin, Y. T. Overexpression of galectin-1 at the tumor invasion front is associated with poor prognosis in early-stage oral squamous cell carcinoma. *Oral Oncol.* **44**, 325–334 (2008).
- ¹⁷⁶ Wu, M. H., Hong, T. M., Cheng, H. W., Pan, S. H., Liang, Y. R., Hong, H. C., Chiang, W. F., Wong, T. Y., Shieh, D. Bin, Shiau, A. L., Jin, Y. T. & Chen, Y. L. Galectin-1-Mediated tumor invasion and metastasis, Up-Regulated matrix metalloproteinase expression, and reorganized actin cytoskeletons. *Mol. Cancer Res.* **7**, 311–318 (2009).
- ¹⁷⁷ Jung, E. J., Moon, H. G., Bok, I. C., Jeong, C. Y., Joo, Y. T., Lee, Y. J., Hong, S. C., Choi, S. K., Ha, W. S., Jae, W. K., Lee, C. W., Jong, S. L. & Park, S. T. Galectin-1 expression in cancer-associated stromal cells correlates tumor invasiveness and tumor progression in breast cancer. *Int. J. Cancer* **120**, 2331–2338 (2007).
- ¹⁷⁸ Bacigalupo, M. L., Manzi, M., Espelt, M. V., Gentilini, L. D., Compagno, D., Laderach, D. J., Wolfenstein-Todel, C., Rabinovich, G. A. & Troncoso, M. F. Galectin-1 Triggers Epithelial-Mesenchymal Transition in Human Hepatocellular Carcinoma Cells. *J. Cell. Physiol.* **230**, 1298–1309 (2015).
- ¹⁷⁹ He, X. J., Tao, H. Q., Hu, Z. M., Ma, Y. Y., Xu, J., Wang, H. J., Xia, Y. J., Li, L., Fei, B. Y., Li, Y. Q. & Chen, J. Z. Expression of galectin-1 in carcinoma-associated fibroblasts promotes gastric cancer cell invasion through upregulation of integrin $\beta 1$. *Cancer Sci.* **105**, 1402–1410 (2014).
- ¹⁸⁰ Chong, Y., Tang, D., Gao, J., Jiang, X., Xu, C., Xiong, Q., Huang, Y., Wang, J., Zhou, H., Shi, Y. & Wang, D. Galectin-1 induces invasion and the epithelial-mesenchymal transition in human gastric cancer cells via non-canonical activation of the hedgehog signaling pathway. *Oncotarget* **7**, 83611–83626 (2016).
- ¹⁸¹ Tang, D., Zhang, J., Yuan, Z., Zhang, H., Chong, Y., Huang, Y., Wang, J., Xiong, Q., Wang, S., Wu, Q., Tian, Y., Lu, Y., Ge, X., Shen, W. & Wang, D. PSC-derived Galectin-1 inducing epithelial-mesenchymal transition of pancreatic ductal adenocarcinoma cells by activating the NF- κ B pathway. *Oncotarget* **8**, 86488–86502 (2017).
- ¹⁸² Shih, T. C., Liu, R., Wu, C. Te, Li, X., Xiao, W., Deng, X., Kiss, S., Wang, T., Chen, X. J., Carney, R., Kung, H. J., Duan, Y., Ghosh, P. M. & Lam, K. S. Targeting galectin-1 impairs castration-resistant prostate cancer progression and invasion. *Clin. Cancer Res.* **24**, 4319–4331 (2018).
- ¹⁸³ Cimmino, F., Schulte, J. H., Zollo, M., Koster, J., Versteeg, R., Iolascon, A., Eggert, A. & Schramm, A. Galectin-1 is a major effector of TrkB-mediated neuroblastoma aggressiveness. *Oncogene* **28**, 2015–2023 (2009).
- ¹⁸⁴ Sanchez-Vega, F., Mina, M., Armenia, J., Chatila, W. K., Luna, A., La, K. C., Dimitriadou, S., Liu, D. L., Kantheti, H. S., Saghafeinia, S., Chakravarty, D., Daian, F., Gao, Q., Bailey, M. H., Liang, W. W., Foltz, S. M., Shmulevich, I., Ding, L., Heins, Z., Ochoa, A., Gross, B., Gao, J., Zhang, H., Kundra, R., Kandath, C., Bahceci, I., Dervishi, L., Dogrusoz, U., Zhou, W., Shen, H., Laird, P. W., Way, G. P., Greene, C. S., Liang, H., Xiao, Y., Wang, C., Lavarone, A., Berger, A. H., Bivona, T. G., Lazar, A. J., Hammer, G. D., Giordano, T., Kwong, L. N., McArthur, G., Huang, C., Tward, A. D., Frederick, M. J., McCormick, F., Meyerson, M., Cancer Genome Atlas Research Network, Van Allen, E. M., Cherniack, A. D., Ciriello, G., Sander, C. & Schultz, N. Oncogenic Signaling Pathways in The Cancer Genome Atlas. *Cell* **173**, 321–337.e10 (2018).
- ¹⁸⁵ Paz, A., Haklai, R., Elad-Sfadia, G., Ballan, E. & Kloog, Y. Galectin-1 binds oncogenic H-Ras to mediate Ras membrane anchorage and cell transformation. *Oncogene* **20**, 7486–7493 (2001).
- ¹⁸⁶ Elad-Sfadia, G., Haklai, R., Balan, E. & Kloog, Y. Galectin-3 augments K-ras activation and triggers a ras signal that attenuates ERK but not phosphoinositide 3-kinase activity. *J. Biol. Chem.* **279**, 34922–34930 (2004).
- ¹⁸⁷ Chung, L. Y., Tang, S. J., Sun, G. H., Chou, T. Y., Yeh, T. S., Yu, S. L. & Sun, K. H. Galectin-1 promotes lung cancer progression and chemoresistance by upregulating p38 MAPK, ERK, and cyclooxygenase-2. *Clin. Cancer Res.* **18**, 4037–4047 (2012).
- ¹⁸⁸ Sundblad, V., Quintar, A. A., Morosi, L. G., Niveloni, S. I., Cabanne, A., Smecuol, E., Mauriño, E., Mariño, K. V, Bai, J. C., Maldonado, C. A. & Rabinovich, G. A. Galectins in Intestinal Inflammation: Galectin-1 Expression Delineates Response to Treatment in Celiac Disease Patients. *Front. Immunol.* **9**, 379 (2018).
- ¹⁸⁹ Mendez-Huergo, S. P., Hockl, P. F., Stupirski, J. C., Maller, S. M., Morosi, L. G., Pinto, N. A., Berón, A. M., Musuruana, J. L., Nasswetter, G. G., Cavallasca, J. A. & Rabinovich, G. A. Clinical Relevance of Galectin-1 and Galectin-3 in Rheumatoid Arthritis Patients: Differential Regulation and Correlation With Disease Activity. *Front. Immunol.* **9**, (2019).

- ¹⁹⁰ Toscano, M. A., Martínez Allo, V. C., Cutine, A. M., Rabinovich, G. A. & Mariño, K. V. Untangling Galectin-Driven Regulatory Circuits in Autoimmune Inflammation. *Trends Mol. Med.* **24**, 348–363 (2018).
- ¹⁹¹ Rabinovich, G. A., Daly, G., Dreja, H., Taylor, H., Riera, C. M., Hirabayashi, J. & Chernajovsky, Y. Recombinant Galectin-1 and Its Genetic Delivery Suppress Collagen-Induced Arthritis via T Cell Apoptosis. *J. Exp. Med.* **190**, 385–398 (1999).
- ¹⁹² Iqbal, A. J., Cooper, D., Vugler, A., Gittens, B. R., Moore, A. & Perretti, M. Endogenous Galectin-1 Exerts Tonic Inhibition on Experimental Arthritis. *J. Immunol.* **191**, 171–177 (2013).
- ¹⁹³ Martínez Allo, V. C., Hauk, V., Sarbia, N., Pinto, N. A., Croci, D. O., Dalotto-Moreno, T., Morales, R. M., Gatto, S. G., Manselle Cocco, M. N., Stupirski, J. C., Deladoey, Á., Maronna, E., Marcaida, P., Durigan, V., Secco, A., Mamani, M., Dos Santos, A., Catalán Pellet, A., Pérez Leiros, C., Rabinovich, G. A. & Toscano, M. A. Suppression of age-related salivary gland autoimmunity by glycosylation-dependent galectin-1-driven immune inhibitory circuits. *Proc. Natl. Acad. Sci. U. S. A.* **117**, (2020).
- ¹⁹⁴ Santucci, L., Fiorucci, S., Rubinstein, N., Mencarelli, A., Palazzetti, B., Federici, B., Rabinovich, G.A. and Morelli, A. Galectin-1 suppresses experimental colitis in mice. *Gastroenterology* 124:1381-1394 (2003).
- ¹⁹⁵ Toscano, M. A., Commodaro, A. G., Ilarregui, J. M., Bianco, G. A., Liberman, A., Serra, H. M., Hirabayashi, J., Rizzo, L. V & Rabinovich, G. A. Galectin-1 suppresses autoimmune retinal disease by promoting concomitant Th2- and T regulatory-mediated anti-inflammatory responses. *J. Immunol.* **176**, 6323–6332 (2006).
- ¹⁹⁶ Zanon, C. de F., Sonehara, N. M., Girol, A. P., Gil, C. D. & Oliani, S. M. Protective effects of the galectin-1 protein on in vivo and in vitro models of ocular inflammation. *Mol. Vis.* **21**, 1036–1050 (2015).
- ¹⁹⁷ Perone, M. J., Bertera, S., Shufesky, W. J., Divito, S. J., Montecalvo, A., Mathers, A. R., Larregina, A. T., Pang, M., Seth, N., Wucherpfennig, K. W., Trucco, M., Baum, L. G. & Morelli, A. E. Suppression of Autoimmune Diabetes by Soluble Galectin-1. *J. Immunol.* **182**, 2641–2653 (2009).
- ¹⁹⁸ Gómez-Touriño, I., Sánchez-Espinel, C., Hernández-Fernández, A., González-Fernández, Á., Pena-González, E., Rodríguez, J., García-López, J. M. & Varela-Calvino, R. Galectin-1 synthesis in type 1 diabetes by different immune cell types: Reduced synthesis by monocytes and Th1 cells. *Cell. Immunol.* **271**, 319–328 (2011).
- ¹⁹⁹ Pérez, C. V., Gómez, L. G., Gualdoni, G. S., Lustig, L., Rabinovich, G. A. & Guazzone, V. A. Dual roles of endogenous and exogenous galectin-1 in the control of testicular immunopathology. *Sci. Rep.* **5**, 12259 (2015).
- ¹⁰⁰⁰ Ge, X. N., Ha, S. G., Greenberg, Y. G., Rao, A., Bastan, I., Blidner, A. G., Rao, S. P., Rabinovich, G. A. & Sriramarao, P. Regulation of eosinophilia and allergic airway inflammation by the glycan-binding protein galectin-1. *Proc. Natl. Acad. Sci.* **113**, E4837–E4846 (2016).
- ¹⁰⁰¹ Stys, P. K., Zamponi, G. W., van Minnen, J. & Geurts, J. J. G. Will the real multiple sclerosis please stand up? *Nat. Rev. Neurosci.* **13**, 507–514 (2012).
- ¹⁰⁰² Stancic, M., van Horssen, J., Thijssen, V. L., Gabius, H.-J., van der Valk, P., Hoekstra, D. & Baron, W. Increased expression of distinct galectins in multiple sclerosis lesions. *Neuropathol. Appl. Neurobiol.* **37**, 654–671 (2011).
- ¹⁰⁰³ Mendez-Huergo, S. P., Maller, S. M., Farez, M. F., Mariño, K., Correale, J. & Rabinovich, G. A. Integration of lectin–glycan recognition systems and immune cell networks in CNS inflammation. *Cytokine Growth Factor Rev.* **25**, 247–255 (2014).
- ¹⁰⁰⁴ Steinman, L. Assessment of animal models for MS and demyelinating disease in the design of rational therapy. *Neuron* **24**, 511–514 (1999).
- ¹⁰⁰⁵ Furlan, R., Cuomo, C. & Martino, G. Animal Models of Multiple Sclerosis. in *Neural Cell Transplantation: Methods and Protocols* (eds. Gordon, D. & Scolding, N. J.) 157–173 (Humana Press, 2009). doi:10.1007/978-1-60327-931-4_11.
- ¹⁰⁰⁶ Passos, G. R. Dos, Sato, D. K., Becker, J. & Fujihara, K. Th17 Cells Pathways in Multiple Sclerosis and Neuromyelitis Optica Spectrum Disorders: Pathophysiological and Therapeutic Implications. *Mediators Inflamm.* **2016**, 5314541 (2016).

- ¹¹⁰⁷ Lawrence Steinman, M. D. Multiple Sclerosis: A Coordinated Immunological Attack against Myelin in the Central Nervous System. *Cell* **85**, 299–302 (1996).
- ¹¹⁰⁸ Rostami, A. & Ciric, B. Role of Th17 cells in the pathogenesis of CNS inflammatory demyelination. *J. Neurol. Sci.* **333**, 76–87 (2013).
- ¹¹⁰⁹ Stromnes, I. M., Cerretti, L. M., Liggitt, D., Harris, R. A. & Goverman, J. M. Differential regulation of central nervous system autoimmunity by T(H)1 and T(H)17 cells. *Nat. Med.* **14**, 337–342 (2008).
- ¹¹¹⁰ Mari, E. R., Rasouli, J., Ciric, B., Moore, J. N., Conejo-Garcia, J. R., Rajasagi, N., Zhang, G. X., Rabinovich, G. A. & Rostami, A. Galectin-1 is essential for the induction of MOG35–55-based intravenous tolerance in experimental autoimmune encephalomyelitis. *Eur. J. Immunol.* **46**, 1783–1796 (2016).
- ¹¹¹¹ Salama, A. D., Chitnis, T., Imitola, J., Ansari, M. J. I., Akiba, H., Tushima, F., Azuma, M., Yagita, H., Sayegh, M. H. & Khoury, S. J. Critical role of the programmed death-1 (PD-1) pathway in regulation of experimental autoimmune encephalomyelitis. *J. Exp. Med.* **198**, 71–78 (2003).
- ¹¹¹² Starossom, S. C., Mascanfroni, I. D., Imitola, J., Cao, L., Raddassi, K., Hernandez, S. F., Bassil, R., Croci, D. O., Cerliani, J. P., Delacour, D., Wang, Y., Elyaman, W., Khoury, S. J. & Rabinovich, G. A. Galectin-1 Deactivates Classically Activated Microglia and Protects from Inflammation-Induced Neurodegeneration. *Immunity* **37**, 249–263 (2012).
- ¹¹¹³ Semerano, L., Minichiello, E., Bessis, N. & Boissier, M. C. Novel Immunotherapeutic Avenues for Rheumatoid Arthritis. *Trends Mol. Med.* **22**, 214–229 (2016).
- ¹¹¹⁴ Takayanagi, H., Juji, T., Miyazaki, T., Iizuka, H., Takahashi, T., Isshiki, M., Okada, M., Tanaka, Y., Koshihara, Y., Oda, H., Kurokawa, T., Nakamura, K. & Tanaka, S. Suppression of arthritic bone destruction by adenovirus-mediated *\textit>textit*sk gene transfer to synoviocytes and osteoclasts. *J. Clin. Invest.* **104**, 137–146 (1999).
- ¹¹¹⁵ Rabinovich, G. A. Apoptosis as a target for gene therapy in rheumatoid arthritis. *Mem. Inst. Oswaldo Cruz* **95**, 225–233 (2000).
- ¹¹¹⁶ Duris, F. H., Fava, R. A. & Noelle, R. J. Collagen-Induced Arthritis as a Model of Rheumatoid Arthritis. *Clin. Immunol. Immunopathol.* **73**, 11–18 (1994).
- ¹¹¹⁷ Xibillé-Friedmann, D., Rivera-Bahena, C. B., Rojas-Serrano, J., Burgos-Vargas, R. & Montiel Hernández, J.-L. A decrease in galectin-1 (Gal-1) levels correlates with an increase in anti-Gal-1 antibodies at the synovial level in patients with rheumatoid arthritis. *Scand. J. Rheumatol.* **42**, 102–107 (2013).
- ¹¹¹⁸ Harjacek, M., Diaz-Cano, S., De Miguel, M., Wolfe, H., Maldonado, C. A. & Rabinovich, G. A. Expression of galectins-1 and -3 correlates with defective mononuclear cell apoptosis in patients with juvenile idiopathic arthritis. *J. Rheumatol.* **28**, 1914–1922 (2001).
- ¹¹¹⁹ Sartor, R. B. Mechanisms of disease: pathogenesis of Crohn’s disease and ulcerative colitis. *Nat. Clin. Pract. Gastroenterol. Hepatol.* **3**, 390–407 (2006).
- ¹¹²⁰ Santucci, L., Fiorucci, S., Rubinstein, N., Mencarelli, A., Palazzetti, B., Federici, B., Rabinovich, G. A. & Morelli, A. Galectin-1 suppresses experimental colitis in mice. *Gastroenterology* **124**, 1381–1394 (2003).
- ¹¹²¹ Muglia, C. I., Gobbi, R. P., Smaldini, P., Delgado, M. L. O., Candia, M., Zanuzzi, C., Sambuelli, A., Rocca, A., Toscano, M. A., Rabinovich, G. A. & Docena, G. H. Inflammation Controls Sensitivity of Human and Mouse Intestinal Epithelial Cells to Galectin-1. *J. Cell. Physiol.* **231**, 1575–1585 (2016).
- ¹¹²² Rubio-Tapia, A., Hill, I. D., Kelly, C. P., Calderwood, A. H. & Murray, J. A. ACG Clinical Guidelines: Diagnosis and Management of Celiac Disease. *Off. J. Am. Coll. Gastroenterol. ACG* **108**, 656–676 (2013).
- ¹¹²³ Commodaro, A. G., Bueno, V., Belfort, R. & Rizzo, L. V. Autoimmune uveitis: The associated proinflammatory molecules and the search for immunoregulation. *Autoimmun. Rev.* **10**, 205–209 (2011).
- ¹¹²⁴ Romero, M. D., Muiño, J. C., Bianco, G. A., Ferrero, M., Juarez, C. P., Luna, J. D. & Rabinovich, G. A. Circulating anti-galectin-1 antibodies are associated with the severity of ocular disease in autoimmune and infectious uveitis. *Investig. Ophthalmol. Vis. Sci.* **47**, 1550–1556 (2006).

- ^[125] Silva, C. A., Cocuzza, M., Carvalho, J. F. & Bonfá, E. Diagnosis and classification of autoimmune orchitis. *Autoimmun. Rev.* **13**, 431–434 (2014).
- ^[126] Dettin, L., Rubinstein, N., Aoki, A., Rabinovich, G. A. & Maldonado, C. A. Regulated expression and ultrastructural localization of galectin-1, a proapoptotic β -galactoside-binding lectin, during spermatogenesis in rat testis. *Biol. Reprod.* **68**, 51–59 (2003).
- ^[127] Iglesias, M. M., Rabinovich, G. A., Ivanovic, V., Sotomayor, C. & Wolfenstein-Todel, C. Galectin-1 from ovine placenta - Amino-acid sequence, physicochemical properties and implications in T-cell death. *Eur. J. Biochem.* **252**, 400–407 (1998).
- ^[128] von Wolff, M., Wang, X., Gabius, H. J. & Strowitzki, T. Galectin fingerprinting in human endometrium and decidua during the menstrual cycle and in early gestation. *Mol. Hum. Reprod.* **11**, 189–194 (2005).
- ^[129] Blois, S. M., Ilarregui, J. M., Tometten, M., Garcia, M., Orsal, A. S., Cordo-Russo, R., Toscano, M. A., Bianco, G. A., Kobelt, P., Handjiski, B., Tirado, I., Markert, U. R., Klapp, B. F., Poirier, F., Szekeres-Bartho, J., Rabinovich, G. A. & Arck, P. C. A pivotal role for galectin-1 in fetomaternal tolerance. *Nat. Med.* **13**, 1450–1457 (2007).
- ^[130] Ramhorst, R. E., Giribaldi, L., Fraccaroli, L., Toscano, M. A., Stupirski, J. C., Romero, M. D., Durand, E. S., Rubinstein, N., Blaschitz, A., Sedlmayr, P., Genti-Raimondi, S., Fainboim, L. & Rabinovich, G. A. Galectin-1 confers immune privilege to human trophoblast: Implications in recurrent fetal loss. *Glycobiology* **22**, 1374–1386 (2012).
- ^[131] Vasen, G., Battistone, M.A., Croci, D.O., Brukman, N.G., Weigel Muñoz, M., Stupirski, J.C., Rabinovich, G.A., and Cuasnicú, P.S. The galectin-1-glycan axis controls sperm fertilizing capacity by regulating sperm motility and membrane hyperpolarization. *FASEB J* **29**, 4189-4200 (2015).
- ^[132] Freitag, J., Berod, L., Kamradt, T. & Sparwasser, T. Immunometabolism and autoimmunity. *Immunol. Cell Biol.* **94**, 925–934 (2016).
- ^[133] Girotti, M. R., Salatino, M., Dalotto-Moreno, T. & Rabinovich, G. A. Sweetening the hallmarks of cancer: Galectins as multifunctional mediators of tumor progression. *J. Exp. Med.* **217**, e20182041 (2020).
- ^[134] Navarro, P., Martínez-Bosch, N., Blidner, A. G. & Rabinovich, G. A. Impact of Galectins in Resistance to Anticancer Therapies. *Clin. Cancer Res.* (2020) doi:10.1158/1078-0432.CCR-18-3870.
- ^[135] Cagnoni, A. J., Pérez Sáez, J. M., Rabinovich, G. A. & Mariño, K. V. Turning-Off Signaling by Siglecs, Selectins, and Galectins: Chemical Inhibition of Glycan-Dependent Interactions in Cancer. *Front. Oncol.* **6**, 109 (2016).

Bios



Gabriel Adrián Rabinovich

Obtained his degree in Biochemistry (1993) and his PhD in Immunology (1999) from the School of Chemical Sciences

at the National University of Córdoba, Argentina. Currently, he is Senior Investigator of CONICET, Head of the Laboratory of Immunopathology at the Institute of Biology and Experimental Medicine and Professor of Immunology at the School of Exact and Natural Sciences, University of Buenos Aires. He is member of several academies including the US National Academy of Sciences and is visiting professor at international universities. He received several awards including the Argentinean Investigator Award and the Guggenheim, Bunge & Born and Konex Awards.



Camila Agustina Bach

Obtained her degree in Biology (2020) from the University of Buenos Aires and is pursuing a degree to become a Biology Professor. Currently, she is a PhD

student at the Laboratory of Immunopathology at the Institute of Biology and Experimental Medicine and a teaching assistant of Immunochemistry at the University of Buenos Aires. Her research focuses on deciphering the role of the Galectin1-Glycan interactions in resistance to cancer immunotherapeutic modalities, particularly in lung and kidney cancer.



Anabela Cutine

Obtained her degree in Biology (2015) from the University of Buenos Aires and is currently a PhD student at the Institute of Biology and Experimental Medicine and a teaching assistant of Immunology at Maimonides University. Her research focuses on deciphering the role of B cells, plasma cells and immunoglobulins in intestinal inflammatory diseases from a glycoimmunological perspective.



Lorena Laporte

Obtained her degree in Biochemistry (2013) and completed a Postgraduate residency in Clinical Microbiology at the Institute of Infectious Diseases (ANLIS Dr Carlos G Malbran) (2018) and is currently a PhD student from the University of Buenos Aires. Her ongoing research is developed at the Immunopathology Lab at the Institute of Biology and Experimental Medicine (IBYME – CONICET). The main goal of her work is to study the role of galectins and glycans in the crosstalk between skin immune system and the host microbiota.



Yamil Damián Mahmoud

He obtained his degree in Biotechnology (2018) and in Bioinformatics (2020), and is currently a PhD student from the University of Buenos Aires. Yamil is conducting his research activities at the Translational Immuno Oncology Lab at the Institute of Biology and Experimental Medicine. His research focuses on the bioinformatic study of biomarkers of response and resistance to immunotherapies and targeted therapies in melanoma using a multidisciplinary approach involving computational biology, genomics, immunology and cancer biology. He aims to identify biomarkers of response to these therapies and the underlying biological mechanisms associated with resistance in order to propose novel therapeutic targets for melanoma patients.



Montana Nicolle Manselle Cocco

She obtained her degree in Biological Sciences (2018) and is currently a PhD student from the University of Buenos Aires and is pursuing a degree in Bioinformatics. Her research activities are carried out at the Laboratory of Immunopathology at the Institute of Biology and Experimental Medicine, where she studies the immunomodulatory functions of proto-type galectins and their relevance as a potential immunotherapeutic target in renal cancer. Montana is working at the interface of immunology, cancer biology, immunotherapy and glycobiology using both experimental and bioinformatic approaches. Her main goal is to enhance understanding of the molecular mechanisms underlying response to immunotherapies



Mora Massaro

Obtained her degree in Biology (2020) from the National University of Mar del Plata. Mora is currently a PhD student from the University of Buenos Aires, performing her research activities at the Institute of Biology and Experimental Medicine. Her project is focused on the study of molecular and/or genetic signatures associated with the glycoimmunological axis in intestinal bowel diseases and colitis-associated colorectal cancer. She aims to identify and validate biomarkers that will allow patient stratification and will eventually contribute for the early detection of colitis-associated colorectal cancer in clinical settings.



Joaquín Pedro Merlo

He obtained his degree in Biotechnology (2016) and is pursuing a degree in Bioinformatics. Joaquin is currently a PhD student at University of Buenos Aires and is doing his research activities at the Translational Immuno Oncology Lab at the Institute of Biology and Experimental Medicine (IBYME-CONICET). His research is focused on the study of biomarkers of response to immunotherapies in melanoma patients. By means of machine learning algorithms and bioinformatic tools, Joaquin aims to study known biomarkers, and propose new ones, in order to obtain new tools for patient diagnosis.



Ramiro Martín Perrotta

He obtained his bachelor's degree in Biotechnology (2015) from the National University of Quilmes, and is currently a PhD student at the Immunopathology Lab based at the Institute of Biology and Experimental Medicine (IBYME-CONICET) in Buenos Aires, Argentina. He is pursuing a PhD in Biological Chemistry from the Faculty of Exact and Natural Sciences at the University of Buenos Aires (FCEN-UBA), planning to graduate in May-June 2021. He received several awards including the Fulbright-Argentina scholarship for Future Leaders, the AACR scholar in training award and the AAI trainee abstract award. He works at the interface between oncology and immunology focusing on breast cancer early dissemination and metastasis.



Nicolas Sarbia

He obtained his degree in Biochemistry (2016) and is currently a PhD student from the University of Buenos Aires. He is finishing his doctoral thesis

at the Immunopathology Lab at the Institute of Biology and Experimental Medicine, studying the role of galectin-glycan interactions in the interaction between triple-negative breast cancer and B lymphocytes. His work may support the use of galectins as target for breast cancer immunotherapy.



Florencia Veigas

She obtained her degree in Biotechnology (2017) and is currently a PhD student from the University of Buenos Aires and a teaching assistant at the Argentine University of Enterprise. Florencia is performing her research activities at the Translational Immuno-Oncology Lab at the Institute of Biology and Experimental Medicine. Her research focuses on the study of the molecular mechanisms underlying resistance to immunotherapy and targeted therapy in melanoma using a multidisciplinary approach involving immunology, cancer biology and bioinformatics. She aims to identify predictive biomarkers of response and propose novel therapeutic strategies to enhance patients' outcomes and overcome resistance mechanisms.

Coordination Chemistry of Nitric Oxide and Biological Signaling

José A. Olabe

INQUIMAE (UBA-CONICET), Facultad de Ciencias Exactas y Naturales, Universidad de Buenos Aires, Argentina.
 E-mail: olabe@qi.fcen.uba.ar

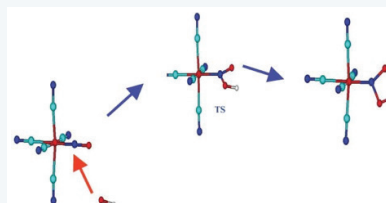
Dedicated to Prof. Wolfgang Kaim in his 70th birthday

Abstract

Nitric Oxide (NO) is a key intermediate in the nitrogen redox cycles that operate in soils, water and biological fluids, affording reversible interconversions between nitrates to ammonia and vice-versa. The discovery of its biosynthesis in mammals for signaling purposes generated a research explosion on the ongoing chemistry occurring in specific cellular compartments, centered on NO reactivity toward O_2 , thiols, amines, and transition metals, as well as derivatives thereof. The present review deals with the coordination chemistry of NO toward selected iron and ruthenium centers. We place specific attention to the three redox states of the nitrosyl group: NO^+ , NO and NO^-/HNO , describing changes in structure and reactivity as coordination takes place. Noteworthy are the results with the most reduced nitroxyl-species that allow establishing the changes in the measurable pK_a values for the HNO-bound complexes, also revealing the abrupt decrease in reducing power and trans-releasing abilities of the protonated species over the unprotonated ones, NO^- . Comparative results using non-heme and heme proteins and models prove useful for suggesting further improvements in the current research status of complex enzymatic behavior.

Keywords:

nitric oxide, nitroxyl, nitrous oxide, nucleophilic/electrophilic addition, disproportionation, nitrosation, dioxygenation, hydrogen sulfide, thionitrous acid, thionitrites, perthionitrites



The picture describes the addition of OH^- into the N-atom of bound NO^+ in the $[(FeCN)_5(NO)]^{2-}$ (nitroprusside) ion, leading to the bound intermediate $[(FeCN)_5(NO_2H)]^{3-}$.

Introduction

Modern studies in physiology and biochemistry point to some endogenously generated small molecules, dissolved gases that are free to diffuse in solutions and permeate membranes. More than the products of metabolism, their production is regulated to fulfill messenger functions involved in signal transduction, with specific cellular and molecular targets. They have been evolutionary conserved in eukaryotes, from bacteria to plant and mammalian cells, and use to act cooperatively. Main examples are nitric oxide (NO), carbon monoxide (CO), and hydrogen sulfide (H_2S). They are frequently called “gasotransmitters”, excluding the not endogenously generated dioxygen (O_2), despite that it fulfills the main described properties, among them the signaling abilities. By focusing on NO, and leaving CO aside now, we will discuss in this review the biorelevant chemistry of the latter molecules in an integrated way.[1,2]

NO, an environmental pollutant and toxin, gained prestige in the 1980s after the discovery of its biosynthesis in mammals for signaling purposes,[3] and the recognition of functions in plant biology.[4] NO is produced by a five-e-oxidation of L-arginine with O_2 , catalyzed by the iron based nitric oxide synthase isozymes in the endothelium, nerves,

and macrophages: e-NOS, n-NOS, and i-NOS, respectively. NO subsequently targets another iron enzyme, soluble guanylate cyclase (sGC), a high affinity NO-sensor that produces blood pressure control through vasodilation, as well as nerve signal transduction and immune defense. NO is also produced by reductive conversion from nitrite (NO_2^-) in soils and seawater, in denitrifying bacteria and fungi, catalyzed by copper or iron heme anaerobic nitrite reductases (NIR). It is thought to be similarly produced *in vivo* by reaction of NO_2^- with deoxy-Hb and -Mb for hypoxic vasodilation, a process also related with curing of meat. Other NO-binding iron heme isozymes are nitrophorins, that serve as NO carriers in the saliva of blood-sucking insects. Given its toxicity beyond the μM level, regulatory enzymatic NO production displays at 1-10 nM concentrations. Removal of NO is accomplished in mammals and in some bacteria under nitrosative stress, mainly through autoxidation forming nitrate (NO_3^-). A catalytic depletion of NO giving nitrous oxide (N_2O) is afforded by heme NO-reductases (NOR) in denitrifying bacteria and fungi.[5,6]

Elucidating the biorelevant mechanistic chemistry of NO and redox derivatives is a complex task. The targets for NO-biological signaling can be the direct reactions with O_2 , thiols (RSH) and hydrogen sulfide (H_2S), amines, and radical species. Besides, dioxygen (O_2), superoxide (O_2^-), and hydrogen peroxide (H_2O_2) have their own signaling abilities. The mutual interactions of all potential components at a given cellular microenvironment must be considered, as well as the corresponding rate constants and local concentrations of species.[1,7,8] Intermediate/products of those reactions such as nitrosothiolates (RSNO) might also produce a signaling cascade. In protein nitrosations implying modifications of a thiol group, how RSNOs are formed and how specificity is achieved for activating a given biological function are mostly unknown.[9] Most relevant to our present focus, transition metal ions can provide novel signaling features, depending on the nature of available metal-binding sites, tuning abilities exerted by coligands, second-sphere interactions with counterions or residues in vicinal protein chains, or with solvent media. Thus, the reactivity of “free” NO can be greatly modified upon coordination, as done by the multifunctional metalloenzymes necessary for the biosynthesis, transport, sensing and detoxification of NO.[6,10]

Following a brief survey on the basic solution physical and chemical properties of NO, NO_x and redox derivatives,[1,7] the coordination chemistry will be emphasized mainly by revisiting our work with a non-heme iron complex (pentacyanonitrosylferrate(II), “nitroprusside”),[11] and by using ruthenium nitrosyl models,[12] thus providing appropriate frameworks for comparison with the most biorelevant iron heme proteins. Recent aspects of the “crosstalk” of NO with H_2S will be presented, comprising the intermediacy of thionitrous acid (NOSH), nitrososulfides (thionitrites, NOS^-) and nitrosodisulfides (perthionitrites, NOS_2^-).[13] Hopefully, this account will address challenging mechanistic questions pointing to a best understanding of the role of transition metals in biological signaling. Only the main original articles related to the chemistry described will be cited, instead we provide the reader access to the most current literature, with emphasis on reviews.

1. Properties of aqueous NO and redox derivatives NO^+ , NO^- , HNO , NO_x

NO is thermodynamically very unstable in water ($\Delta G_{\text{f, aq}, 298\text{K}}^\circ = 102 \text{ kJ/mol}$), although it is persistent as a monomer, soluble in the mM range (increasing to 3-15 mM/atm in aprotic solvent), nearly non-polar, hydrophobic, diffusible, and able to freely pass the cell boundaries.[1,7] Figure 1 shows a Molecular Orbital (MO) bonding description, with the highest energy unpaired electron in an antibonding orbital, and an N-O bond order of 2.5. Remarkably, aqueous NO shows no significant tendency to dimerize, with an apparently unfavorable dimerization equilibrium constant.[14] In contrast, dimerization reactions for most inorganic radicals are very fast and effectively irreversible, except for NO_2 , SO_2^- and a few others.[14] Neither does NO disproportionate in water, as other oxo-nitrogenated radicals do (NO_2 and N_2O_2^-), though it evolves gradually to N_2O and NO_2 in pressurized NO gas-cylinders. The colligation reactions of NO with paramagnetic substrates are nearly diffusion-controlled ($\sim 10^{10} \text{ M}^{-1}\text{s}^{-1}$), as with NO_2 and CO_2^- , giving N_2O_3 and NOCO_2^- respectively.[14] Very fast reactions take place with biorelevant radicals as thiyl (RS^\cdot), peroxy (ROO^\cdot) and tyrosyl (PhO^\cdot). Fast radical quenching by NO on enzyme systems serve as regulatory or inhibitory functions; many chain-carrying radicals oxidize important biological macromolecules, and a protective role for NO can be established.[1,7,14]

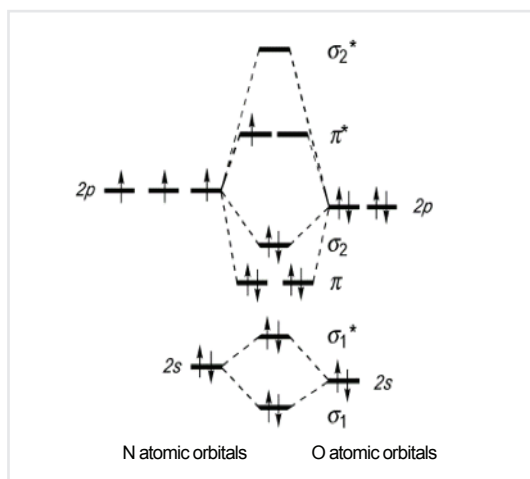
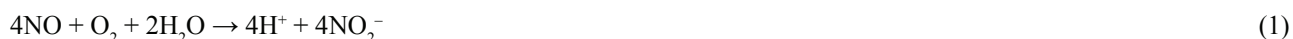


Figure 1. Molecular orbital diagram for NO

A third order rate law has been verified for the aqueous autoxidation reaction (1): $d[\text{NO}_2^-]/dt = 4k_{\text{ox}} [\text{NO}]^2[\text{O}_2]$, with $k_{\text{ox}} = 2 \times 10^6 \text{ M}^{-2}\text{s}^{-1}$ (25°C, pH independent). It is believed that intermediate $\text{NO}_2\cdot$ production is rate-limiting, followed by association with NO giving N_2O_3 , that hydrolyzes to nitrite.[7,14] Following several reports on the mechanisms, ONOONO , $\text{NO}_2\cdot$ and N_2O_3 have been proposed as oxidizing intermediates, depending on added substrates.[15] ONOONO would be generated by the reaction of NO with a peroxyxynitrite radical formed in the initial step: $\text{ONOO}\cdot$ (or alternatively, with a weakly bound $\text{NO}\cdot\text{O}_2$ species). No mention has been made at all on a NO-dimer as a putative endergonic precursor intermediate, subsequently reactive toward O_2 .



Alternatively, $\text{NO}_2\cdot$ is the final product in aprotic solvents, which raises the question on the different damaging capability of the autoxidation reaction depending on the local polarity in cells. The rate of NO-decay depends on its initial concentration: in aerated solutions and high concentrations of NO (μM to mM), the reaction takes place in seconds or less, whereas the decay is much slower at physiological concentrations ($\leq 100 \text{ nM}$). For example, at 1 mM NO and $250 \mu\text{M}$ O_2 , the first $t_{1/2}$ is 0.5 s, whereas at more physiological levels of 10 nM NO and $50 \mu\text{M}$ O_2 , the $t_{1/2}$ is ~ 50 hours.[5,7] As $t_{1/2}$ decreases, the flux of reactive nitrogen species (RNS) increases, as might occur with other damaging reactive oxygen species (ROS, viz., $\text{O}_2\cdot^-$, H_2O_2), and requires modulation of NO production, accomplished by NOS isozymes on demand. Thus, NO may be involved in diverse biological functions. Most important is the very fast colligation reaction (2):

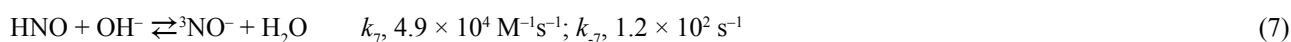


A maximized production of strongly oxidizing peroxyxynitrite (ONOO^-) can be reached upon colocalized disposal of the reactants, a process that can be inhibited by superoxide dismutase enzymes (SOD). In contrast, NO shows no reaction with H_2O_2 , although the latter might be toxic by reacting with reduced metal ions (Fe^{II} , Cu^{I} , leading to $\text{OH}\cdot$), or behave as signaling agent by reacting with thiols, showing kinetic selectivity in the oxidations to sulfenic acids ($\text{RSH} + \text{H}_2\text{O}_2 \rightarrow \text{RSOH} + \text{H}_2\text{O}$). Decomposition of H_2O_2 is regulated by catalase and peroxidase enzymes.[1,7]

Turning to the charged diatomic moieties, Figure 1 shows that NO^+ and NO^- are accessible states upon one-electron removal or addition. Stable NO^+ can be isolated (viz., with BF_4^-) and solubilized in organic solvents. Despite its bond order 3, akin to CO and N_2 , NO^+ is *extremely* reactive in aqueous solutions as an electrophile toward OH^- , giving HNO_2 . On the other hand, one-electron addition to NO leads to the ground-state (GS) triplet $^3\text{NO}^-$ (bond order 2, akin to O_2) through the single occupation of each MO. A singlet excited state (ES), $^1\text{NO}^-$, can be reached by pairing both electrons in one of the MO's. To the relevant reduction potentials in eqs (3,4), we include an estimated value to produce ^1HNO (nitroxyl, azanone, with a GS singlet), given by eq (5), at pH 7.4. We also quote the pH-dependent conversion to NO_2^- in reaction (6), which means that NO is a mild oxidant at pH 7, $E = 0.37 \text{ V}$ (all these redox potentials are referenced to NHE). [1,7,14] The data suggest that neither one- e^- oxidations nor one- e^- reductions of NO could be rapidly established under biorelevant conditions (reactions 4 and 5 are spin-forbidden); therefore, we might conclude that NO has time to diffuse from a cell to another and react accordingly (viz., with locally available highly reactive reductants such as H_2S or thiols, see below).



There is an enormous interest on the chemical properties of aqueous HNO₂[16,17] which equilibrates with ³NO⁻ through reaction (7). Reactions (8) and (9) show the different reactivity toward O₂ of the protonated and deprotonated species, although ONOOH has been questioned as a product in reaction (8).[7] Note that the extremely fast reactions (2) and (9) are isoelectronic.



HNO becomes a dominant species at pH 7, based on the estimated value of pK_a ~11.4 for deprotonation into GS ³NO⁻. HNO decays rapidly forming N₂O through pH-dependent pathways attributed to self-dimerization of HNO. For reaction (10), a nucleophilic addition step of ³NO⁻ to the N atom of HNO has been proposed, leading to *cis*-N₂O₂H⁻ that rapidly decomposes to N₂O.[17]



We also highlight the mutual reactivity of HNO/NO giving hyponitrite radicals, N₂O₂⁻ (pK_a of HN₂O₂, 5.6), whose chemistry has been characterized by pulse radiolysis and flash photolysis.[18] The radicals form either by one-electron oxidation of aqueous hyponitrite, N₂O₂²⁻, or by one-electron reduction of NO. In the latter case, the precursor can be either HNO, reaction (11), or ³NO⁻, which reacts much faster (3 × 10⁹ M⁻¹s⁻¹). The chemistry of N₂O₂⁻ might be most biorelevant under colocalized generation of NO/HNO. In a complex process, the N₂O₂⁻ radicals can disproportionate further in a rate-limiting bimolecular step, followed by fast reactions producing N₂O and NO₂⁻, with NO and N₃O₃⁻ as catalytic intermediates.[18] We refer the reader to recent articles and reviews on the mechanistic chemistry of N₂O production, most relevant to greenhouse effects, comprising the chemistry of NOR enzymes that generates N₂O in soils.[19-21]



Finally, reaction (12) shows the *reversible* oxidative ability of HNO toward thiols (*viz.*, as residues in proteins) that produces sulfenamide intermediates RSNHOH in the first step, followed by attack by a second RSH to give hydroxylamine (HA) and disulfides. Depending on concentrations, the process can evolve irreversibly giving sulfinamides RS(O)NH₂. [1,7]



Endogenous synthesis of HNO is feasible though controversial.[16,17] It might occur through similar oxidative routes as for NO-production through NOS, although by a *four*-electron oxidation under *deficient* conditions of the tetrahydrobiopterin (BH₄) cofactor. Studies *in vitro* suggest its formation from HA or other amino alcohols, through peroxidation catalyzed by diverse heme proteins.[17] Direct NO-reductive routes to HNO by ascorbate, tyrosine, thiols and H₂S have been reported, evolving irreversibly to N₂O and oxidized species.[22,23] Though the redox potential value in reaction (5) allows questioning the accessibility of ¹HNO by single electron transfer, a recalculated value at -0.12 V (NHE) sustains a lower barrier for PCET that might couple favorably with the fast, exergonic reactions of the intermediates.[24] Most significant is the assumed general outcome that NO and NO⁻/HNO could be *easily interconverted* in biological media, depending on the pH and redox state of the environment.

2. Basic transition metal coordination chemistry of NO⁺, NO, NO⁻. The Enemark-Feltham formalism and beyond

The three redox states of the nitrosyl diatomic group can be stabilized by complexation to metal ions.[12] NO binds *covalently* to transition metals M forming diverse structural types as mononuclear, NO-bridging and cluster compounds. We focus on mononuclear species with coordination numbers (CN) 6 and 5. The Enemark and Feltham MO formalism allows describing and predicting the *main* geometrical and reactivity features.[25] By using the {MNO}ⁿ symbolism (n is

the electron count for the metal d and π^*_{NO} orbitals), the M-N-O fragment is defined as a single entity, without assuming any electronic distribution at the M,N,O atoms. Linear M-N-O geometries are predicted for complexes with $n \leq 6$, with increasingly bent structures for $n = 7$ and 8. As no role is assigned to the coligands, we must advance further by evaluating their influence on the structural, spectroscopic and reactivity properties. We must also consider the σ and π bonding interactions between M and NO. Figure 2 includes simplified diagrams of MO energy levels for $\{\text{MNO}\}^n$ systems with $n = 6, 7, 8$. [26]

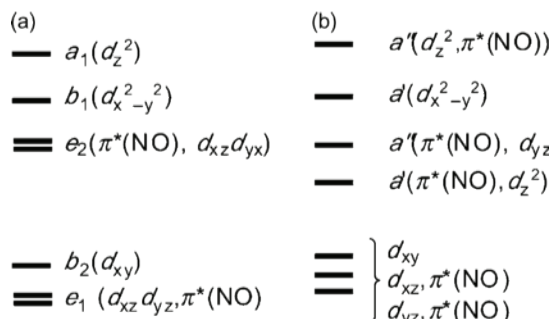


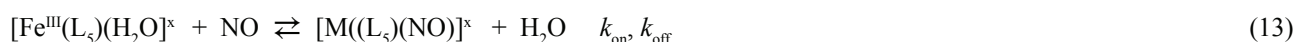
Figure 2. Molecular orbitals in 6-coordinate $\{\text{MNO}\}^n$ complexes, with M–N–O in (a) linear situation: $n = 6$, and (b) bent situations: $n = 7, 8$. From reference 26.

We will present selected cases of nitrosyl coordination compounds with different coligand types, for the three values of n , including the total spin states S_T , basic X-ray structural data, and IR spectral information on most relevant stretching frequencies, $\nu_{\text{N-O}}$ and, when available, $\nu_{\text{Fe-NO}}$. An emphasis will be placed on *iron* examples for non-heme and heme-coordination environments, and on some model nitrosyl ruthenium complexes. We aim at getting a comprehensive insight into the redox chemistry of the three redox states of nitrosyl, also including HNO, in well-defined coordination environments. Complementary spectroscopic results (UV-vis, EPR, NMR, Mössbauer) and DFT calculations will be considered. A more comprehensive description of biorelevant nitrosyl complexes can be found elsewhere. [10,12,26,27]

3. $\{\text{MNO}\}^6$ complexes. Close-to-Linear geometries. Dominant electrophilic reactivity: nitrosation reactions

3.1. Synthesis, bonding, and spectroscopies

Table 1 shows a selection of 6C metallonitrosyl-complexes, [28-39] usually prepared by mixing NO with Fe(III) (d^5) precursors. Reaction (13) describes a situation for L coligands, either equatorial or axial with respect to nitrosyl, with an occasional multidentate character. We deal with the “ferri-heme” nitrosyls, which in many cases originate in *high-spin* labile porphyrin Fe^{III} centers (d^5 , $S = 5/2$) that react *fast* and *reversibly* with NO ($S = 1/2$), giving *low-spin* diamagnetic nitrosyl-products ($S_T = 0$), with $k_{\text{on}} = \sim 10^5 \text{ M}^{-1}\text{s}^{-1}$ and $k_{\text{off}} = 1-50 \text{ s}^{-1}$. [40,41] That moderate NO-lability has been found for $\{\text{FeNO}\}^6$ complexes generated under flash-photolysis and excess NO conditions. On the other hand, *very stable* and comprehensively characterized model complexes have been recently synthesized, [33] namely the 6C $[\text{Fe}(\text{TPP})(\text{NO}) (\text{MI})]^+$ ($\text{MI} = 1\text{-methylimidazole}$) and $[\text{Fe}(\text{TPP})(\text{NO})(\text{X})]$ ($\text{X} = \text{Cl}^-, \text{Br}^-$) complexes, through the oxidation of corresponding $\{\text{FeNO}\}^7$ precursors in the absence of excess NO gas; the products showed very low values of k_{off} that made NO-binding essentially irreversible. [33] For stronger-field coligands like amines, cyanides, etc., the reactants may comprise *low-spin* aqua-complexes (d^5 , $S = 1/2$) that bind NO much *slower* and *irreversibly* giving *also* diamagnetic products, like the nitroprusside ion, best known as a sodium dihydrate salt, $\text{Na}_2[\text{Fe}(\text{CN})_5\text{NO}]\cdot 2\text{H}_2\text{O}$ (SNP), with $k_{\text{on}} = 0.3 \text{ M}^{-1}\text{s}^{-1}$. [42]



Alternatively, HNO_2 may react with Fe(II) (d^6) precursors as in reaction (14), through binding and subsequent fast proton-assisted dehydration. High-spin ferrous aqua-complexes react much faster than the ferric ones through dissociative mechanisms; [41] corresponding low-spin complexes such as $[\text{Fe}^{\text{II}}(\text{CN})_5\text{H}_2\text{O}]^{3-}$ react much slower ($k_{\text{on}(14)} \sim 300 \text{ M}^{-1}\text{s}^{-1}$). [43] Also, NOBF_4 can react directly with 5C Fe(II) complexes in non-aqueous media. In other methods, reduced species like arginine or hydroxylamine can be oxidized to bound NO^+ .



Table 1 shows that most complexes display *nearly* linear M-N-O groups with \angle MNO lying at 170-180°, with high IR stretching frequencies $\nu_{\text{N-O}}$ at 1950-1900 cm^{-1} . The reported values for $\nu_{\text{Fe-NO}}$ lie in the 650-580 cm^{-1} range.[6,29] Nitrosyl myoglobin (MbNO), with an axial histidine ligand, is an example among the heme NO-proteins with *weak* N-imidazolic ligands, as cd_1 NIR, nitrosyl horseradish peroxidase (HRPNO) and most of the nitrophorins.[10]

Figure 2A shows that the 6 electrons can fully occupy the predominantly metal orbitals e_1 and b_2 (C_{4v} symmetry), under sufficiently strong-field situations. Whilst b_2 is essentially nonbonding, e_1 is *strongly* π bonding, mixing the degenerate metal d_{xz} , d_{yz} with the π_{NO}^* orbitals. In a general way, these π “back-bonding” interactions depend on the metal M, its charge and electronic configuration. In contrast the Fe-NO σ interaction is very weak, as observed for poorly σ -donor diatomic species with multiple bonds. Consistent with $S_1 = 0$, a limiting $\text{Fe}^{\text{II}}\text{NO}^+$ GS configuration corresponds with a short and linear Fe-N-O unit that maximizes the π interaction. The latter implies a net transfer of the charge density of one electron from iron to the NO^+ ligand, which strengthens the Fe-NO bond and weakens the N-O bond, thus explaining the lowering of $\nu_{\text{N-O}}$ from 2390 cm^{-1} in free NO^+ to 1950-1900 cm^{-1} in the bound species. In other words, some of the triple-bond character of free NO^+ is lost upon coordination, resulting in a real distribution that must be considered intermediate between $\text{Fe}^{\text{II}}\text{NO}^+$ and $\text{Fe}^{\text{III}}\text{NO}$. It must be remarked, however, that not all $\{\text{FeNO}\}^6$ compounds are of $\text{Fe}(\text{II})\text{-NO}^+$ type: the *high-spin* complex $[\text{Fe}(\text{TMG3tren})(\text{NO})]^{3+}$ has been described as $\text{Fe}(\text{IV})\text{-NO}^-$. [44]

Table 1 includes two porphyrin nitrosyl complexes with axial sulfur ligands having distinctive low values of $\nu_{\text{N-O}}$ at 1850 cm^{-1} and a pronounced bending with \angle MNO reaching 160°. Correspondingly diminished $\nu_{\text{Fe-NO}}$ values locate at 549-530 cm^{-1} . Whilst the first example is a model nitrosyl compound with a *trans* thiophenolate ligand,[35] the second one is the nitrosyl adduct of the “ferri-heme” protein, P450nor,[37] containing cysteinyl as the *trans* ligand. In addition to π bonding, a new type of σ -*trans* interaction has been described:[6] the donor sulfur-ligand forms a S-Fe σ bond (mainly with iron d_{z^2}), admixed with the (unoccupied) delocalized Fe-N-O σ^* orbital, antibonding with respect to both the Fe-NO and N-O bonds. Hence, partial occupation of this orbital decreases $\nu_{\text{N-O}}$ and $\nu_{\text{Fe-NO}}$ simultaneously. Other specific geometrical changes were reported for the model 6C NO-compound,[35] which we do not analyze here; we remark that it shows a nearly equal (slightly *lower*) value of $d_{\text{Fe-S}}$ with respect to the NO-unbound reactant, *i.e.*, no significant structural *trans* effect is onset, in contrast with the $n = 7$ systems that produce significant *elongations* in the *trans* Fe-L distances upon coordination,[45] as analyzed later.

A new series of $n = 6$ $[\text{Fe}(\text{TPP})(\text{SPh})(\text{NO})]$ model complexes has been synthesized containing electron-poor thiophenolates with variable donor strengths and pK_a values;[36] a fine tuning of the H-bonding influence on the S-ligands allows sensing the changes in the IR stretchings, confirming that the decrease of both $\nu_{\text{N-O}}$ and $\nu_{\text{Fe-NO}}$ correlate with the increasing binding strengths of the *trans* thiophenolate groups. These second-sphere H-bonding and electronic interactions appear as crucial for controlling the degree of activation of the Fe-N-O unit for P450nor catalysis during the first step of N_2O production, and also determine distinctive catalytic roles for other $n = 6$ intermediates in cyt P450 monooxygenases, in chloroperoxidase (CPO) and NOSSs, all with thiolate ligands in differently H-bonded environmental pockets.

Though not included in Table 1, previous results with other non-sulfur strong donor *trans*-ligands showed the same geometric changes (*viz.*, $\text{C}_6\text{H}_4\text{F}$, OH^-),[12,45] suggesting that even the minor \angle MNO deviations from 180° might be due to electronic effects rather than to steric restrictions.[34] The overall spread in $\nu_{\text{N-O}}$ (1950-1850 cm^{-1}) allows concluding that the complexes with the higher frequencies reflect a greater NO^+ -character. The significance of the IR results has been clarified by normal coordinate analysis calculations (NCA), which show comparatively high values for the N-O and Fe-N force constants, at ~ 14 -15 and 4 $\text{mdyn}/\text{\AA}$, respectively. On the other hand, the bending of the Fe-N-O units down to 160° has been attributed to a different orbital origin, namely the strong π donation by the thiolates.[6]

Table 1. $n = 6$. Selected 6-coordinated metallonitrosyl complexes, $\{MNO\}^6$ ($M = Fe, Ru$), with different coligands

Compound	S_i	ν_{N-O} (cm^{-1})	d_{M-NO} (Å)	d_{N-O} (Å)	\angle_{MNO} ($^\circ$)	$d_{M-L,trans}$ (Å)	Ref
$Na_2[Fe(CN)_5(NO)] \cdot 2H_2O$ ^a	0	1960	1.6656(7)	1.133(1)	176.03(7)	1.9257(9)	28,29
$[Fe(cyclam-ac)(NO)]Cl(ClO_4) \cdot H_2O$ ^b	0	1903	1.663	1.133	175.6	1.883	30
$Mb^{III}NO$ ^c	0	1927	1.68(2)	1.13(1)	180(4)	2.04(2)	31
$[Fe(TPP)(MI)(NO)]^+$ ^d	0	1896	1.6275(3)	1.148(5)	176.3(4)	1.973(3)	32,33
$[Fe(TPP)(NO)(Cl)]$	0	1880	1.668(9)	1.209(8)	180	2.099(4)	33
$[Fe(TPP)(O_2CCF_3)(NO)]$	0	1907	1.618(8)	1.151(8)	175.8(6)	1.899(6)	34
$[Fe(OEP)(SR-H_2)(NO)]^e$	0	1870	1.671(9)	1.187(9)	159.6(8)	2.356(3)	35,36
P450 ^{nor} -NO	0	1851	1.63	1.16	161	2.3	37
$[Ru(Me_3[9]aneN_3)(bpy)(NO)](BF_4)_3$ ^f	0	1919	1.761(2)	1.128(3)	173.2(3)	2.128(4)	38
$[Ru(Me_3[9]aneN_3)(bpym)(NO)](BF_4)_3$ ^g	0	1947	1.776(5)	1.133(7)	172.5(4)	2.110(6)	39

Abbreviations: cyclam-ac: 1,4,8,11-tetraazacyclotetradecane-1-acetate; Mb^{III}: “ferri”-myoglobin; por: porphyrine(2-); MI: 1-methylimidazole; TPP: 5,10,15,20-tetraphenylporphyrin(2-); OEP: octaethylporphyrin(2-); P450^{nor}: Fungal cytochrome P450 NO reductase; SR-H₂: S-2,6-(CF₃CONH)₂C₆H₃; Me₃[9]aneN₃: 1,4,7-trimethyl-1,4,7-triazacyclononane; bpy: 2,2'-bipyridine; bpym: 2,2'-bipyrimidine.

a) X-ray diffraction, 50 K, ref. 28; ν_{N-O} , ref. 29, 77 K. b) X-ray diffraction, 100 K; ν_{N-O} in CD₃CN. c) Geometric data from XAFS, ν_{N-O} by resonance Raman. d) ν_{N-O} corresponds to BF₄⁻ salt, ref. 32. X-ray, with PO₂F₂⁻ salt, ref. 33. Calculated geometrical data (BP86/TZVP, with a porphyrine²⁻ ligand), see ref. 6. e) corrected value of ν_{N-O} in ref. 36 with respect to previous report in ref. 35. f) Compound [1-NO]³⁺, see text; ν_{N-O} in ATR mode; calculated DFT (B3LYP) are available. g) Compound [3-NO]³⁺, see text; data as in f).

The highest value of ν_{N-O} for nitroprusside in Table 1 is remarkable.[29] Given that cyano-ligands are strong σ -donors, one might expect a lower value, as described above for the thiolate-complexes. However, the bound cyanides also display specific H-bonds with water,[29,46] which diminishes the iron electron density and consequent π -bonding ability toward nitrosyl. Upon dehydration of $Na_2[Fe(CN)_5NO] \cdot 2H_2O$ or upon dissolving the salt in acetonitrile rather than in water, ν_{N-O} decreases by $\sim 40\text{ cm}^{-1}$. [46] These examples highlight the importance of considering both the first and second coordination spheres, accounting for interactions either with the solvents, counterions, or the neighboring residues located at distal and/or proximal positions with respect to the NO-group. Interestingly, the nitroprusside ion clearly shows a negative *trans*-influence of NO⁺, with the axial Fe-C distance becoming *shorter* than the equatorial ones by 0.1 Å (this is also nicely reflected in the changes of ν_{C-N}); moreover, the iron atom is displaced upwards above the equatorial plane toward the NO group.[28] More generally, the axial L becomes inert toward dissociation from iron under the electron-withdrawing influence of the NO⁺-group,[47] accounting for the very poor number of available 5C complexes[45] (note however a recent isolation and X-ray characterization of 5C $[Fe(TPP)(NO)]BF_4$).[33] Remarkably enough, the pK_a for axial H₂O might decrease to ~ 3 , which means that the Fe^{II}NO⁺ fragment reaches the behavior of a Fe(III) center.[47] Such a deprotonation of *trans*-H₂O at pH 7 generates significant changes in the kinetic/mechanistic parameters for the aqueous nitrosylation/denitrosylation reactions of Fe(III)-porphyrin models.[41]

UV-vis spectroscopy has been a pioneering tool for describing the electronic structure and assigning optical transitions. Early theoretical calculations with $[Fe(CN)_5(NO)]^{2-}$ indicated a composition of the HOMO (b_2) of about 85% d_{xy} , 14% π_{CN}^* , and only 1.6% π_{CN}^* , revealing a poor π back-donation to CN⁻. [48] In contrast, the e_g MO comprised $\sim 25\%$ π_{NO}^* , indicating substantial Fe-NO π back bonding. The need of an adequate modeling of the solution environment has been emphasized, as DFT calculations using continuum models appeared as inadequate because the specific H-bonds between the bound cyanides and water are not accounted for; best results were achieved by using a ZINDO approach with point-charges located along the axis behind the cyano-ligands.[49] Good DFT results have been obtained for other Fe- and Ru complexes included in Table 1. Whilst the orbital compositions of the HOMOs are diverse, the LUMOs become

predominantly π^*_{NO} in all nitrosyl complexes calculated so far, with significant metal d participation. Finally, Mössbauer spectroscopy aids in describing the atomic electron densities. Small isomer shifts (δ) at $\sim 0 \text{ mm s}^{-1}$ and a large quadrupole splitting (ΔE_Q) at $1.7\text{-}2.0 \text{ mm s}^{-1}$ support a limiting $\text{Fe}^{\text{II}}\text{NO}^+$ description for a variety of iron compounds.[30]

3.2. NO-dissociation reactions. Why is NO released so fast in the nitrosyl “ferri-hemes”?

As shown above, the strong multiple bonds in the Fe-N-O fragment determine the *thermal inertness* of $[\text{Fe}(\text{CN})_5(\text{NO})]^{2-}$ toward NO-dissociation, consistent with the GS dominant $\text{Fe}^{\text{II}}\text{NO}^+$ configuration. In striking contrast, the so-called “ferri-heme” nitrosyls, also with strong bonds in the GS, display moderate values of k_{off} , both in model nitrosyl-porphyrins and in proteins like Mb^{III}NO or Hb^{III}NO.[40,41] In this context, the electronic structure of $[\text{Fe}(\text{TPP})(\text{Im})(\text{NO})]\text{BF}_4$ has been studied with nuclear resonance vibrational spectroscopy (NRVS), coupled to NCA and DFT calculations.[6,32] After confirming $\text{Fe}^{\text{II}}\text{NO}^+$ as the GS (with a dissociation energy of 125 kJ/mol), low-energy ES's have been calculated: a low-spin $\text{Fe}^{\text{III}}\text{NO}$ ($S_1 = 0$), slightly above the GS, has a Fe-NO dissociation energy of 42 kJ/mol, a weaker (longer) Fe-NO bond, and a lower $\nu_{\text{Fe-NO}}$. Most importantly, another higher energy ES, $\text{Fe}^{\text{III}}\text{NO}$ ($S_1 = 2$), was found to be dissociative with respect to the Fe-NO bond. Therefore, an easy thermal access to these ES's would explain the large values of k_{off} found for NO, that would constitute a general property of all the “ferri-heme” nitrosyls. The facile thermal NO-release is a crucial step in the mechanistic chemistry of the NIR enzymes, providing for a regeneration of the active aqua-sites for NO_2^- rebinding, and might also determine the role of the nitrophorins, favoring NO-dissociation upon injection of the saliva of the insects into the tissues of the victim for inducing vasodilation. The NOS isozymes afford such a $\text{Fe}^{\text{III}}\text{NO}$ intermediate for supporting the catalytic NO-production and release. In brief, in all Fe^{III} -heme nitrosyls, NO forms strong Fe-NO/N-O bonds in the GS ($\text{Fe}^{\text{II}}\text{NO}^+$ distribution), though it behaves as a labile ligand because of an easy thermal access to low energy ESs. Besides, as highlighted in section 3.1., *mutual* interactions are onset between the nitrosyl and the trans-L ligand. Thus, weaker Fe-NO bonds can be predicted for the complexes containing stronger donor *trans*-L's, associated with an enhanced $\text{Fe}^{\text{III}}\text{NO}$ character.

3.3. Electrophilic reactivity of NO^+ -complexes

Bonding descriptions predict that the N-atom at the delocalized M-N-O LUMO in $\{\text{MNO}\}^6$ complexes might be the site of attack for diverse nucleophiles (:B), with reversible adduct formation, reaction (15):[12,27]



Studies have been addressed with a series of group 8 metals, L coligands (CN^- , NH_3 , Cl^- , polypyridines, EDTA, etc.), and different B nucleophiles like OH^- ,[50] N-binding hydrides[51] (NH_3 , NH_2OH , N_2H_4 , N_3H , and derivatives), S-binding ones: SR^- , SH^- , SO_3^{2-} , and others. [52-55] Given the potential reductive capabilities of B, the adducts generally decompose irreversibly through redox reactions involving oxidation of B and NO^+ -reduction.[12,27]

3.3.1. Addition of OH^- to $\{\text{MNO}\}^6$ complexes. A linear free energy relation

The non-redox character of $\text{B} = \text{OH}^-$ describes a simplest situation from the mechanistic perspective, reaction (16):[50]



All the studied metal nitrosyls show the same global stoichiometry. Second order rate-laws support a mechanism with a slow bimolecular addition step of OH^- , followed by fast deprotonation of the $[\text{ML}_5(\text{NO}_2\text{H})]$ intermediates. Figure 3 shows a typical example for the reaction of $[\text{Ru}(4\text{-Mepy})(\text{NH}_3)_4(\text{NO})]^{3+}$ with excess OH^- , forming $[\text{Ru}(4\text{-Mepy})(\text{NH}_3)_4(\text{NO}_2)]^+$.

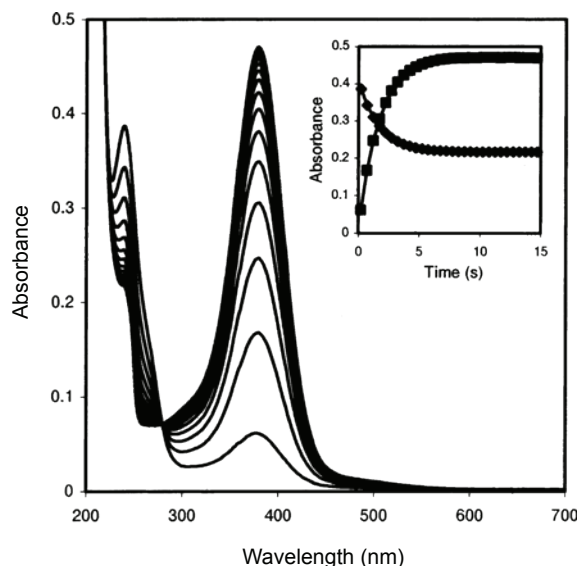
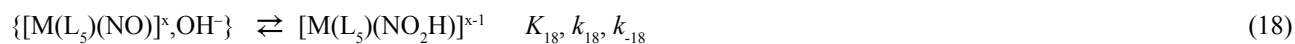


Figure 3. Successive spectra for the reaction of 4×10^{-6} M $[\text{Ru}(4\text{-Mepy})(\text{NH}_3)_4(\text{NO})]^{3+}$ with 0.015 M OH^- . $I = 1\text{M}$ (NaCl), $T = 35^\circ\text{C}$. Inset: Traces of the decay of nitrosyl reactant at 240 nm, and build-up of nitrite-product at 378 nm. From reference 50.

The rate constants and activation parameters have been determined, as well as values of $v_{\text{N-O}}$ and $E_{\text{NO}^+/\text{NO}}$ for a comprehensive set of nitrosyl-complexes (mainly Ru). The dependence of the pseudo-first order rate constants k_{obs} on the concentration of OH^- allowed deriving a generalized mechanistic proposal, reactions (17-19):



Reaction (17) comprises a fast association preequilibrium, prior to the relevant unimolecular nucleophilic addition step (18) that forms the HNO_2 adduct-intermediate. The latter may go back to the reactants or deprotonate rapidly as in eq (19) to form the final NO_2^- -product, which is generally most stable toward nitrite-dissociation. The addition rate constants k_{OH} can be obtained by fitting the plots of k_{obs} (s^{-1}) against $[\text{OH}^-]$, which behave linearly at moderate-to-high concentrations of OH^- , though reaching a pH-independent behavior at low pH's. Figure 4 shows how $\ln k_4$ [50] (which corresponds to $\ln k_{18}$ in our mechanistic scheme), depends linearly on the redox-potential $E_{\text{NO}^+/\text{NO}}$, with a slope of $\sim 20 \text{ V}^{-1}$; some members of the *trans*- $[\text{Ru}(\text{py})_4(\text{L})(\text{NO})]^{x+}$ (in the parallel line) show lower rates than expected, probably because of steric hindrance for the OH^- -access. For reaction (18), k_{18} (s^{-1}) correlates with other nucleophilicity indicators such as the calculated charge at the MNO moieties.[50] Note that k_{18} (s^{-1}) can be estimated according to: $k_{\text{OH}} = K_{\text{ip}} \times k_{18}$, by using calculated values for K_{ip} that depend on the charges of the reacting complexes. The experimental k_{OH} values ($\text{M}^{-1}\text{s}^{-1}$) reflect the trends in the values of k_{18} , with a *minor influence* of K_{ip} . [56] Following the work in ref. 50, new complexes have been measured (*viz.*, $[\text{Ru}(\text{bpy})(\text{tpm})(\text{NO})]^{3+}$, $[\text{Ru}(\text{EDTA})(\text{NO})]$), and the results have been included in subsequent reviews, [11,27,51] with very minor deviations in the corresponding slopes.

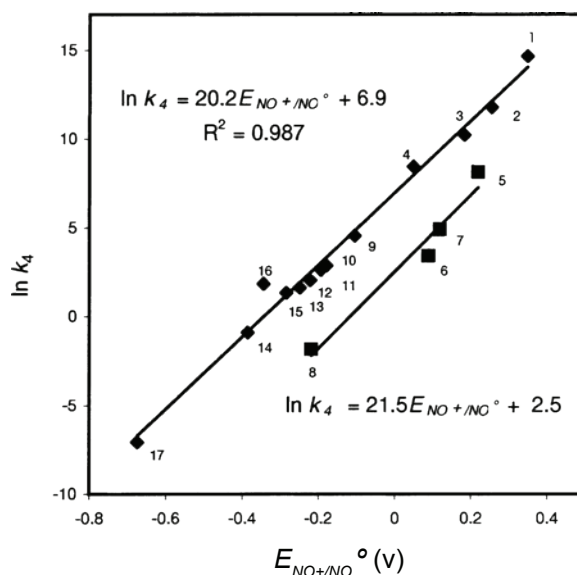


Figure 4. LFER plot of $\ln k_4$ (corresponds to $\ln k_{18}$, see text) against E_{NO^+/NO° (vs Ag/AgCl 3M; 0.21 V vs NHE) for the reactions of several nitrosyl-complexes with OH^- : 1. *cis*-[Ru(AcNO)(bpy)₂(NO)]³⁺; 2. *cis*-[Ru(bpy)(trpy)(NO)]³⁺; 3. *cis*-[Ru(bpy)₂(NO₂)(NO)]²⁺; 4. *cis*-[Ru(bpy)₂(Cl)(NO)]²⁺; 5. *trans*-[(NC)Ru(py)₄(CN)Ru(py)₄(NO)]³⁺; 6. *trans*-[Ru(Cl)(NO)(py)₄]²⁺; 7. *trans*-[Ru(NCS)(NO)(py)₄]²⁺; 8. *trans*-[Ru(NO)(OH)(py)₄]²⁺; 9. *trans*-[Ru(NH₃)₄(NO)(pz)]³⁺; 10. *trans*-[Ru(NH₃)₄(nic)(NO)]³⁺; 11. *trans*-[Ru(Clpy)(NH₃)₄(NO)]³⁺; 12. *trans*-[Ru(NH₃)₄(NO)(py)]³⁺; 13. *trans*-[Ru(4-Mepy)(NH₃)₄(NO)]³⁺; 14. *trans*-[Ru(his)(NH₃)₄(NO)]³⁺; 15. [Fe(CN)₅(NO)]²⁻; 16. [Ru(CN)₅(NO)]²⁻; 17. [Os(CN)₅(NO)]²⁻. From reference 50.

Figure 4 describes a linear free-energy relationship (LFER), as found in the trends of kinetic vs thermodynamic parameters for reactions governed by the same mechanism. Remarkably, the correlation spans ~10 orders of magnitude in the values of k_4 , covering around 1 V in the redox potentials. The value of the slope is close to that predicted for LFER's in weakly coupled outer-sphere, one-electron transfer reactions (19.4 V^{-1} or $0.5/RT$), under a Marcus' treatment for cross reactions that can be extended to associative mechanistic situations. The increase in rate constants and redox potentials correlates with an increase in both the activation enthalpies and entropies. While the trends in the entropies relate to the changes in solvation, the increase in the enthalpic barriers accounts for the reorganization of the linear M-N-O moieties to angular M-NO₂H ones.[50]

As part of the DFT analysis, Figure 5 describes the optimized geometries for the initial steps of the OH^- -addition into nitroprusside. Figure 6 shows the corresponding geometries for other selected ruthenium nitrosyl-complexes. A detailed account of computational methodologies, results, and interpretations for additions in the series of $[ML_5NO]^x$ complexes can be found elsewhere. [27,50,56]

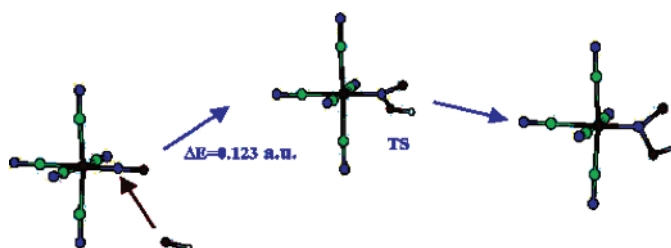


Figure 5. Optimized geometries for the initial steps of the reaction of $[Fe(CN)_5(NO)]^{2-}$ with OH^- leading to the transition state and the $[Fe(CN)_5(NO_2H)]^{3-}$ intermediate. Relative energies (y-coordinate) are not drawn to scale. From reference 50.

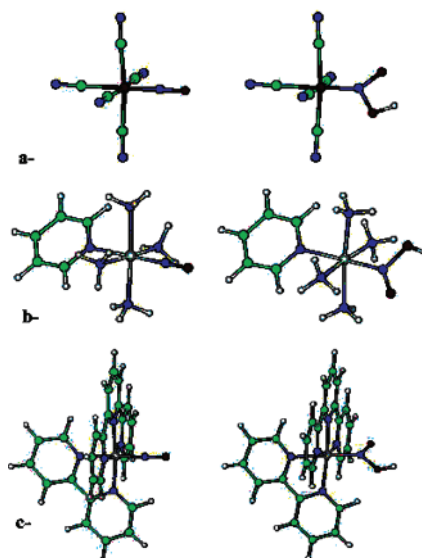
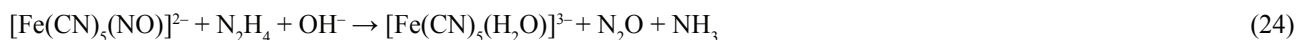
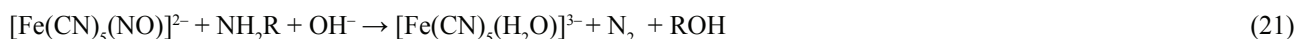


Figure 6. Optimized geometries at the B3LYP/6-31G** level for representative reactants and OH⁻ addition intermediates: (a): [Fe(CN)₅(NO)]²⁻; (b) *trans*-[Ru(NH₃)₄(py)(NO)]³⁺; (c) *cis*-[Ru(bpy)(trpy)(NO)]³⁺. From reference 50.

The OH⁻-additions have not been directly studied for the reactions of heme-nitrosyl proteins and models;[40,41] instead, the Fe-NO₂H intermediates, assumed to be transiently formed during the reactions of Fe(III)-hemes with an excess of NO (eq 13), led to [Fe^{II}(por)(NO)] + HNO₂ as final products, in a so-called “reductive-nitrosylation” process (*i.e.*, no bound-nitrite products were generated, in contrast with the non-hemes).[41] By using data for the measured decay of [Fe(por)(H₂O)(NO)]⁺ at different pHs, we made an estimation of values for $k_{OH^-} \sim 10^3 \text{ M}^{-1}\text{s}^{-1}$ for Hb^{III}NO and Mb^{III}NO (from the linear plots of the rate constants *vs* [OH⁻]).[56] The results for the heme proteins compare qualitatively well with those from the classical complexes located at the upper right part of Fig. 4. We extended this analysis to other Fe^{III}-models with substituted-porphyrins bearing different charges: porf⁸⁻, TPPS⁴⁺, (TMPyP)⁴⁺ and porf⁸⁺. [41,56] The values of k_{OH^-} were in the range 10³-10⁸ M⁻¹s⁻¹, increasing in the previous order, as predicted by the onset of rate-determining nucleophilic addition steps (eq18), determined by the increased electrophilicities at the {MNO} moieties, induced by the electron-attractive abilities of the more positively charged substituents at the porphyrin cores. The latter results and interpretations preclude a more detailed quantitative analysis, owing to the complex porphyrin moieties (with many factors influencing the kinetic parameters),[41] and the perturbations that arise when using excess NO for the onset of the initial equilibrium reaction (13).[33] A better scenario could arise by using the pure isolated n = 7 nitrosyl-complexes as direct precursors for the oxidized porphyrin Fe^{II}NO⁺ reactants that subsequently would react with OH⁻. [33]

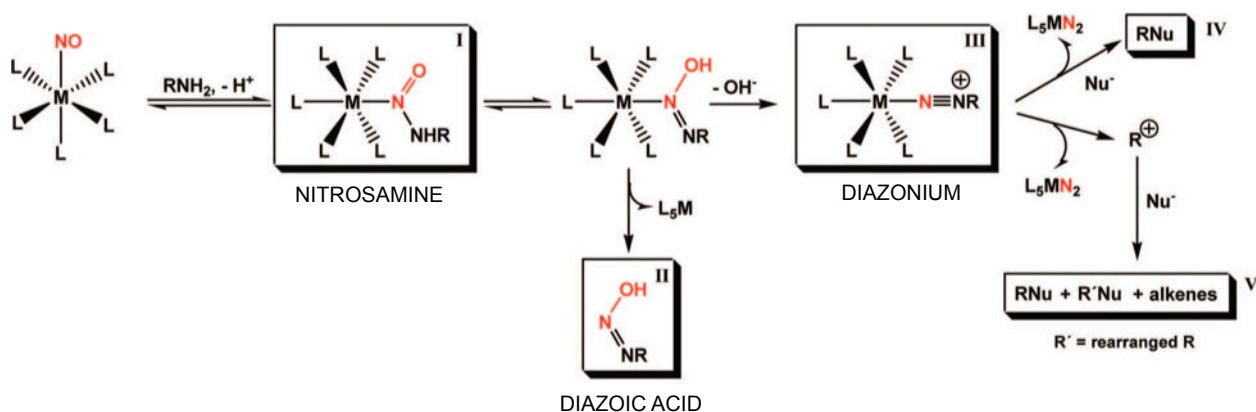
3.3.2. Additions of N-hydrides to nitroprusside. Linkage isomers and N₂O/N₂ release

Small nitrogenated hydrides are active nucleophiles in aqueous media toward bound NO⁺, according to the following stoichiometries:[51]



Reactions (20-24) comprise additions on the N atom of the M-N-O fragment, coupled with deprotonation, as evidenced by pH-dependent rate laws with a first order behavior in complex- and nucleophile-concentrations. All the adducts reorganize with subsequent generation of gaseous products, N₂ and/or N₂O, and a final production of labile [Fe(CN)₅(H₂O)]³⁻, that can be trapped by scavenger ligands such as pyridines or pyrazines. Remarkably, if the reactions with primary/secondary amines or amino acids are carried out in *nonaqueous solvents*, different stoichiometries and mechanisms lead to variable organic products, depending on the amine.[57-59] Scheme 1 describes the reaction pathways

for the aliphatic amines, with the intermediacy of stabilized diazonium species that yield mainly the corresponding diamines.[60]



Scheme 1

In contrast with the H-bonds established by the bound cyanides with water, weaker acceptor aprotic solvents make the iron center more electron-rich, leading to an increased back-bonding to the nitrosyl group,[46] that aids stabilizing the diazonium ligand. As a result, changes in the nitrosating ability of nitroprusside in lipophilic media might be predicted as compared to water.[60]

Figure 7 describes the theoretical (DFT) description of the N_2H_4 -intermediates in reaction (24), and Scheme 2 describes the proposed steps for the overall process, with subsequent deprotonation and N-N cleavage, leading to NH_3 and to the side-on η^2-N_2O and end-on η^1-N_2O isomers.[61]

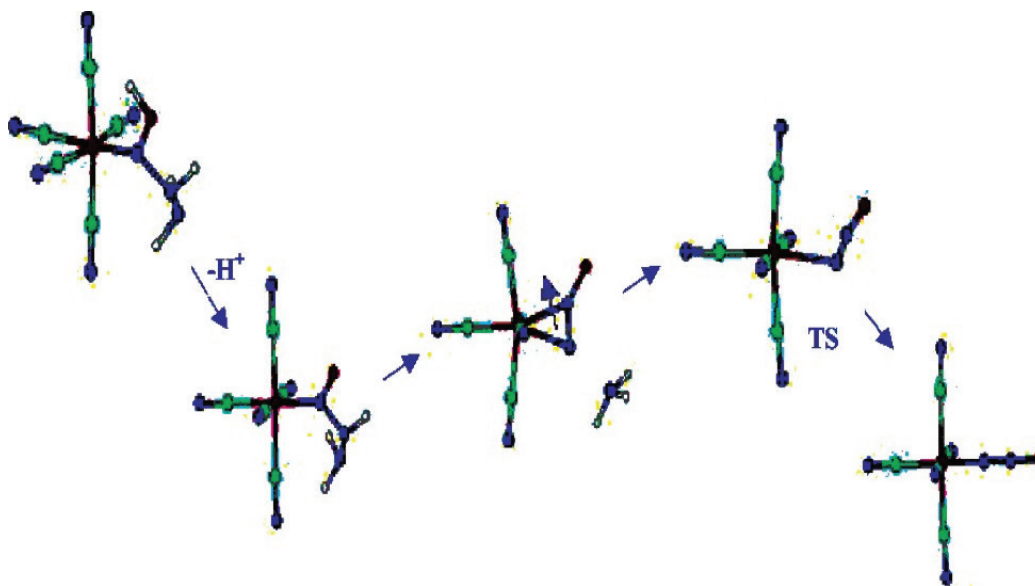
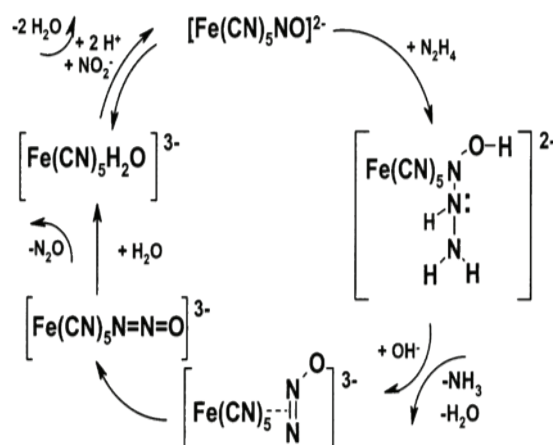


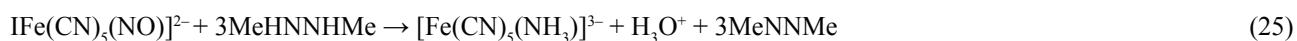
Figure 7. Schematic representation of the calculated stable intermediates for the reaction of $[Fe(CN)_5(NO)]^{2-}$ with hydrazine rendering the N_2O -bound species. The structures correspond to singular points in the potential hypersurface, calculated at a B3LYP-6-31G** level. Relative energies (y-coordinate) are not drawn to scale. All adducts and intermediates, except for the first one, bear charge 3^- . From reference 61.



Scheme 2

The final products N_2O and $[Fe(CN)_5(H_2O)]^{3-}$ allow further coordination of NO^+ coming from nitrite. Studies using labeled nitroprusside (^{15}NO) led to a quantitative identification of the gaseous product $^{14}N^{15}NO$, with no label at NH_3 . This fact, together with DFT evidence, supports the proposed catalytic reduction of NO_2^- by N_2H_4 occurring in appropriate conditions. Interestingly, the addition of N_2H_4 to other nitrosyl complexes led to azide-formation, not to N_2O . The prediction of the N_2O -linkage isomers reminds the results on the NO -analogs described elsewhere.[27-29] Direct spectroscopic evidence exists only for the coordination of η^1-N_2O on some Ru- and Os-complexes. The involvement of η^2-N_2O and η^1-N_2O in reaction (24) is supported by the consistent geometrical and IR parameters derived from the DFT treatment,[61] a general feature for all the hydrides.[51] A similar approach proved useful to describe the side-on and end-on N_2 -linkage isomers.[51]

In the N_2O -forming reactions of Me-substituted derivatives of N_2H_4 adding to nitroprusside, closely related stoichiometries and mechanisms have been found for methylhydrazine and 1,1-dimethylhydrazine, forming methylamine and dimethylamine as products, respectively. The rates decrease by a factor of 10 for each Me-substitution, supporting an attack through the NH_2 groups. Remarkably, the reaction with 1,2-dimethylhydrazine follows a route with a very different stoichiometry. It comprises a full six-electron reduction of NO^+ to NH_3 , with formation of azomethane, reaction (25). The mechanism involves the production of two-electron reduced intermediates, $[Fe(CN)_5(HNO)]^{3-}$ and $[Fe(CN)_5(NH_2OH)]^{3-}$. [61]



The attack of N-binding nucleophiles to bound NO^+ is at the heart of the mechanisms of NO_2^- -reductions in soils by bacteria and reducing enzymes, evolving to gaseous products, N_2/N_2O . The binding of NO_2^- into an Fe^{II} center giving bound- NO^+ (cf. reaction 14) is considered the first step toward further reactivity of the nitrite reductase (NIR) enzymes. Overall, the fascinating diversity of stoichiometries and mechanisms observed by exerting subtle variations in the structure of N_2H_4 and substituted derivatives adding to the electrophilic Fe-N-O center calls attention to the complexities found in Nature for the action of different NIRs, as seen by looking at the recently proposed detailed mechanism for the six-electron reductions on the heme-based cytochrome *c* NIR enzyme, controlled by the concerted H-bonding interactions of different adjacent amino acids to the active centers along each of the one-electron reduction processes down to NH_3 . [62]

Finally, the described addition-chemistry of NH_2OH (HA) allows highlighting the biorelevance of this endogenously generated molecule, closely related to the oxidative chemistry of arginine, hydroxyurea, etc.[17] The catalytic disproportionation of NH_2OH is aided by coordination into $[Fe(CN)_5(H_2O)]^{3-}$, [63] and Fe^{III} -porphyrinate compounds, [64] and studies have been extended to substituted *N*-alkylhydroxylamines: $CH_3N(H)OH$, $(CH_3)_2NOH$, [65] and *O*-methylhydroxylamine. [66] Biochemically significant mechanistic differences (comprising $Fe^{II,III}$ cycling and formation of different radical intermediates) reflect in the production of NH_3 and diverse oxidation products when using either HA (N_2 , HNO , N_2O , and NO^+) or the substituted derivatives.

3.3.3. Addition of thiolates (RS^-) and HS^- . The “Gmelin” reaction

Adducts of nitroprusside with aliphatic thiols RSH (including cysteine and glutathione) form faster than with OH^- or amines, and lead to pH-dependent second-order rate constants for the formation of bound nitrosothiolates, $[Fe(CN)_5(NOSR)]^{3-}$. [52,53] Red colors develop up to the completion of the reversible reaction (26), at pHs 9-10, though plunging the adducts

into buffers at pH 4-6 effected its dissociation. Subsequent slower color fading due to redox decomposition of the nitrosothiolate fragment leads to reaction (27):



From the pH-dependence of k_p , only RS^- showed to be reactive, not RSH . [53] The values of k_p ($3 \times 10^3 - 4 \times 10^4 \text{ M}^{-1}\text{s}^{-1}$, 25°C) vary little for all studied thiols, with similar values of ΔH^\ddagger ($\sim 33 \text{ kJ/mol}$). Negative activation entropies ($\sim -50 \text{ J/K mol}$) agree with the association of like charges. There is a much larger variation in the values of k_d (12 to $3 \times 10^3 \text{ s}^{-1}$). The influence on the kinetic parameters of protonation, charge, steric effects, and solvation features of different groups in the thiols was reported. [53] Interesting mechanistic changes as compared to $[\text{Fe}(\text{CN})_5(\text{NO})]^{2-}$ were found for cysteine reacting with $[\text{Ru}(\text{CN})_5(\text{NO})]^{2-}$ and other positively charged Ru-nitrosyls, showing a two-step addition process that led to the production of N_2O . [54] Remarkably, similar LFER relations as found with OH^- additions were also obtained for the much faster RS^- additions to a wide set of electrophilic Ru-nitrosyl-complexes. [54] Overall, the latter results showed large stoichiometric and kinetic/mechanistic variations related to the different nucleophilic abilities of SR^- and OH^- , as well as to the controlled changes of redox potentials of the electrophilic nitrosyl-complexes through an adequate design. The latter properties might be useful for better understanding how functional specificity is attained for thiolate nucleophiles in protein nitrosation processes, through the fine tuning of their reactivities under the influence of nearby electrostatic fields or the interactions with vicinal charged residues.

The putatively similar “Gmelin” reaction ($[\text{Fe}(\text{CN})_5(\text{NO})]^{2-}$ with H_2S) has been studied for a long time. [55] There is a renewed interest in disclosing how HS^- behaves mechanistically in a different way as RS^- . For “Gmelin”, HS^- behaves as a poorer nucleophile (k_p , $190 \text{ M}^{-1}\text{s}^{-1}$), and the stoichiometry leads to N_2O , S_8 , and Prussian-blue type species. [55] The reported mechanism was questioned and a new proposal has been raised. [67] There are still unsolved issues on the identity of the pH-dependent emerging intermediates, probably *bound* thionitrous acid $\{(\text{H})\text{SNO}\}$, thionitrite NOS^- , perthionitrite NOS_2^- , and HNO . [68,72] Such N/S intermediates have been known for a long time, though their biorelevance is of much recent interest. [69] They can be generated as free species following transnitrosation reactions like (28) and (29) and provide an input to the emerging studies on the chemistry of sulfides and disulfides as biologically relevant signaling species.



The highly controversial issues around the chemistry and physiological relevance of the $\text{NO}/\text{H}_2\text{S}$ “crosstalk” reactions have been recently considered, [13,71,72] and contribute to display a promising scenario for best interpreting the complex coordination chemistry involved in the “Gmelin” process, which most probably includes the onset of the three redox states of the bound nitrosyl ligand, as well as corresponding redox steps for the sulfur species (HS^- , HS^\cdot , S^\cdot) as crucial intermediates, thus highlighting the specific role of disulfides and polysulfides when H_2S is used as a nucleophile in place of thiols.

4. $\{\text{MNO}\}^7$ complexes. Partially bent 6C and 5C geometries. A diverse picture of electronic structures and nucleophilic reactivities

4.1. Synthesis, bonding, and spectroscopies

Direct mixing of NO with labile d^6 $\text{Fe}(\text{II})$ -aqua complexes forms stable $\{\text{MNO}\}^7$ species, reaction (30). The products can be also obtained from the $n = 6$ or $n = 8$ precursors, by chemical/electrochemical means.



The Enemark and Feltham formalism leaves room for large variations of the electronic structure mediated by metal-ligand covalency, leading all the way from $\text{Fe}^{\text{III}}\text{NO}^-$ to $\text{Fe}^{\text{II}}\text{NO}^\cdot$ and $\text{Fe}^{\text{I}}\text{NO}^+$ limiting electronic distributions. [6,73] Complexes with ground states $S_t = 3/2$ or $S_t = 1/2$ have been identified. Figure 1B allows for high-spin or low-spin distributions, according to ligand field strengths. Non heme complexes like $[\text{Fe}(\text{EDTA})(\text{NO})]$ and $[\text{Fe}(\text{H}_2\text{O})_5(\text{NO})]^{2+}$ react with NO forming $S_t = 3/2$ products, as also done by some Fe metalloproteins. [41,74] X-ray, Resonance Raman, XAFS, MCD and Mössbauer spectroscopies, and theoretical calculations, support an electronic description of nitrosyl products as $\text{Fe}^{\text{III}}\text{NO}^-$, comprising antiferromagnetic coupling between high-spin ferric ($S = 5/2$) and $^3\text{NO}^\cdot$ ($S = 1$). For the $S_t =$

$3/2$ $[\text{Fe}(\text{L}_5)(\text{NO})]^x$ complexes in reaction (30), values of k_{on} are 10^6 - 10^8 $\text{M}^{-1} \text{s}^{-1}$, whereas k_{off} varies around 10^{-1} - 10^3 s^{-1} , depending on L. Water exchange measurements and activation parameters support dissociative-interchange mechanisms for these highly labile systems, which behave as potential catalysts for NO removal from gas streams.[41] Though the nitrosyl complexes with high-spin iron systems are most relevant to mechanistic studies on the NO-reductases,[74] we will not further address the $S = 3/2$ systems in this article.

For $S_t = 1/2$ with a low spin d^6 metal, the single electron must occupy the lower energy π^*_{NO} orbital, and a σ bond can be established with the vacant d_{z^2} metal orbital, leading to a delocalized singly occupied molecular orbital (SOMO) over the Fe-N-O subunit, $\pi^*_{\text{NO},d_{z^2}}$ (Fig.1B).[6] Figure 8 shows the latter bonding interaction, exemplified by a 6C ferrous heme nitrosyl with an axial histidine, and the *antibonding* combination of d_{z^2} with the σ -orbital of histidine. The σ -trans effect of NO manifests in the competition of the σ -donor orbitals, π^*_{NO} (π^*_h in Figure 8) and σ (his), for the iron d_{z^2} orbital.

A *weakening* (or eventually *breaking*) of the Fe-L ligand *trans* to NO can lead to either CNs 6 or 5 respectively, both biologically relevant. Given the non-zero spins, EPR is particularly informative on the detailed electronic structure, together with IR, MCD and Mössbauer spectroscopies, and X-ray diffraction.[45,75]

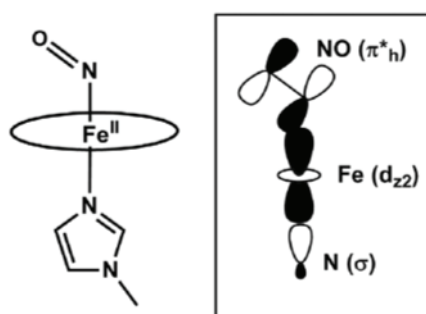


Figure 8. The key σ -bonding orbital for 6C heme-nitrosyls. From reference 113.

**Table 2.** Selected 6C and 5C metallonitrosyl complexes, {MNO}⁷ (M = Fe, Ru)^a

Compound	S_t	ν_{N-O}^{-1} (cm^{-1})	d_{M-NO} (\AA)	d_{N-O} (\AA)	\angle_{MNO} ($^\circ$)	d_{M-L} (\AA)	Ref
6C							
$Na_3[Fe(CN)_5(NO)].2NH_3$	$\frac{1}{2}$	(1650) 1608 ^b	(1.737)	(1.199)	(146.6)	(1.914)	49,76
$[Fe(cyclam-ac)(NO)](PF_6)$	$\frac{1}{2}$	1615 (1600)	1.722 (1.723)	1.167 (1.204)	148.7 (140.6)	2.012 (1.981)	30
$[Mn^{II}NO]^c$	$\frac{1}{2}$	1613	1.76(2)	1.12(1)	150(2)	2.05(2)	31
$[Fe(TPP)(MI)(NO)]^d$	$\frac{1}{2}$	1630	1.750	1.182	138	2.173	77
$[Fe(por)(SPh)(NO)]$	$\frac{1}{2}$	(1617)	(1.766)	(1.194)	(139)	(2.513)	6
$[Ru(Me_3[9]aneN_3)(bpy)(NO)](BF_4)_2^e$	$\frac{1}{2}$	1611 (1620)	1.852(2) (1.90)	1.177(3) (1.22)	141.6(2) (142.4)	2.169(2) (2.22)	38
$[Ru(Me_3[9]aneN_3)(bpym)(NO)](BF_4)_2^e$	$\frac{1}{2}$	1606 (1614)	1.851(2) (1.90)	1.184(3) (1.22)	141.2(2) (142.1)	2.166(2) (2.22)	39
5C							
$(NEt_4)_2[Fe(CN)_4(NO)]$ sqp	$\frac{1}{2}$	1755 ^f	1.565	1.161	177.1		78
$[Fe(TPP)(NO)]$ sqp	$\frac{1}{2}$	1697	1.740	1.42	146		79
$[Fe(TPPBr_8)(NO)]$ sqp ^g	$\frac{1}{2}$	1726 ^e	1.75 (1.711)	1.42 (1.182)	146 (144.4)		80,81

a) Calculated DFT data in parenthesis. b) ν_{N-O} in nujol. c) Geometrical data by XAFS; ν_{N-O} by resonance Raman. d) DFT calculations in ref. 77. e) ν_{N-O} in ATR mode. f) ν_{N-O} in CH_3CN . g) X-ray exp. and DFT calculated values, from refs. 80 and 81, respectively.

4.1.1. 6C complexes

All indicators agree with the population of the π^*_{MNO} orbital upon reduction of the $n = 6$ species, supporting a $Fe^{II}NO^\bullet$ dominant electron distribution. Values of ν_{N-O} at 1610-1650 cm^{-1} are much lower by ~ 300 cm^{-1} . A significant decrease has been also found for the stretching mode ν_{Fe-NO} (*viz.*, from 580 cm^{-1} in the $n = 6$ $[Fe(TPP)(NO)(MI)]^+$ complex⁶ to ~ 440 cm^{-1} in $[Fe(TPP)(NO)(MI)]$, (with the δ_{FeNO} bending mode assigned at ~ 560 cm^{-1}).^[77] The force constants were reported at 2.57 and 11.55 $mdyn/\text{\AA}$ for ν_{Fe-NO} and ν_{N-O} , respectively. In addition to $Mn^{II}NO$, other proteins like bovine heart CCO^{II-NO} and P450cam^{II-NO} reproduce the IR data. The $\angle MNO$ s drop to 140-150 $^\circ$, and *both* d_{M-NO} and d_{N-O} are consistently enlarged.^[6,10]

The $Fe^{II}NO^\bullet$ distribution has been confirmed by Mössbauer spectroscopy; the greater and smaller values of δ and ΔE_Q with respect to $n = 6$ systems do not reflect oxidation state changes at the iron site but the different degrees of back-bonding with the changing chemical character of the NO ligand. The π -acceptor abilities have been proposed to follow the trend $NO^+ > CO > NO^\bullet$.³⁰

EPR studies with the series of $[M(CN)_5(NO)]^{3-}$ anions (M = Fe, Ru, Os), generated *in situ* by reducing the NO^+ -precursors in CH_3CN frozen solutions at 3.5 K, yielded a detailed picture of the influence of changing the metals for a same coligand environment.^[82] The typical axial spectra with one ^{14}N hyperfine coupling constant are diagnostic of the main $M^{II}NO^\bullet$ distribution. From the high-level DFT calculations, most pronounced changes in $\angle MNO$ (close to 145 $^\circ$) and d_{N-O}/d_{M-NO} were consistent with X-ray and IR data. The lowering of symmetry implies removal of degeneracy of the e_2 orbitals, with the unpaired electron located in the π^*_σ SOMO (π^*_{NO,dz^2}), cf. Fig. 1B. The calculated compositions of

the SOMO's for the three ions show that the spin density is not only confined to the nitrosyl part of the molecule (about two-thirds share on the nitrogen atom, with a sizable metal contribution). The strongly increasing spin-orbit coupling from Fe < Ru < Os has been detected through both the experimental and calculated data. The effect is most pronounced for Os, where g_3 and the calculated isotropic value g_{av} are lowest and the total g anisotropy g_1-g_3 is largest. Similar results arise from DFT data with the iron systems of Table 2: the cyclam-ac complexes and [Fe(por)(MI)(NO)]. The calculations support the smaller degree of back-bonding for NO (20% mixture of π^*_σ in the *bonding* MO) compared to NO⁺ (28%). The EPR studies have been extended to diverse non-heme[83] and porphyrin[84] [Ru^{II}(L₄)(X)(NO)]^x complexes.

A recent comprehensive EPR study with Ru-complexes allowed studying fine details on the influence of bidentate coligand variations for the [Ru(Me₃[9]aneN₃)](L²)(NO)]ⁿ⁺ series. [39] Figure 9 shows the EPR spectra for three compounds with different L²: 4,4'-(bpy) ([1-NO]²⁺), its methoxy-substituted derivative, [2-NO]²⁺, and 2,2'-bipyrimidine, [3-NO]²⁺ (cf. Table 2). Table 3 allows a close view to the spin-Hamiltonian parameters.

The trends in the average g and Δg values suggest an increment on the spin density on the metal fragment as the donor ability of L² grows; also, the A_2 hyperfine coupling tensor indicates a decrease in the spin density on the N atom of NO along the same series. It was concluded that both trends are due to higher spin delocalization from the NO ligand to ruthenium with increasing donor properties of L², which seemed counterintuitive in principle, though confirmed by the results in Table 4 on the computation of Mülliken spin densities and the compositions of the SOMOs.[39]

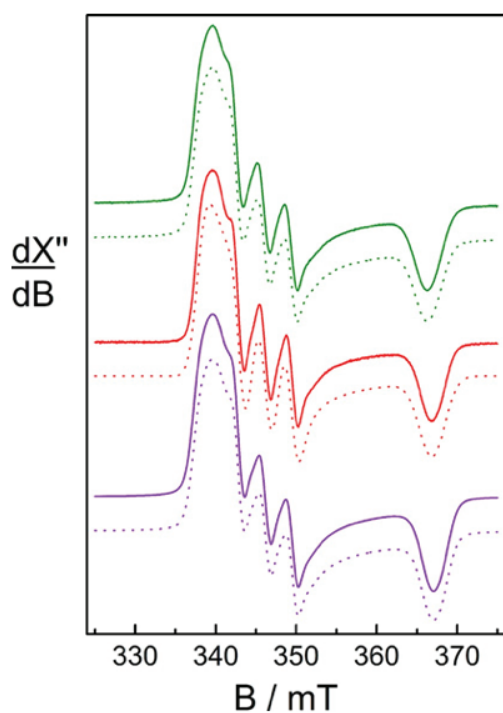


Figure 9. X-band EPR spectra of three [Ru(Me₃[9]aneN₃)(L²)(NO)](BF₄)₂ compounds with different L² coligands: 4,4'-(bpy) (red, [1NO]²⁺), its methoxy-substituted derivative, (violet, [2NO]²⁺), and 2,2'-bipyrimidine (green, [3NO]²⁺), in dry CH₃CN/Bu₄NPF₆ (0.2 M) at 85 K. Experimental spectra as full lines and computer-simulated spectra as dotted lines. From reference 39.

Table 3. EPR Spectroscopic Data of the {RuNO}⁷ Species^a

	g_1	g_2	g_3	Δg	g_{av}^b	A_1	A_2	A_3
[3-NO] ²⁺	2.0312(1)	1.9926(1)	1.8823(1)	0.1488(2)	1.9697(1)	12.1(2)	30.42(9)	n.d.
[1-NO] ²⁺	2.0303(1)	1.9916(1)	1.8792(1)	0.1511(1)	1.9681(1)	10.96(7)	30.35(5)	n.d.
[2-NO] ²⁺	2.0307(1)	1.9911(1)	1.8780(1)	0.1527(2)	1.9676(1)	12.7(1)	29.8(1)	n.d.

^a X-band EPR spectra obtained in CH₃CN/Bu₄NPF₆ (0.2 M) at 85 K. A_1 , A_2 , and A_3 are shown in units of 10⁻⁴ cm⁻¹. The numbers in parentheses show the 95% confidence interval. ^b g_{av} is calculated from $g_{av} = [(g^2 + g^2 + g^2)/3]^{1/2}$. n.d.: not distinguishable from 0. From reference 39. See Figure 9 for the identification of the three nitrosyl-complexes.

	Mülliken δ_{spin}		Orbital composition of the SOMO / %	
	Ru	NO	Ru	NO
[3-NO] ²⁺	0.0826	0.874	18.4	76.1
[1-NO] ²⁺	0.0876	0.871	19.5	75.2
[2-NO] ²⁺	0.0960	0.864	20.5	74.3

Figure 10 represents the computed SOMO for [1-NO]²⁺, which results from the predominantly σ overlap between the d_{z^2} (and to a lower extent d_{xz}) Ru orbitals and the NO centered π^*_{RuNO} orbital.

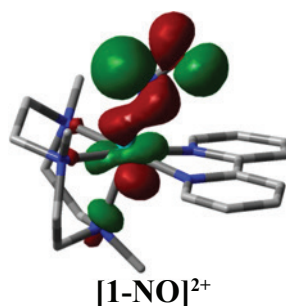


Figure 10. SOMO of the species [Ru(Me₃[9]aneN₃)](bpy)(NO)]²⁺, [1-NO]²⁺, computed after a corresponding orbital transformation. From reference 38.

The increase in spin delocalization from NO to Ru was ascribed to an increase in the energy of the d_{Ru} orbitals when L² behaves as a better donor; this draws the d-manifold closer in energy to the π^*_{RuNO} orbital, thus enhancing not only the spin delocalization but most noticeably the σ -trans effect characteristic of {MNO}⁷ species, consistent with the observed lengthening of the *trans* Ru-N₂ bond (Table 2).[39]

4.1.2. 5C complexes

We close Table 2 with results for selected 5C iron complexes, with cyanides and porphyrins as coligands. Distinctive features can be appreciated for sqp (NEt₄)₂[Fe(CN)₄(NO)]:[78] *i*) \angle FeNO is close to linear. *ii*) the Fe-N bond is shorter than others by 0.16 Å. *iii*) the Fe atom is most displaced upwards toward nitrosyl, by ca. 0.1 Å. *iv*) the Fe-CN distances (not shown here) are remarkably short (0.3 Å shorter with respect to nitroprusside), revealing an enhanced σ -bonding of cyanide to iron. All indicators suggest a *dominant* Fe^INO⁺ configuration, that is confirmed by the IR data showing a high upward shift of ν_{N-O} to 1746 cm⁻¹. The EPR spectrum is also distinctive, with a *g* value of 2.024, interpreted in terms of coupling to a single ¹⁴N nucleus, *A*(¹⁴N) = 15.2 G, and to four ¹³C nuclei. Removal of axial cyanide from [Fe^{II}(CN)₅(NO)]³⁻ to give [Fe(CN)₄(NO)]²⁻ causes the iron d_z^2 orbital to shift from being an almost pure metal orbital to an admixed character, giving a SOMO σ -orbital bonding over the whole Fe-N-O fragment. [Fe^{II}(CN)₅(NO)]³⁻ has a SOMO of π type with respect to the FeNO direction, with *A*(¹⁴N) = 38 G.

A comprehensive description of the electronic structures of [Fe(TPP)(NO)] and the 6C derivative [Fe(TPP)(MeIm)(NO)] has been accomplished for the first time[85] by using diverse spectroscopies: UV-vis, ¹H NMR, Vibrational (IR/Raman), including isotope-substitutions and force-constant calculations by normal coordinate analysis, MCD and quantum chemical calculations. Binding equilibrium constants for diverse *N-trans* ligands into the 5C species have been also determined. The 5C and 6C complexes contain \angle FeNOs around 140° and similar medium-strong π -backbonds. For 5C complexes, σ donation from the SOMO π^* orbital of NO into d_{z^2} of Fe^{II} forms a Fe-NO σ -bond that leads to a significant transfer of spin density from NO to iron; thus, the 5C complex has an intermediate Fe^{II}NO[•]/Fe^INO⁺ character (with ~50% in Fe and NO), whilst the 6C analog shows to be a Fe^{II}NO[•] complex. A similar situation holds for 5C [Fe(TPPBr₃)(NO)]. [81]

4.2. Labilization of trans ligands

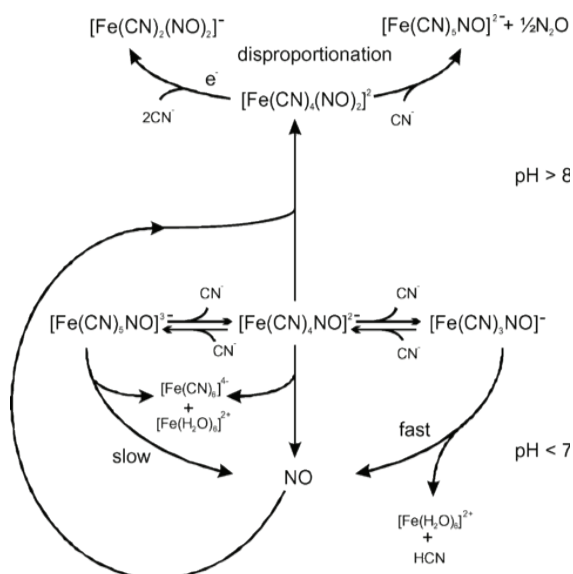
Some 6C complexes in Table 2 represent a generalized pattern for aqueous nitrosyls with *monodentate* labile *trans*-ligands, to which we might add $[\text{Fe}^{\text{II}}(\text{cyclam})(\text{Cl})(\text{NO})]^+$ and $[\text{Ru}^{\text{II}}(\text{NH}_3)_4(\text{L})(\text{NO})]^{2+}$. [30,47] However, the Fe-cyclam-ac and Ru-azamacrocyclic complexes behave as robust species in solution because the *trans*-positions to nitrosyl are blocked by an arm of the polydentate ligand; nevertheless, the X-ray structures confirm relative elongations of the *trans* M-L bonds as well. The 6C \rightarrow 5C conversions behave as reversible equilibria, as described for the iron cyano-nitrosyls in reaction (31), with a binding constant $K_{31} = 1.46 \times 10^4 \text{ M}^{-1}$ ($k_{\text{on}} = 4.1 \times 10^6 \text{ M}^{-1}\text{s}^{-1}$, $k_{\text{off}} = 2.8 \times 10^2 \text{ s}^{-1}$). [86] The value of K_{31} indicates a *weak trans* labilization of cyanide, consistent with its *strong* σ -donor ability to iron. However, the pH influences the concentrations of 6C/5C species, with the 5C one increasing with acidity, according to cyanide-trapping by protonation, reaction (32); thus, both species coexist $\sim 50\%$ each at pH 7.4. [87] On the other hand, 6C iron nitrosyl hemes with weak N-binding imidazole (ImH) ligands have lower binding constants in the range $10\text{-}100 \text{ M}^{-1}$ and display stronger *trans* labilizations, (reaction 33). [77]



The release of N-histidine from sGC revealed a role for NO as an essential cellular signaling agent. Ensuing the very fast NO-coordination into the 5C high spin Fe^{II} center in sGC, the transient low spin 6C intermediate releases the proximal histidine ligand, thus triggering a conformational change that activates the catalytic domain of the enzyme, mediating the conversion of GTP to the biochemical messenger cyclic guanosine monophosphate, cGMP, with final vasodilation. The mechanistic details on this important bioreaction are still under scrutiny; [88-90] we expand later on this issue, after discussing the chemical properties of $[\text{Fe}(\text{CN})_5\text{NO}]^{3-}$ below.

4.3. NO-ligand interchange, dinitrosyl formation and disproportionation reactions of one-electron-reduced nitroprusside. Implications for sGC activation/deactivation

Given that the current use of nitroprusside in vascular therapy implies a rapid onset of the physiological vasodilatory response upon injection in the bodily fluids, the thiolates appeared as responsible for the build-up of $[\text{Fe}(\text{CN})_5\text{NO}]^{3-}$ after addition into the Fe-NO⁺ moiety, with ensuing decay of $[\text{Fe}(\text{CN})_5\text{NOSR}]^{3-}$, cf. reactions (26) and (27). As $[\text{Fe}(\text{CN})_5\text{NO}]^{3-}$ is inert toward NO-release ($k_{-\text{NO}} = \sim 10^{-5} \text{ M}^{-1}\text{s}^{-1}$), [43] 5C $[\text{Fe}(\text{CN})_4\text{NO}]^{2-}$ has been suggested as the putative NO-labile species. We afforded a detailed study on the *spontaneous* thermal decomposition of equilibrated solutions of $[\text{Fe}(\text{CN})_5\text{NO}]^{3-}$ and $[\text{Fe}(\text{CN})_4\text{NO}]^{2-}$ in the pH range 4-10. Scheme 3 summarizes the reactivity picture, supported by a combined use of UV-vis, IR and EPR spectroscopies. [91]



Scheme 3



The pH conditions were crucial for analyzing the results. At pH 7, initially predominant $[\text{Fe}(\text{CN})_4\text{NO}]^{2-}$ (λ_{max} , 615 nm) decays *also slowly*, $k_{\text{off}} \sim 10^{-5} \text{ s}^{-1}$. A faster decomposition occurs at pH 4-5, with successive cyanide- and NO-release, forming Prussian blue-type precipitates. It has been proposed that $[\text{Fe}(\text{CN})_4\text{NO}]^{2-}$ might be a precursor of fast NO-release in biorelevant media *if* the cyano-ligands were exposed to donor interactions with specific acceptor sites in protein residues, promoting decomposition under physiological conditions.[92] At pH > 8, $[\text{Fe}(\text{CN})_5\text{NO}]^{3-}$ (λ_{max} , 345 nm) becomes predominant, and the slow NO[•]-release leads to the formation of an EPR-*silent* intermediate, I_1 , with a characteristic UV-vis spectrum, and $\nu_{\text{N-O}}$ at 1695 cm^{-1} . I_1 is a precursor of NO-disproportionation into $[\text{Fe}(\text{CN})_5\text{NO}]^{3-}$ and N_2O , displaying a rigorous 1:0.5 molar stoichiometry. The IR and EPR evidence suggest that I_1 is a *dinitrosyl* compound, $[\text{Fe}(\text{CN})_4(\text{NO})_2]^{2-}$ (probably a *trans-syn* species, based on preliminary DFT calculations), proposed to be formed by self-dissociation of NO from $[\text{Fe}(\text{CN})_5\text{NO}]^{3-}$ and rebinding into the aqua-site generated by the *trans*-cyanide labilization. Interestingly, a closely related complex, $[\text{Fe}(\text{por})(\text{NO})_2]$, has been prepared and characterized, although at low temperatures, showing very similar DFT structural and spectroscopic properties as I_1 .[93,94] Thus, the identification of I_1 as $[\text{Fe}(\text{CN})_4(\text{NO})_2]^{2-}$ under room-temperature conditions is quite unusual; we confirmed a product with similar properties as I_1 for the reaction of $[\text{Fe}(\text{CN})_4\text{NO}]^{2-}$ with excess NO, with $k_{\text{on}} = 4.3 \times 10^4 \text{ M}^{-1} \text{ s}^{-1}$.[91] Remarkably, the decay of I_1 leads to a new EPR active intermediate I_2 , indicative of the so-called “ $g = 2.03$ ” dinitrosyls, which are biologically relevant and labile species, active toward vasodilation.[92] These $[\text{Fe}(\text{L})_2(\text{NO})_2]$ complexes have a pseudo-tetrahedral arrangement for $\text{L} =$ thiolates, imidazoles, and likely for cyanide as well.

We consider useful to analyze the above results in the context of available data on the mechanism of sGC activation. Although the crystal structure of the complete protein is lacking, sGC is known to be a heterodimer with two α - β subunits, one of them (β) containing a high spin 5C ferrous heme with proximal histidine coordination.[88] It is accepted that the first step comprises fast NO binding ($k_{\text{on}} = 4.5 \times 10^8 \text{ M}^{-1} \text{ s}^{-1}$) giving a highly reactive 6C NO complex as a precursor of histidine release and consequent enzyme activation, implying a structural reordering that leads to vasodilation. Based on a measured second order rate law in NO found for the activation rate of sGC under excess NO-conditions, the formation of a dinitrosyl intermediate has been under controversy when considering the detailed mechanistic issues.[88] From recent work under physiological conditions it might be assumed that the dinitrosyl species does not form.[89,90] Estrin and coworkers studied a functional heme analog of sGC, cytochrome *c*' , which includes three amino acid residues positioned near the distal and proximal sites.[95] Figure 11 shows a calculated structure corresponding to the first 6C intermediate, still containing bound histidine.

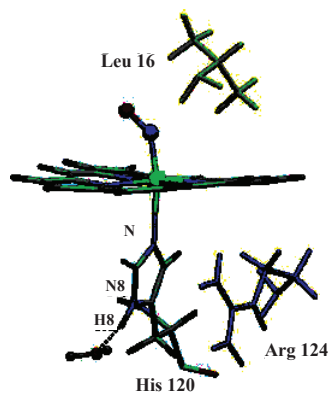


Figure 11. Calculated first 6C NO-intermediate upon reaction of cyt *c*' (from AXCP, alcaligenes xylosoxidans) with NO. From reference 95.

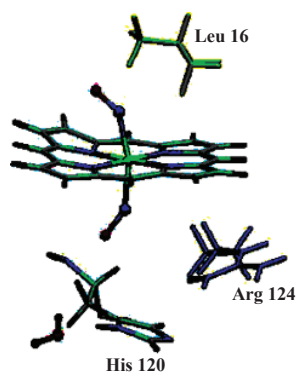
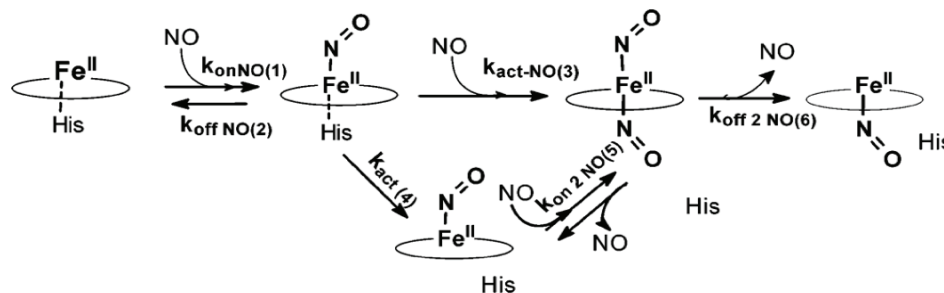


Figure 12. 6C di-NO complex in cyt *c*' from AXCP (alcaligenes xylosoxidans), proposed to be formed upon histidine displacement in the complex of Figure 11 by a second NO. From reference 95.

The conditions for the histidine release have been studied in detail, and Scheme 4 has been proposed for the successive steps during the activation process.[95] After the first NO-binding event, the 6C reactive intermediate leads to a 5C-NO heme complex and free histidine, in a spontaneous uncatalyzed process, k_{act} (4). Under excess NO, a faster activation ensues under a second-order regime, k_{act} (3). Whilst the first 6C \rightarrow 5C slow conversion contains a NO bound at the *distal* site, the fast process leads to additional NO-binding at the *proximal* site, either through direct occupation of the free site arising after histidine release, or through a concerted interchange of histidine with NO. Figure 12 shows a calculated structure for the 6C dinitrosyl intermediate, surprisingly like the one experimentally found and calculated for $[\text{Fe}(\text{por})(\text{NO})_2]$,[93,94] as well as for $[\text{Fe}(\text{CN})_4(\text{NO})_2]^{2-}$ (I_1).[91]

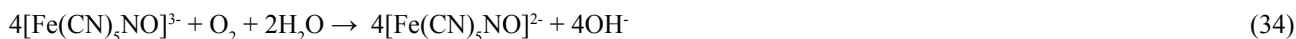


Scheme 4

The final step implies a release of NO giving a 5C-NO heme. How the second NO is released with histidine rebinding for the active site regeneration remains unknown, however. In their comprehensive study, the authors extended the analysis of the activation process to the movements of free histidine 120 and arginine 124 residues in the proximal environment, as well as a leucine 16 in the distal one (see Figure 11). We will not extend here on the relevance of the latter studies for comparing with the role of sGC, for which many structural mechanistic questions are still unsolved. Instead, we believe that given the general instability of the dinitrosyl species and the demonstrated disproportionation route for $[\text{Fe}(\text{CN})_4(\text{NO})_2]^{2-}$ (I_1), the cyt *c'* intermediate could also lead to bound NO/HNO and NO^+ at the proximal and distal sites, respectively, as suggested by a calculated *linear* Fe-N-O group at an energy minimum of the distal site,[95] suggesting a fleeting NO^+ -character and a putative site for thiolate attack followed by RSNO formation and release. Besides, the strong donor NO^- at the proximal site might facilitate the ligand release at the distal site and/or react with the excess NO either through NO⁻/NO interchange or N_2O release. The latter reactivity modes could lead to final rebinding of histidine and recovery of the high spin 5C Fe^{II} resting state, allowing for the catalytic turnover steps evolving through the 6C mono- and di-nitrosyls. Whilst the relevance of a role for a second NO in the regulation of the conformational protein change seems well supported by the kinetic data, the full reactivity route for the dinitrosyl intermediate (eventually comprising a third NO molecule reacting with the dinitrosyl), might merit further consideration by the biochemical community.

4.4. Nucleophilic reactivity toward O_2 (dioxygenation reactions)

A nucleophilic reactivity might be anticipated for the electron-rich NO-complexes. This has been observed for $[\text{Fe}(\text{CN})_5(\text{NO})]^{3-}$ (under excess cyanide conditions), and reaction (34) describes the stoichiometry.[96]



A second-order rate law operates: $-1/4d[\text{Fe}(\text{CN})_5\text{NO}^{3-}]/dt = k_{34}[\text{Fe}(\text{CN})_5\text{NO}^{3-}][\text{O}_2]$, with $k_{34} = (3.5 \pm 0.2) \times 10^5 \text{ M}^{-1}\text{s}^{-1}$ at 25 °C, pH 10. The rate constant was insensitive to changes in pH (9–11) and ionic strength (0.1–1 M). However, for pH < 10 and without added cyanide, the oxidation rate *decreased* markedly. We discarded an initial outer-sphere electron transfer step, given the endergonic barrier for the one-electron O_2 reduction. DFT computations allowed proposing reaction (35) as an initial addition step, forming a new covalent bond between NO and O_2 , leading to an Fe^{III} -peroxynitrite species, as shown in Figure 13. In the reaction of *free* NO with O_2 , either ONOO⁻ or a species with some degree of association, $\text{NO} \cdots \text{O}_2$ have been proposed in the first step.[15]

The process follows through the fast reactions (36) and (37), both probably involving several steps, in which the oxidation equivalents remain bound to the metal all along the full process, according with the experimentally found 4:1 global stoichiometry, with no other by-products.





The spin unrestricted DFT calculations provided strong evidence for identification of the first intermediate; the geometry optimization procedure demonstrates that the SOMO is localized on iron(III) and not at the terminal O-atom, with Mülliken spin densities close to one, calculated either in vacuum or in solvated conditions (PCM + 6H₂O). Given that the geometrical parameters and stretching frequencies are consistent with a bound N-peroxynitrite anion, we might discard the alternative descriptions containing either Fe(II)-N(O)O₂⁻, or the Fe(III)-OON(O)⁻ isomer.

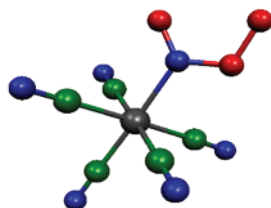


Figure 13. DFT-calculated intermediate, $[\text{Fe}^{\text{III}}(\text{CN})_5(\text{N}(\text{O})\text{O}_2)]^{3-}$, B3LYP/6-31††, with PCM + 6H₂O. For N(O)O₂⁻ bound to Fe: d(N=O), 1.205 Å; ν(N=O), 1590 cm⁻¹; d(N-O), 1.352 Å, ν(N-O), 784 cm⁻¹; d(O-O), 1.369 Å; ν(O-O), 913 cm⁻¹. See the Supp. Inf. in Ref. 96 for details on the calculations and other parameters derived from the geometry optimization.

Under steady state conditions for $[\text{Fe}^{\text{III}}(\text{CN})_5\text{N}(\text{O})\text{O}_2]^{3-}$, and using a limiting approach, a first-order rate law in each reactant is obtained, with $k_{35} = k_{\text{ad}} = k_{\text{O}_2}$. Second order rate laws have been found for the autoxidation reactions of other nitrosyl complexes with n = 7.[97,99] Figure 14 displays a plot of ln k_{O2} against E_{NO+/NO}.

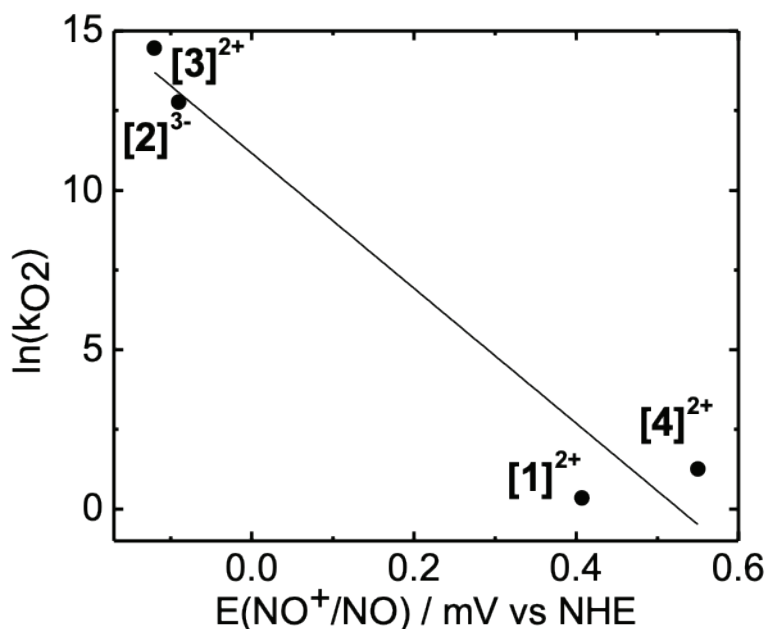


Figure 14. Plot of ln k_{O2} vs E_{NO+/NO} for the reactions of O₂ with different complexes: [1]: [Ru(Me₃[9]aneN₃)(bpy)(NO)]²⁺;^[97] [2]: [Fe^{II}(CN)₅(NO)]³⁻;^[97] [3]: [Ru^{II}(NH₃)₅(NO)]²⁺;^[98] and [4]: Ru^{II}(bpy)(tpm)(NO)]²⁺.^[99] Extracted from reference [97].

The *negative slope* of $-21 \pm 1 \text{ V}^{-1}$ agrees with the theoretical Marcus-type behavior for bimolecular reactions with associative character. Indeed, a better correlation might be expected by including data for new complexes, preferentially in the mid-potential region. The slow-reacting complexes display significant deviations, as also observed for Mb^{II}NO,

for which a corresponding point was included in a similar plot;[12] (it could be added in Fig. 14, close to $[1]^{2+}$). The deviations are not unexpected, due to the possible competing NO-dissociation in the rate-determining step ($k_{\text{off}(\text{NO})} \sim 10^{-4} \text{ s}^{-1}$ for $\text{Mb}^{\text{II}}\text{NO}$).[12,96] On the other hand, the autoxidation of the electron rich complex $[\text{Ru}^{\text{II}}(\text{DMAP})_4(\text{NO})(\text{OH})]^+$ was unmeasurably fast (we estimate a point at the upper-left side of the plot, out of Fig. 13).[100] Not unexpectedly, the latter figure resembles Fig. 4, bearing a *positive* slope, covering the *electrophilic* additions of OH^- into $[\text{ML}_5(\text{NO}^+)]$ complexes.

It can be concluded that 6C is a necessary condition to achieve autoxidation of NO-complexes, given the *unreactivity* of 5C $[\text{Fe}(\text{CN})_4\text{NO}]^{2-}$ at neutral/low pH, in agreement with the electron push by the sixth ligand that increases the radical character of NO (see the previous analysis of the EPR results for 6C/5C systems). Other 5C complexes were found to react with O_2 in aprotic solvents, but *only in the presence of a base*, which allowed formation of the 6C reactive species. [12] Indeed, that the redox potentials of the $\text{MNO}^+/\text{MNO}^\bullet$ couples could predict the NO-autoxidation reactivity is quite significant; eventually, some NO^\bullet -coordination compounds could provide a *fast route for NO-consumption*, as shown below.

In the NOS-catalyzed endogenous production of NO by oxidation of L-arginine with O_2 , a 6C $\text{Fe}^{\text{II}}\text{-NO}$ intermediate (containing cysteinate as a *trans*-ligand to NO) played a crucial role in the global catalytic/regulatory cycle by reacting with O_2 and giving NO_3^- , which was rapidly released.[101] In this way, regeneration of the labile aqua-site (5C high-spin Fe^{III}) allowed performing the catalytic turnover through subsequent reduction to $\text{Fe}(\text{II})$ and O_2 -coordination for reacting with the arginine substrate. By using *variants* of n- and i-NOS isoforms, the rate constants for dioxygenation reactions of bound NO, k_{O_2} , were found in the range $10^2\text{-}10^4 \text{ M}^{-1}\text{s}^{-1}$, depending on the presence/absence of substrate (L-arg), cofactor (BH_4) and/or H-bonding interactions either at the distal- or proximal heme sites. Oxygen binding to the NOS ferrous heme is extremely fast (ill-defined k_{O_2} , reported to be higher than $10^5 \text{ M}^{-1}\text{s}^{-1}$),[101] and thus the corresponding point might be well located up- and left-wards (out of the plot) in Figure 14. Thus, the mechanisms appear to be similar for the heme- and non heme systems (both affording N-bound peroxynitrite initial intermediates), by using the values of k_{O_2} for pure NOS and $E_{\text{NO}^+/\text{NO}}$ ($\sim -0.3 \text{ V}$). However, the smaller denitrosylation rates for the NOS-surrogates lead to strong deviations. This is not a surprise, given that in contrast to the diffusional encounter of reactants for the non heme nitrosyls, a restricted access of O_2 to the distal pocket has been demonstrated for the NOS isozymes;[101] thus, the rates are not controlled solely by k_{O_2} (direct reactivity of O_2 to nitrosyl), and therefore the observed denitrosylation rates become much lower for the enzymatic systems.

5. Strongly bent 6C and 5C $\{\text{MNO}\}^8$ complexes. Highly reducing and nucleophilic

The title compounds containing Fe^{II} and Ru^{II} centers have been generated (and sometimes isolated) from one-electron electrochemical or chemical reductions of the $\{\text{MNO}\}^7$ analogs using hydrides, dithionite, cobaltocene, etc., under anaerobic conditions in non-aqueous media. Aqueous $\text{Co}^{\text{III}}\text{-NO}^-$ complexes can be generated through oxidation of Co^{II} reactants. There is a need of well characterized *iron* complexes in *aqueous solutions*. [17]

Figure 1b shows that for $n = 8$ conditions either both π_{NO}^* MOs can be singly occupied ($S_t = 1$), or two electrons can fully locate at the lower energy orbital ($S_t = 0$). In the latter case, both 6C and 5C compounds might be predicted, though 5C is likely favored, given the *very strong trans* interaction associated with the most pronounced σ donation from π_{NO}^* to d_{z^2} , with an increase in the antibonding character of the *trans* M-L bond. As shown below, these predictions are well realized.[102]

Table 5 show selected examples for 6C and 5C situations. We include the scarce examples of related Fe- and Ru-complexes already displayed in Tables 1 and 2, namely those containing the same coligands. The Co-examples reflect the abundance of this metal for binding nitroxyl ligands, which becomes useful here for searching in the bonding changes upon metal variations.[103,104]

**Table 5.** Selected 6C and 5C metallonitrosyl complexes, {MNO}^g (M = Fe, Ru, Co)

Compound	S_t	ν_{N-O}^{-1} (cm^{-1})	d_{M-NO} (Å)	d_{N-O} (Å)	\angle_{MNO} ($^\circ$)	d_{M-L} (Å)	Ref
6C							
[Fe(cyclam-ac)NO] ^a	0	1271 ^b (1274)	(1.752)	(1.261)	(122.4)	(2.127)	30
[Ru(Me ₃ [9]aneN ₃)(bpy)(NO)] ⁺	0	1315 ^c (1404)	(1.91)	(1.27)	(122.9)	(2.41)	39
[Co(en) ₂ (Cl)(NO)] ⁺	0	1611	1.820(11)	1.043(17)	124.4(11)		103
5C							
[Fe(CN) ₄ (NO)] ³⁻ tbp, ^e	0	(1581)	(1.637)	(1.22)	(171.2)		46
[Co(TPP)(NO)] sqp	0	1681	1.830	1.149	123.4		104
[Fe(TPPBr ₈)(NO)] ⁻ sqp ^f	0	1540 ^g	1.814(4)	1.194(5)	122.4(3)		105

a) Values in parenthesis are from DFT calculations. b) in CD₃CN solution. c) in CH₃CN solution. d) isolated as a ClO₄⁻ salt. e) not isolated, only DFT data. It is probably a product of the NMR titration of [Fe(CN)₅(HNO)]³⁻ with OH⁻, after reaching pH 10, see text and Figure 15. f) Structural data from an isolated Co(Cp)₂⁺ salt; corresponding DFT calculations in ref. 81. g) in CH₂Cl₂ solution or as an evaporated solid film, ref. 81.

For [Fe(cyclam-ac)(NO)], the pronounced bending of $\angle FeNO$ (near 120°, sp² nitrogen), the elongated bonds in the Fe-N-O moieties, and a notoriously low value of ν_{N-O} at 1271 cm⁻¹, confirmed by isotopic labelling and theoretical calculations, allowed proposing a low-spin Fe^{II}NO⁻ distribution, supported by $S_t = 0$ and Mössbauer results.[30] A similar behavior of the indicators for 6C [Ru(Me₃[9]aneN₃)(bpy)(NO)]⁺ reflects the increased population of the delocalized π_{RuNO}^* orbital as compared to the n = 6, 7 analogs.[39] The NO⁻ ligand appears to engage in stable M^{II}-NO⁻ bonds in both complexes, inert to dissociation. Though still not able to release the *trans*-ligand, the enhanced *trans*-releasing effect manifests in the elongation of the *trans* Fe-O and Ru-N₍₂₎ bonds by 0.15 and 0.19 Å respectively with respect to the corresponding n = 7 complexes. A detailed look at all indicators for both Fe and Ru series demonstrate that the back bonding acceptor capacity of the nitrosyl group increases strongly according to NO⁻ < NO < NO⁺, with conversion from a strong nucleophile to a strong electrophile. Interestingly, the 6C Co^{III} nitroxyl complex shows an increased value of ν_{N-O} , probably related to the weaker π -interaction for M^{III} as compared to M^{II} centers.[103] The nitroxylcobalamine analog (NOcbl, not shown) behaves similarly.[12]

Notoriously, there is no 6C [Fe(CN)₅(NO)]⁴⁻ complex in Table 5; it was calculated by DFT as *unstable in water*, leading to 5C tpb [Fe(CN)₄(NO)]³⁻ upon cyanide release.[46] Similarly, 6C [Fe(NO)(Cl)(cyclam)] decomposes readily by releasing the chloride ligand in CH₃CN.[30] The DFT data for 5C tpb [Fe(CN)₄(NO)]³⁻ (not isolated) shows a close to linear $\angle FeNO$ and a short Fe-N distance; by also considering the value of ν_{N-O} at 1581 cm⁻¹, an Fe^INO electronic distribution was proposed, and the protonation feasibility was estimated.[46] The 5C [Fe(por)(NO)]⁻ was also unstable, though Table 5 includes a *stable* species, *isolated* by reducing an n = 7 electron-poor model iron porphyrin in CH₂Cl₂ with cobaltocene, leading to [Co(C₅H₅)₂][Fe(TFPBr₈)(NO)].[81,105] It has been described as having an intermediate Fe^{II}NO⁻/Fe^INO distribution. This strategy allowed preparing a similar heme-like salt of [Fe(LN₄)(NO)]⁻,[12] as well as a picket-fence porphyrin [Fe(3,5-Me-BAFP)(NO)]⁻, in THF solution.[102]

Trans labilizations and facile generation of 5C complexes explain the abundance of sqp Co-nitroxyl porphyrins and some [Co(LN₄)(NO)] analogs.[12] A common low-spin Co^{III}NO⁻ electronic distribution is currently accepted for all 6C and 5C Co-complexes. On the other hand, well characterized examples with metals of the 2nd or 3rd transition series are known (tpb NO⁻ complexes of Os^{II}, Ir^{III}, Re^I, and even Pt^{IV}).[17]

Given the extreme electron-rich character of NO⁻ complexes, the M-N-O moieties are prone to react with electrophilic reagents. This was early observed with 5C [CoL₄NO] complexes (L₄, multidentate planar anions) reacting with O₂ in acetone, in the presence of nitrogen- and phosphorus bases B, to yield the corresponding 6C nitro-compounds, [CoL₄(NO₂)(B)]. The bimolecular rate constants for the O₂-additions depended on the basicity of the B ligands *trans* to the nitroxyl group, and peroxyxynitrite intermediates have been proposed.[12,27] A similar reactivity toward O₂ has been observed for the “based-on” 6C NOcbl, and for other complexes in Table 5, which indeed react with O₂. [12] Like the n = 7 species, 6C appears as a requirement for O₂-reactivity. Protonation at the nitrogen lone pair of bound-NO⁻ is also feasible, as seen below.

6. HNO (nitroxyl, azanone) complexes (n = 8)

6.1. Synthesis, spectroscopic characterization, and trans-L releasing ability of bound HNO

6C HNO non heme complexes have been prepared with Fe, Ru, Os, Ir, and Re metals, with ancillary coligands, since the pioneering work leading to X-ray structures of $[\text{Os}(\text{Cl})_2(\text{CO})(\text{PPh}_3)_2(\text{HNO})]$ and $[\text{Ir}(\text{H})(\text{Cl})_2(\text{PPh}_3)_2(\text{HNO})]$. Most isolated complexes are insoluble in water. Good characterizations of bound HNO were achieved using ^1H NMR, IR, and RR spectroscopies. Both σ and *mainly* π interactions contribute to HNO stabilization upon coordination.[17] In Table 6, we first include two examples of *aqueous* systems comprising $[\text{Fe}^{\text{II}}(\text{CN})_5(\text{HNO})]^{3-}$ and $\text{Mb}^{\text{II}}(\text{HNO})$, together with related Fe-, Ru-, and Os-models. The values of $\nu_{\text{N-O}}$ at 1350-1390 cm^{-1} remain nearly constant for all complexes; remarkably, they are also coincident with the values found for diverse structurally related $[\text{Fe}^{\text{II}}(\text{CN})_5(\text{L})]^{n-}$ nitroso compounds, with L = NOBz, NOSR, etc.[12] The distances and angles are close to those for the 6C NO^- -analogs (cf. Table 5), though $\nu_{\text{N-O}}$ affords greater values in $\text{Fe}^{\text{II}}\text{-HNO}$ than in $\text{Fe}^{\text{II}}\text{-NO}^-$, probably related to different solvations.

Table 6. ^1HNO complexes (6C protonated $\text{MNO}\}^8$ systems, with M = Fe^{II}, Ru^{II}, Os^{II}; $S_t = 0$)

Compound ^a	$\nu_{\text{N-O}}$ (cm^{-1})	$d_{\text{M-O}}$ (\AA)	$d_{\text{N-O}}$ (\AA)	\angle_{MNO} ($^\circ$)	$d_{\text{M-L}}$ (\AA)	$^1\text{H NMR}$ (δ , ppm)/(J, Hz)	Ref.
$[\text{Fe}(\text{CN})_5(\text{HNO})]^{3-}$	1384 ^b	(1.783)	(1.249)	(137.5)	(1.915)	20.0 ^b / 71.14	45,106
$[\text{Mb}(\text{HNO})]$	1385 ^c	1.82(2)	1.24(1)	131.6	2.09	14.8 ^c / 72.5	31
$[\text{Fe}(\text{cyclam-ac})(\text{HNO})]^+$	(1351)	(1.780)	(1.268)	(126.3)	(1.994)		30
$[\text{Ru}(\text{Me}_3[9]\text{aneN}_3)(\text{bpy})(\text{HNO})]^{2+}$	(1376)	(1.93)	(1.28)	(127.5)	(2.22)		38
$[\text{Ru}(\text{py}^{\text{bu}}\text{S}_4)(\text{HNO})]^+$	1358 ^d	1.875(7)	1.242(9)	130.0(6)		19.56 ^e	108
$[\text{Ru}(\text{ttp})(1\text{-MeIm})(\text{HNO})]$	1380 ^d					13.64 ^f / 71.1	109
$[\text{Os}(\text{Cl})_2(\text{CO})(\text{PPh}_3)_2(\text{HNO})]$	1410 ^g	1.915(6)	1.193(7)	136.9(6)		21.2 ^h / 75	110

a) Data in parenthesis correspond to DFT calculations. b) pH 6 for ATR/RR; 25% D₂O for NMR. c) geometrical and vibrational data in aqueous/glycerol at 10 K. NMR data at pH 10 in D₂O. d) in KBr. e) in THF-d₈. f) in CDCl₃. g) in nujol. h) in benzene-d₆.

Figure 15 describes the two-step titration of aqueous nitroprusside with dithionite at pH 10.[106] Just after the addition of the first drops of dithionite, a *red color* develops which *immediately disappears upon stirring*, giving a *yellow-orange* absorption band centered at 345 nm that grows steadily up to the completion of the first-equivalent reduction. This is indicative of formation of the one-electron reduced product $[\text{Fe}(\text{CN})_5(\text{NO})]^{3-}$ in the first step,[86,87] although seemingly not in a direct way, see below section 6.3. Through the onset of the second-equivalent reduction, the latter species decays and transforms into a final *red* product with λ_{max} at 445 nm (I_{445}), which is moderately stable for hours, slowly turning back to $[\text{Fe}(\text{CN})_5(\text{NO})]^{3-}$, with a $t_{1/2} = 50$ min.

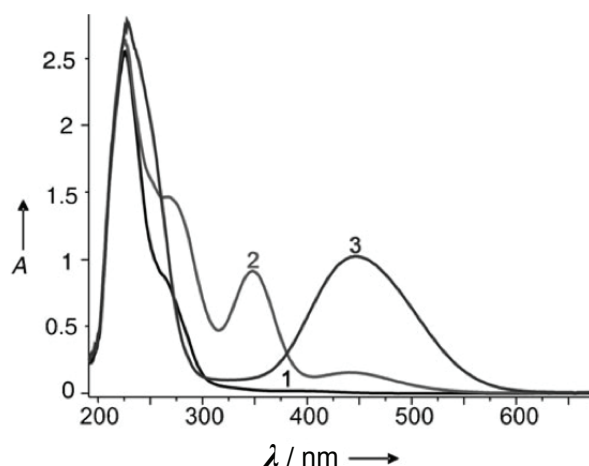


Figure 15. UV-vis titration (pH 10, $T = 25\text{ }^{\circ}\text{C}$), of $3 \times 10^{-4}\text{ M}$ $[\text{Fe}^{\text{II}}(\text{CN})_5(\text{NO})]^{2-}$ (1) with two sequential 1-equivalent additions of $\text{S}_2\text{O}_4^{2-}$, giving the reduced complexes: 2, $[\text{Fe}^{\text{II}}(\text{CN})_5(\text{NO})]^{3-}$, and 3: I_{445} . The latter product 3 is probably a mixture of two-electron reduced complexes, see text. From reference 106.

By shifting the pH from 10 to 6-7 immediately after the end of dithionite-titration, the absorbance maximum at 445 nm was maintained, and I_{445} became even more robust under anaerobic conditions, with an *extremely slow* first order decay, $k_{\text{obs}} = \sim 10^{-7}\text{ s}^{-1}$. Thus, I_{445} did not generate N_2O , neither released cyanide in time scale of hours.[107] We might tentatively identify I_{445} (at pH 10) as a mixture of two-electron reduced products, namely $[\text{Fe}(\text{CN})_5(\text{HNO})]^{3-}$, $[\text{Fe}(\text{CN})_5(\text{NO})]^{4-}$, and $[\text{Fe}(\text{CN})_4(\text{NO})]^{3-}$, as analyzed below.

Figure 16 shows the titration of the robust I_{445} complex generated at pH 6, with OH^- , as followed by ^1H NMR. The inset (top left) displays the initial NMR features, with a notoriously downfield ^1H signal, split into a doublet upon coupling within the ^{15}N labeled species (Table 6). Indeed, the ^1H signal shows *unequivocally* that I_{445} corresponds to $[\text{Fe}(\text{CN})_5(\text{HNO})]^{3-}$ at pH 6, also supported by complementary spectroscopic evidence (IR, RR). The intensity of the NMR signal decays along the titration, with complete disappearance in the 8.8-10 pH-range. An apparent $\text{p}K_a$ of 7.7 was assigned initially to deprotonation of $[\text{Fe}(\text{CN})_5(\text{HNO})]^{3-}$ giving $[\text{Fe}^{\text{II}}(\text{CN})_5(\text{NO})]^{4-}$, eq 38. That assignment was put into question by new ^{17}O NMR evidence stating that the ^{17}O signal was maintained up to pH 10, which allowed proposing a $\text{p}K_a$ at ~ 10 -11,[111] more in agreement with the estimated value for $\text{Mb}^{\text{II}}\text{-HNO}$.[112] The intriguing 7.7 number was traced to an artifact related to a rapid H-exchange between bound HNO and water, acid and/or base-catalyzed.[111]

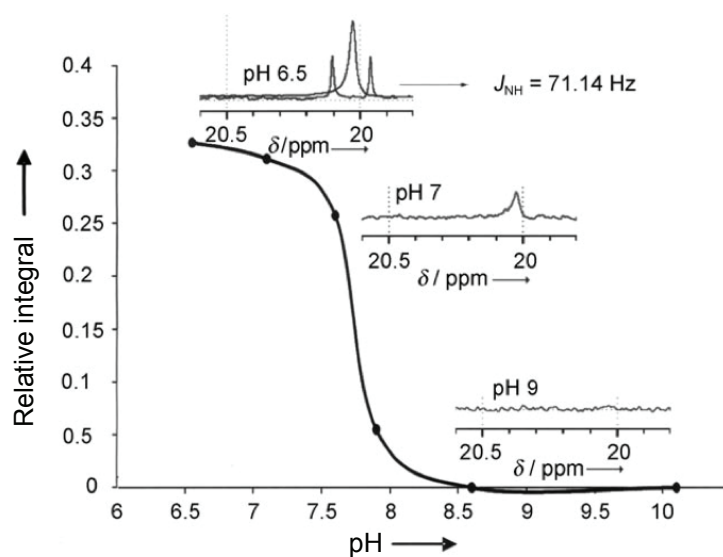
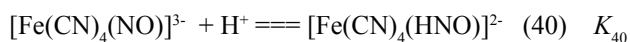
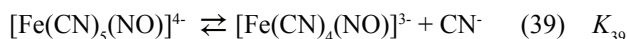
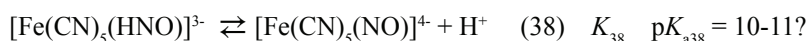


Figure 16. ^1H NMR titration of $[\text{Fe}(\text{CN})_5(\text{HNO})]^{3-}$, with OH^- . Inset, top left: signal splitting upon ^{15}N labeling of the $\text{Fe}^{\text{II}}(\text{nitrosyl})$ moieties. From reference 106.

Based on calibrated DFT calculations, Lehnert and colleagues have suggested that $[\text{Fe}(\text{CN})_4(\text{NO})]^{3-}$, resulting from the fast *trans*-cyanide labilization from $[\text{Fe}(\text{CN})_5(\text{NO})]^{4-}$ during the ongoing titration process (eq 39), might suffer a *competitive protonation* with free cyanide, eqs 40 and 41 ($\text{p}K_a(\text{HCN}) = 9.2$). Therefore, the 7.7 feature would correspond to the $\text{p}K_a$ of $[\text{Fe}(\text{CN})_4(\text{HNO})]^{2-}$. [17]



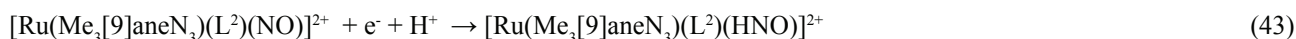
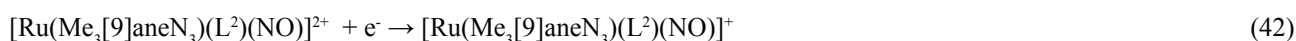
The onset of the precedent equilibria along the addition of OH^- and the consideration of available and estimated values of K in reactions 38-41 allow proposing that $[\text{Fe}(\text{CN})_5(\text{NO})]^{4-}$ is the dominant nitroxyl species at the end of titration (pH 10), with some equilibrated $[\text{Fe}(\text{CN})_5(\text{HNO})]^{3-}$ and $[\text{Fe}(\text{CN})_4(\text{NO})]^{3-}$. We might conclude that both the ^1H and ^{17}O NMR evidence, as well as our results on the unchanged absorptivity of I_{445} in the pH range 6-10 [106] strongly support a new $\text{p}K_a$ estimation in the range 10-11 for the $[\text{Fe}(\text{CN})_5(\text{HNO})]^{3-} \rightarrow [\text{Fe}^{\text{II}}(\text{CN})_5(\text{NO})]^{4-}$ conversion.

In high contrast with $[\text{Fe}(\text{CN})_5(\text{NO})]^{4-}$ (whose *trans*-cyanide labilization might be a few orders of magnitude stronger than for $[\text{Fe}(\text{CN})_5(\text{NO})]^{3-}$, cf. K_{31}), the absence of *trans*-cyanide labilization in $[\text{Fe}(\text{CN})_5(\text{HNO})]^{3-}$ becomes remarkable. It relates to the N-protonation, which decreases the σ -bonding of HNO toward the metal. Besides, cyanides are good σ -donors that enrich the electron density at Fe^{II} and strengthen the π bonding interaction with HNO. The nearly equal axial and equatorial Fe-C distances calculated for $[\text{Fe}(\text{CN})_5(\text{HNO})]^{3-}$, [46] and DFT calculations with other HNO-complexes [17] are consistent with experimental results on HNO being unable to activate sGC. [17,113]

The need for synthesizing other iron heme models for best disclosing the biorelevant properties of bound HNO has been elusive because of the putative instabilities of the used iron-porphyrin species toward disproportionation, as observed for 5C NO-complexes in non-aqueous solvents. By adding acetic acid to $[\text{Fe}(3,5\text{-Me-BAFP})(\text{NO})]^-$ in THF, the UV-vis changes in the Soret bands were assigned to the binding of HNO in a 5C complex, which seems consistent. [102] Pellegrino and Doctorovich isolated the $n = 7$ sodium salt of $[\text{Fe}(\text{TPPS})(\text{NO})]^{4-}$, and observed the UV-vis changes upon one-electron reduction *in aqueous medium*. [114] By using CV methodologies described below, the dependence of $E_{\text{NO}, \text{H}^+/\text{HNO}}$ on the pH led to a $\text{p}K_a$ of 9.7 for the supposed 5C $[\text{Fe}(\text{TPPS})(\text{HNO})]^n$. The conclusion is also plausible, though the product might be a 6C species, probably with OH^- or phosphate binding to the 5C intermediate.

6.2. The influence of changing the coligands on the $\text{p}K_a$ of bound HNO, correlated with changes in the redox potentials

By expanding the experimental approach on the $[\text{Ru}(\text{Me}_3[9]\text{aneN}_3)(\text{bpy})(\text{NO})]^{3,2,1+}$ species that allowed determining the $\text{p}K_a$ of the HNO-bound one by using a potential/pH diagram, [38] Slep and coworkers made a significant synthetic progress by isolating three members of the $n = 7$ series with L^2 coligands of different donor abilities, namely $[\text{Ru}(\text{Me}_3[9]\text{aneN}_3)(\text{bpy})(\text{NO})]^{2+}$ ($[1\text{-NO}]^{2+}$), $[\text{Ru}(\text{Me}_3[9]\text{aneN}_3)(\text{MeObpy})(\text{NO})]^{2+}$ ($[2\text{-NO}]^{2+}$) and $[\text{Ru}(\text{Me}_3[9]\text{aneN}_3)(\text{bpym})(\text{NO})]^{2+}$ ($[3\text{-NO}]^{2+}$). [39] In this way, reversible cyclic voltammograms (Figure 17) were obtained by dissolving the pure solids (very stable under anaerobic conditions) in acetonitrile solutions, and by oxidizing and reducing them, with corresponding one-electron waves giving the $n = 6$ and $n = 8$ species, respectively. Figure 18 discloses the UV-vis spectra starting with $[3\text{-NO}]^{2+}$ in aqueous medium, obtained with spectroelectrochemical reductions complemented by controlled potential coulometry. The one-electron nature of the redox events was confirmed, and two distinct spectra emerged upon reduction in acid or alkaline solutions, at pH 2.5 and 12.5. The latter situation corresponds to the actual $\{\text{RuNO}\}^{7/8}$ one-electron conversion represented by eq 42, while the former involves a pH-dependent proton-coupled one-electron reduction, eq 43. By fitting the experimental data with an adequate Nernstian model, numerical values for both standard redox potentials can be obtained, as well as for K_a , the acidity constant of bound HNO.



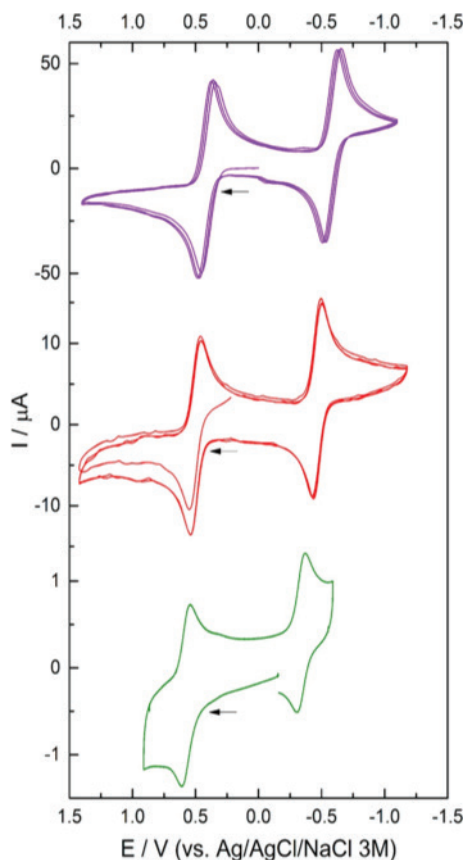


Figure 17. Cyclic Voltammograms obtained (E / V vs. Ag/AgCl/NaCl 3M) of $[3\text{-NO}]^{2+}$ (green) in dry $\text{CH}_3\text{CN}/\text{Bu}_4\text{NPF}_6$ (0.2 M) at 298 K. Scan rate, 100 mV s^{-1} , E vs Ag/AgCl/NaCl (3M). From reference 39.

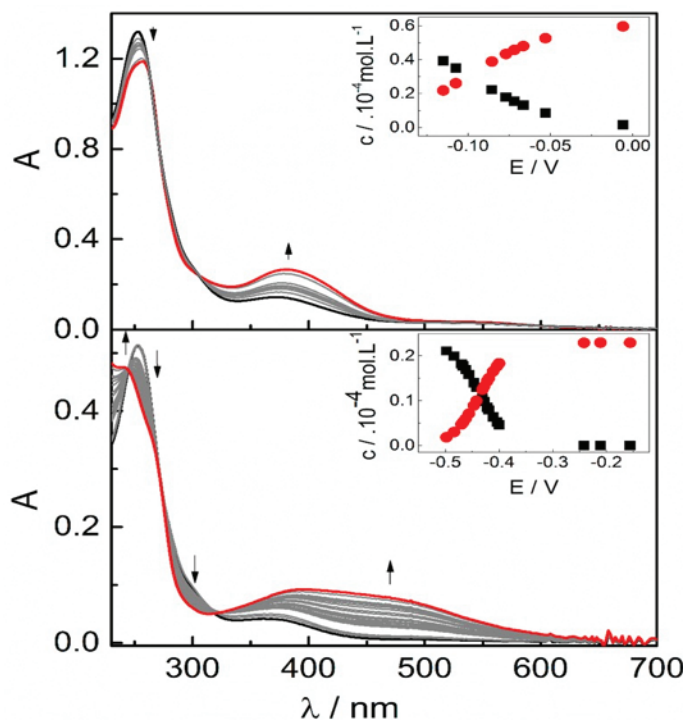


Figure 18. UV-vis spectra obtained by spectroelectrochemistry of $[3\text{-NO}]^{2+}$ in aqueous media [$I = 1 \text{ M NaCl}$ and E vs Ag/AgCl/NaCl (3 M)] at 298 K under anaerobic conditions. The insets show the fraction of the different species as obtained from global analysis. Top: One-electron reduction at pH 2.5 (phosphate buffer). Bottom: One-electron reduction at pH 12.5 (phosphate buffer). From reference 39.

Figure 19 displays an overlap of Pourbaix diagrams, obtained for each of the three complexes, that allow visualizing the corresponding pK_a 's of the HNO-complexes. The latter information is gathered in Table 7. The E^0 values for the redox couples $[\text{RuNO}]^{6/7}$ and $\{\text{RuNO}\}^{7/8}$ behave similarly, with a remarkable decrease in the order $[3\text{-NO}]^{2+} > [1\text{-NO}]^{2+} > [2\text{-NO}]^{2+}$. The trends reflect the increasing donor properties of L^2 , as also described for the acetonitrile solution experiments. The most striking result is the impressive change in the pK_a values of bound HNO spanning a range of three pH units triggered by relatively subtle modifications of L^2 , with virtually no detectable structural changes of the complexes. The linear correlation between pK_a values and the reduction potential for the $[\text{RuNO}]^{6/7}$ and $\{\text{RuNO}\}^{7/8}$ conversions is reasonable, as both are likewise affected by the electronic density modulation introduced by L^2 . These remarkable results highlight the bioinorganic relevance of allowing modulation of HNO/NO⁻ conversions in metallonitrosyl systems that might influence either the *trans* release and/or the reducing capabilities, based on the contrasting structural and redox properties of bound HNO vs NO⁻.

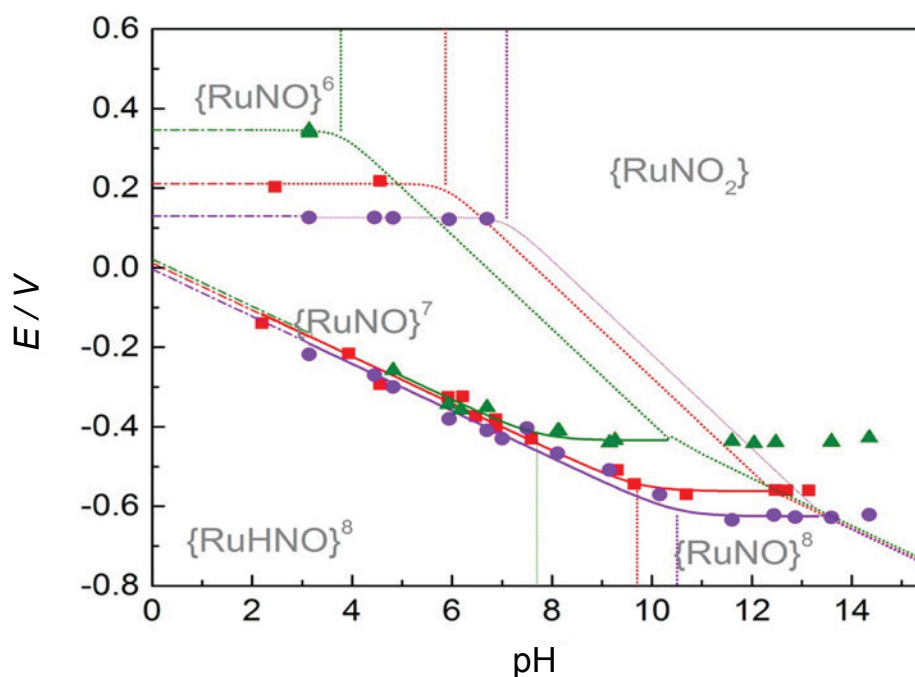


Figure 19. Comparison of the Pourbaix diagrams obtained for $[1\text{-NO}]^{2+}$ (red), $[2\text{-NO}]^{2+}$ (violet), and $[3\text{-NO}]^{2+}$ (green), collected by CV/SWV/SEC in different buffer solutions [$I = 1 \text{ M NaCl}$, at 298 K, E vs $\text{Ag}/\text{AgCl}/\text{NaCl}$ (3M)]. From reference 39.

Table 7. Reduction Potentials and pK_a (HNO) Obtained from the Pourbaix Diagrams^a

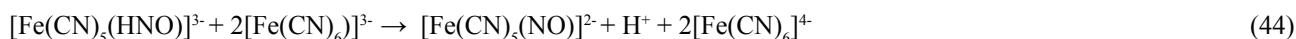
	$E_{\text{NO}/\text{HNO}}^0 / \text{V}$	$E_{\text{NO}/\text{NO}^-}^0 / \text{V}$	$pK_{\text{a HNO}}$
$[3\text{-NO}]^{n+}$	0.021(5)	-0.434(4)	7.7(1)
$[1\text{-NO}]^{n+}$	0.011(9)	-0.562(8)	9.7(2)
$[2\text{-NO}]^{n+}$	-0.004(9)	-0.625(8)	10.5(2)

^a Reduction potential referenced to Ag/AgCl 3M. From reference 39.

6.3. The redox properties of bound HNO and NO⁻

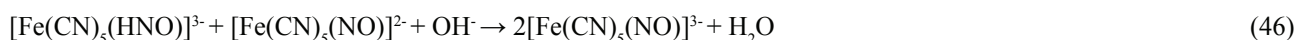
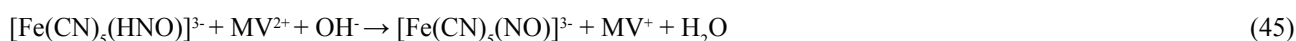
This issue is crucially relevant for biological systems and merits a detailed consideration. We found that $[\text{Fe}(\text{CN})_5(\text{HNO})]^{3-}$ was *unreactive* at pH 6 toward *weak* oxidants like methylviologen (MV^{2+} , $E = -0.44 \text{ V}$) and nitroprusside ($E = 0.05 \text{ V}$).^[107] By using the mild oxidant $[\text{Fe}(\text{CN})_6]^{3-}$ ($E = 0.4 \text{ V}$), a slow reactivity of $[\text{Fe}(\text{CN})_5(\text{HNO})]^{3-}$ through a second order rate law was observed for reaction (44), with $k_{44} = 70 \text{ M}^{-1}\text{s}^{-1}$, much lower than the rate constants for $[\text{Fe}(\text{CN})_6]^{3-}$ reacting with other $[\text{Fe}^{\text{II}}(\text{CN})_5(\text{L})]^{n-}$ ions by metal-centered redox interchange ($k \sim 10^5 \text{ M}^{-1}\text{s}^{-1}$). The magnitude of k_{44} is similar to that found for free HNO reacting with $[\text{Fe}(\text{CN})_6]^{3-}$, and also consistent with the redox potential estimated

through the reversible one-electron wave found in the CV of $[\text{Fe}(\text{CN})_5(\text{HNO})]^{3-}$ at pH 6 ($E_{1/2} = 0.32$ V), assigned to the $[\text{Fe}(\text{CN})_5(\text{NO})]^{3-}$, $\text{H}^+ / [\text{Fe}(\text{CN})_5(\text{HNO})]^{3-}$ redox couple.[107]



A mechanistic analysis in terms of Marcus cross-reaction predictions suggests a NO-centered proton-coupled PCET route for reaction (44), associated with a high reorganization energy. The latter results put into question the claimed high reducing power of HNO, either free or bound to metal centers (cf. eq 5, ~ -0.5 V at pH 7).[7]

In remarkable contrast, the results at pH 10 with the same weak oxidants led to immediate production of the viologen radical, reaction (45), as well as to a quantitative formation of the comproportionation product, $[\text{Fe}(\text{CN})_5(\text{NO})]^{3-}$, reaction (46).[107] The latter reaction explains the striking red \rightarrow orange color changes upon stirring during the initial onset of dithionite titration, see above 6.1. This is confirmatory evidence of emerging deprotonation of bound HNO at pH 10, and consequently a much higher reducing power of bound NO^- compared to HNO.



It can be concluded that the nitroxyl-binding chemical properties are regulated by the pH and redox state of the environment. As demonstrated for the non-heme systems, iron-heme proteins could afford such a regulatory mission on demand, by an appropriate use of ligands (either in axial or equatorial positions), as well as by a controlled location of either external electric fields or specific H-bonding interactions with backbone residues close to the reactive sites.

Conclusions

A comprehensive picture of the structure and reactivity of nitric oxide (NO) and redox derivatives (NO^+ , NO^-/HNO , NO_x) has been presented, focusing on the coordination chemistry in transition metal centers, mainly iron and ruthenium. Though the properties can be roughly described by the total electron content in the frontier metal/ π_{NO}^* orbitals, a deeper insight has been provided that takes into account the influence of the axial and/or equatorial coligands, as well as the second-sphere interactions, for controlling the $\sigma - \pi$ interactions and the actual atomic electronic distributions. Different reactivity modes of the M-N-O groups, mainly ligand formation/dissociations, electrophilic and nucleophilic additions, disproportionations, acid-base and redox reactions have been addressed in a biologically relevant context, by using an adequate model approach that combines the structural, spectroscopic, and theoretical information most relevant for understanding the enzyme functions. New results on the chemical interactions with O_2 and other gasotransmitters like H_2S point to new developments in the field of biological signaling.

Acknowledgements

To my coworking colleagues and students at INQUIMAE, in the “end of the world” and not so in the end, as reported in the citations, that have sustained and enriched our scientific approach. Support from CONICET, the University of Buenos Aires and the Volkswagen Foundation are gratefully acknowledged.

References

- [1] Bianco, C. L.; Toscano, J. P.; Fukuto, J. M. An Integrated View of the Chemical Biology of NO, CO, H_2S , and O_2 . In *Nitric Oxide*, Elsevier Inc., 2017, Chapter 2, pp. 9-21.
- [2] Kevil, C.; Cortese-Krott, M. M.; Nagy, P.; Papapetropoulos, A.; Feelisch, M. Szabo, C. Cooperative Interactions Between NO and H_2S : Chemistry, Biology, Physiology, Pathophysiology. In *Nitric Oxide*, Elsevier Inc., 2017, Chapter 5, pp. 83-85.
- [3] Ignarro, L. J. Nitric Oxide is not just blowing in the wind. *Brit. J. Pharmacol.* **2019**, *176*, 131-146.
- [4] Yu, M.; Lamattina, L.; Spoel, S. H.; Loake, G. J. Nitric Oxide function in plant biology: a redox cue in deconvolution. *New Phytol.* **2014**, *202*, 1142-1156.
- [5] Feelisch, M.; Stamler, J. S., Eds. *Methods in Nitric Oxide Research*, J. Wiley & Sons: Chichester, 1996.

- [6] Goodrich, L. E.; Paulat, F.; Praneeth, V. K. K.; Lehnert, N. Electronic Structure of Heme-Nitrosyls and its Significance for Nitric Oxide Reactivity, Sensing, Transport and Toxicity in Biological Systems. *Inorg. Chem.* **2010**, *49*, 6293-6316.
- [7] Ford, P.C.; Miranda, K. M. The Solution Chemistry of Nitric Oxide and Other Reactive Nitrogen Species. *Nitric Oxide*, **2020**, *103*, 31-46.
- [8] Cortese-Krott, M.; Koning, A.; Kühnle, G.; Nagy, P.; Bianco, C.; Pasch, A.; Wink, D.; Fukuto, J.; Jackson, A.; van Goor, H.; Olson, K.; Feelisch, M. The Reactive Species Interactome: Evolutionary Emergence, Biological Significance, and Opportunities for Redox Metabolomics and Personalized Medicine. *Antioxid. Redox Signaling*. **2017**, *27*, 684-712.
- [9] Broniowska, K. A.; Hogg, N. The Chemical Biology of S-Nitrosothiols. *Antioxid. Redox Signaling*. **2012**, *17*, 969-980.
- [10] Lehnert, N.; Berto, T. C.; Galinato, M. G. I.; Goodrich, L. E. The Role of Heme-Nitrosyls in the Biosynthesis, Transport, Sensing, and Detoxification of Nitric Oxide (NO) in Biological Systems: Enzymes and Model Complexes. In *Handbook of Porphyrin Science*; World Scientific: NJ, **2011**, *14*, 1-247 (Chapter 263).
- [11] Olabe, J. A. The coordination chemistry of nitrosyl in cyanoferrates. An exhibit of bioinorganic relevant reactions. *Dalton Trans.* **2008**, 3633-3648.
- [12] Bari, S. E.; Olabe, J. A.; Slep, L. D. Three Redox States of Metallonitrosyls in Aqueous Solution. *Adv. Inorg. Chem.* **2015**, *67*, 87-144.
- [13] Marcolongo, J. P.; Zeida, A.; Slep, L. D.; Olabe, J. A. Thionitrous Acid/Thionitrite and Perthionitrite Intermediates in the "Crosstalk" of NO and H₂S. *Adv. Inorg. Chem.* **2017**, *70*, 277-309.
- [14] Stanbury, D. M. Reactivity of Inorganic Radicals in Aqueous Solution. In *Physical Inorganic Chemistry, Reactions, Processes, and Applications*, Bakac, A. Ed., Wiley, 2010, Chapter 9, pp 395-427.
- [15] Goldstein, S.; Czapski, G. Kinetics of Nitric Oxide Autoxidation in Aqueous Solution in the Absence and Presence of Various Reductants. The Nature of the Oxidizing Intermediates. *J. Am. Chem. Soc.* **1995**, *117*, 12078-12084.
- [16] Fukuto, J. A recent history of nitroxyl chemistry, pharmacology, and therapeutic potential. *Brit. J. Pharmacol.* **2019**, *176*, 135-146.
- [17] Doctorovich, F.; Farmer, P. J.; Martí, M. M. Eds. *The Chemistry and Biology of Nitroxyl (HNO)*, Elsevier Inc. 2017.
- [18] Poskrebyshev, G. A.; Shafirovich, V.; Lyman, S. V. Disproportionation Pathways of Aqueous Hyponitrite Radicals (HN₂O₂⁻ / N₂O₂⁻). *J. Phys. Chem. A* **2008**, *112*, 8295-8302.
- [19] Bringas, M.; Semelak, J.; Estrin, D. A. Theoretical investigation of the mechanism of the nitroxyl decomposition in aqueous solution. *J. Inorg. Biochem.* **2016**, *162*, 102-108.
- [20] Wright, A. M.; Hayton, T. W. Understanding the Role of Hyponitrite in Nitric Oxide Reduction. *Inorg. Chem.* **2015**, *54*, 9330-9341.
- [21] Speelman, A. L.; Lehnert, N. Heme versus Non-Heme Iron-Nitroxyl {FeN(H)O}⁸ Complexes: Electronic Structure and Biologically Relevant Reactivity. *Acc. Chem. Res.* **2014**, *47*, 1106-1116.
- [22] Suárez, S. A.; Neuman, N. I.; Muñoz, M.; Alvarez, L.; Bikiel, D.E.; Brondino, C. D.; Ivanovic-Burmazovic, I.; Miljkovic, J. L.; Filipovic, M. R.; Martí, M. A.; Doctorovich, F. Nitric Oxide Is Reduced to HNO by Proton-Coupled Nucleophilic Attack by Ascorbate, Tyrosine, and Other Alcohols. A New Route to HNO in Biological Media? *J. Am. Chem. Soc.* **2015**, *137*, 4720-4727.
- [23] Suárez, S. A.; Muñoz, M.; Alvarez, L.; Venancio, M. F.; Rocha, W. R.; Bikiel, D. E.; Martí, M. A.; Doctorovich, F. HNO Is Produced by the Reaction of NO with Thiols. *J. Am. Chem. Soc.* **2017**, *139*, 14483-14487.
- [24] Venancio, M. F.; Doctorovich, F.; Rocha, W. R. Solvation and Proton-Coupled Electron Transfer Reduction Potential of ²NÖ to ¹HNO in Aqueous Solution: A Theoretical Investigation. *J. Phys. Chem. B* **2017**, *121*, 6618-6625.
- [25] Enemark, J. H.; Feltham, R. D. Principles of structure, bonding and reactivity for metal nitrosyl complexes. *Coord. Chem. Rev.* **1974**, *13*, 339-406.
- [26] McCleverty, J. A. Chemistry of Nitric Oxide Relevant to Biology. *Chem. Rev.* **2004**, *104*, 403-418.

- [27] Olabe, J. A. Chemistry of Bound Nitrogen Monoxide and Related Redox Species. In *Physical Inorganic Chemistry, Reactions, Processes, and Applications*, Bakac, A. Ed., Wiley, 2010, Chapter 7, pp 281-337.
- [28] Carducci, M. D.; Pressprich, M. R.; Coppens, P. Diffraction Studies of Photoexcited Crystals: Metastable Nitrosyl-Linkage Isomers of Sodium Nitroprusside. *J. Am. Chem. Soc.* **1997**, *119*, 2669-2678.
- [29] Chacón Villalba, M. E.; Güida, J. A.; Varetto, E. L.; Aymonino, P. J. The Structure of the FeNO Group in Two Metastable States (MS1 and MS2) of the Nitroprusside Anion in Na₂[Fe(CN)₅NO]·2H₂O. Infrared Spectra and Quantum Chemistry Calculations for the Normal and the ¹⁵N and ¹⁸O Isotopic Substituted Substance. *Inorg. Chem.* **2003**, *42*, 2622-2627.
- [30] García Serres, R.; Grapperhaus, C. A.; Bothe, E.; Bill, E.; Weyhermüller, T.; Neese, F.; Wieghardt, K. Structural, Spectroscopic, and Computational Study of an Octahedral, Non-Heme {FeNO}⁶⁻⁸ Series: [Fe(NO)(cyclam-ac)]^{+2,+1,0}. *J. Am. Chem. Soc.* **2004**, *126*, 5138-5153.
- [31] Immoos, C. E.; Sulc, F. J.; Farmer, P. J.; Czarnecki, K.; Bocian, D.; Levina, A.; Aitken, J. B.; Armstrong, R.; Lay, P. A. Bonding in HNO-Myoglobin as Characterized by X-ray Absorption and Resonance Raman Spectroscopies. *J. Am. Chem. Soc.* **2005**, *127*, 814-815.
- [32] Praneeth, V. K. K.; Paulat, F.; Berto, T. C.; DeBeer George, S.; Nather, C.; Sulok, C. D.; Lehnert, N. Electronic Structure of Six-Coordinate Iron(III)-Porphyrin Adducts: The Elusive Iron(III)-NO(radical) State and Its Influence on the Properties of These Complexes. *J. Am. Chem. Soc.* **2008**, *130*, 15288-15303.
- [33] McQuarters, A. B.; Kampf, J. W.; Alp, E. E.; Hu, M.; Zhao, J.; Lehnert, N. Ferric Heme-Nitrosyl Complexes: Kinetically Robust or Unstable Intermediates? *Inorg. Chem.* **2017**, *56*, 10513-10528.
- [34] Xu, N.; Goodrich, L. E.; Lehnert, N.; Powell, D. R.; Richter-Addo, G. B. Preparation of the Elusive [(por)Fe(NO)(O-ligand)] Complex by Diffusion of Nitric Oxide into a Crystal of the Precursor. *Angew. Chem. Int. Ed.* **2013**, *52*, 3896-3900.
- [35] Xu, N.; Powell, D. R.; Cheng, L.; Richter-Addo, G. B. The first structurally characterized nitrosyl heme thiolate. *Chem. Commun.* **2006**, 2030-2032.
- [36] Hunt, A. P.; Lehnert, N. The Thiolate Trans Effect in Heme {FeNO}⁶ Complexes and Beyond: Insight into the Nature of the Push Effect. *Inorg. Chem.* **2019**, *58*, 17, 11317-11332.
- [37] Shimizu, H.; Obayashi, E.; Gomi, Y.; Arakawat, S.; Park, Y.; Nakamura, S.; Adachi, I.; Shoun, H.; Shiro, Y. Proton delivery in NO reduction by fungal nitric-oxide reductase: Cryogenic crystallography, spectroscopy, and kinetics of ferric-NO complexes of wild-type and mutant enzymes. *J. Biol. Chem.* **2000**, *275*, 4816-4825.
- [38] Codesido, N. O.; Weyhermüller, T.; Olabe, J. A.; Slep, L. D. Nitrosyl-Centered Redox and Acid-Base Interconversions in [Ru(Me₃[9]aneN₃)(bpy)(NO)]^{3,2,1+}. The pK_a of HNO for its Nitroxyl Derivative in Aqueous Solution. *Inorg. Chem.* **2014**, *53*, 981-997.
- [39] Levin, N.; Codesido, N. O.; Marcolongo, J. P.; Alborés, P.; Weyhermüller, T.; Olabe, J. A.; Slep, L. D. Remarkable Changes of the Acidity of Bound Nitroxyl (HNO) in the [Ru(Me₃[9]aneN₃)(L²)(NO)]ⁿ⁺ Family (n = 1-3). Systematic Structural and Chemical Exploration and Bioinorganic Chemistry Implications. *Inorg. Chem.* **2018**, *57*, 12270-12281.
- [40] Ford, P. C.; Melo Pereira, J. C.; Miranda, K. M. Mechanisms of nitric oxide reactions mediated by biologically relevant metal centers. *Struct. Bond.* **2014**, *154*, 99-136.
- [41] Franke, A.; Roncaroli, F.; van Eldik, R. Mechanistic Studies on the Activation of NO by Iron and Cobalt Complexes. *Eur. J. Inorg. Chem.* **2007**, 773-798.
- [42] Roncaroli, F.; Olabe, J. A.; van Eldik, R. Kinetics and Mechanism of the Formation of Nitroprusside from Aquapentacyanoferrate(III) and NO: Complex-Formation is Controlled by Outer-Sphere Electron Transfer. *Inorg. Chem.* **2002**, *41*, 5417-5425.
- [43] Roncaroli, F.; Olabe, J. A.; van Eldik, R. Kinetics and Mechanism of the Interaction of Nitric Oxide with Pentacyanoferrate(II). Formation and Dissociation of [Fe(CN)₅NO]³⁻. *Inorg. Chem.* **2003**, *42*, 4179-4189.

- [44] Speelman, A. L.; Zhang, B.; Krebs, C.; Lehnert, N. Structural and Spectroscopic Characterization of a High-Spin {FeNO}⁶ Complex with an Iron(IV)-NO⁻ Electronic Structure. *Angew. Chem. Int. Ed.* **2016**, *55*, 6685-6688.
- [45] Wyllie, G. R. A.; Scheidt, W. R. Solid-State Structures of Metalloporphyrin NO_x Compounds *Chem. Rev.* **2002**, *102*, 1067-1089.
- [46] Estrin, D. A.; Baraldo, L. M.; Slep, L. D.; Barja, B. C.; Olabe, J.A.; Paglieri, L.; Corongiu, G. Theoretical and Experimental Study of Medium Effects on the Structure and Spectroscopy of the [Fe(CN)₅NO]²⁻ Ion. *Inorg. Chem.* **1996**, *35*, 3897-3903.
- [47] Bezerra, C. W. B.; da Silva, S. C.; Gambardella, M. T. P.; Santos, R. H. A.; Plicas, L. M. A.; Tfouni, E.; Franco, D. W. Water π -Donation in trans-Tetrammineruthenium(II): Effect on Coordinated Water Properties Induced by a Trans NO Ligand. *Inorg. Chem.* **1999**, *38*, 5660-5667.
- [48] Manoharan, P. T.; Gray, H. B. Electronic Structures of Metal Pentacyanonitrosyls. *Inorg. Chem.* **1966**, *6*, 823-839.
- [49] González Lebrero, M. C.; Scherlis, D. A.; Estiú, G. L.; Olabe, J. A.; Estrin, D. A. Theoretical Investigation of the Electronic Structure of Pentacyano(L)ferrate(II) Complexes with NO⁺, NO and NO⁻ Ligands. Redox Interconversion, Protonation and Cyanide-Releasing Reactions. *Inorg. Chem.* **2001**, *40*, 4127-4133.
- [50] Roncaroli, F.; Ruggiero, M. E.; Franco, D. W.; Estiú, G. L.; Olabe, J. A. Kinetic, Mechanistic, and DFT Study of the Electrophilic Reactions of Nitrosyl Complexes with Hydroxide. *Inorg. Chem.* **2002**, *41*, 5760-5769.
- [51] Olabe, J. A.; Estiú, G. L. Theoretical Characterization of Stable η^1 -N₂O, η^2 -N₂O, η^1 -N₂, and η^2 -N₂ Bound-Species. Intermediates in the Addition Reactions of Nitrogen Hydrides with the Pentacyanonitrosylferrate(II) Ion. *Inorg. Chem.* **2003**, *42*, 4873-4880.
- [52] Morando, P. J.; Borghi, E. B.; Schteingart, L. M.; Blesa, M. A. The Reaction of Cysteine with the Pentacyanonitrosylferrate(II) Ion. *J. Chem. Soc. Dalton Trans.* **1981**, 435-440.
- [53] Johnson, M. D.; Wilkins, R. G. Kinetics of the primary interaction of pentacyanonitrosylferrate(2-) (nitroprusside) with aliphatic thiols. *Inorg. Chem.* **1984**, *23*, 231-235.
- [54] Roncaroli, F.; Olabe, J. A. The Reactions of Nitrosyl Complexes with Cysteine. *Inorg. Chem.* **2005**, *44*, 4719-4727.
- [55] Quiroga, S. L.; Almaraz, A. E.; Amorebieta, V. T.; Perissinotti, L. L.; Olabe, J. A. Addition and Redox Reactivity of Hydrogen Sulfides (H₂S/HS⁻) with Nitroprusside: New Chemistry of Nitrososulfide Ligands. *Chem. Eur. J.* **2011**, *17*, 4145-4146.
- [56] Roncaroli, F.; Videla, M.; Slep, L. D.; Olabe, J. A. New features in the redox coordination chemistry of metal nitrosyls {M-NO⁺; M-NO⁻; M-NO⁻(HNO)}, *Coord. Chem. Rev.* **2007**, *251*, 1903-1930.
- [57] Doctorovich F.; Trapani, C. The reaction of pentacyanonitrosylferrate(II) with primary amines as a source of stabilized aliphatic diazonium ions: a new route to secondary amines. *Tetrahedron Letters*, **1999**, *40*, 4635-4638.
- [58] Doctorovich, F.; Escola, N.; Trapani, C.; Estrin, D. A.; Turjanski, A. G.; González Lebrero, M. C.; Stabilization of Aliphatic and Aromatic Diazonium Ions by Coordination: An Experimental and Theoretical Study. *Organometallics* **2000**, *19*, 3810-3817.
- [59] Doctorovich, F.; Granara, M.; Di Salvo, F. The reaction of [Ru(bpy)₂(NO)Cl]²⁺ and [Fe(CN)₅NO]²⁻ with benzylamine: coordinated nitrosyl as an oxidizing agent. *Transition Met. Chem.* **2001**, *26*, 505-509.
- [60] Doctorovich, F.; Di Salvo, F. Performing Organic Chemistry with Inorganic Compounds: Electrophilic Reactivity of Selected Nitrosyl Complexes. *Acc. Chem. Res.* **2007**, *40*, 985-993.
- [61] Gutiérrez, M. M.; Amorebieta, V. T.; Estiú, G. L.; Olabe, J. A. The Electrophilic Reactions of Pentacyanonitrosylferrate(II) with Hydrazine and Substituted Derivatives. Catalytic Reduction of Nitrite and Theoretical Prediction of η^1 -, η^2 -N₂O Bound Intermediates. *J. Am. Chem. Soc.* **2002**, *124*, 10307-10319.
- [62] Bykov, D.; Neese, F. Six-Electron Reduction of Nitrite to Ammonia by Cytochrome c Nitrite Reductase. Insights from Density Functional Theory Studies. *Inorg. Chem.* **2015**, *54*, 9303-9316.

- [663] Alluisetti, G. E.; Almaraz, A. E.; Amorebieta, V. T.; Doctorovich, F.; Olabe, J. A. Metal-Catalyzed Anaerobic Disproportionation of Hydroxylamine: Role of Diazene and Nitroxyl Intermediates in the Formation of N_2 , N_2O , NO^+ , and NH_3 . *J. Am. Chem. Soc.* **2004**, *126*, 13432-13442.
- [664] Bari, S. E.; Amorebieta, V. T.; Gutierrez, M. M.; Olabe, J. A.; Doctorovich, F. J. Disproportionation of hydroxylamine by water-soluble iron(III) porphyrinate compounds. *J. Inorg. Biochem.* **2010**, *104*, 30-36.
- [665] Gutiérrez, M. M.; Alluisetti, G. E.; Gaviglio, C.; Doctorovich, F.; Olabe, F. D.; Amorebieta, V. T. Catalytic disproportionation of N-alkylhydroxylamines bound to pentacyanoferrates. *Dalton Trans.* **2009**, 1187-1194.
- [666] Gutiérrez, M. M.; Olabe, J. A.; Amorebieta, V. T. Disproportionation of O-Methylhydroxylamine Catalyzed by Aquapentacyanoferrate(II). *Inorg. Chem.* **2011**, *50*, 8817-8825.
- [667] Filipovic, M. R.; Eberhardt, M.; Prokopovic, V.; Mijuskovic, A.; Orescanin-Dusic, Z.; Reeh, P.; Ivanovic-Burmazovic, I. Beyond H_2S and NO Interplay: Hydrogen Sulfide and Nitroprusside React Directly to Give Nitroxyl (HNO). A New Pharmacological Source of HNO. *J. Med. Chem.* **2013**, *56*, 1499-1508.
- [668] Gao, Y.; Toubaei, A.; Kong, X.; Wu, G. Solving the 170-Year-Old Mystery about Red-Violet and Blue Transient Intermediates in the Gmelin Reaction. *Chem. Eur. J.* **2015**, *21*, 1-7.
- [669] Cortese-Krott, M. M.; Butler, A.; Woolins, J. D.; Feelisch, M. Inorganic sulfur-nitrogen compounds: from gunpowder chemistry to the forefront of biological signaling. *Dalton Trans.* **2016**, *45*, 5908-5919.
- [670] Marcolongo, J. P.; Morzan, U. N.; Zeida, A.; Scherlis, D. A.; Olabe, J. A. Nitrosodisulfide $[S_2NO]^-$ (perthionitrite) is a true intermediate during the “cross-talk” of nitrosyl and sulphide. *Phys. Chem. Chem. Phys.* **2016**, *18*, 30047-30052.
- [671] Ivanovic-Burmazovic, I.; Filipovic, M. R. Saying NO to H_2S : A Story of HNO, HSNO, and $SSNO^-$. *Inorg. Chem.* **2019**, *58*, 4039-4051.
- [672] Marcolongo, J. P.; Venancio, M. F.; Rocha, W. R.; Doctorovich, F.; Olabe, J. A. NO/H_2S “Crosstalk” Reactions. The Role of Thionitrites (SNO^-) and Perthionitrites ($SSNO^-$). *Inorg. Chem.* **2019**, *58*, 14981-4997.
- [673] Hunt, A. P.; Lehnert, N. Heme-Nitrosyls: Electronic Structure Implications for Function in Biology. *Acc. Chem. Res.* **2015**, *48*, 2117-2125.
- [674] Berto, T. C.; Speelman, A. L.; Zheng, S.; Lehnert, N. Mono- and dinuclear non-heme iron-nitrosyl complexes: Models for key intermediates in bacterial nitric oxide reductases. *Coord. Chem. Rev.* **2013**, *257*, 244-259.
- [675] Lehnert, N.; Scheidt, W. R.; Wolf, M. W. Structure and Bonding in Heme-Nitrosyl Complexes and Implications for Biology. *Struct. Bond.* **2014**, *154*, 155-224.
- [676] Nast, R.; Schmidt, J. Cyanonitrosylferrate und Cyanocarbonylnitrosyl-ferrate niedriger Oxydationsstufen. *Z. anorg. Allg. Chem.* **1976**, *421*, 15-23.
- [677] Lehnert, N.; Sage, J. T.; Silvernail, N.; Scheidt, W. R.; Alp, E. E.; Sturhahn, W.; Zhao, J. Oriented Single-Crystal Nuclear Resonance Vibrational Spectroscopy of $[Fe(TPP)(MI)(NO)]$: Quantitative Assessment of the *trans* Effect of NO . *Inorg. Chem.* **2010**, *49*, 7197-7215.
- [678] Schmidt, J.; Kühr, H.; Dorn, W. L.; Kopf, J. Nitrosyl-Tetracyano-Ferrat(I). *Inorg. Nucl. Chem. Lett.* **1974**, *10*, 55-61.
- [679] Silvernail, N. J.; Olmstead, M. M.; Noll, B. C.; Scheidt, W. R. Tetragonal to Triclinic—A Phase Change for $[Fe(TPP)(NO)]$. *Inorg. Chem.* **2009**, *48*, 971-977.
- [680] Bohle, D. S.; Hung, C. H. Ligand Promoted Rapid Dissociations from Ferrous Porphyrin Nitrosyls. *J. Am. Chem. Soc.* **1995**, *117*, 9584-9585.
- [681] Pellegrino, J.; Bari, S. E.; Bikiel, D. E.; Doctorovich, F. Successful Stabilization of the Elusive Species $\{FeNO\}^8$ in a Heme Model. *J. Am. Chem. Soc.* **2010**, *132*, 989-995.
- [682] Wanner, M.; Scheiring, T.; Kaim, W.; Slep, L. D.; Baraldo, L. M.; Olabe, J. A.; Zalis, S.; Baerends, E. J. EPR Characteristics of the $[(NC)_5M(NO)]^{3-}$ Ions ($M = Fe, Ru, Os$). An Experimental and DFT Study Establishing NO as a Ligand. *Inorg. Chem.* **2001**, *40*, 5704-5707.

- [83] Frantz, S.; Sarkar, B.; Sieger, M.; Kaim, W.; Roncaroli, F.; Olabe, J. A.; Zalis, S. EPR Insensitivity of the Metal-Nitrosyl Spin-Bearing Moiety in Complexes $[L_nRu^{II}-NO]^k$. *Eur. J. Inorg. Chem.* **2004**, 2902-2907.
- [84] Singh, P.; Das, A. K.; Sarkar, B.; Niemeyer, M.; Roncaroli, F.; Olabe, J. A.; Fiedler, J.; Zalis, S.; Kaim, W. Redox Properties of Ruthenium Nitrosyl Porphyrin Complexes with Different Axial Ligation: Structural, Spectroelectrochemical (IR, UV-VIS-NIR, ESR) and Theoretical Studies. *Inorg. Chem.* **2008**, 47, 7106-7113.
- [85] Praneeth, W. W. W.; Nather, C.; Peters, G.; Lehnert, N. Spectroscopic Properties and Electronic Structure of Five- and Six-Coordinate Iron(II) Porphyrin NO Complexes: Effect of the Axial N-Donor Ligand. *Inorg. Chem.* **2006**, 45, 2795-2811.
- [86] Cheney, R. P.; Simic, M. G.; Hoffman, M. Z.; Taub, I. A.; Asmus, K. D. One-Electron Reduction of Pentacyanonitrosylferrate(II) Ion in Aqueous Solution. *Inorg. Chem.* **1997**, 16, 2187-2192.
- [87] Schwane, J. D.; Ashby, M. T. FTIR Investigation of the Intermediates Formed in the Reaction of Nitroprusside with Thiolates. *J. Am. Chem. Soc.* **2002**, 124, 6822-6823.
- [88] Derbyshire, E. R.; Marletta, M. A. Structure and Regulation of Soluble Guanylate Cyclase. *Annu. Rev. Biochem.* **2012**, 81, 533-559.
- [89] Guo, Y.; Suess, D. L.; Herzik Jr., M. A.; Iavarone, A. T.; Britt, R. D.; Marletta, M. A. *Nature Chemical Biology*, **2017**, 13, 1216-1221.
- [90] Guo Y.; Marletta, M. A. Structural Insight into H-NOX Gas Sensing and Cognate Signaling Regulation. *ChemBioChem* **2019**, 20, 7-19.
- [91] Roncaroli, F.; van Eldik, R.; Olabe, J. A. Release of NO from Reduced Nitroprusside Ion. Iron-Dinitrosyl Formation and NO-Disproportionation Reactions. *Inorg. Chem.* **2005**, 44, 2781-2790.
- [92] Butler, A. R.; Megson, I. L. Non-Heme Iron Nitrosyls in Biology. *Chem. Rev.* **2002**, 102, 1155-1165.
- [93] Lorkovic, I.; Ford, P. C. Nitric Oxide Addition to the Ferrous Nitrosyl Porphyrins Fe(P)(NO) Gives trans-Fe(P)(NO)₂ in Low-Temperature Solutions. *J. Am. Chem. Soc.* **2000**, 122, 6516-6517.
- [94] Conradie, J.; Wondimagegn, T.; Ghosh, A. Molecular Structure and Conformation of Dinitrosylheme. *J. Am. Chem. Soc.* **2003**, 125, 4968-4969.
- [95] Martí, M.; Capece, L.; Crespo, A.; Doctorovich, F.; Estrin, D. A. Nitric Oxide Interaction with Cytochrome c' and its Relevance to Guanylate Cyclase. Why Does the Iron Histidine Bond Break? *J. Am. Chem. Soc.* **2005**, 127, 7721-7728.
- [96] Videla, M.; Roncaroli, F.; Slep, L. D.; Olabe, J. A. Reactivity of Reduced Nitroprusside, $[Fe(CN)_5NO]^{3-}$, toward Oxygen. *J. Am. Chem. Soc.*, **2007**, 129, 278-279.
- [97] Levin, N.; Osa Codesido, N.; Bill, E.; Weyhermüller, T.; Segantin Gaspari, A. P.; Santana da Silva, R.; Olabe, J. A.; Slep, L. D. Structural, Spectroscopic, and Photochemical Investigation of an Octahedral NO-Releasing $\{RuNO\}^7$ Species. *Inorg. Chem.* **2016**, 55, 7808-7810.
- [98] Armor, J. N.; Hoffman, M. Z. Reactivity of coordinated nitrosyls. IV. One-electron reactivity of ruthenium(III) nitrosylpentaammine ion in aqueous solution. *Inorg. Chem.* **1975**, 14, 444-446.
- [99] Videla, M.; Jacinto, J. S.; Baggio, R.; Garland, M. T.; Singh, P.; Kaim, W.; Slep, L. D.; Olabe, J. A. New Ruthenium Nitrosyl-Complexes with Tris(1-pyrazolyl)methane (tpm) and 2,2'-Bipyridine (bpy) Coligands. Structure, Spectroscopy, Electrophilic and Nucleophilic Reactivities of Bound Nitrosyl. *Inorg. Chem.* **2006**, 45, 8608-8617.
- [100] Osa Codesido N.; De Candia, A. G.; Weyhermüller, T.; Olabe, J. A.; Slep, L. D. An electron-rich $\{RuNO\}^6$ complex: trans-[Ru(DMAP)₄(NO)(OH)]²⁺ (DMAP = 4-N,N'(dimethylaminopyridine). Structure and reactivity. *Eur. J. Inorg. Chem.*, **2012**, 4301-4309.
- [101] Tejero, J.; Hunt, A. P.; Santolini, J.; Lehnert, N.; Stuehr, D. J. Mechanism and regulation of ferrous heme-nitric oxide (NO) oxidation in NO synthases. *J. Biol. Chem.* **2019**, 294, 7904-7916.

- [102] Goodrich, L.; Roy, S.; Ercan Alp, E.; Zhao, J.; Hu, M. Y.; Lehnert, N. Electronic Structure and Biologically Relevant Reactivity of Low-Spin $\{\text{FeNO}\}^8$ Porphyrin Model Complexes: New Insight from a Bis-Picket Fence Porphyrin. *Inorg. Chem.* **2013**, *52*, 7766-7780.
- [103] Weaver, D. L.; Snyder, D. A. Crystal and molecular structure of trans-chloronitrosylbis(ethylenediamine)cobalt(III) perchlorate. *Inorg. Chem.* **1970**, *9*, 2760-2767.
- [104] Grande, L. M.; Noll, B. C.; Oliver, A. G.; Scheidt, W. R. Dynamics of NO Motion in Solid-State $[\text{Co}(\text{tetraphenylporphinato})(\text{NO})]$. *Inorg. Chem.* **2010**, *49*, 6552-6557.
- [105] Hu, B.; Li, J. One Electron Makes Differences: From Heme $\{\text{FeNO}\}^7$ to $\{\text{FeNO}\}^8$. *Angew. Chem. Int. Ed.* **2015**, *52*, 10579-10582.
- [106] Montenegro, A. C.; Amorebieta, V. T.; Slep, L. D.; Martín, D. F.; Roncaroli, F.; Murgida, D. H.; Bari, S. E.; Olabe, J. A. Three Redox States of Nitrosyl: NO^+ , NO^\bullet and NO^-/HNO Interconvert Reversibly on the Same Pentacyanoferrate(II) Platform. *Angew. Chem. Int. Ed.* **2009**, *48/23*, 4213-4216.
- [107] Montenegro, A. C.; Bari, S. E.; Olabe, J. A. Reactivity of iron(II)-bound nitrosyl hydride (HNO , nitroxyl) in aqueous solution. *J. Inorg. Biochem.* **2013**, *118*, 108-114.
- [108] Sellmann, D.; Gottschalk-Gaudig, T.; Haussinger, D.; Heinemann, F. W.; Hess, B. A. $[\text{Ru}(\text{HNO})(\text{py}^{\text{bu}}\text{S}_4)]$, the First HNO Complex Resulting from Hydride Addition to a NO Complex ($\text{py}^{\text{bu}}\text{S}_4^{2-} = 2,6\text{-Bis}(2\text{-mercapto-}3,5\text{-di-tert-butylphenylthio})\text{dimethylpyridine}(2-)$). *Chem. Eur. J.* **2001**, *7*, 2099-2103.
- [109] Lee, J.; Richter-Addo, G. B. A nitrosyl hydride complex of a heme model $[\text{Ru}(\text{ttp})(\text{HNO})(1\text{-MeIm})]$ ($\text{ttp} = \text{tetratolylporphyrinato dianion}$). *J. Inorg. Biochem.* **2004**, *98*, 1247-1250.
- [110] Wilson, R. D.; Ibers, J. A. Coordinated nitrosyl hydride: structural and spectroscopic study of dichlorocarbonyl(nitrosyl hydride)bis(triphenylphosphine)osmium(II). *Inorg. Chem.* **1979**, *18*, 336-343.
- [111] Gao, Y.; Toubaei, A.; Kong, X.; Wu, G. Acidity and Hydrogen Exchange Dynamics of Iron(II)-Bound Nitroxyl in Aqueous Solution. *Angew. Chem.* **2014**, *126*, 11731-11735.
- [112] Lin, R.; Farmer, P. J. The HNO Adduct of Myoglobin: Synthesis and Characterization. *J. Am. Chem. Soc.* **2000**, *122*, 2393-2394.
- [113] Goodrich, L. E.; Lehnert, N. The *trans* effect of nitroxyl (HNO) in ferrous heme systems: Implications for soluble guanylate cyclase activation by HNO . *J. Inorg. Biochem.* **2013**, *118*, 179-186.
- [114] Mazzeo, A.; Pellegrino, J.; Doctorovich, F. Water-Soluble Nitroxyl Porphyrin Complexes $\text{Fe}^{\text{II}}\text{TPPSHNO}$ and $\text{Fe}^{\text{II}}\text{TPPSNO}^-$ Obtained from Isolated $\text{Fe}^{\text{II}}\text{TPPSNO}$. *J. Am. Chem. Soc.* **2019**, *141*, 18521-18530.

Bio



José A. Olabe

José A. Olabe was born in San Sebastián (Spain), and performed undergraduate, doctoral and postdoctoral studies at La Plata

University (Argentina). He was a Visiting Professor at SUNY, Stony Brook, and is an Emeritus Professor at the University of Buenos Aires. As a member of the National Research Council, his research interest deals with the coordination chemistry of small nitrogenated molecules to biologically relevant transition metal centers, with emphasis on the kinetic and mechanistic properties.

INSTRUCTIONS FOR AUTHORS

GUIDELINES

1. Length

Research reviews should not be less than 7000 words or more than 10,000 words (plus up to 15 figures and up to 50 references).

2. Structure

Whenever possible articles should adjust to the standard structure comprising:

- (a) Graphical abstract,
- (b) Abstract,
- (c) Introduction describing the focus of the review,
- (d) Article main body including assessment and discussion of available information (may be further subdivided),
- (e) Conclusions,
- (f) Bibliography.

3. Format

Authors must submit their articles in a Microsoft Word archive. Figures must be embedded in the article and also submitted in a separate .zip or .rar file.

4. References

References must be numbered in the text ([1] [2] [3]) and identified with the same numbers in the *References* section. Up to 50 references are allowed. The following are examples to take into account in each case.

BOOKS:

- Single author

Chung, R. *General Chemistry: Fundamental Knowledge*, 2nd ed.; McGuffin-Hill: Kansas City, 2003.

- More than one author

Chung, R.; Williamson, M. *General Chemistry: Fundamental Knowledge*, 2nd ed.; McGuffin-Hill: Kansas City, 2003.

- Edited Book

Kurti, F. Photodissociation and Reactive Scattering. In *The Rise of Chemical Physics*; White, AD, Ed.; Wilson: New Jersey, 2007; Vol. 128; p. 257.

- Book in Series

Goth, V. Polymer Chemistry. In *The Foundational Course in Organic Chemistry*; ACDC Symposium Series 1151; American Chemical Fraternity: Seattle, 2014; pp 123-149.

- Article from a reference book

Powder and Metallurgy. *Dictionary of Chemical Technology*, 3rd ed.; Wilson: New Jersey, 1971; Vol. 12, pp 68-82.

ARTICLES:

- Article in a scientific journal

Evans, A.; Stitch, M.; Smithers, ET; Nope, JJ Complex Aldol Reactions to the Total Synthesis of

Phorboxazole B. *J. Am. Chem. Soc.* 2012, 122, 10033-10046.

- Article in a popular/non-scientific magazine

Tatum, CJ Super Organics. *Wireless*, June 2001, pp 76-93.

- Article from an online journal

Turkey-Lopez, E. Inexact Solutions of the Quantum Double Square-Well Potential. *Chem. Ed.* [Online] 2007, 11, pp. 838-847. <http://chemeducator.org/bibs/0011006/11060380lb.htm> (accessed Aug 5, 2019).

PUBLICATION ETHICS

The journal considers that the primary objective of all submissions must be a contribution of relevant and appropriate content, and that all review processes must be structured based on that general criterion. Therefore, there is an emphasis on the concern to maintain the highest quality and ethics standards in the reception, evaluation and publication of articles. These standards include the three participants of the process: author, reviewer and editor.

1. Author's responsibilities

- Submitted manuscripts should maintain rigorous scientific criteria for data validation and conclusions.
- All data (Figures, Tables, etc.) reproduced from previous published articles must give the appropriate recognition to the source. Plagiarism is cause enough to reject the submission.
- Authorship must include all individuals who have contributed in a substantial way to the composition, prior investigation, and execution of the paper. Minor contributions must be acknowledged, but these contributors should not be listed as authors. The main author or authors of the article will make sure that all participants of the paper have approved the final version of the document submitted.
- All authors must reveal in their final manuscript any financial or other type of conflict of interests that might interfere with the results and interpretations in their research. All funding received to carry out the project must be acknowledged.
- After the article is published, in the event an author notices a crucial fault or inaccuracy, he or she should immediately report that fault or inaccuracy, so that an Erratum can be issued as soon as possible.

2. Reviewer's responsibilities

Reviewing is a time-consuming process that is carried out *ad honorem* by *bona fide* scientists conversant with the subject of the reviewed paper. The quality and the ethical standards of the journal depend critically on the quality of the reviewing process, and the following guidelines are established:

- All documents sent to the journal for review will be considered confidential documents and will not be discussed with external third parties.
- When invited, a potential reviewer should decline if: (a) the subject of the article is not within his/her area of expertise; (b) there is any kind of conflict of interest; (c) if the review cannot be finished within the period established by the journal.
- Any criticism or objections to the paper should be done in a neutral tone and based on reasonable grounds, not limited to simple opinions or purely subjective expressions.

3. Editor's responsibilities

- The editors are responsible for selecting the papers that will be published in the journal. The Editorial Management must comply with the ethical standards of the journal, as well as with all legal guidelines, including the prohibition of plagiarism and any other form of copyright infringement.
- The editors will evaluate and make decisions on the articles sent to the journal regardless of the

gender, sexual orientation, religious beliefs, ethnic origin, nationality or political ideology of the authors.

- Revealing information identifying reviewers is forbidden.
- The final version of all materials can be published only with the prior approval of their author.
- The editors will refrain from publishing manuscripts that imply a conflict of interests because of any possible connection with other institutions, companies and authors.
- Before deciding to send an article to a peer review, the editors are committed to thoroughly read all texts received and determine their appropriateness to the thematic universe of the journal.
- If a misbehavior or unethical action by an author or reviewer is identified, the editors must request the informer of such conduct or action to provide the evidence that may justify a possible investigation. All accusations will be handled seriously until reliable results are obtained regarding its truthfulness or falseness. If an investigation takes place, the editors are responsible for choosing the appropriate way in which it will be carried out. They can also request the advice and assistance from the Editorial Board, as well as from reviewers and authors.
- In the event a serious non-malicious mistake or a dishonest conduct by an author or a reviewer is proved, the editors shall act according to the nature and seriousness of the case. The actions the editors may take include, but are not limited to: notifying the author or reviewer of the existence of a serious mistake or misapplication of the ethical standards of the journal; writing a strong statement that reports and warns about a bad practice or unethical behavior; publishing that statement; unilaterally withdrawing the reported paper from the review or publication process; revoking the paper if it has already been published; communicating the journal's decision and the reasons behind it to the general public; and banning paper submissions by the people involved for a certain period of time.

PRIVACY STATEMENT

The names and email addresses entered in this journal site will be used exclusively for the stated purposes of this journal and will not be made available for any other purpose or to any other party.

NEXT ISSUE

Vol. 2, No. 2

TO BE PUBLISHED ON MARCH 15, 2021

We are preparing a special issue covering the ongoing R&D projects on COVID-19 in Argentina.

ISSN 2683-9288



Science Reviews

from the end of the world

Centro de Estudios sobre Ciencia, Desarrollo
y Educación Superior

538 Pueyrredón Av. - 2° C - Second building

Buenos Aires, Argentina - C1032ABS

(54 11) 4963-7878/8811

sciencereviews@centroredes.org.ar

www.scirevfew.net

